Journal of
Mechanics of
Materials and Structures

JOURNAL OF MECHANICS OF MATERIALS AND STRUCTURES

jomms.org

Founded by Charles R. Steele and Marie-Louise Steele

Cover design: Alex Scorpan   Cover photo: Ev Shafrir

See http://jomms.org for submission guidelines.

msp

MODELLING OF ACOUSTODIFFUSIVE SURFACE WAVES IN PIEZOELECTRIC-SEMICONDUCTOR COMPOSITE STRUCTURES

J. N. SHARMA, K. K. SHARMA AND ASHWANI KUMAR

We investigate the propagation of interfacial surface waves in a composite consisting of homogeneous isotropic semiconductor halfspace coated with a thin layer of homogeneous, transversely isotropic, piezo-electric material. The mathematical model of the problem consists of a coupled system of partial differential equations of motion, diffusion of electrons, and a Gauss equation along with the boundary conditions to be satisfied at the interface and free surface of the composite structure.

The secular equation that governs the wave propagation at the interface has been obtained in compact form after solving the mathematical model analytically. The secular equations in the case of stress-free, isoconcentrated and stress-free, impermeable semiconductor halfspaces have also been deduced as special cases. The complex secular equation has been solved using the functional iteration method along with the irreducible Cardano's method via MATLAB programming for CdSe-Si, CdSe-Ge, PZT-Si and PZT-Ge composite structures.

The computer-simulated results have been presented graphically in terms of phase velocity, attenuation coefficient, and specific loss factor of energy dissipation versus wave number and lifetime of charge carrier field in the considered structures. The work may be useful for the construction and design of surface acoustic wave devices.

1. Introduction

Surface acoustic waves bonded to piezoelectric surfaces have found significant use in various branches of science and technology, especially in the case of interconnected physical fields. These waves were first discovered by Rayleigh [1885], who explained their propagation and characteristics. In [White 1967], the phenomena of surface elastic wave propagation, transduction, and amplification in a piezoelectric semiconductor with special emphasis in relation to electronic devices were discussed. In [Bleustein 1968] the propagation of surface acoustic waves at the free surface of a piezoelectric halfspace was predicted. Gulyaev [1969] explained that a pure transverse wave can propagate along the surface of a homogeneous piezoelectric solid with polarization vector parallel to the surface of the substrate. In [de Lorenzi and Tiersten 1975; Maugin and Daher 1986] nonlinear theories for deformable semiconductors were developed.

Maruszewski [1989] analyzed the effect of interactions between elastic, thermal, and charge carrier fields on Rayleigh waves in addition to electron longitudinal waves in semiconductors. In [Sharma and Thakur 2006] a detailed account of plane harmonic generalised elastothermodiffusive waves in

semiconductor materials was given, suggesting that there are significant modifications in the phase velocities and attenuation coefficients of these waves due to the interactions of mechanical, thermal, and charge carrier fields. In [Sharma and Pathania 2006] the thermoelastic waves in coated homogeneous anisotropic materials were studied to show that anisotropy has significant effect on the phase velocity and attenuation profiles. In [Sharma et al. 2007] it was found that the age of carrier fields also effects wave propagation in semiconductor materials. In [Sharma et al. 2009] it was observed that semiconductor materials exhibit more internal friction with the age of the carrier fields than that of thermal relaxation time. In [Sharma and Pal 2004] the Lamb wave propagation in a transversely isotropic piezothermoelastic plate was investigated. In [Sharma et al. 2010] the propagation of surface waves in a piezoelectric halfspace coated with a semiconductor layer was analyzed.

In [Kagan 1997] the surface wave propagation in a piezoelectric crystal underlying a conducting layer was considered. It was predicted that the electric field excited by the wave in crystal would penetrate into the conducting layer. In [Wang and Varadan 2002] the dispersion characteristics and mode shapes of wave propagation in a piezoelectric layer bonded to the metal substrate were studied. In [Wang 2002] an investigation was conducted into wave propagation in a semiinfinite metallic surface bonded to a layer of piezoelectric material. It was found that the piezoelectric effects dominated the dispersive characteristics at higher wave numbers.

Trolier-Mckinstry and Muralt [2004] explained that thin-film piezoelectric materials offer a number of advantages in microelectromechanical systems and the resulting properties are dominantly dependant on the characteristics of piezoelectric film. In [Du et al. 2007] the Love waves in a functionally graded material layer bonded to a semiinfinite, homogeneous solid were investigated. It was observed that the material properties enable Love waves to propagate along the surface of the layer and may be useful in reducing the dimension of surface acoustic wave (SAW) devices. Jin et al. [2002] studied the Lamb wave propagation in a metallic semiinfinite medium covered with a piezoelectric layer. It was found that the dispersion curves are asymptotic to the transverse velocity of the piezoelectric layer with increasing wave number. In [Melkumyan and Mai 2009] shear surface waves guided by a gap between dissimilar piezoelectric halfspaces were studied. It was concluded that the gap waves were mainly concentrated at the interface of the piezoelectric halfspaces and decayed exponentially away from it. In [Liu et al. 2004] the propagation of surface acoustic waves in a layered halfspace were analyzed, finding that the maximum change in phase velocity occurs for large values of the product of wave number and film thickness.

The design and micromachining of PZT/CdSe thin-layered composites for device applications requires more research in future. Therefore, it is worth investigating the wave propagation parameters in these materials. Keeping in view the wide range applications of composite structures and the above-referred work, an attempt has been made here to study the propagation of surface waves at the interface of a piezoelectric-semiconductor composite structure. The phase velocity, attenuation coefficient, and specific loss factor of energy dissipation for different modes of wave propagation have been computed numerically from the analytically developed model in four types of composite structures: CdSe-Si, PZT-Si, CdSe-Ge, and PZT-Ge. The effect of carrier lifetime has also been taken into account.

The present study shows that PZT-Ge is a good combination for piezoelectric-semiconductor device applications. According to [Muralt and Baborowski 2004] such composites can find applications in ultrasonic transducers and acoustic sensors.

2. Formulation of the problem

Consider a homogeneous isotropic semiconductor halfspace whose surface is coated with a thin layer of homogeneous, transversely isotropic, piezoelectric material of thickness h as shown in Figure 1. The origin of the coordinate system $O - xyz$ is taken at any point on the interface plane and the z-axis points vertically downward into the semiconductor halfspace. Thus, the semiconductor halfspace is represented by $z \geq 0$ and the piezoelectric layer occupies the region $-h \leq z \leq 0$ whose poling direction also aligns along the z-axis. The x-axis is chosen along the direction of wave propagation in such a way that all particles on the line parallel to the y-axis are equally displaced. Therefore, all the field quantities are independent of the y-coordinate and hence we restrict our investigation to the plane strain problem only.

Further, the disturbance is assumed to be confined in the neighborhood of the interface ($z = 0$), and hence vanishes as $z \rightarrow \infty$. The basic governing equations of motion, Gauss equation, and electron diffusion for the composite structure under study, in the absence of body forces and electric sources, are given below.

(i) Homogeneous isotropic n-type semiconductor halfspace [Maruszewski 1989; Sharma et al. 2007]:

$$\mu \nabla^2 \vec{u}^s + (\lambda + \mu) \nabla \nabla \cdot \vec{u}^s - \lambda^n \nabla N = \rho^s \ddot{\vec{u}}^s, \tag{1}$$

$$\rho^s D^n \nabla^2 N - \rho^s \left(1 + t^n \frac{\partial}{\partial t}\right) \dot{N} - a_2^n T_0 \lambda^T \nabla \cdot \dot{\vec{u}}^s = -\left(1 + t^n \frac{\partial}{\partial t}\right) \left(\frac{\rho^s}{t_n^+}\right) N. \tag{2}$$

(ii) Homogeneous transversely isotropic piezoelectric (6 mm class) layer [Sharma and Pal 2004]:

$$c_{11} u_{,xx}^P + c_{44} u_{,zz}^P + (c_{13} + c_{44}) w_{,xz}^P + (e_{15} + e_{31}) \phi_{,xz}^P = \rho^P \ddot{u}^P, \tag{3}$$

$$(c_{13} + c_{44}) u_{,xz}^P + c_{44} w_{,xx}^P + c_{33} w_{,zz}^P + e_{15} \phi_{,xx}^P + e_{33} \phi_{,zz}^P = \rho^P \ddot{w}^P, \tag{4}$$

$$(e_{15} + e_{31}) u_{,xz}^P + e_{15} w_{,xx}^P + e_{33} w_{,zz}^P - \varepsilon_{11} \phi_{,xx}^P - \varepsilon_{33} \phi_{,zz}^P = 0, \tag{5}$$

where the notation $\nabla^2 = \partial^2/\partial x^2 + \partial^2/\partial z^2$, $N = n - n_0$, $a_2^n = a^{Qp}/a^Q$, and $\lambda^T = (3\lambda + 2\mu)\alpha_T$ is used. Here λ and μ are Lamè parameters, ρ^s is the density, λ^n are the elastodiffusive constants of electrons, D^n are the diffusion coefficients of electrons, t_n^+ and t^n are the life and relaxation times of the carriers fields, n_0 and n are the equilibrium and nonequilibrium values of electron concentration, and α_T is the coefficient of linear thermal expansion of the semiconductor material. The quantities a^{Qp} and a^Q are flux-like constants and T_0 is the uniform temperature; $\vec{u}^s = (u^s, 0, w^s)$ and $\vec{u}^P = (u^P, 0, w^P)$ are the displacement vectors for semiconductor and piezoelectric materials, respectively. The quantities ϕ^P, ρ^P, c_{ij}, and e_{ij} are the electric potential, density, elastic parameters, and piezoelectric constants, respectively; ε_{11} and
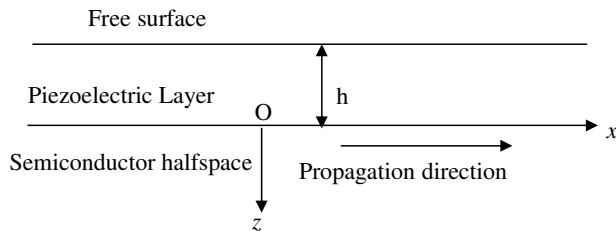

Figure 1. Geometry of the problem.

ε_{33} are the electric permittivity perpendicular to and along the axis of symmetry of the piezoelectric material, respectively.

In the above equations the superposed dots on various quantities denote time differentiation and comma notation is used for spatial derivatives. Throughout this paper the superscripts p and s on the field quantities and material parameters refer to piezoelectric and semiconductor materials, respectively.

The nonvanishing components of stresses, current density, and electric displacement in both the media are

$$\tau_{zz}^s = (\lambda + 2\mu)\frac{\partial w^s}{\partial z} + \lambda \frac{\partial u^s}{\partial x} - \lambda^n N, \quad \tau_{xz}^s = \mu\left(\frac{\partial u^s}{\partial z} + \frac{\partial w^s}{\partial x}\right), \quad J_z^s = -eD^n N_{,z}, \tag{6}$$

for the semiconductor medium and

$$\tau_{zz}^p = c_{13}\frac{\partial u^p}{\partial x} + c_{33}\frac{\partial w^p}{\partial z} + e_{33}\frac{\partial \phi^p}{\partial z},$$

$$\tau_{xz}^p = \frac{c_{44}}{2}\left(\frac{\partial u^p}{\partial z} + \frac{\partial w^p}{\partial x}\right) + e_{15}\frac{\partial \phi^p}{\partial x}, \tag{7}$$

$$D_z^p = e_{31}\frac{\partial u^p}{\partial x} + e_{33}\frac{\partial w^p}{\partial z} - \varepsilon_{33}\frac{\partial \phi^p}{\partial z},$$

in the case of the piezoelectric material. Here τ_{ij}^s and τ_{ij}^p are the stress tensors. The quantities J_z^s and $N_{,z}$ respectively denote the current density and carrier density gradient in the semiconductor material; D_z^p is the electric displacement vector of the piezoelectric material and e is the electronic charge.

2.1. Boundary conditions. The requirement of continuity of stresses, displacements, electric field, and current density at the interface ($z = 0$) of the two media leads to the following interfacial boundary conditions:

$$\tau_{zz}^p = \tau_{zz}^s, \quad \tau_{xz}^p = \tau_{xz}^s, \quad u^p = u^s, \quad w^p = w^s, \quad \phi^p = N, \quad D_z^p = J_z^s. \tag{8}$$

Also the surface ($z = -h$) of the piezoelectric material is assumed to be stress-free and charge-free, which leads to the conditions

$$\tau_{zz}^p = 0, \quad \tau_{xz}^p = 0, \quad D_z^p = 0. \tag{9}$$

In order to simplify the above model, we define the following dimensionless quantities:

$$x' = \frac{\omega^* x}{v_l}, \qquad z' = \frac{\omega^* z}{v_l}, \qquad t' = \omega^* t, \qquad t^{n'} = \omega^* t^n,$$

$$t_n^{+'} = \omega^* t_n^+, \qquad N' = \frac{N}{n_0}, \qquad D_z^{p'} = \frac{\rho^s v_l^2}{\lambda^n n_0 e_{33}}D_z^p, \qquad u^{s'} = \frac{\rho^s \omega^* v_l}{\lambda^n n_0}u^s,$$

$$w^{s'} = \frac{\rho^s \omega^* v_l}{\lambda^n n_0}w^s, \qquad u^{p'} = \frac{\rho^s \omega^* v_l}{\lambda^n n_0}u^p, \qquad w^{p'} = \frac{\rho^s \omega^* v_l}{\lambda^n n_0}w^p, \qquad \tau_{ij}^{p'} = \frac{\tau_{ij}^p}{\lambda^n n_0},$$

$$\tau_{ij}^{s'} = \frac{\tau_{ij}^s}{\lambda^n n_0}, \qquad J_z^{s'} = \frac{J_z^s}{en_0 v_l}, \qquad c_1 = \frac{c_{33}}{c_{11}}, \qquad c_2 = \frac{c_{44}}{c_{11}},$$

$$c_3 = \frac{c_{13}+c_{44}}{c_{11}}, \qquad e_1 = \frac{e_{15}+e_{31}}{e_{33}}, \qquad v_l^2 = \frac{\lambda + 2\mu}{\rho^s}, \qquad e_2 = \frac{e_{15}}{e_{33}},$$

$$\bar{\varepsilon} = \frac{\varepsilon_{11}}{\varepsilon_{33}}, \qquad \eta_3 = \frac{\varepsilon_{33}c_{11}}{e_{33}^2}, \qquad \omega' = \frac{\omega}{\omega^*}, \qquad c' = \frac{c}{v_l},$$

$$v_p = \sqrt{\frac{c_{11}}{\rho^p}}, \qquad \bar{\rho} = \frac{\rho^p}{\rho^s}, \qquad \bar{\lambda}_n = \frac{\lambda^n n_0}{\lambda^T T_0}, \qquad \delta_1^2 = \frac{v_l^2}{v_p^2},$$

$$\phi^{p'} = \varepsilon_p \phi^p, \qquad \varepsilon_p = \frac{e_{33}\omega^* \rho^s v_l}{c_{11}\lambda^n n_0}, \qquad \varepsilon_n = \frac{a_2^n \lambda^{T^2} T_0 \bar{\lambda}_n}{\rho^s(\lambda + 2\mu)n_0}, \qquad \omega^* = \frac{v_l^2}{D^n}, \tag{10}$$

$$\delta^2 = \frac{v_t^2}{v_l^2}, \qquad v_t^2 = \frac{\mu}{\rho^s}.$$

Here ω^* is the characteristic frequency and v_l and v_t are, respectively, the longitudinal and shear wave velocities.

On substituting quantities (10) in (1)–(7), we obtain

$$\delta^2 \nabla^2 \vec{u}^s + (1 - \delta^2)\nabla\nabla \cdot \vec{u}^s - \nabla N = \ddot{\vec{u}}^s, \tag{11}$$

$$\nabla^2 N - \left[-\frac{1}{t_n^+} + \left(1 - \frac{t^n}{t_n^+}\right)\frac{\partial}{\partial t} + t^n \frac{\partial^2}{\partial t^2}\right]N - \varepsilon_n \nabla \cdot \dot{\vec{u}}^s = 0, \tag{12}$$

$$u_{,xx}^p + c_2 u_{,zz}^p + c_3 w_{,xz}^p + e_1 \phi_{,xz}^p = \delta_1^2 \ddot{u}^p, \tag{13}$$

$$c_3 u_{,xz}^p + c_2 w_{,xx}^p + c_1 w_{,zz}^p + e_2 \phi_{,xx}^p + \phi_{,zz}^p = \delta_1^2 \ddot{w}^p, \tag{14}$$

$$e_1 u_{,xz}^p + e_2 w_{,xx}^p + w_{,zz}^p - \eta_3 \bar{\varepsilon}\phi_{,xx}^p - \eta_3 \phi_{,zz}^p = 0, \tag{15}$$

$$\tau_{zz}^s = (1 - 2\delta^2)\frac{\partial u^s}{\partial x} + \frac{\partial w^s}{\partial z} - N, \quad \tau_{xz}^s = \delta^2\left(\frac{\partial u^s}{\partial z} + \frac{\partial w^s}{\partial x}\right), \quad J_z^s = -N_{,z} \tag{16}$$

$$\tau_{zz}^p = \frac{\bar{\rho}}{\delta_1^2}\left\{(c_3 - c_2)\frac{\partial u^p}{\partial x} + c_1\frac{\partial w^p}{\partial z} + \phi_{,z}^p\right\}, \quad \tau_{xz}^p = \frac{\bar{\rho}}{\delta_1^2}\left\{\frac{c_2}{2}\left(\frac{\partial u^p}{\partial z} + \frac{\partial w^p}{\partial x}\right) + e_2\phi_{,x}^p\right\},$$

$$D_z^p = (e_1 - e_2)\frac{\partial u^p}{\partial x} + \frac{\partial w^p}{\partial z} - \eta_3\phi_{,z}^p. \tag{17}$$

The scalar and vector point potential functions ϕ^s and ψ^s in the semiconductor medium through the relations are introduced as

$$u^s = \frac{\partial \phi^s}{\partial x} + \frac{\partial \psi^s}{\partial z}, \quad w^s = \frac{\partial \phi^s}{\partial z} - \frac{\partial \psi^s}{\partial x}, \tag{18}$$

to facilitate the solutions in semiconductor material.

Using relations (18) in (11) and (12), we obtain

$$\nabla^2 \phi^s - N - \ddot{\phi}^s = 0, \tag{19}$$

$$\nabla^2 \psi^s = \frac{\ddot{\psi}^s}{\delta^2}, \tag{20}$$

$$\nabla^2 N - \left[-\frac{1}{t_n^+} + \left(1 + \frac{t^n}{t_n^+}\right)\frac{\partial}{\partial t} + t^n\frac{\partial^2}{\partial t^2}\right]N - \varepsilon_n \nabla^2 \dot{\phi}^s = 0. \tag{21}$$

Equation (20) corresponds to purely transverse waves in the semiconductor which get decoupled from rest of the motion and are not affected by the charge carrier fields.

3. Formal solution of the problem

We assume the harmonic wave solution of the form

$$(\psi^s, \phi^s, N, u^p, w^p, \phi^p) = (\bar{\psi}^s, \bar{\phi}^s, \bar{N}, \bar{u}^p, \bar{w}^p, \bar{\phi}^p) \exp\{ik(x - ct)\}, \tag{22}$$

where $c = \omega/k$ is the phase velocity and k and ω are the wave number and angular frequency, respectively.

Upon imposing solution (22) in (13)–(15) and (19)–(21), straightforward algebraic simplifications lead to the following formal solution satisfying the radiation conditions in both the media:

(i) Semiconductor (n-type) halfspace ($z \geq 0$):

$$(\phi^s, N) = \sum_{i=1}^{2}(1, S_i)A_i^s e^{-n_i z} \exp\{ik(x - ct)\}, \quad \psi^s = A_3^s \exp\{-\beta z + ik(x - ct)\}. \tag{23}$$

(ii) Piezoelectric (6 mm class) layer $0 \leq z \leq -h$:

$$u^p = \sum_{i=1}^{3}(A_i^p e^{m_i z} + B_i^p e^{-m_i z}) \exp\{ik(x - ct)\},$$

$$(w^p, \phi^p) = \sum_{i=1}^{3}(M_i, P_i)(A_i^p e^{m_i z} - B_i^p e^{-m_i z}) \exp\{ik(x - ct)\}, \tag{24}$$

where

$$\alpha^2 = k^2(1 - c^2), \qquad S_i = n_i^2 - \alpha^2, \qquad n_i^2 = k^2(1 - c^2 a_i^2), \quad i = 1, 2,$$

$$\beta^2 = k^2\left(1 - \frac{c^2}{\delta^2}\right), \qquad \xi = (1 - \delta_1^2 c^2), \tag{25}$$

$$A = (c_1\bar{\varepsilon} + c_2 - \delta_1^2 c^2)\eta_3 + 2e_2, \qquad\qquad B = (c_2 - \delta_1^2 c^2)\eta_3\bar{\varepsilon} + e_2^2,$$

$$a_1^2 + a_2^2 = 1 + t^n + i\omega^{-1}\left(1 + \varepsilon_n - \frac{t^n}{t_n^+}\right) + \frac{1}{\omega^2 t_n^+}, \qquad a_1^2 a_2^2 = t^n + i\omega^{-1}\left(1 - \frac{t^n}{t_n^+}\right) + \frac{1}{\omega^2 t_n^+}, \tag{26}$$

$$m_1^2 m_2^2 + m_2^2 m_3^2 + m_3^2 m_1^2 = k^4 \frac{c_2 B + \xi A - c_3(c_2\eta_3\bar{\varepsilon} + 2e_1 e_2) + e_1^2(c_2 - \delta_1^2 c^2)}{c_2(1 + \eta_3 c_1)},$$

$$m_1^2 + m_2^2 + m_3^2 = k^2 \frac{c_2 A + \xi(1 + \eta_3 c_1) - c_3(c_3\eta_3 + 2e_1) + c_1 e_1^2}{c_2(1 + \eta_3 c_1)}, \qquad m_1^2 m_2^2 m_3^2 = k^6 \frac{\xi B}{c_2(1 + \eta_3 c_1)}, \tag{27}$$

$$M_i = \frac{-ikm_i\{c_3\eta_3(m_i^2 - k^2\bar{\varepsilon}) + e_1(m_i^2 - k^2 e_2)\}}{(c_1 m_i^2 - k^2 c_2 + \delta_1^2 k^2 c^2)(m_i^2 - k^2\bar{\varepsilon})\eta_3 + (m_i^2 - k^2 e_2)^2}, \quad i = 1, 2, 3,$$

$$P_i = \frac{ike_1 m_i}{\eta_3(m_i^2 - k^2\bar{\varepsilon})} + \frac{(m_i^2 - k^2 e_2)}{\eta_3(m_i^2 - k^2\bar{\varepsilon})}M_i, \quad i = 1, 2, 3. \tag{28}$$

Substituting the solutions (23) in (16) and (18), we obtain the normal stress, shear stress, current density, and displacements for the semiconductor material as

$$\tau_{zz}^s = \left(p \sum_{i=1}^{2} A_i^s e^{-n_i z} + q A_3^s e^{-\beta z} \right) \exp\{ik(x - ct)\}, \tag{29}$$

$$\tau_{xz}^s = \left(-\sum_{i=1}^{2} f_i A_i^s e^{-n_i z} + p A_3^s e^{-\beta z} \right) \exp\{ik(x - ct)\}, \tag{30}$$

$$J_z^s = \sum_{i=1}^{2} S_i n_i A_i^s \exp\{-n_i z + ik(x - ct)\}, \tag{31}$$

$$u^s = \left(ik \sum_{i=1}^{2} A_i^s e^{-n_i z} - \beta A_3^s e^{-\beta z} \right) \exp\{ik(x - ct)\}, \tag{32}$$

$$w^s = -\left(\sum_{i=1}^{2} n_i A_i^s e^{-n_i z} + ik A_3^s e^{-\beta z} \right) \exp\{ik(x - ct)\}, \tag{33}$$

where

$$p = \delta^2(k^2 + \beta^2), \quad q = 2ik\delta^2\beta, \quad f_i = 2ik\delta^2 n_i \ \ (i = 1, 2), \quad A_i^s \ \ (i = 1, 2, 3)$$

are the unknowns to be determined. Similarly, we obtain expressions for normal stress, shear stress, and electric displacement for the piezoelectric layer by using (24) in (17) as

$$(\tau_{zz}^p, D_z^p) = \sum_{i=1}^{3} \{(y_i, b_i)(A_i^p e^{m_i z} + B_i^p e^{-m_i z}) \exp\{ik(x - ct)\}\},$$

$$\tau_{xz}^p = \sum_{i=1}^{3} d_i (A_i^p e^{m_i z} - B_i^p e^{-m_i z}) \exp\{ik(x - ct)\}, \tag{34}$$

where

$$y_i = \frac{\bar{\rho}}{\delta_1^2}\{ik(c_3 - c_2) + c_1 m_i M_i + m_i P_i\}, \quad d_i = \frac{\bar{\rho}}{\delta_1^2}\left\{\frac{c_2}{2}(m_i + ikM_i) + ike_2 P_i\right\},$$

$$b_i = ik(e_1 - e_2) + m_i(M_i - \eta_3 P_i), \tag{35}$$

and A_i^p and B_i^p $(i = 1, 2, 3)$ are the unknowns to be determined.

4. Secular equation

Considering the formal solution for various field quantities obtained in the previous section and employing the boundary conditions (8) and (9), we obtain a system of nine coupled homogeneous algebraic equations in nine unknowns A_i^s, A_i^p, and B_i^p $(i = 1, 2, 3)$. This system has a nontrivial solution if the determinant of the coefficients of A_i^s, A_i^p, and B_i^p $(i = 1, 2, 3)$ vanishes. After lengthy algebraic reductions and simplifications, the secular equation for the propagation of guided waves in the considered

composite structure is obtained as

$$\tanh(m_1 h) = \frac{g_{12}(g_{21}g_{33} - g_{31}g_{23}) - g_{13}(g_{21}g_{32} - g_{31}g_{22})}{g_{11}(g_{22}g_{33} - g_{32}g_{23})}, \tag{36}$$

where

$$g_{11} = b_{21}b_{14} - \frac{b_{11}b_{24}}{\sinh(m_1 h)}, \qquad\qquad g_{1i} = \frac{b_{2i}b_{14} - b_{1i}b_{24}}{\cosh(m_1 h)}, \quad i = 2, 3,$$

$$g_{2i} = b_{3i}b_{14} - b_{1i}b_{34}, \qquad i = 1, 2, 3, \qquad g_{3i} = b_{4i}b_{14} - b_{1i}b_{44}, \quad i = 1, 2, 3. \tag{37}$$

Here b_{ij} $(i, j = 1, 2, 3, 4)$ are given by

$$b_{1i} = a_{3i}(a_{25}a_{16} - a_{15}a_{26}) - a_{2i}(a_{35}a_{16} - a_{15}a_{36}), \qquad\qquad i = 1, 2,$$

$$b_{1j} = (a_{3j}a_{16} - a_{1j}a_{36})(a_{25}a_{16} - a_{15}a_{26}) - (a_{2j}a_{16} - a_{1j}a_{26})(a_{35}a_{16} - a_{15}a_{36}), \qquad j = 3, 4,$$

$$b_{21} = a_{41}(a_{25}a_{16} - a_{15}a_{26}) - \frac{a_{21}(a_{45}a_{16} - a_{15}a_{46})}{\sinh(m_1 h)},$$

$$b_{22} = a_{42}(a_{25}a_{16} - a_{15}a_{26}) - a_{22}(a_{45}a_{16} - a_{15}a_{46}),$$

$$b_{2j} = (a_{4j}a_{16} - a_{1j}a_{46})(a_{25}a_{16} - a_{15}a_{26}) - (a_{2j}a_{16} - a_{1j}a_{26})(a_{45}a_{16} - a_{15}a_{46}), \qquad j = 3, 4, \tag{38}$$

$$b_{3i} = a_{5i}(a_{25}a_{16} - a_{15}a_{26}) - a_{2i}(a_{55}a_{16} - a_{15}a_{56}), \qquad\qquad i = 1, 2,$$

$$b_{3j} = (a_{5j}a_{16} - a_{1j}a_{56})(a_{25}a_{16} - a_{15}a_{26}) - (a_{2j}a_{16} - a_{1j}a_{26})(a_{55}a_{16} - a_{15}a_{56}), \qquad j = 3, 4,$$

$$b_{4i} = a_{6i}(a_{25}a_{16} - a_{15}a_{26}) - a_{2i}(a_{65}a_{16} - a_{15}a_{66}), \qquad\qquad i = 1, 2,$$

$$b_{4j} = (a_{6j}a_{16} - a_{1j}a_{66})(a_{25}a_{16} - a_{15}a_{26}) - (a_{2j}a_{16} - a_{1j}a_{26})(a_{65}a_{16} - a_{15}a_{66}), \qquad j = 3, 4.$$

The quantities a_{ij} $(i, j = 1, \ldots, 6)$ are defined in the Appendix.

5. Solution of secular equation

In general, the wave number and hence the phase velocities of the waves are complex quantities, therefore the waves will be attenuated in space. In order to solve the secular equation (36), we take

$$c^{-1} = V^{-1} + i\omega^{-1}Q, \tag{39}$$

where $k = R + iQ$, $R = \omega/V$, and R and Q are real numbers. Here, it may be noted that V and Q respectively represent the phase velocity and attenuation coefficient of the waves. Using representation (39) in various relevant relations, the complex roots m_i^2 $(i = 1, 2, 3)$ can be computed from (27) with the help of Cardano's method. The roots m_i^2 are further used to solve the secular equation (36) to obtain the phase velocity and attenuation coefficient of the surface waves by using the functional iteration numerical technique outlined below.

In general the secular equation (36) is of the form $c = \phi(c)$ which on using representation (39) leads to a system of two real equations $f(V, Q) = 0$ and $g(V, Q) = 0$. In order to apply the functional iteration method we write $V = f^*(V, Q)$ and $Q = g^*(V, Q)$, where the functions f^* and g^* are selected in such a way that they satisfy the conditions

$$\left|\frac{\partial f^*}{\partial V}\right| + \left|\frac{\partial f^*}{\partial Q}\right| < 1, \quad \left|\frac{\partial g^*}{\partial V}\right| + \left|\frac{\partial g^*}{\partial Q}\right| < 1, \tag{40}$$

for all V, Q in the neighborhood of the root. If (V_0, Q_0) is an initial approximation of the root, then we can construct the successive approximations according to the formulae

$$
\begin{aligned}
V_1 &= f^*(V_0, Q_0), & Q_1 &= g^*(V_1, Q_0), \\
V_2 &= f^*(V_1, Q_1), & Q_2 &= g^*(V_2, Q_1), \\
&\vdots & &\vdots \\
V_{n+1} &= f^*(V_n, Q_n), & Q_{n+1} &= g^*(V_{n+1}, Q_n).
\end{aligned}
\tag{41}
$$

The sequence (V_n, Q_n) of approximations of the root will converge to the actual root provided (V_0, Q_0) lies in the neighborhood of the actual root. For an initial value of $c = c_0 = (V_0, Q_0)$, the roots m_i ($i = 1, 2, 3$) are computed from (27) by using Cardano's method for each value of the nondimensional wave number (R) for the assigned frequency. The values of m_i so obtained are then used in the secular equation (36) to find the current values of V and Q each time, which are further used to generate the sequence (41). The process is terminated as and when the condition $|V_{n+1} - V_n| < \varepsilon$, ε being an arbitrarily small number to be selected at random in order to achieve the desired accuracy level, is satisfied. The procedure is continuously repeated for different values of nondimensional wave number to obtain the corresponding values of the phase velocity and attenuation coefficient. Thus, the real phase velocity and attenuation coefficient during the propagation of Rayleigh-type waves in the composite structure under study can be computed from the dispersion relation (36).

5.1. *Specific loss.* The specific loss is the direct method of defining the internal friction for a material. According to [Kolsky 1963], in the case of a sinusoidal plane wave of small amplitude, the specific loss $\Delta W / W$ equals 4π times the ratio of the absolute value of the imaginary part of k to the real part of k. Here

$$
\frac{\Delta W}{W} = 4\pi \left| \frac{\operatorname{Im}(k)}{\operatorname{Re}(k)} \right| = 4\pi \left| \frac{Q}{R} \right| = 4\pi \left| \frac{VQ}{\omega} \right|.
\tag{42}
$$

6. Special cases of wave solution

In the case where the piezoelectric layer is absent ($h = 0$), the composite structure reduces to a semiconductor halfspace subjected to stress-free, isoconcentrated or stress-free, impermeable boundary conditions. The secular equation (36) in this case reduces to the following two equations:

$$
(k^2 + \beta^2)^2 (n_1 + n_2) = 4k^2 \beta (n_1 n_2 + \alpha^2),
\tag{43}
$$

$$
(k^2 + \beta^2)^2 (n_1^2 + n_1 n_2 + n_2^2 - \alpha^2) = 4k^2 \beta n_1 n_2 (n_1 + n_2).
\tag{44}
$$

Equation (43) corresponds to the secular equation which governs the surface wave motion in the case of stress-free, isoconcentrated boundary conditions prevailing at the surface of the semiconductor halfspace and (44) refers to the secular equation for the stress-free, impermeable surface of the semiconductor halfspace.

Equations (43) and (44) have similar forms as that of the thermoelastic Rayleigh frequency equation [Maruszewski 1989; Sharma et al. 2007] and hence electron concentration produces the same type of surface effects as the heat flux conduction/heat transfer phenomenon. In the case where electron and

elastic fields are uncoupled ($\varepsilon_n = 0$), from (26) we have

$$a_1^2 = 1, \quad a_2^2 = t^n + i\omega^{-1}\left(1 - \frac{t^n}{t_n^+}\right) + \frac{1}{t_n^+\omega^2},$$

so that $n_1^2 = \alpha^2$. Consequently (43) and (44) collapse to

$$(k^2 + \beta^2)^2 = 4k^2\alpha\beta. \tag{45}$$

This is the famous Rayleigh frequency equation [Graff 1975] in a stress-free elastic halfspace.

7. Numerical results and discussion

The analytical solutions for various field quantities obtained lead to the transcendental secular equation (36) which contains complete information about the effect of different interacting fields and lifespan of the charge carriers on the phase velocity, attenuation coefficient, and specific loss factor of energy dissipation. In order to illustrate the theoretical results obtained above, we now present some numerical results for four composite structures, namely, CdSe-Si, CdSe-Ge, PZT-Si, and PZT-Ge. The material parameters and constants for the semiconductor halfspace and piezoelectric layer used in the numerical computations are given in Tables 1 and 2, respectively.

The numerical computations were performed by employing the procedure outlined in Section 5 with the help of MATLAB programming. The computations were performed for the first three modes of wave propagation in the considered composite structures. In the following discussion, Rh denotes the nondimensional wave number for surface waves travelling at the interface of the semiconductor halfspace and piezoelectric layer while R represents the wave number for Rayleigh surface waves at the free surface of the semiconductor halfspace.

Figures 2 and 3 present the variations of phase velocity of surface waves at the interface of the composites CdSe-Ge and PZT-Ge, respectively, versus wave number Rh for the first three modes of wave propagation. The waves are noticed to be dispersive in nature in both cases. There is a sharp decrease in the phase velocity at long wavelengths. It is clear that the maximum fall in the phase velocity occurs for $0 \le Rh \le 2$. At small wavelengths phase velocity almost attains a constant value for $Rh \ge 2$. Initially the higher modes of wave propagation have large phase velocity as compared to that of lower-order modes. Moreover, the velocity profiles are observed to be similar for the considered composite structures with

Sample number	Quantity	Unit	Si	Ge
1	ρ^s	$Kg\,m^{-3}$	2.3×10^3	5.3×10^3
2	λ	$N\,m^{-2}$	0.64×10^{11}	0.48×10^{11}
3	μ	$N\,m^{-2}$	0.65×10^{11}	0.53×10^{11}
4	D^n	$m^2\,s^{-1}$	0.35×10^{-2}	1×10^{-2}
5	n_0	m^{-3}	10^{20}	10^{20}
6	α_T	K^{-1}	2.6×10^{-6}	5.8×10^{-6}

Table 1. Physical data for n-type Si and Ge semiconductors [Maruszewski 1989; Sharma and Thakur 2006].

Sample number	Quantity	Unit	CdSe	PZT-4
1	ρ^p	$\mathrm{kg\,m^{-3}}$	5.504×10^3	7.5×10^3
2	c_{11}	$\mathrm{Nm^{-2}}$	7.41×10^{10}	13.2×10^{10}
3	c_{13}	$\mathrm{Nm^{-2}}$	3.93×10^{10}	7.3×10^{10}
4	c_{33}	$\mathrm{Nm^{-2}}$	8.36×10^{10}	11.5×10^{10}
5	c_{44}	$\mathrm{Nm^{-2}}$	1.32×10^{10}	2.6×10^{10}
6	e_{31}	$\mathrm{Cm^{-2}}$	-0.160	-4.1
7	e_{33}	$\mathrm{Cm^{-2}}$	0.347	14.1
8	e_{15}	$\mathrm{Cm^{-2}}$	-0.138	10.5
9	ε_{11}	$\mathrm{C^2N^{-1}m^{-2}}$	8.26×10^{-11}	7.1×10^{-9}
10	ε_{33}	$\mathrm{C^2N^{-1}m^{-2}}$	9.03×10^{-11}	5.8×10^{-9}
11	ε_0	F/m	8.854×10^{-12}	8.854×10^{-12}

Table 2. Physical data for 6 mm class CdSe [Sharma and Pal 2004] and PZT-4 [Jin et al. 2002] piezoelectric materials.

the exception that phase velocity possesses large magnitude in the case of the PZT-Ge composite as compared to that the CdSe-Ge one. It is worth noting that all the modes of wave propagation start with higher phase velocity at long wavelengths, showing the cutoff frequencies for their existence. The penetration power of the long wavelength surface waves is higher than that of short wavelengths. Thus at long wavelengths the medium gets disturbed to its maximum and the coupling between various interacting fields become operative, thereby increasing the phase velocity and hence the speed of the surface waves. This is in contrast to short-wavelength waves which just follow the surface without much disturbance to the core material. This agrees with the conclusion drawn in [Lowrie 2007].
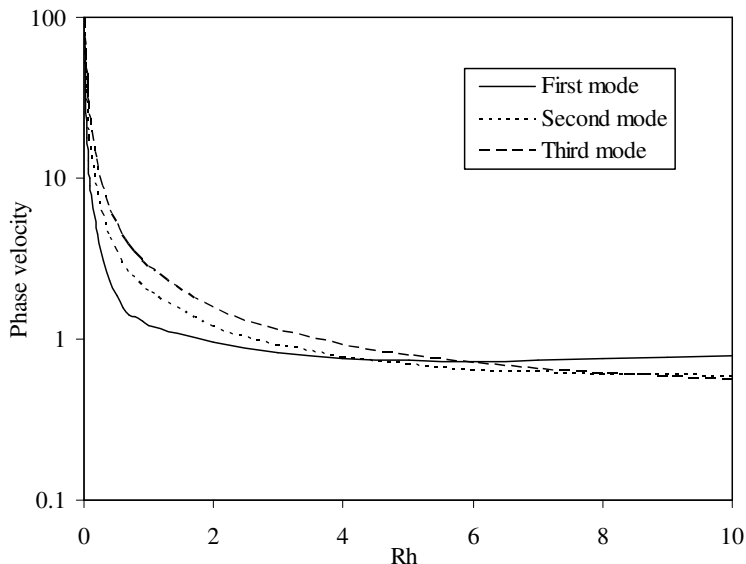

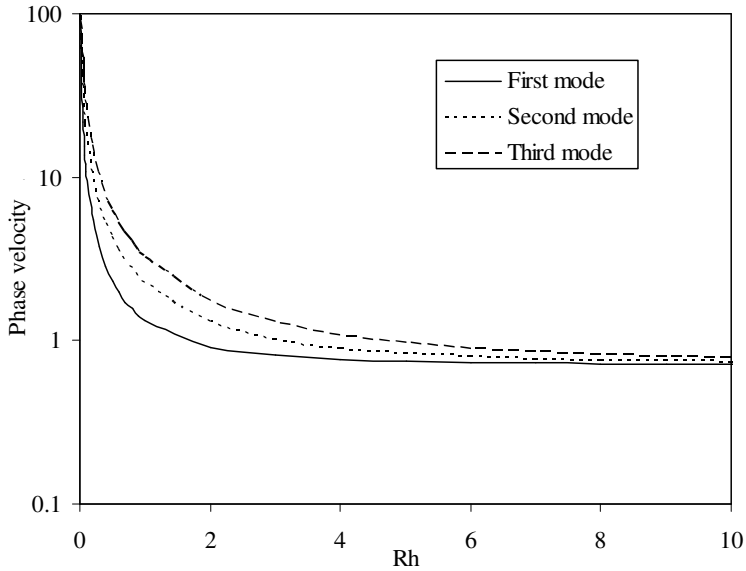**Figure 2.** Phase velocity versus Rh for CdSe-Ge composite.

Figure 3. Phase velocity versus Rh for PZT-Ge composite.

Figure 4 shows the variation of the attenuation coefficient with wave number Rh for the CdSe-Ge composite. Here the attenuation coefficient increases with Rh for all the modes. The lower-order modes of wave propagation possess larger attenuation than the higher modes.

Figure 5 presents the variations of the attenuation coefficient with wave number Rh in the PZT-Ge composite. In this case the attenuation coefficient first increases with Rh to attain maximum value and decreases afterwards with Rh. The maxima for attenuation coefficients shift towards larger values of Rh with increasing mode of wave propagation. Moreover, the PZT-Ge composite possesses a smaller
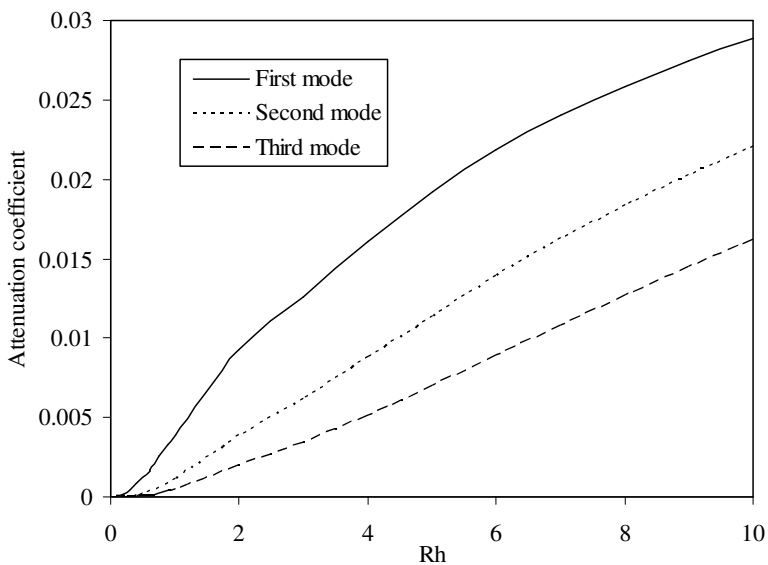

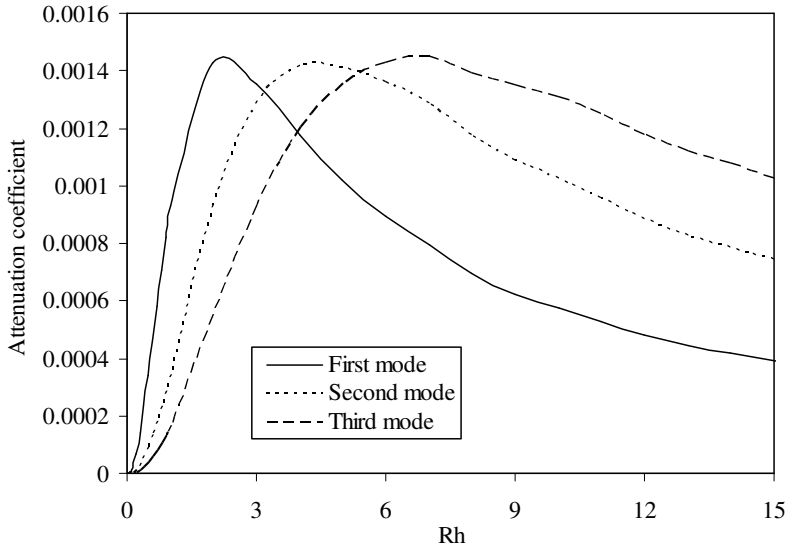**Figure 4.** Attenuation coefficient versus Rh for CdSe-Ge composite.

Figure 5. Attenuation coefficient versus *Rh* for PZT-Ge composite.

attenuation coefficient than that of the CdSe-Si composite structure.

Figures 6 and 7 represent the variations of the specific loss factor of energy dissipation with wave number *Rh* in the composites CdSe-Ge and PZT-Ge, respectively. The specific loss factor of waves in these composites follows similar trends as those of their attenuation coefficients. The variations of phase velocity with age of the charge carrier field for all the considered composites are shown in Figure 8. The phase velocity profiles possess almost uniform behaviour with the lifetime except in the CdSe-Ge composite where it has a slightly large value at 0.1 ps in comparison to the neighboring points, which may
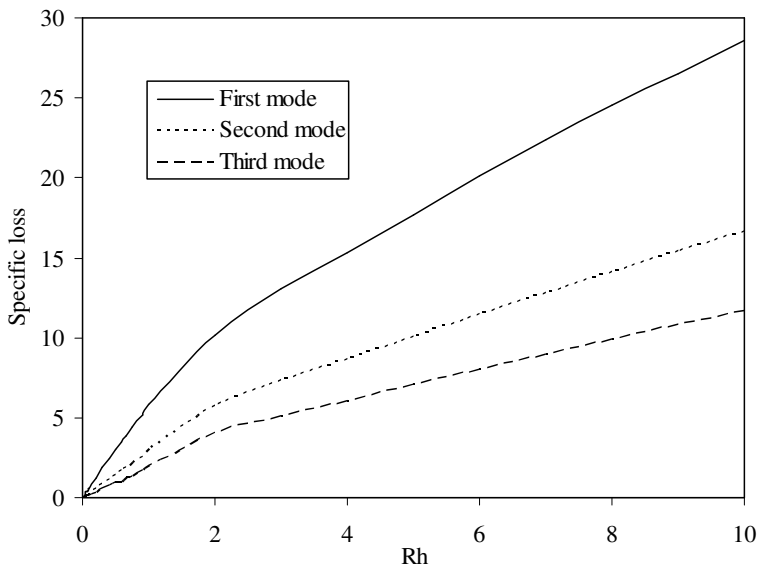

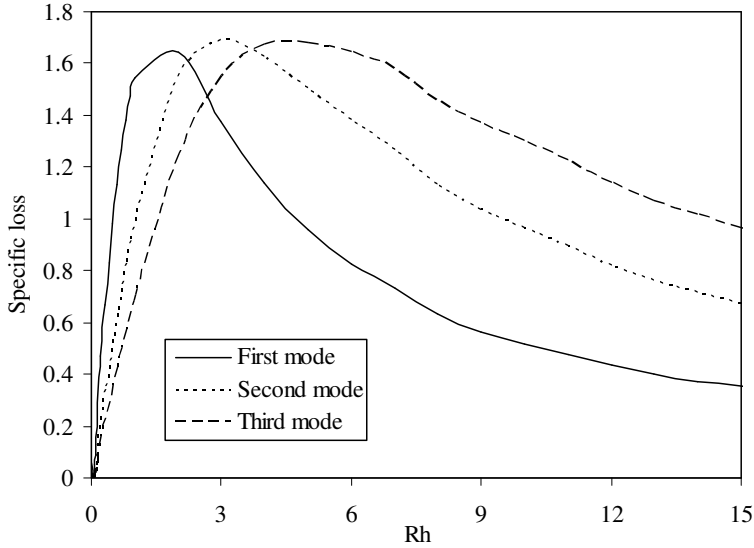**Figure 6.** Specific loss versus *Rh* for CdSe-Ge composite.

Figure 7. Specific loss versus *Rh* for PZT-Ge composite.

be attributed to numerical instability at that point. It is also evident from the phase velocity profiles that the magnitude of phase velocity is highest for PZT-Ge and lowest in the case of the CdSe-Si composite. Figure 9 shows the variations of the attenuation coefficient with the lifetime of the carrier field in the considered composites. It is evident that for CdSe-Si and CdSe-Ge the magnitude of attenuation has a uniform value up to $t_n^+ = 0.1$ ps and decreases afterwards. However, in the PZT-Ge and PZT-Si composites, the variations of the attenuation coefficient remain almost constant with lifetime. This comparative study reveals that the PZT-Ge composite has the lowest attenuation while the CdSe-Si exhibits the highest
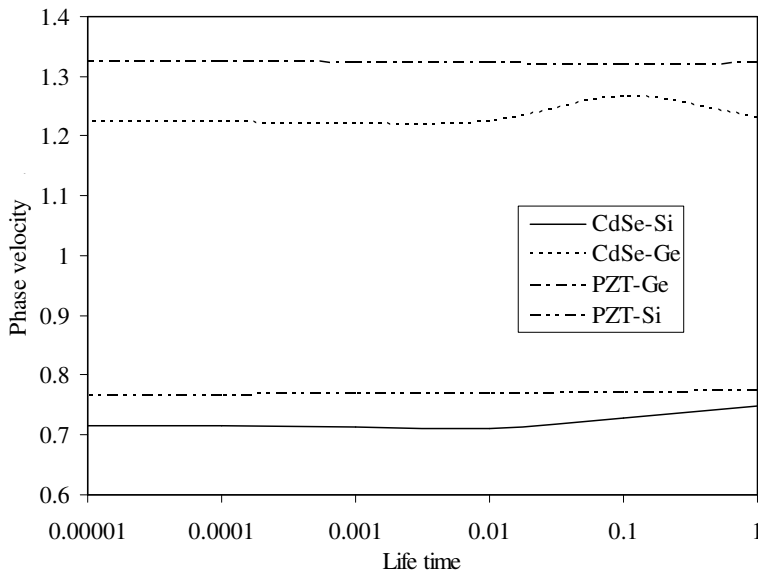
Figure 8. Phase velocity versus lifetime (in ps) of carrier field.
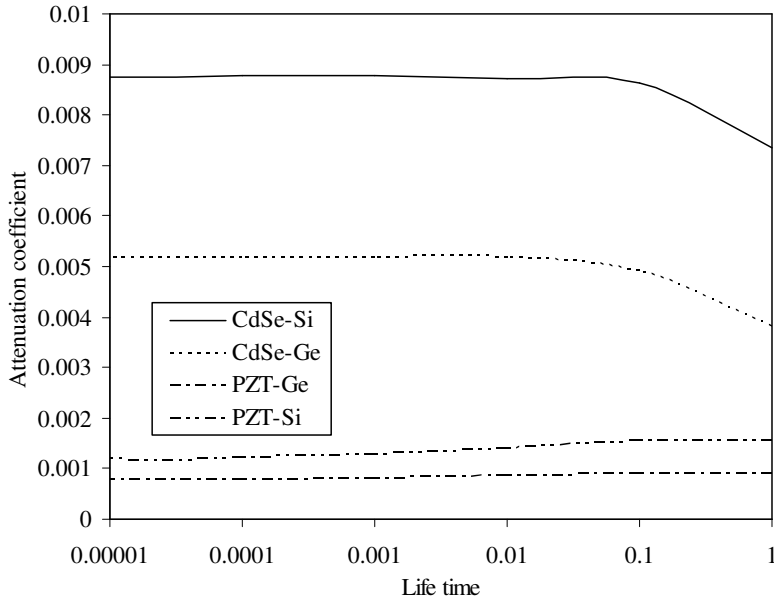
Figure 9. Attenuation coefficient versus lifetime (in ps) of carrier field.

attenuation among all the considered structures. The PZT-Ge composite is a combination of higher density materials in comparison to CdSe-Si, which has low density, and therefore the phase velocity is large in value in the former composite because acoustic waves travel faster in the denser medium than in the rarer one.

Figures 10–14 show the variations of various wave characteristics in the silicon semiconductor half-space. Figure 10 represents the variations of phase velocity with wave number R in the semiconductor
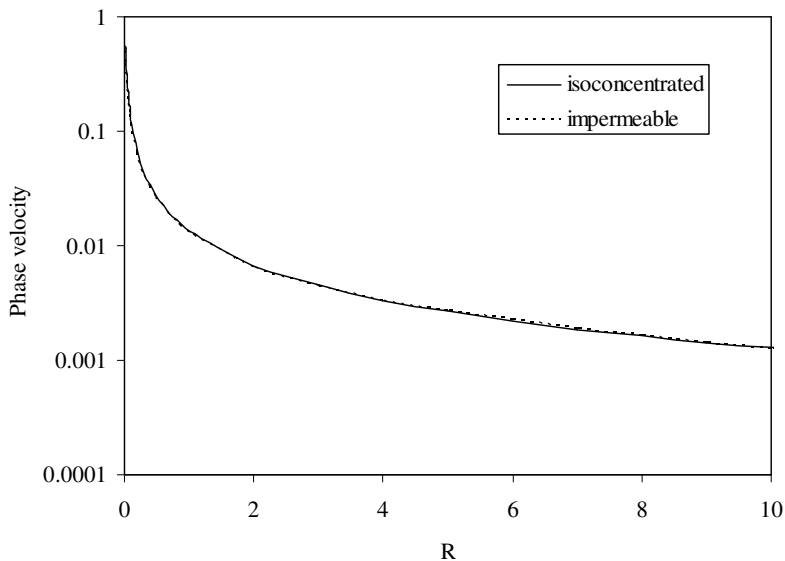
Figure 10. Phase velocity versus R in semiconductor halfspace.
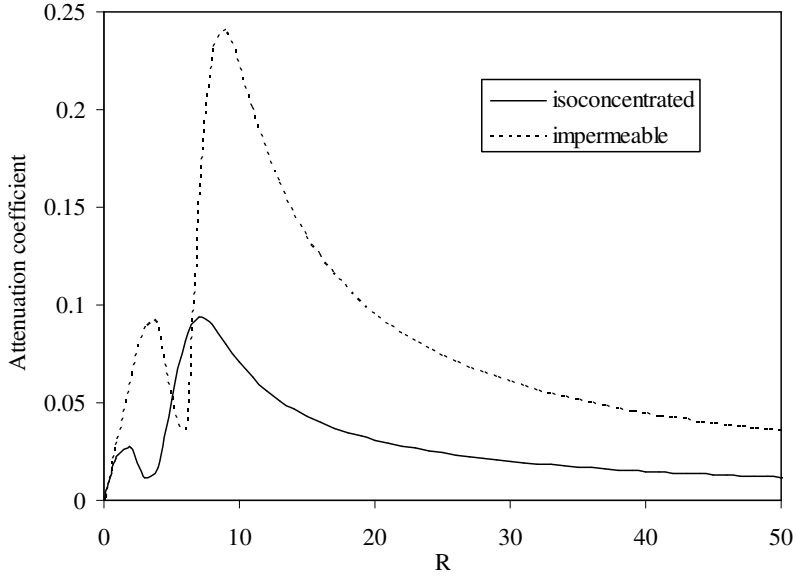
Figure 11. Attenuation coefficient versus R in semiconductor halfspace.

halfspace under stress-free and isoconcentrated as well as stress-free and impermeable boundary conditions. The waves are again attenuated and dispersive in character for the same reason as explained for Figures 2 and 3. However, there is a sharp decay in the phase velocity of these waves in the range $0 \leq R \leq 2$ which attains an almost constant value for $R \geq 2$. It may be noticed that the phase velocities have almost equal magnitudes in the case of both the boundary conditions prevailing at the surface of the semiconductor halfspace. Figure 11 shows the variations of the attenuation coefficient with wave number R for stress-free and isoconcentrated as well as stress-free and impermeable boundary conditions

Figure 12. Specific loss versus R in semiconductor halfspace.

Figure 13. Phase velocity versus lifetime (in ps) of carrier field in semiconductor halfspace.

at the surface of the halfspace. The attenuation coefficient increases in the range $0 \leq R \leq 2$, decreases for $2 \leq R \leq 3$ and a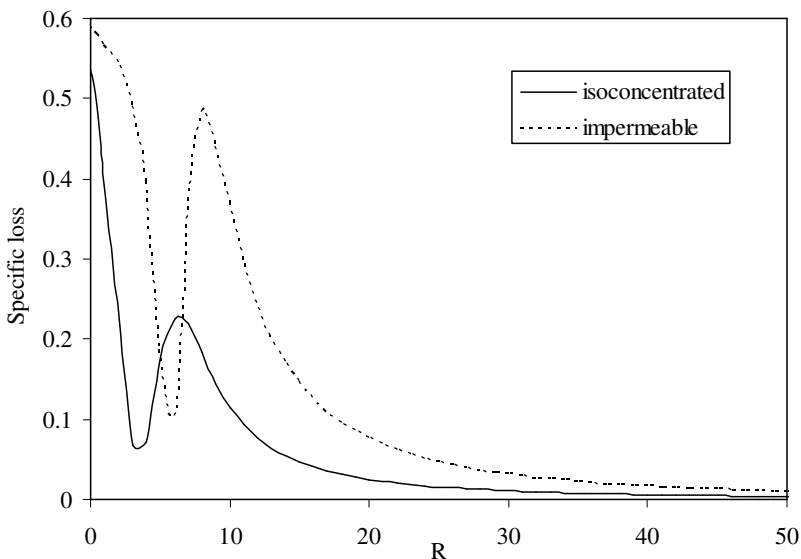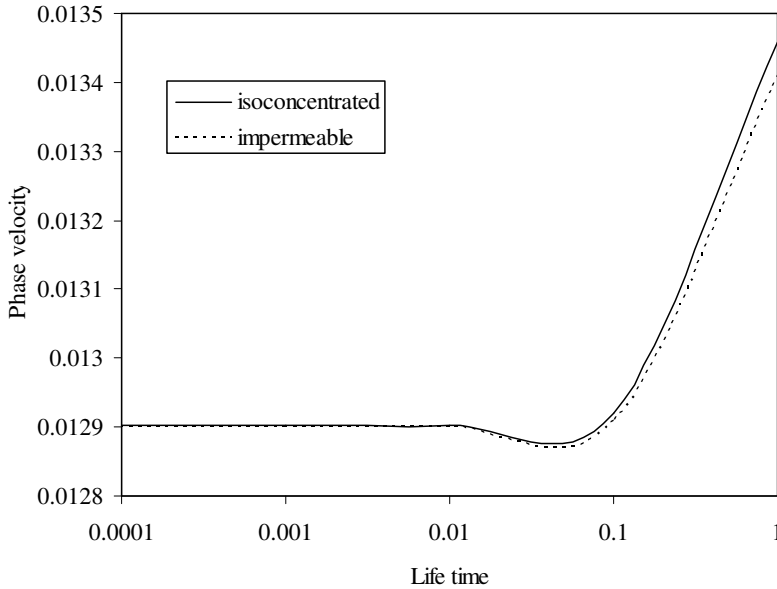gain increases for $3 \leq R \leq 7$ before it decreases with R for stress-free and isoconcentrated boundary conditions. Similar trends of variations are also noticed in the case of stress-free and impermeable conditions with the exception that in this case the attenuation has a high magnitude. Figure 12 presents the variations of the specific loss factor of energy dissipation with wave number R. The specific loss factor decreases for $0 \leq R \leq 3$ and increases for $3 \leq R \leq 6$, before it starts decreasing with R in the case of stress-free and isoconcentrated boundary conditions at the surface of the halfspace. In the case of stress-free and impermeable boundary conditions it also follows a similar trend. The specific loss factor has a large magnitude in the case of impermeable conditions as compared to that for the isoconcentrated one. The attenuation and specific loss profiles show some oscillatory behaviour at long wavelengths, which is attributed to the fact that the acoustic waves penetrate significantly deep into the medium under such situations forcing the various coupling parameters of the interacting fields to become operative. Whereas at short wavelengths, both these quantities show smooth behaviour as the waves mainly travel along the surface, causing the least disturbance to the medium. Figure 13 shows the variations of phase velocity with lifetime of the charge carriers in the semiconductor halfspace. Phase velocity remains almost constant up to $t_n^+ = 0.01$ ps and then increases rapidly in the case of both boundary conditions. The generation and recombination of the electrons become more frequent with decreasing lifetime. Moreover, the wave field interaction with the newly generated electron imparts some energy to it, which results in decreasing the phase velocity of the wave. The magnitude of the phase velocity is slightly higher for the stress-free and isoconcentrated boundary conditions as compared to other conditions. The variations of the attenuation coefficient with lifetime for the semiconductor halfspace are shown in Figure 14. The attenuation coefficient decreases with decreasing lifetime for both boundary conditions. The attenuation coefficient has a large magnitude in the case of stress-free and impermeable conditions as compared to that for stress-free and isoconcentrated conditions for $t_n^+ \geq 0.1$ ps.
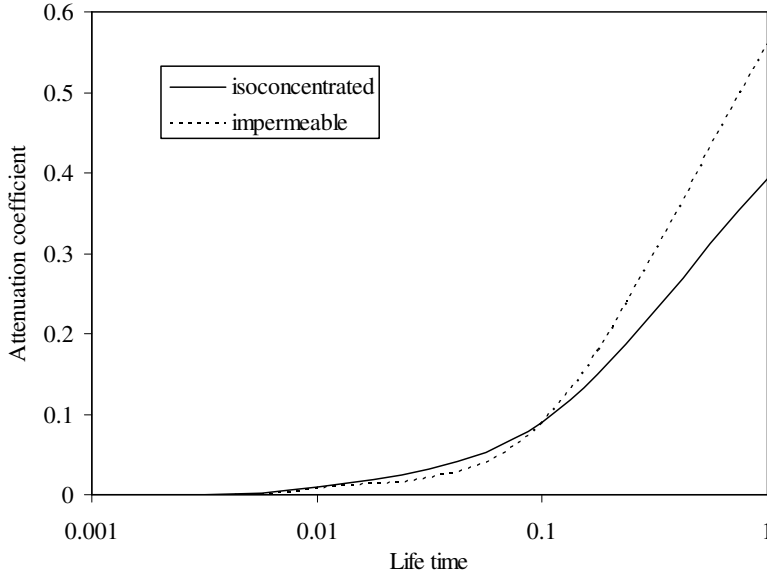
Figure 14. Attenuation coefficient versus lifetime (in ps) in semiconductor halfspace.

Figures 15 and 16 show the plots of computer-simulated results in respect of phase velocities and attenuation coefficients of first mode of wave propagation at $t_n^+ = 1$ ps in all the considered structures. Close inspection of the phase velocity and attenuation coefficient profiles in Figures 15 and 16 reveals that for the same choice of patch/core material in the composite structure, these quantities follow similar trends in their variations. It is clear that the phase velocity decreases from its initial high value at long wavelengths to become steady at short wavelengths in all the composites. The phase velocity has a large
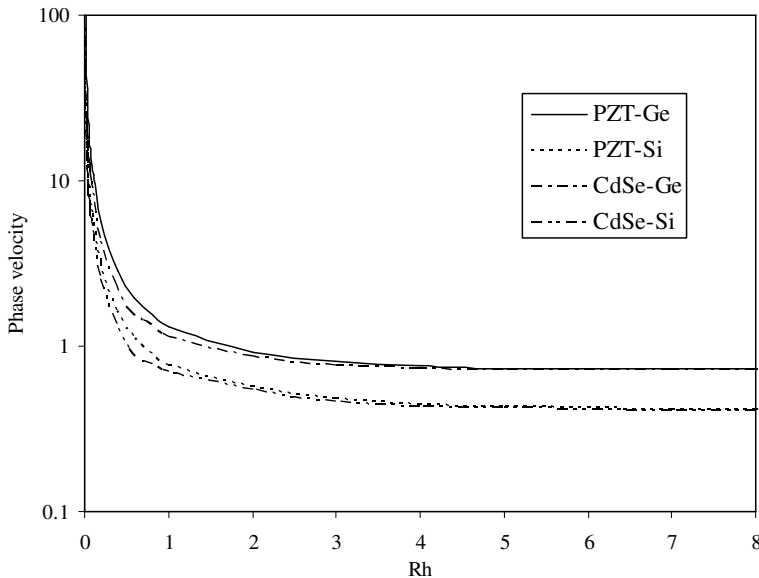
Figure 15. Phase velocity versus *Rh* for PZT-Ge, PZT-Si, CdSe-Ge, and CdSe-Si composites.
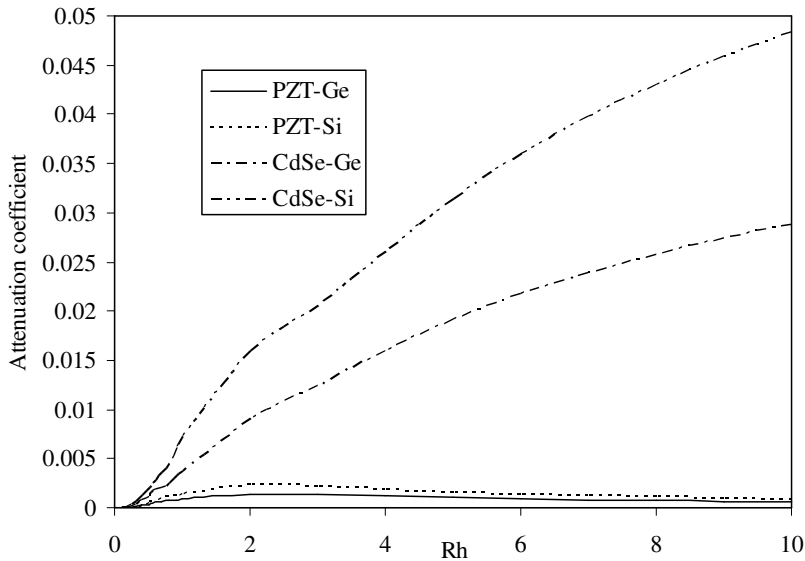
Figure 16. Attenuation coefficient versus Rh for PZT-Ge, PZT-Si, CdSe-Ge, and CdSe-Si composites.

magnitude in the composites with Ge cores as compared to those with Si. Moreover, the phase velocity attains a higher magnitude for the PZT patch than for the CdSe patch with the same choice of core material. The profiles of the attenuation coefficient follow similar trends in their variations for the same patch materials. In the case of the PZT patch, the attenuation initially increases to attain its maximum value and decreases afterwards with increasing wave number; it increases at all wave numbers for the CdSe patch. The attenuation coefficient possesses large values for the CdSe patch in comparison to that of the PZT patch for the same choice of core material. However, the attenuation is higher for the Si core than the Ge one. This shows that the PZT-Ge composite has low attenuation and high phase velocity, which indicates that the wave signal can travel longer distances in this structure. This is attributed to the fact that the characteristics of the composites consisting of thin-layered structures are dominated by the layer properties [Wang 2002; Trolier-Mckinstry and Muralt 2004]. Moreover, the generalised Rayleigh surface waves usually follow the interface surface as their guiding surface by causing less disturbance to the core material than in the patch. Thus the physical properties of the patch material play a more vital role in their propagation than those of the core. Hence, it is worth mentioning that the piezoelectric patch improves the functioning of surface wave devices (SAW) made up of semiconductor materials.

Conclusions

A functional iteration numerical technique along with Cardano's method has been successfully used to solve the complex secular equation in order to compute the phase velocities, attenuation coefficients, and specific loss factors of energy dissipation in CdSe-Si, CdSe-Ge, PZT-Si, and PZT-Ge composite structures. The phase velocity profiles show dispersive character in all the considered composites. Its magnitude decreases sharply at long wavelengths and becomes steady and uniform at short wavelengths. Higher-order modes of wave propagation have larger phase velocity compared to lower-order modes. In

CdSe-Si and CdSe-Ge composites, the attenuation as well as the specific loss factor of energy dissipation increase with increasing wave number, whereas both these quantities first increase and then decrease with increasing wave number in PZT-Si and PZT-Ge composites. Higher-order modes possess less attenuation and specific loss than lower-order ones. Phase velocity remains almost uniform in all the composites with the lifetime of the charge carriers. The attenuation in CdSe-Si and CdSe-Ge composites remains almost constant at short lifetimes and decreases with increasing lifetime. However, attenuation is noticed to be nearly constant in PZT-Si and PZT-Ge structures. In the n-type silicon halfspace, the phase velocity is noticed to be dispersive in nature. The attenuation profiles show oscillatory behaviour initially, then decrease after attaining maximum value, and finally become steady at large wave numbers for both types of considered boundary conditions. The specific loss factor also shows oscillatory behaviour at long wavelengths but becomes uniform at short wavelengths. Phase velocity remains constant at short lifetimes and increases at large values of the lifetime of the charge carrier field in the case where considered conditions prevail at the surface of semiconductor halfspace. The attenuation decreases with decreasing lifetime of the charge carriers for both types of boundary conditions. This study may be applicable to the design of piezoelectric thin-film devices.

Appendix

The coefficients a_{ij} used in (38) are given by

$$a_{13} = -P_3 \beta S_2 n_2 n^R - P_3(\beta p + ikq)p^S,$$

$$a_{1i} = (b_j - b_3)n^R + (y_j - y_3)p^S, \qquad\qquad i = 4, 5, \; j = i - 3,$$

$$a_{16} = \beta b_3 n^R + (q + \beta y_3)p^S,$$

$$a_{2i} = M_i P_3 - P_i M_3, \qquad\qquad i = 1, 2,$$

$$a_{23} = \{M_3 \beta S_2 - P_3(k^2 - \beta n_2)\}n^R - P_3(\beta p + ikq)p^N,$$

$$a_{2i} = (y_j - y_3)p^N, \qquad\qquad i = 4, 5, \; j = i - 3,$$

$$a_{26} = -ikn^R + (q + \beta y_3)p^N,$$

$$a_{3i} = d_i P_3 - P_i d_3, \qquad\qquad i = 1, 2,$$

$$a_{33} = \{d_3 \beta S_2 - P_3(ikp - \beta f_2)\}n^R - P_3(\beta p + ikq)p^F,$$

$$a_{3i} = (y_j - y_3)p^F, \qquad\qquad i = 4, 5, \; j = i - 3,$$

$$a_{36} = pn^R + (q + \beta y_3)p^F,$$

$$a_{41} = P_3 y_1 - P_1 y_3 \frac{\sinh(m_3 h)}{\sinh(m_1 h)},$$

$$a_{42} = P_3 y_2 \sinh(m_2 h) - P_2 y_3 \sinh(m_3 h),$$

$$a_{43} = \beta S_2 y_3 \sinh(m_3 h)n^R,$$

$$a_{4i} = \{y_i \cosh(m_i h) - y_3 \cosh(m_3 h)\}n^R, \qquad\qquad i = 4, 5, \; j = i - 3,$$

$$a_{46} = \beta y_3 \cosh(m_3 h)n^R,$$

$$a_{5i} = P_3 d_i \cosh(m_i h) - P_i d_3 \cosh(m_3 h), \quad i = 1, 2,$$
$$a_{53} = \beta S_2 d_3 \cosh(m_3 h) n^R,$$
$$a_{5i} = \{ d_i \sinh(m_i h) - d_3 \sinh(m_3 h) \} n^R, \quad i = 4, 5, \ j = i - 3,$$
$$a_{56} = \beta d_3 \sinh(m_3 h) n^R,$$
$$a_{6i} = P_3 b_i \sinh(m_i h) - P_i b_3 \sinh(m_3 h), \quad i = 1, 2,$$
$$a_{63} = \beta S_2 b_3 \sinh(m_3 h) n^R,$$
$$a_{6i} = \{ b_i \cosh(m_i h) - b_3 \cosh(m_3 h) \} n^R, \quad i = 4, 5, \ j = i - 3,$$
$$a_{66} = \beta b_3 \cosh(m_3 h) n^R,$$

where

$$n^R = (n_1^2 - n_2^2)(\beta p + ikq),$$
$$p^S = \beta S_2 (S_1 n_1 - S_2 n_2) - \beta S_2 n_2 (n_1^2 - n_2^2),$$
$$p^N = \beta S_2 (n_2 - n_1) - (n_1^2 - n_2^2)(k^2 - \beta n_2),$$
$$p^F = \beta S_2 (f_2 - f_1) - (n_1^2 - n_2^2)(ikp - \beta f_2).$$

References

[Bleustein 1968] J. L. Bleustein, "A new surface wave in piezoelectric materials", *Appl. Phys. Lett.* **13**:12 (1968), 412–414.

[Du et al. 2007] J. Du, X. Jin, J. Wang, and K. Xian, "Love wave propagation in functionally graded piezoelectric material layer", *Ultrasonics* **46**:1 (2007), 13–22.

[Graff 1975] K. F. Graff, *Wave motion in elastic solids*, Clarendon Press, Oxford, 1975.

[Gulyaev 1969] Y. V. Gulyaev, "Electroacoustic surface waves in solids", *JETP Letters* **9**:1 (1969), 37–38.

[Jin et al. 2002] J. Jin, Q. Wang, and S. T. Quek, "Lamb wave propagation in a metallic semi-infinite medium covered with piezoelectric layer", *Int. J. Solids Struct.* **39**:9 (2002), 2547–2556.

[Kagan 1997] V. D. Kagan, "Propagation of a surface acoustic wave in a layered system containing a two-dimensional conducting layer", *Semiconductors* **31**:4 (1997), 407–410.

[Kolsky 1963] H. Kolsky, *Stress waves in solids*, Dover Press, New York, 1963.

[Liu et al. 2004] H. Liu, J. J. Lee, and Z. M. Cai, "Analysis of nonlinear acoustoelastic effect of surface acoustic waves in laminated structures by transfer matrix method", *Mech. Res. Commun.* **31**:6 (2004), 667–675.

[de Lorenzi and Tiersten 1975] H. G. de Lorenzi and H. F. Tiersten, "On the interaction of the electromagnetic field with heat conducting deformable semiconductors", *J. Math. Phys.* **16**:4 (1975), 938–957.

[Lowrie 2007] W. Lowrie, *Fundamental of geophysics*, Cambridge University Press, New York, 2007.

[Maruszewski 1989] B. Maruszewski, "Thermodiffusive surface waves in semiconductors", *J. Acoust. Soc. Am.* **85**:5 (1989), 1967–1977.

[Maugin and Daher 1986] G. A. Maugin and N. Daher, "Phenomenological theory of elastic semiconductors", *Int. J. Eng. Sci.* **24**:5 (1986), 703–731.

[Melkumyan and Mai 2009] A. Melkumyan and Y.-w. Mai, "Electroelastic gap waves between dissimilar piezoelectric materials in different classes of symmetry", *Int. J. Solids Struct.* **46**:21 (2009), 3760–3770.

[Muralt and Baborowski 2004] P. Muralt and J. Baborowski, "Micromachined ultrasonic transducers and acoustic sensors based on piezoelectric thin films", *J. Electroceramics* **12**:1-2 (2004), 101–108.

[Rayleigh 1885] L. Rayleigh, "On waves propagated along the plane surface of an elastic solid", *Proc. London Math. Soc.* **7**:1 (1885), 4–11.

[Sharma and Pal 2004] J. N. Sharma and M. Pal, "Propagation of Lamb waves in a transversely isotropic piezothermoelastic plate", *J. Sound Vib.* **270**:4-5 (2004), 587–610.

[Sharma and Pathania 2006] J. N. Sharma and V. Pathania, "Thermoelastic waves in coated homogeneous anisotropic materials", *Int. J. Mech. Sci.* **48**:5 (2006), 526–535.

[Sharma and Thakur 2006] J. N. Sharma and N. Thakur, "Plane harmonic elasto-thermodiffusive waves in semiconductor materials", *J. Mech. Mater. Struct.* **1**:5 (2006), 813–835.

[Sharma et al. 2007] J. N. Sharma, N. Thakur, and S. Singh, "Propagation characteristics of elasto-thermodiffusive surface waves in semiconductor material half-space", *J. Therm. Stresses* **30**:4 (2007), 357–380.

[Sharma et al. 2009] J. N. Sharma, N. Thakur, and S. Singh, "Elasto-thermodiffusive (ETNP) surface waves in semiconductor materials", *Int. J. Solids Struct.* **46**:11-12 (2009), 2309–2319.

[Sharma et al. 2010] J. N. Sharma, K. K. Sharma, and A. Kumar, "Surface waves in a piezoelectric-semiconductor composite structure", *Int. J. Solids Struct.* **47**:6 (2010), 816–826.

[Trolier-Mckinstry and Muralt 2004] S. Trolier-Mckinstry and P. Muralt, "Thin film piezoelectrics for MEMS", *J. Electroceramics* **12**:1-2 (2004), 7–17.

[Wang 2002] Q. Wang, "Wave propagation in a piezoelectric coupled solid medium", *J. Appl. Mech.* (*ASME*) **69**:6 (2002), 819–824.

[Wang and Varadan 2002] Q. Wang and V. K. Varadan, "Wave propagation in piezoelectric coupled plates by use of interdigital transducer, I: dispersion characteristics", *Int. J. Solids Struct.* **39**:5 (2002), 1119–1130.

[White 1967] R. M. White, "Surface elastic-wave propagation and amplification", *IEEE Trans. Electron Devices* **14**:4 (1967), 181–189.

J. N. SHARMA: jns@nitham.ac.in
Department of Mathematics, National Institute of Technology, Hamirpur 177005, India

K. K. SHARMA: kks@nitham.ac.in
Department of Physics, National Institute of Technology, Hamirpur 177005, India

ASHWANI KUMAR: puri_nit@yahoo.com
Department of Physics, National Institute of Technology, Hamirpur 177005, India

msp

DYNAMIC FRACTURE TESTS OF POLYMETHYLMETHACRYLATE USING A SEMICIRCULAR BEND TECHNIQUE

SHENG HUANG, SHENG-NIAN LUO, BRYAN S. A. TATONE AND KAIWEN XIA

We adopt a recently developed technique, dynamic semicircular bend testing, to measure the fracture initiation toughness, fracture propagation toughness, and fracture velocity of polymethylmethacrylate (PMMA). A modified split Hopkinson pressure bar system is used to apply the dynamic load. In this method, both the fracture initiation toughness and fracture energy, and thus the average fracture propagation toughness, are determined. The initiation toughness is found to be similar to the propagation toughness, and both toughnesses are loading rate-dependent. Our initiation toughness values for PMMA are in accord with those reported in the independent literature. The fracture velocity increases and then becomes saturated as the propagation toughness increases. We also measure the fracture surface roughness of the recovered fragments. While the surface roughness increases with the fracture energy, the increase of surface area alone is not sufficient to accommodate the increase in fracture energy, suggesting other energy dissipation mechanisms in the dynamic fracture process besides free surface creation.

1. Introduction

Polymethylmethacrylate (PMMA) is a homogeneous and isotropic polymer that is widely used in many applications for its transparency, high yield strength, and low density and cost. However, it is brittle at room temperature. There is a sustained interest in understanding fracture in such polymers. Many studies have been conducted on the fracture of PMMA under quasistatic conditions [Kobayashi et al. 1972], while limited attempts have been made to measure the dynamic fracture properties of brittle solids (including PMMA), primarily due to the difficulties in experimentation and subsequent data interpretation [Maigre and Rittel 1995]. For example, a significant inertial effect can exist during high-loading rate loading as demonstrated by Böhme and Kalthoff [1982]. In their experiments, a three-point bend sample was loaded dynamically by a drop weight, and they showed that the crack tip stress intensity factor (SIF) history measured with the shadow optical method of caustics did not synchronize with the load histories at the supporting points due to the inertial effect. This inertial effect may subsequently complicate the data reduction and interpretation.

The inertial effect on the fracture toughness can be separated with optical methods [Dally 1979; Kobayashi and Dally 1977b; Rosakis et al. 1984; Xia et al. 2006], which normally require high-speed photography. For other testing methods, the inertial problem can be circumvented with the combination of experimental measurements and numerical simulations [Maigre and Rittel 1995], but this process is rather tedious to apply. Recently, Owen et al. [1998] observed that the SIFs obtained by directly

measuring the crack tip opening are consistent with those calculated with the quasistatic equation when the dynamic stress equilibrium of the specimen is roughly achieved in split Hopkinson tension bar testing. This concept was subsequently adopted in [Weerasooriya et al. 2006] for ceramics in split Hopkinson pressure bar (SHPB) testing using a dynamic four-point bend method.

For static fracture, there is only one fracture toughness, namely fracture initiation toughness. Fracture initiation toughness is also relevant in dynamic fracture. There are a few studies on dynamic initiation toughness for PMMA [Wada 1992; Wada et al. 1993; Rittel and Maigre 1996]. In addition, there is a fracture propagation toughness that characterizes material resistance to a propagating crack during dynamic fractures. Because propagation toughness is directly related to energy consumption during fracture failure processes, it is desirable to measure both toughnesses for dynamic fractures. Fracture propagation toughness is usually measured using optical methods for transparent polymers or polished metals [Kobayashi and Dally 1977b; Dally 1979; Rosakis et al. 1984; Xia et al. 2006]. In a recently developed dynamic semicircular bend (SCB) method [Chen et al. 2009], fracture initiation toughness, fracture energy (and thus average fracture propagation toughness), and average fracture velocity can be measured simultaneously. The measurement of fracture energy also allows us to gain insight into the energy dissipation mechanisms during dynamic fractures.

The fracture propagation toughness is commonly a monotonically increasing function of crack velocity. This relationship was first proposed in [Kobayashi and Dally 1977a; Dally 1979] for PMMA using a dynamic photoelasticity method. Rosakis et al. [1984] reached a similar conclusion using wedge loaded cantilever beam specimens made of AISI 4030 steel. More evidence for this dependence was subsequently observed by using three-point bend specimens loaded in a drop weight tower in [Zehnder and Rosakis 1990]. At low fracture speed, the dependence of SIF on fracture velocity is weak, while at higher crack speeds it becomes quite pronounced. As the fracture velocity is close to its limiting value, the fracture toughness can be very large as compared to the static value. This leads to the notion of a limiting fracture velocity beyond which the fracture cannot propagate no matter how hard it is driven. Similar results were also observed for 2024-T3 aluminum [Owen et al. 1998]. Other researchers, for instance Évora et al. [2005], clearly observed that the SIF continues to increase under a constant maximum velocity, supporting the limiting fracture velocity postulation. This limiting fracture velocity during dynamic loading is also of interest for PMMA.

In this study, we use the semicircular bend (SCB) method (originally proposed in [Chong and Kuruppu 1984] and extended in [Chen et al. 2009] to dynamic testing for brittle materials) to perform fracture testing on PMMA with split Hopkinson pressure bar (SHPB) and notched SCB specimens. Section 2 addresses the SCB sample preparation and SHPB setup for SCB testing, and Section 3, the measurement techniques and data reduction methodology. The results and discussion on the initiation and propagation fracture toughnesses, and fracture velocity under different loading rates, are presented in Section 4. This section also discusses the correlation between fracture surface toughness and fracture energy as regards the energy dissipation mechanisms during dynamic fracture. Conclusions are given in Section 5.

2. Experimental setup and sample preparation

A 25 mm diameter SHPB system (Figure 1) is used to apply the dynamic load. The bars are made of 7075 aluminum alloy, which has a yielding strength of 455 MPa and Young's modulus of 71.8 GPa. The
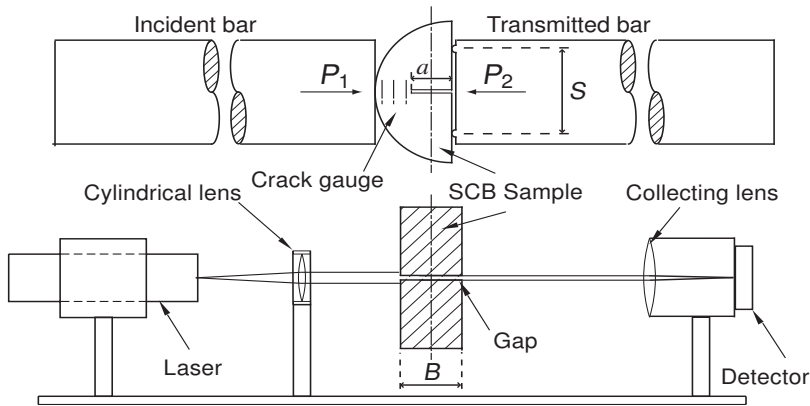
Figure 1. Schematics of the SHPB system, notched SCB sample, and LGG system.

lengths of the striker, incident, and transmitted bars are 300 mm, 2500 mm, and 1500 mm, respectively. The strain gauge stations on the incident and transmitted bars are 933 mm and 500 mm away from the respective bar-sample interfaces. When the striker bar impacts the incident bar, a compressive wave is generated and propagates into the sample (see Figure 1). The interaction of the incident wave with the sample results in two waves: the reflected wave propagating back into the incident bar and the transmitted wave propagating into the transmitted bar. The incident wave, reflected wave, and transmitted wave are denoted with subscripts i, r, and t, respectively. The respective loading forces on the incident and transmitted ends of the specimen are:

$$P_1 = AE(\varepsilon_i + \varepsilon_r), \qquad P_2 = AE\varepsilon_t, \tag{1}$$

where E is the Young's modulus of the bar material, A is the cross-sectional area of the bar, and ε are the strains. The strain gauge signals are relayed to the Wheatstone bridge circuits, amplified, and then recorded by an eight-channel Sigma digital oscilloscope (Nicolet). The striker velocity is measured by a laser-detector system.

A PMMA rod (radius $R = 19.05$ mm) is sliced into discs (thickness $B = 16$ mm) that are in turn split into semicircular shapes. A 1.6 mm wide and 6 mm long notch is then introduced into the sample, with a sharp tip of radius 0.15 mm (Figure 2). This radius is comparable to that used in the dynamic fracture tests of PMMA of [Maigre and Rittel 1995]. For compression-bend loading, the SCB specimen is placed in tangential contact with the incident bar and in point contact with two pins on the transmitted bar separated by a distance S (see Figure 1).

We adopt a laser gap gauge (LGG) system to measure the time-resolved crack surface opening displacement (CSOD; see Figure 1). The details of the LGG system are presented in [Chen et al. 2009]. The amount of light passing through the notch increases with increasing notch width during opening, and is recorded by the LGG system as voltage signals. The voltage is linearly proportional to the gap width and thus the CSOD. Because PMMA is transparent, blue ink is sprayed on the specimen near the notch region to block the laser light except in the notched area (Figure 2a). To measure the crack propagation velocity, three 0.5 mm (in diameter) pencil leads and break-wire circuits are attached to the sample with instant brittle glue as crack gauges. They essentially detect the onset of fracture at three different positions. The
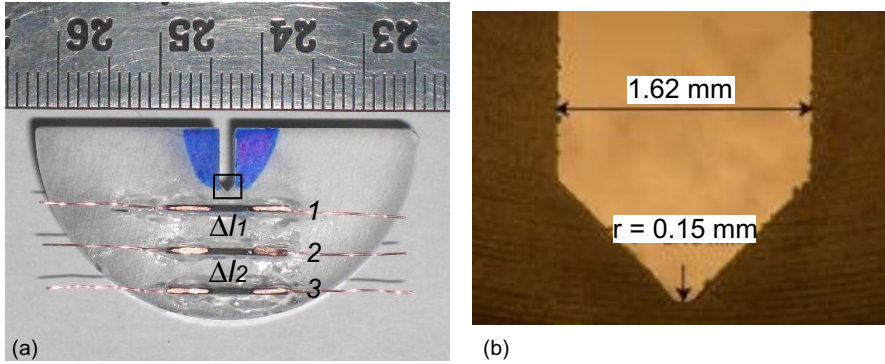
Figure 2. (a) Photo of a PMMA SCB sample with crack gauges 1–3. A fine division in the scale denotes 1 mm. (b) Amplified image of the region marked with a rectangle in (a), showing the crack and tip dimensions.

leads are flattened along the axis in order to improve their bonding strength with the PMMA specimen.

It is critical to achieve dynamic force balance in the specimen during dynamic loading. To this end, we utilize the pulse shaper technique, which was detailed in [Frew et al. 2005]. In traditional SHPB tests, the sharp rising front of the incident wave causes a sudden increase of load in the sample at the end in contact with the incident bar. For brittle materials, this type of load may induce undesired damage to the sample, leading to significant complications and possibly errors in interpreting the measurements. We used a black rubber disc of 2.5 mm diameter and 2 mm thickness as the pulse shaper. This method normally yields an incident pulse with a ramp front of about $100 \, \mu s$ in duration, which allows the sample to achieve force balance throughout the loading stage of the deformation.

Figure 3 shows the forces on both ends of the specimen in a typical test. Equation (1) states that the dynamic force on the incident-bar side of the specimen (P_1) is proportional to the sum of the incident (In) and reflected (Re) stress waves, and that on the transmission-bar side (P_2) to the transmitted (Tr) stress wave. For SCB tests, P_2 is equally distributed to the two supporting pins. As shown in Figure 3,

Figure 3. Dynamic force histories in a typical dynamic SCB test.

the dynamic forces on both sides of the specimen are almost identical during the entire dynamic loading period. Inertial effects are thus approximately eliminated because there is no global force difference in the specimen. Given negligible inertial effects, we can then perform quasistatic analysis [Chen et al. 2009].

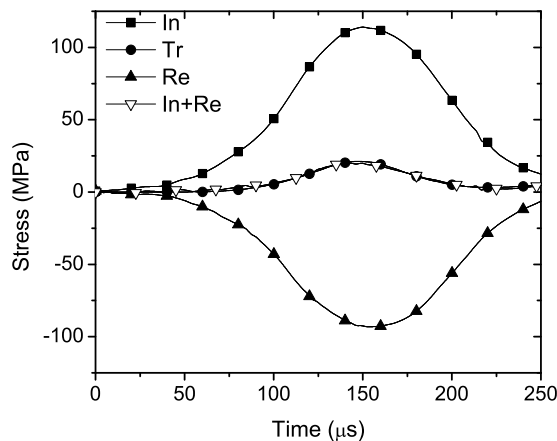## 3. Measurement techniques and data reduction

3.1. *Loading history and fracture velocity.* Figure 4 shows the loading history (P_2) and corresponding CSOD history during a dynamic SCB test. We denote the time zero (A) as the arrival time of the incident pulse at the sample. Because dynamic force balance is achieved, time instant B (102 μs), when the load reaches its peak, corresponds to the fracture initiation in the specimen, as in a quasistatic experiment. The slope of the CSOD increases with time and approaches a terminal constant beginning at instant C (136 μs). The two vertical lines passing through points B and C divide the entire deformation period into three stages. In stage I, the crack opens up elastically; in stage II, the crack propagates dynamically; in stage III, the fracture separates the sample completely into two pieces. The terminal separation velocity of the two fragments is the linear slope in CSOD after instant C. This velocity $v = 12.3$ m/s is twice the individual fragment terminal velocity. At instant D (180 μs), the completely separated fragments fly further away from each other.

We use high-speed photographs to illustrate qualitatively these representative instants (Figure 5). These photos are taken with a Photron SA-1 high-speed camera at 180 thousand frames per second. Each frame contains 125×125 pixels. Figure 5 shows the crack initiation at instant B, complete fracture at instant C, and pure rotation of the fragments with respect to the contact point of the specimen with the incident bar at instant D, consistent with the strain gauge measurements (Figure 4). The gauges were glued on the other side of the specimen for this test.

Crack propagation lasts about $\Delta t_{BC} = 34$ μs. Given the crack distance $L_s = R - a = 12.7$ mm for this test, we estimate the average crack growth velocity as $v_f = 374$ m/s. We also use crack gauges to estimate
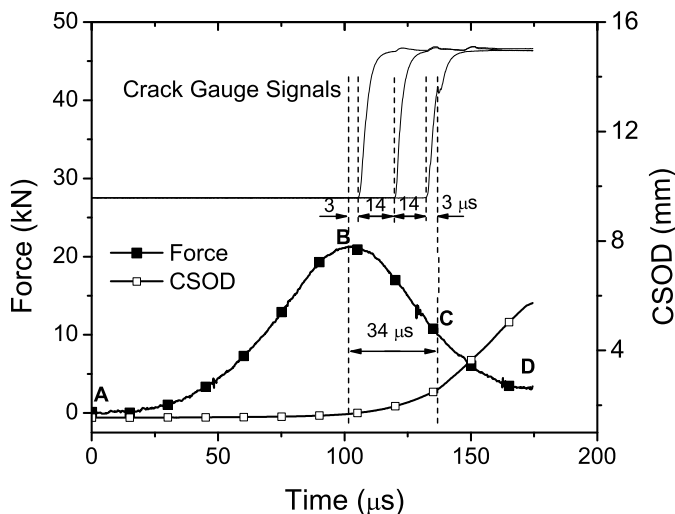

Figure 4. Typical loading history and CSOD history of the SCB specimen tested in SHPB. Top inset: crack gauge signals at three locations.
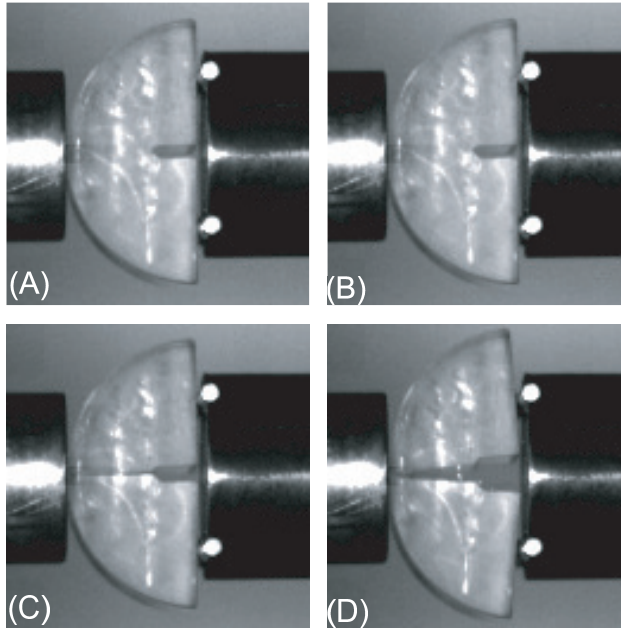
Figure 5. High-speed camera snapshots of a dynamic SCB test. A: time zero, B: $\sim 102\,\mu$s, C: $\sim 136\,\mu$s, D: $\sim 180\,\mu$s.

the fracture propagation velocity. Three crack gauges made of pencil lead are separated by $\Delta_{l_1} = 5.55$ mm and $\Delta_{l_2} = 4.43$ mm (see Figure 2). The time separations between the arrivals of the fracture onset signals are $\Delta_{t_1} = 14\,\mu$s, and $\Delta_{t_2} = 14\,\mu$s, respectively (see Figure 4). Thus the corresponding average fracture velocities are $v_1 = 396$ m/s, and $v_2 = 309$ m/s. The fracture velocity appears to decreases as the crack propagates during dynamic loading. The first gauge is cemented at about 1.2 mm away from the crack tip in order to avoid interfering with crack initiation. This explains the $3\,\mu$s delay between the crack initiation and the breaking of the first crack gauge. The fracture velocity as measured with LGG is consistent with the crack gauge results. One advantage of the LGG is that it is a noncontact method.

3.2. *Calculation of initiation fracture toughness.* The stress intensity factor (SIF) of the mode-I fracture of the SCB specimen can be calculated from (2), in analogy to the rectangular three-point bending method in the ASTM standard E399-06e2 [ASTM 1997]:

$$K_I(t) = \frac{P(t)S}{BR^{3/2}} Y(a/R),\qquad(2)$$

where $P(t)$ is the measured load force history, and $Y(a/R)$ a dimensionless geometry factor which can be calculated with a standard finite element software package (for example, ANSYS) [Barsoum 1977]. The initiation fracture toughness K_{IC}^d corresponds to the peak load $P_{\max}$ [Chen et al. 2009].

3.3. *Calculation of propagation fracture energy and toughness.* The propagation fracture energy and fracture toughness can be deduced based on energy conservation and the strain gauge and LGG measurements. Similarly, Zhang et al. [2000] used a high-speed camera instead of a LGG to estimate the fragment residual velocities. The energy carried by a stress wave (incident, reflected, or transmitted) is

[Kolsky 1953]:

$$W = \int_0^t E\varepsilon^2 A C \, d\tau, \tag{3}$$

where E is the Young's modulus, A is the cross-sectional area, and C is the wave speed of the bar. The total energy absorbed by the specimen then is $\Delta W = W_i - W_r - W_t$. Part of the total energy absorbed is used to create new crack surfaces, namely the total fracture energy W_G; the other part remains in the fragments as the residue kinetic energy (K). That is, $\Delta W = W_G + K$. Note that there may be some residual strain energy in the fragments. However, the fragment releases the strain energy at the speed of elastic wave velocity; the strain energy release is virtually at the same pace as the release of the far-field load. We thus assume that this strain energy is negligible.

For the rotating fragments, the moment of inertia is I, and the total rotational kinetic energy is $K = I\omega^2/2$, where the fragment angular velocity ω is estimated from the CSOD data. The average propagation fracture energy is $G_c = W_G/A_c$, where A_c is the area of the crack surfaces created. Here we use the projected area for crack surface area. Assuming the plane strain, the average dynamic propagation fracture toughness is:

$$K_I^P = \sqrt{G_c E/(1 - v^2)}, \tag{4}$$

where $E = 3.24 \, \text{GPa}$ and $v = 0.35$ are the Young's modulus and Poisson's ratio of the specimen respectively, with the values taken from the literature [Needleman and Rosakis 1999].

4. Results and discussion

Fifteen SCB samples of PMMA are tested at various impact velocities, and all of them are split cleanly into two equal pieces with smooth fracture surfaces, as shown in Figure 6. The results are summarized in Table 1, including loading rate $\dot{K}_I$, initiation fracture toughness K_{IC}^d, total fracture energy W_G, average fracture energy G_C, average crack growth velocity v_f, and propagation fracture toughness K_I^P.
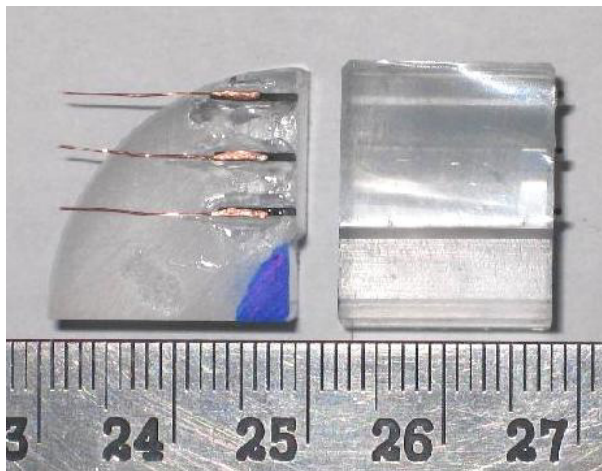
Figure 6. Typical PMMA samples recovered after fracture: side view (left) and fracture surface (right).

Sample	$\dot{K}_I$ (GPa m$^{1/2}$/s)	v_f (m/s)	K_{IC}^d (MPa m$^{1/2}$)	W_G (J)	G_c (J/m^2)	K_I^P (MPa m$^{1/2}$)
1	19	267	2.46	0.24	5.97×10^2	1.50
2	22	285	2.61	0.35	8.56×10^2	1.80
3	30	270	2.63	0.23	5.83×10^2	1.48
4	49	283	2.70	0.35	8.55×10^2	1.79
5	54	328	2.77	0.45	1.11×10^3	2.04
6	71	338	3.68	0.93	2.26×10^3	2.91
7	74	342	3.61	0.99	2.47×10^3	3.05
8	79	356	3.28	0.52	1.29×10^3	2.20
9	86	357	3.79	0.80	1.97×10^3	2.72
10	117	365	4.91	2.10	5.52×10^3	4.69
11	121	358	5.17	2.20	5.68×10^3	4.56
12	142	377	9.60	3.51	8.61×10^3	5.69
13	145	374	7.57	6.95	1.72×10^4	8.06
14	160	375	8.08	6.53	1.62×10^4	7.82
15	169	369	8.69	7.54	1.89×10^4	8.44

Table 1. Summary of experimental results.

4.1. *Loading rate effect.* The loading rate may have a considerable effect on the fracture toughness of a solid under dynamic loading. We characterize the loading rate with $\dot{K}_I$ obtained from the time evolution of SIF (K_I). Figure 7 shows loading and unloading in terms of SIF in a typical test. During the loading period, K_I increases with time and then reaches a constant (maximum) during 75–100 μs, followed by a drop before unloading; this maximum loading rate is adopted as the loading rate in a specific test, and also denoted as $\dot{K}_I$ for simplicity. In this work, fifteen different loading rates are explored; for each loading rate, the initiation and propagation fracture toughnesses of a SCB specimen are determined (see Table 1 and Figure 8).

Both the initiation and propagation fracture toughnesses increase with loading rate. At a given loading rate, the initiation fracture toughness is slightly higher than the propagation toughness (except in one case
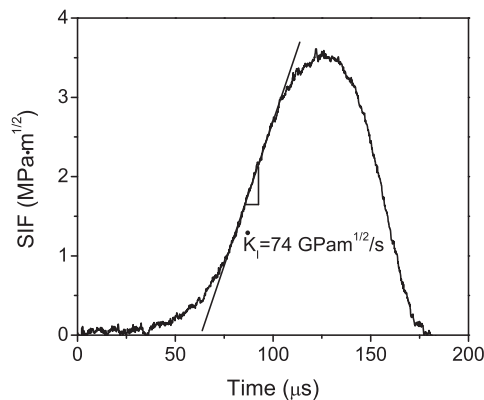
Figure 7. Typical SIF-time curve for determining loading rate.
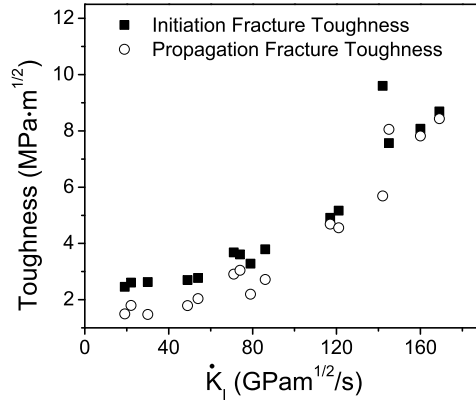
Figure 8. Initiation and propagation toughnesses of PMMA under different loading rates.

at $145\,\mathrm{GPa\,m^{1/2}/s}$). From the roughness measurement discussed below, the fracture surfaces are smooth. However, there is a finite radius at the tip of the notch prefabricated for crack initiation, which may lead to larger initiation toughness.

Figure 9 compares our results for fracture toughness with those reported in the literature [Wada 1992; Wada et al. 1993; Rittel and Maigre 1996]. It can be seen that at high loading rates (10^4–$10^5\,\mathrm{MPa\,m^{1/2}/s}$), our data agree well with those of this last reference, further confirming the validity of the dynamic SCB method. The dynamic SCB method has advantages such as simplicity. Our result at low loading rates is also in accord with previous data.

The fracture toughness ($\dot{K}_I$) data can be described with an exponential form:

$$K_I^d/K_{I0} = \exp(\dot{K}_I/\dot{K}_{I0}), \tag{5}$$

where K_{I0} and $\dot{K}_{I0}$ are fitting parameters. Fitting (3) to our data only yields $K_{I0} = 1.85\,\mathrm{MPa\,m^{1/2}}$ and $\dot{K}_{I0} = 1.0 \times 10^5\,\mathrm{MPa\,m^{1/2}/s}$ in the loading rate range of 10^{-1}–$10^5\,\mathrm{MPa\,m^{1/2}/s}$ (dashed curve, Figure 9). If both present and previous data are used, we obtain $K_{I0} = 1.47\,\mathrm{MPa\,m^{1/2}}$ and $\dot{K}_{I0} = 1.2 \times 10^5\,\mathrm{MPa\,m^{1/2}/s}$ (solid line, Figure 9) in a wide range of loading rates (10^{-2}–$10^5\,\mathrm{MPa\,m^{1/2}/s}$).
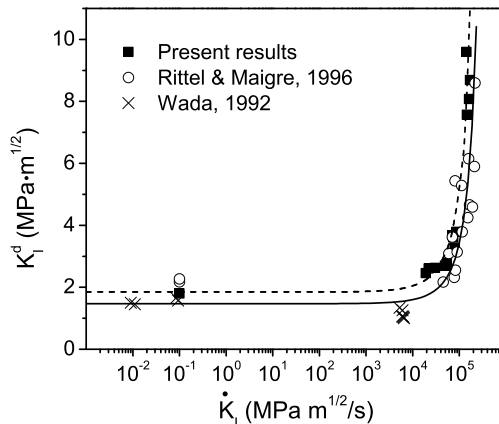
Figure 9. Comparison of previous and present initiation fracture toughness results.
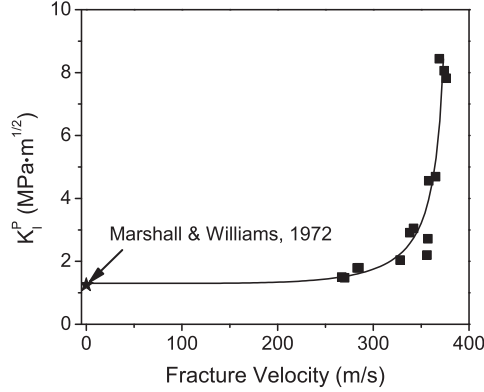
Figure 10. The fracture velocity-propagation toughness curve.

Further experiments are desirable to establish whether these results can be extrapolated to even lower or higher loading rates.

4.2. *Fracture velocity.* The propagation fracture toughness is believed to be a function of fracture velocity [Zehnder and Rosakis 1990]. Our experiments show the increase of propagation fracture toughness K_I^P with increasing fracture velocity (Figure 10). For example, K_I^P is 7.82 MPa m$^{1/2}$ at the highest fracture velocity (386 m/s) achieved, and decreases to 1.5 MPa m$^{1/2}$ at 267 m/s. At low velocities, the propagation fracture toughness is relatively insensitive to fracture velocity, but it increases drastically as the fracture velocity v_f approaches a limiting value v_l. Thus, the fracture velocity becomes saturated at high K_I^P.

The relationship between fracture velocity and fracture propagation toughness can be described empirically as [Anderson 2005]:

$$K_I^P = \frac{K_{IA}}{1 - (v_f/v_l)^m}, \tag{6}$$

where m is a constant, and K_{IA} is the fracture arrest toughness which corresponds to K_I^P at zero fracture velocity. Fitting our data to the equation yields

$$v_l = 385 \, \text{m/s}, \quad m = 5.44, \quad K_{IA} = 1.3 \, \text{MPa m}^{1/2}$$

(see Figure 10). The value of K_{IA} as predicted from our results at $v_f > 250$ m/s is in excellent agreement with the averaged fracture toughness obtained at low fracture velocities ($v_f \sim 0$) in [Marshall and Williams 1973]. This is not surprising, though, because K_{IA} represents the fracture toughness limit at zero crack velocity. It is noted that the relation presented in the equation is not universal. It applies to the sample geometry presented in this work, and the sample geometry presented by Rosakis and his coworkers, but it may not be applicable to other sample geometries.

The observation of the limiting fracture velocity (385 m/s) is also interesting. In [Rittel and Maigre 1996] a fracture velocity of 306 m/s was reported at an initiation toughness of 6.15 MPa m$^{1/2}$, consistent with our results (365 m/s at 5.17 MPa m$^{1/2}$). Our experiment configuration is similar to that of Rittel and Maigre: the sample boundaries are free except for the loading points and thus the edge release is pronounced.
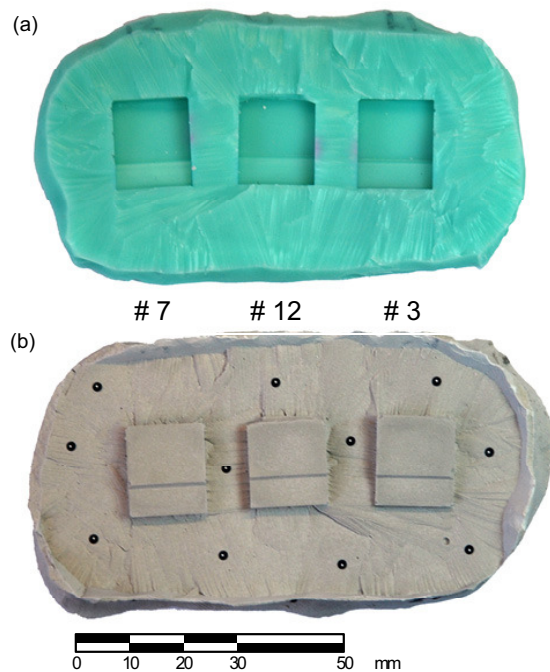
Figure 11. (a) Silicone rubber molds of three SCB fracture surfaces selected for rough-ness evaluation (samples #3, #7, and #12), and (b) the corresponding fracture surface replicas cast from the rubber molds.

4.3. *Fracture surface roughness and fracture energy.* To investigate the relationship between fracture energy and fracture roughness as a function of strain rate, the fracture surface topography of three PMMA SCB specimens loaded at different strain rates is measured with a white light 3D stereotopometric system, the advanced topometric sensor (ATOS) II (GOM mbH).

Digitization of the PMMA fracture surfaces is problematic because of the transparency of PMMA. We thus create replicas of the fractured SCB surfaces via molding and casting: the negative mold of a fracture surface is first made with silicone rubber (Figure 11a), and this mold is then used to cast fracture replicas out of a quick setting flowable anchoring cement (Figure 11b).

Digitization of each replicated fracture surface requires two individual measurements with the ATOS system. The scanning grid size is about $40\,\mu$m by $40\,\mu$m. Transformation of these measurements into a common coordinate system is achieved by affixing several 0.4 mm (diameter) reference points around the boundaries of the fracture surfaces (see Figure 11b). The average deviation between redundant data (that is, overlapping measurements) is termed the mesh deviation, which provides an estimate of the intensity of the average measurement noise of the system [ATOS 2008]. For the three fracture surfaces digitized in this study, the mesh deviation is less than $5\,\mu$m. Following completion of all measurements, the resulting point clouds for each sample are polygonized into triangulated irregular networks using the default triangulation algorithm of the ATOS software (Delaunay triangulation with no smoothing). This process deletes redundant points of the point cloud and discretizes the surfaces into contiguous triangles with vertices defined by neighboring points of the point cloud.

For the current study, the surface roughness coefficient, R_s, is adopted to characterize the roughness of the three replicated SCB fracture surfaces. The value of R_s is given by [Soudani 1978] as follows:

$$R_s = A_t/A_n, \tag{7}$$

where A_t is the true area of the surface defined by the summation of the area of each triangular element, A_i, comprising the 3D surface [Lange et al. 1993], and A_n is the nominal area defined by the projection of the actual area onto a best-fit plane through the surface. For a perfectly flat surface, R_s equals a minimum value of 1, while most fractures in brittle materials have R_s values between 1 and 2 [Belem et al. 2000].

Considering a digitized SCB fracture surface (Figure 12), a plane parallel to the notch plane is used to define the nominal area surface rather than a best-fit plane through the fracture surface. For each sample, the maximum area of the digitized fracture surface, excluding the notch plane and any damaged areas around the perimeter of the primary fracture, is considered when calculating the true surface area and corresponding nominal surface area. As the calculated fracture energy corresponds to the propagation of the primary fracture, inclusion of the damaged areas around the perimeter of the primary fracture resulting from secondary and tertiary fracturing under high strain rates would lead to increased values of R_s that do not represent the roughness of the primary fracture. (Secondary microcracks are not found with optical microscopy, though.) Thus, a potentially misleading relationship between fracture energy and fracture roughness may result. For the three representative samples (#3, #7, and #12), W_G varies from 0.23 to 6.95 J, but the measured values of R_s vary slightly from 1.002 to 1.01.

If we assume that W_G dissipates only in the form of surface energy, W_G should scale linearly with A_t and thus G_c should scale linearly with R_s. However, considering the two extreme cases (samples #3 and #12), G_c for #12 is about 30 times that for #3, while the corresponding ratio for R_s is only 1.01. This observation calls for additional energy dissipation mechanisms during dynamic fracture. Indeed, researchers recently showed the importance of the process zone to the total energy budget in earthquake ruptures, where dynamic rupture may induce damage around the rupture tip [Poliakov et al. 2002]. In the case of PMMA dynamic fracture as studied here, the additional dissipation mechanisms may include the plasticity or viscosity, because no microcracks are observed in the recovered specimen, and remain to be investigated in the future.
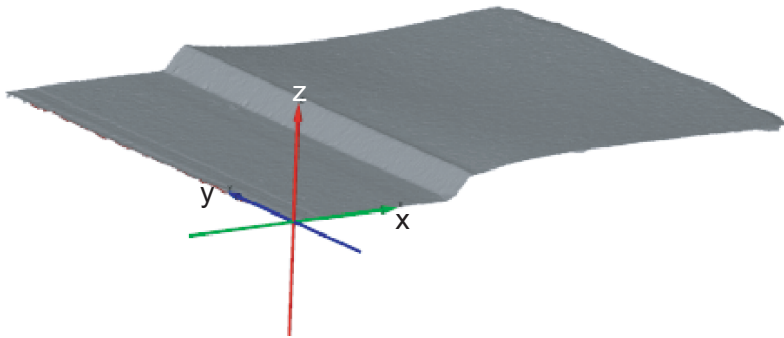

Figure 12. The surface scanning image for sample #12.

5. Conclusion

We have performed dynamic SPHB bending tests on notched semicircular PMMA specimens as well as finite element analysis and postmortem fracture surface roughness measurements, and obtained the initiation fracture toughness, propagation fracture toughness, and fracture velocity at different loading rates. The initiation and propagation toughnesses are similar and both increase with loading rate, the fracture velocity increases with the propagation toughness but reaches its limit at about 385 m/s, and their numerical relations are established. Our results also call for other energy dissipation mechanisms during dynamic fracture of PMMA besides free surface creation.

References

[Anderson 2005] T. L. Anderson, *Fracture mechanics: fundamentals and applications*, 3rd ed., CRC Press, Boca Raton, FL, 2005.

[ASTM 1997] "Standard test method for plane-strain fracture toughness of metallic materials", Standard ASTM E399-90, American Society for Testing and Materials, Philadelphia, 1997, Available at http://tinyurl.com/ASTM-E399-90. Superseded by the active standard.

[ATOS 2008] *ATOS user manual*, Version 6.1, GOM, Braunschweig, 2008.

[Barsoum 1977] R. S. Barsoum, "Triangular quarter-point elements as elastic and perfectly-plastic crack tip elements", *Int. J. Numer. Methods Eng.* **11**:1 (1977), 85–98.

[Belem et al. 2000] T. Belem, F. Homand-Etienne, and M. Souley, "Quantitative parameters for rock joint surface roughness", *Rock Mech. Rock Eng.* **33**:4 (2000), 217–242.

[Böhme and Kalthoff 1982] W. Böhme and J. F. Kalthoff, "The behavior of notched bend specimens in impact testing", *Int. J. Fract.* **20**:4 (1982), R139–R143.

[Chen et al. 2009] R. Chen, K. Xia, F. Dai, F. Lu, and S. N. Luo, "Determination of dynamic fracture parameters using a semi-circular bend technique in split Hopkinson pressure bar testing", *Eng. Fract. Mech.* **76**:9 (2009), 1268–1276.

[Chong and Kuruppu 1984] K. P. Chong and M. D. Kuruppu, "New specimen for fracture toughness determination for rock and other materials", *Int. J. Fract.* **26**:2 (1984), R59–R62.

[Dally 1979] J. W. Dally, "Dynamic photoelastic studies of fracture", *Exp. Mech.* **19**:10 (1979), 349–361.

[Évora et al. 2005] V. M. F. Évora, N. Jain, and A. Shukla, "Stress intensity factor and crack velocity relationship for polyester/ TiO$_2$ nanocomposites", *Exp. Mech.* **45**:2 (2005), 153–159.

[Frew et al. 2005] D. J. Frew, M. J. Forrestal, and W. Chen, "Pulse shaping techniques for testing elastic-plastic materials with a split Hopkinson pressure bar", *Exp. Mech.* **45**:2 (2005), 186–195.

[Kobayashi and Dally 1977a] T. Kobayashi and J. W. Dally, "Relation between crack velocity and the stress intensity factor in birefringent polymers", pp. 257–273 in *Fast fracture and crack arrest* (Chicago, 1976), edited by G. T. Hahn and M. F. Kanninen, ASTM STP **627**, American Society for Testing and Materials, Philadelphia, 1977. Paper ID STP27392S.

[Kobayashi and Dally 1977b] T. Kobayashi and J. W. Dally, "System of modified epoxies for dynamic photoelastic studies of fracture", *Exp. Mech.* **17**:10 (1977), 367–374.

[Kobayashi et al. 1972] A. S. Kobayashi, B. G. Wade, and D. E. Maiden, "Photoelastic investigation on the crack-arrest capability of a hole", *Exp. Mech.* **12**:1 (1972), 32–37.

[Kolsky 1953] H. Kolsky, *Stress waves in solids*, Clarendon, Oxford, 1953.

[Lange et al. 1993] D. A. Lange, H. M. Jennings, and S. P. Shah, "Relationship between fracture surface roughness and fracture behavior of cement paste and mortar", *J. Am. Ceram. Soc.* **76**:3 (1993), 589–597.

[Maigre and Rittel 1995] H. Maigre and D. Rittel, "Dynamic fracture detection using the force-displacement reciprocity: application to the compact compression specimen", *Int. J. Fract.* **73**:1 (1995), 67–79.

[Marshall and Williams 1973] G. P. Marshall and J. G. Williams, "The correlation of fracture data for PMMA", *J. Mater. Sci.* **8**:1 (1973), 138–140.

[Needleman and Rosakis 1999] A. Needleman and A. J. Rosakis, "The effect of bond strength and loading rate on the conditions governing the attainment of intersonic crack growth along interfaces", *J. Mech. Phys. Solids* **47**:12 (1999), 2411–2449.

[Owen et al. 1998] D. M. Owen, S. Zhuang, A. J. Rosakis, and G. Ravichandran, "Experimental determination of dynamic crack initiation and propagation fracture toughness in thin aluminum sheets", *Int. J. Fract.* **90**:1–2 (1998), 153–174.

[Poliakov et al. 2002] A. N. B. Poliakov, R. Dmowska, and J. R. Rice, "Dynamic shear rupture interactions with fault bends and off-axis secondary faulting", *J. Geophys. Res. Solid Earth* **107**:B11 (2002), 2295.

[Rittel and Maigre 1996] D. Rittel and H. Maigre, "An investigation of dynamic crack initiation in PMMA", *Mech. Mater.* **23**:3 (1996), 229–239.

[Rosakis et al. 1984] A. J. Rosakis, J. Duffy, and L. B. Freund, "The determination of dynamic fracture toughness of AISI 4340 steel by the shadow spot method", *J. Mech. Phys. Solids* **32**:6 (1984), 443–460.

[Soudani 1978] S. M. El-Soudani, "Profilometric analysis of fractures", *Metallography* **11**:3 (1978), 247–336.

[Wada 1992] H. Wada, "Determination of dynamic fracture toughness for PMMA", *Eng. Fract. Mech.* **41**:6 (1992), 821–831.

[Wada et al. 1993] H. Wada, M. Seika, C. A. Calder, and T. C. Kennedy, "Measurement of impact fracture toughness for PMMA with single-point bending test using an air gun", *Eng. Fract. Mech.* **46**:4 (1993), 715–719.

[Weerasooriya et al. 2006] T. Weerasooriya, P. Moy, D. Casem, M. Cheng, and W. Chen, "A four-point bend technique to determine dynamic fracture toughness of ceramics", *J. Am. Ceram. Soc.* **89**:3 (2006), 990–995.

[Xia et al. 2006] K. Xia, V. B. Chalivendra, and A. J. Rosakis, "Observing ideal 'self-similar' crack growth in experiments", *Eng. Fract. Mech.* **73**:18 (2006), 2748–2755.

[Zehnder and Rosakis 1990] A. T. Zehnder and A. J. Rosakis, "Dynamic fracture initiation and propagation in 4340 steel under impact loading", *Int. J. Fract.* **43**:4 (1990), 271–285.

[Zhang et al. 2000] Z. X. Zhang, S. Q. Kou, L. G. Jiang, and P.-A. Lindqvist, "Effects of loading rate on rock fracture: fracture characteristics and energy partitioning", *Int. J. Rock Mech. Min.* **37**:5 (2000), 745–762.

SHENG HUANG: sh.huang@utoronto.ca
Department of Civil Engineering and Lassonde Institute, University of Toronto, Toronto M5S 1A4, Canada

SHENG-NIAN LUO: sluo@lanl.gov
Physics Division, Los Alamos National Laboratory, Los Alamos, NM 87545, United States

BRYAN S. A. TATONE: bryan.tatone@utoronto.ca
Department of Civil Engineering and Lassonde Institute, University of Toronto, Toronto M5S 1A4, Canada

KAIWEN XIA: kaiwen@ecf.utoronto.ca
Department of Civil Engineering and Lassonde Institute, University of Toronto, Toronto M5S 1A4, Canada

msp

STRESS AND BUCKLING ANALYSES OF LAMINATES
WITH A CUTOUT USING A {3, 0}-PLATE THEORY

ATILA BARUT, ERDOGAN MADENCI AND MICHAEL P. NEMETH

A semianalytical solution method to predict stress field and structural bifurcation in laminates having a cutout by employing a simple {3, 0}-plate theory is presented. The stress analysis includes both in-plane and bending stress fields. In this theory, the in-plane and out-of-plane displacement fields are respectively assumed in the forms of cubic and uniform through-the-thickness expansions. The cubic expansion ensures the correct behavior of transverse shear deformations while satisfying the condition of zero transverse shear stresses at the laminate faces. The equations of equilibrium for the stress and buckling analysis are derived based on the principle of stationary potential energy. Comparison against the classical laminate and {1, 2}-plate theories proves this semianalytical method credible.

1. Introduction

Understanding the behavior of laminated composite plates is an important part of designing ultralightweight, high-performance aircraft structures. Typically, these structures are relatively thin and are designed by using analyses based on the classical laminated plate theory (CLPT) [Jones 1975]. However, there are instances in which using a higher-order refined theory becomes unavoidable in order to include accurately the effects of transverse shear flexibility on the structural response to obtain an initial design that is conservative or to verify margins of safety of a current design. The refined theories can be classified as *equivalent single-layer*, *layer-wise*, *zigzag*, and *variational asymptotic*. Although there are many different refined plate theories, they have not found wide acceptance in standard industry design practices because of the extensive experience base with CLPT. Thus, the focus of this study is to formulate new, advanced special-purpose analysis and design tools by using a refined plate theory that contains CLPT as an explicit, well-defined subset of the governing equations. A refined theory of this type may be useful in developing nondimensional design parameters that characterize the effects of transverse shear deformation and in extending the current design practice accepted by industry in a cautious building-block manner. Moreover, company-validated legacy computer codes can be retained and updated to include the effects of transverse shear flexibility with only some additional validation costs.

Each of the many refined theories for laminated composite plates has its own merits and range of validity associated with a given class of problems. Obviously, the choice of which theory to use depends on the nature of response characteristics. For example, for global response phenomena, such as elastic buckling and vibration response, that are not characterized by short wavelengths, it is likely that an equivalent single-layer theory would be sufficiently adequate. Attributes of several of these theories have been investigated and discussed in works such as [Liu and Li 1996; Reddy 1997; Altenbach 1998;

Barut et al. 2002; Yu and Hodges 2004; Demasi and Yu 2009]. A recent extensive discussion of the layer-wise and zigzag theories can be found in [Tessler et al. 2009].

In the development of special-purpose analysis tools that account for the effects of transverse shear flexibility for use in preliminary designs, rapid navigation of the design-parameter space is desired. As a result, computational efficiency is a major concern. This desire is driven by the wide range of laminated composite constructions available and the potential weight savings that can be obtained through laminate tailoring. Thus, it follows logically that a relatively simple equivalent single-layer refined plate theory is generally the starting point in the enhancement of legacy analysis tools that are based on CLPT. However, many of these theories, such as the first-order shear deformation theory (FSDT) first derived by Reissner [1944; 1945], do not contain the dependent kinematic variables of CLPT as an explicit subset. In the parlance of functional analysis, when the dependent kinematic variables of CLPT appear explicitly as a subset, the dependent kinematic variables of the refined theory possess a well-conditioned, linearly independent basis that also spans the CLPT subspace — analytically and computationally. According to [Shimpi 1999; Ray 2003], this attribute eliminates the numerical ill-conditioning that causes shear locking in finite element analyses of thin shear-deformable plates that are based on theories that use the rotations of the material line element, which is normal to the plate midplane, as dependent variables. The ill-conditioning arises from the fact that CLPT solutions are not recovered directly, but in an asymptotic sense, as the plate thickness is reduced and the transverse shear stiffness is increased.

There are laminated-plate theories that account for the effects of transverse shear flexibility and that do contain the dependent kinematic variables of CLPT as an explicitly defined subset. Reddy [1990] presented a review of all the existing third-order theories and showed that they are actually special cases of his third-order plate theory [Reddy 1984], in which the in-plane displacement components are cubic through-the-thickness expansions, yielding a quadratic variation of transverse shear strains, and the transverse displacement component is constant through the thickness, excluding the transverse normal deformations. While this formulation is applicable to plates with simply supported boundary conditions [Sun and Hsu 1990], it yields physically unacceptable zero transverse shear strains when both in-plane displacement components are fixed along the plate edges, as pointed out in [Krishna Murty 1987]. The problem was remedied by decomposing the transverse displacement component into separate parts for the displacements associated with bending and shear deformations. This has been applied successfully to stress [Krishna Murty 1987; Iyengar and Chakraborty 2004], buckling [Senthilnathan et al. 1987], and large deflection analyses [Reddy 1987; 1990; Singh et al. 1994] of isotropic and laminated plates. An alternative to decomposing the transverse displacement field in order to avoid zero transverse shearing along fixed-edge boundaries was proposed in [Voyiadjis and Shi 1991] for thick cylindrical shells and later reduced to plate kinematics in [Shi 2007]. In this alternative approach, average displacement and slope variables were utilized that produce an equivalent transverse shear strain energy density. The present study adopts the use of average displacements and slopes around plate boundaries by using Reissner's weighted-average displacement and slope definitions [Reissner 1944; 1945].

Other forms of higher-order theories for plates and shells have also been proposed. For example, [Soldatos and Timarci 1993; Timarci and Aydogdu 2005] employed higher-order theories based on polynomial, trigonometric, hyperbolic, and exponential expansions of in-plane displacements through the thickness and compared their relative accuracy in stress and buckling analyses of plates and shells. Shu and Sun [1994] introduced a third-order shear deformation theory that satisfies continuity of in-plane

displacements and transverse shear stresses between adjacent layers. However, their representation of the displacement variables resembles that of FSDT. Recently, Ray [2003] extended the zeroth-order shear deformation theory (ZSDT) of Shimpi [1999] to perform vibration analysis of simply supported laminated composites. It can be shown that the ZSDT of Shimpi and Ray is a special case of the form introduced in [Timarci and Aydogdu 2005]. The present study employs the kinematics of Shimpi's ZSDT because of its accuracy and simplicity in predicting the responses of laminated plates [Ray 2003]. Because of the cubic and constant through-the-thickness expansions used for the representation of, respectively, the in-plane and transverse displacement components of ZSDT, we use the term {3, 0}-*plate theory*. Notation of this type was originally introduced in [Tessler 1993].

Pertinent to the focus of the present refined single-layer theory, several results have been presented in the literature that show the relative accuracy of third-order plate theories. For example, Reddy [1997] presented results for bending, vibration, and buckling of flat rectangular laminated plates using his third-order plate theory. He presented solutions for simply supported, square, symmetric, and antisymmetric cross-ply laminates under sinusoidal pressure distributions. Transverse deflection of laminates with thickness-to-length ratios (h/L) as large as $\frac{1}{4}$ were compared against the exact elasticity solutions, CLPT and FSDT. Ramm [2000] presented the historical evolution of the FSDT and introduced a second-order plate theory whose kinematics account for both uniform and linear expansion modes in the thickness direction in addition to the transverse shear strains. In particular, in [Noor and Malik 2000] four modeling approaches were studied, based on first-order, second-order, third-order, and discrete-layer theories. Rohwer et al. [2001] presented the existing higher-order theories that are in polynomial form as truncated power series expansions of displacements with constant coefficients. The constant coefficients and truncation of the power series were determined based on term-by-term matching of the power series with the corresponding kinematic representation. They also introduced a generic fifth-order plate theory. Although this theory does not generally satisfy shear and normal traction-free boundary conditions at plate surfaces, it yields more accurate results than the third-order theories for simply supported orthotropic, symmetric, and nonsymmetric cross-ply laminates. In [Bosia et al. 2002] the validity of CLPT and FSDT were investigated by comparing numerical predictions of laminates under bending against experimental measurements. The results indicate that both CLPT and FSDT fail to capture the correct response for plates whose span-to-thickness ratio is lower than 25.

In [Tessler and Saether 1991; Tessler 1993] a second-order shear-deformation theory was introduced that includes quadratic expansions of transverse shear deformations and a linear expansion of transverse normal deformations through the thickness. Similarly, in [Reddy 1990; Barut et al. 2002] third-order plate theories were formulated for thick laminates, taking into account both transverse normal and shear deformations, as well as cubic variation of in-plane deformations. Also, the survey of the existing higher-order plate theories [Ghugal and Shimpi 2002] focuses on first-order, second-order, and various forms of higher-order shear deformation theories that have been developed for isotropic and laminated plates.

None of the previous studies considered laminates with cutouts, which can cause local gradients in the stress and strain fields that may lead to premature structural failure, especially due to structural buckling. Thus, it is important to understand how cutouts affect the transverse shear flexibility of laminates. Therefore, the objective of the present study is to derive the governing equations of a {3, 0}-plate theory for stress and buckling analysis of laminated composite plates under general loading and boundary conditions. This plate theory contains the dependent variables of CLPT as a proper subspace, provides

the quadratic variation of transverse shear stresses through the thickness of the laminate, satisfies the condition of zero transverse shear stresses on the top and bottom surfaces of the laminate, and does not require a transverse shear correction factor.

This study presents a semianalytical solution method for predicting the bending and buckling behavior of a moderately thick laminate with a cutout. While employing the {3, 0}-plate theory, the present approach utilizes the principle of stationary potential energy to derive the governing equations for bending deformation and structural bifurcation. The solutions of these governing equations are obtained by employing global and local function sets that mathematically take into account the presence of cutouts and general boundary conditions. Two sets of results are presented for selected structural configurations with a cutout. These sets are linear-bending analysis results, which address the accurate representation of local through-the-thickness effects, and buckling analysis results, which address global stiffness-critical effects. For both sets of results, all deformations are presumed to be elastic.

2. Overview of the {3, 0}-plate theory

The nonlinear plate theory used in the present study is based on the kinematic equations presented in [Sun and Hsu 1990] and is a special case of the formulation presented in [Soldatos and Timarci 1993; Timarci and Aydogdu 2005]. In particular, the in-plane and transverse displacement fields of a material point (x, y, z) are expressed in Cartesian coordinates (see Figure 1 on page 832) as

$$U_x(x, y, z) = u_x(x, y) - zu_{z,x}(x, y) + \Lambda(z)\Phi_{xz}(x, y), \tag{1a}$$

$$U_y(x, y, z) = u_y(x, y) - zu_{z,y}(x, y) + \Lambda(z)\Phi_{yz}(x, y), \tag{1b}$$

$$U_z(x, y, z) = u_z(x, y), \tag{1c}$$

where the displacements U_x, U_y, and U_z are associated with the x, y, and z-directions, respectively. The functions u_x and u_y represent the in-plane displacements, and u_z represents the out-of-plane displacement of the point $(x, y, 0)$ on the laminate midplane; a subscript after a comma denotes partial differentiation. Inspection of these equations reveals that the kinematic equations of CLPT appear explicitly. The function $\Lambda(z)$ is selected to satisfy the traction-free boundary conditions on shear stresses at the outer, bounding surfaces of a laminate and to satisfy the conditions $U_x(x, y, 0) = u_x(x, y)$ and $U_y(x, y, 0) = u_y(x, y)$. As noted in [Timarci and Aydogdu 2005], the choice of $\Lambda(z)$ is not unique. In the present study, $\Lambda(z)$ is specified as a cubic through-the-thickness distribution, which is one of the special cases examined by Timarci and Aydogdu. Because the corresponding functional representations of the displacement fields consist of cubic polynomial expansions in the through-the-thickness coordinate z for the in-plane displacements and no expansion for the out-of-plane displacement, the theory is denoted herein as a {3, 0}-plate theory based on the notation of [Tessler 1993].

The kinematic assumptions given by (1) are modified forms of those given in [Ray 2003]. In particular, the unknown functions $\Phi_{xz}(x, y)$ and $\Phi_{yz}(x, y)$ are, generally, not the stiffness-weighted transverse shear stress resultants of CLPT, used by Ray and initially suggested in [Shimpi 1999]. This representation permits the application of the plate theory to the entire class of laminated plates and is consistent with full coupling of the transverse shearing stress and transverse shearing strains, through the constitutive equations.

[Reddy 1990] showed that the {3, 0} theory presented herein can be obtained from his {3, 0} theory by a simple transformation of the dependent kinematic variables. As a result, the inherent physical accuracy of the two {3, 0} theories are expected to be identical. However, the computational attributes are likely to be quite different, particularly for large relative values of the transverse shear stiffnesses.

The boundary conditions associated with the {3, 0}-plate theory include terms arising from the presence of higher-order in-plane deformation modes. It is difficult to interpret and associate the higher-order terms, Φ_{xz} and Φ_{yz}, with commonly used boundary displacements and slopes. In this study, this difficulty is avoided by introducing independent boundary displacements, $\tilde{U}_\alpha$, with $\alpha = x, y, z$. Based on the kinematics of the Mindlin plate theory, these boundary displacements are defined as

$$\tilde{U}_x(x, y, z) = \tilde{u}_x(x, y) - z\tilde{\vartheta}_x(x, y), \tag{2a}$$

$$\tilde{U}_y(x, y, z) = \tilde{u}_y(x, y) - z\tilde{\vartheta}_y(x, y), \tag{2b}$$

$$\tilde{U}_z(x, y, z) = \tilde{u}_z(x, y), \tag{2c}$$

in which $\tilde{u}_x(x, y)$, $\tilde{u}_y(x, y)$, and $\tilde{u}_z(x, y)$ represent the weighted-average displacements and $\tilde{\vartheta}_x(x, y)$ and $\tilde{\vartheta}_y(x, y)$ rotations. Their representation in terms of the kinematics of the {3, 0} theory presented herein is achieved by minimizing the error between U_α and $\tilde{U}_\alpha$ ($\alpha = x, y, z$), that is,

$$\min\left[\int_{-h/2}^{h/2} \{(\tilde{U}_x - U_x)^2 + (\tilde{U}_y - U_y)^2 + (\tilde{U}_z - U_z)^2\}\, dz\right]. \tag{3}$$

The minimization of (3) with respect to the independent quantities, $\tilde{u}_\alpha(x, y)$ with $\alpha = x, y, z$ and $\tilde{\vartheta}_\beta(x, y)$ with $\beta = x, y$, leads to the following weighted averages:

$$(\tilde{u}_x, \tilde{u}_y, \tilde{u}_z) = \frac{1}{h}\int_{-h/2}^{h/2}(U_x, U_y, U_z)\, dz, \qquad (\tilde{\vartheta}_x, \tilde{\vartheta}_y) = \frac{12}{h^3}\int_{-h/2}^{h/2} z(U_x, U_y)\, dz. \tag{4}$$

Substituting U_x, U_y, and U_z from (1) into these equations results in the following explicit forms given in terms of the kinematics of the {3, 0} theory:

$$\tilde{u}_\alpha(x, y) = u_\alpha(x, y) \qquad \text{with} \quad \alpha = x, y, z, \tag{5a}$$

$$\tilde{\vartheta}_\beta(x, y) = u_{z,\beta}(x, y) - \frac{6}{5h}\Phi_{\beta z}(x, y) \qquad \text{with} \quad \beta = x, y. \tag{5b}$$

Hence, this representation of the boundary displacements and slopes is the least-squares equivalent of the {3, 0} theory kinematics along the boundary.

The nonlinear strain-displacement relations used in the present study are based on the Green–Lagrange strains of elasticity theory, simplified for a flexible plate-like solid exhibiting small strains and moderately small rotations by using the von Kármán assumptions [Fung and Tong 2001].

The corresponding nonlinear plate strains are obtained by substituting (1) into the simplified Green–Lagrange strains. Work-conjugate stress resultants are identified by substituting the plate strains into the strain energy and then reducing it to a two-dimensional quantity by through-the-thickness integration. The laminate constitutive equations are obtained by substituting the expressions for the laminate strains into the stress-strain relations for a generally orthotropic material, in a state of plane stress, and by then

substituting the resulting equations for the stresses into the definitions of the stress resultants and performing the through-the-thickness integrations. The nonlinear equilibrium equations and the corresponding boundary conditions are obtained by taking the variation of the total potential energy of the laminate and using Green's integral theorem to enforce the fundamental theorem of the calculus of variations.

3. Problem description

The general boundary-value problem considered in the present study consists of a rectangular laminate with an elliptical cutout that is located arbitrarily (Figure 1). The cutout has a semimajor axis and a semiminor axis with lengths $2a$ and $2b$, respectively. As shown in Figure 1, the local Cartesian coordinate system (x', y', z'), whose origin is located at the center of the cutout, coincides with the principal coordinates of the elliptical cutout. The global structural coordinates are denoted by (x, y, z), and the orientation of the cutout with respect to the global horizontal axis is defined by the angle ψ. The laminate is made of K specially orthotropic layers, and each layer has an orientation angle, θ_k, that is defined with respect to the x-axis (see Figure 1). The total laminate thickness is denoted by h. Each layer has a thickness of h_k; elastic moduli E_{11}, E_{22}, and E_{33}; shear moduli G_{12}, G_{23}, and G_{31}; and Poisson's ratios ν_{12}, ν_{23}, and ν_{31}; the subscripts 1, 2, and 3 represent the fiber, transverse, and thickness directions, respectively.

A special, practical set of loading conditions are considered in the present study. As shown in Figure 1, Γ_σ represents the laminate edges that are traction free, and Γ_u denotes the part of the laminate boundary
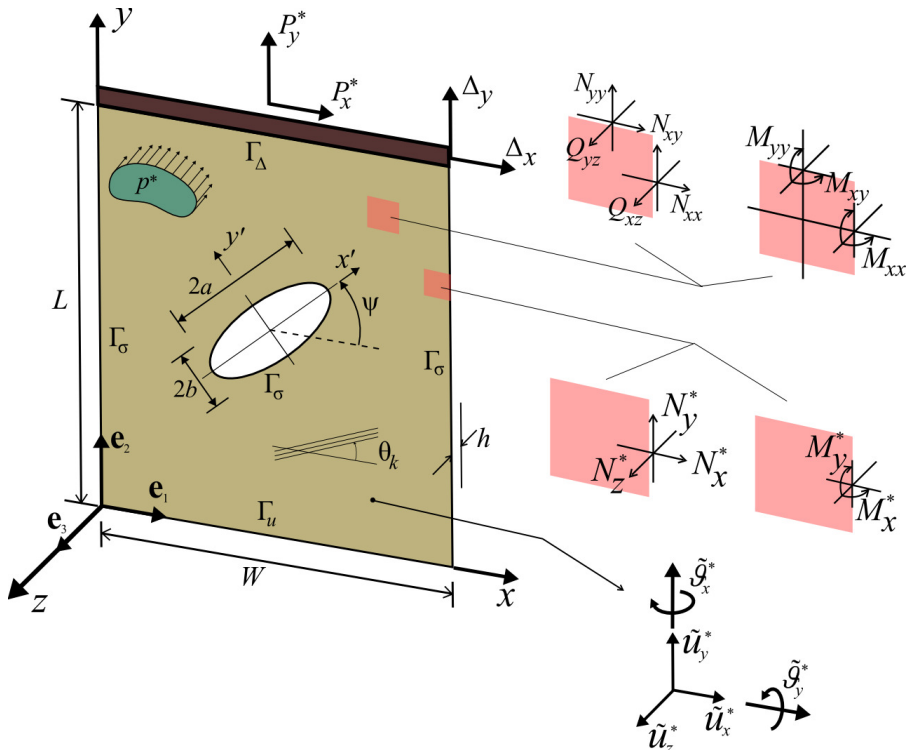

Figure 1. Description of geometry and loading of composite plate with an elliptical cutout.

that is kinematically restrained. The laminate boundary on which the kinematics of the boundary is constrained by uniform edge displacements is represented by Γ_Δ. This boundary can be clamped or simply supported against bending while allowing for uniform in-plane edge displacements. As depicted in Figure 1, uniform edge displacement is achieved in the present study through use of a rigid load fixture (rigid bar) that is subjected to concentrated edge forces. This approach is used to represent the most commonly employed experimental loading conditions. Throughout this paper, a variable with the superscript "$*$" is treated as a *known quantity*, arising from the externally applied loads or from prescribed displacements and rotations.

The laminate can be subjected to an arbitrary lateral distributed load of $p^*(x, y)$ pointing in the negative z-direction, as shown in Figure 1. The positive-valued stress and moment resultants of applied boundary tractions, (N_x^*, N_y^*, N_z^*) and (M_x^*, M_y^*), are applied along the edges as shown in Figure 1. The concentrated forces, P_x^* and P_y^*, applied to the ends of the laminate through a rigid end-bar, as shown in Figure 2, lead to uniform edge displacements with *unknown* magnitudes Δ_x and Δ_y.

The prescribed edge displacements on the midplane $(\tilde{u}_x^*, \tilde{u}_y^*, \tilde{u}_z^*)$ and edge slopes $(\tilde{\vartheta}_x^*, \tilde{\vartheta}_y^*)$ on the x-z and y-z planes, respectively, are imposed as

$$\tilde{u}_i(x, y) = \tilde{u}_i^* \quad (i = x, y, z),$$
$$\tilde{\vartheta}_i = \tilde{\vartheta}_i^* \quad (i = x, y),$$

(6)

where $\tilde{u}_x$, $\tilde{u}_y$, and $\tilde{u}_z$ denote the weighted-average boundary displacements and $\tilde{\vartheta}_x$ and $\tilde{\vartheta}_y$ are the weighted-average slope quantities.

As shown in Figure 2, the kinematic boundary conditions are imposed by employing elastic spring supports. Zero-valued displacement and rotation kinematic boundary conditions are enforced in an indirect manner by specifying values for the spring stiffnesses that are large compared to the corresponding laminate stiffnesses. This approach effectively yields a prescribed kinematic boundary condition in the limit as the relative stiffness of the spring becomes much greater than that of the corresponding laminate stiffness. Similarly, values for the spring stiffnesses can be selected corresponding to a given uniform
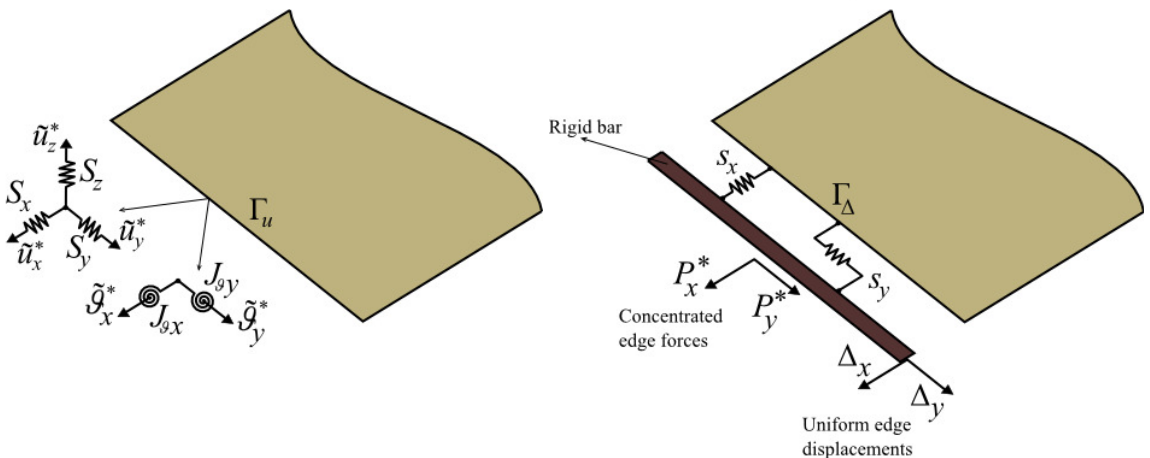

Figure 2. Distributed elastic spring supports along the edges of a laminate.

elastic restraint along an edge, similar to that provided by a rigid end-bar. This capability is important and useful because in some test fixtures, or actual structures, the edge supports may not be stiff enough to simulate a fully clamped boundary condition or flexible enough to simulate a simply supported boundary condition. The extensional and rotational springs have constants S_x, S_y, and S_z associated with the edge displacements and $J_{\vartheta x}$ and $J_{\vartheta y}$ with the slopes. In addition, a rigid end-bar is linked to the plate edge through extensional springs in the directions normal and tangent to the boundary with stiffness values of s_x and s_y. The specification of a sufficiently large value of spring stiffness for s_x and s_y causes the plate edge to behave as a rigid end-bar with uniform displacements, Δ_x and Δ_y. Conversely, a sufficiently small spring stiffness between the plate edge and the rigid end-bar eliminates the presence of a rigid end-bar. In the case of buckling analysis, this type of edge support, commonly used in buckling experiments, permits the determination of the end shortening of the plate.

4. Nonlinear equations of the {3, 0}-plate theory

The nonlinear equations of the plate theory are derived by considering the variation of the total potential energy of the laminate. In the present study, the total potential energy consists of the potential energy of the elastic spring supports in addition to the internal strain energy of deformation and the work of the applied loads.

Strain field and potential energy. The internal strain energy of deformation is generated by the presence of a strain field within a laminate. For the plate kinematics defined by (1), the corresponding nonlinear strain-displacement relations that correspond to small strains and moderate rotations are given by

$$\boldsymbol{\epsilon} = \boldsymbol{\epsilon}^0 + z\boldsymbol{\kappa}^0 + \Lambda(z)\boldsymbol{\Gamma}^0, \tag{7a}$$

$$\boldsymbol{\gamma} = \Lambda'(z)\boldsymbol{\Phi}, \tag{7b}$$

where the vectors $\boldsymbol{\epsilon}$, $\boldsymbol{\gamma}$, $\boldsymbol{\epsilon}^0$, $\boldsymbol{\kappa}^0$, $\boldsymbol{\Gamma}^0$, and $\boldsymbol{\Phi}$ are defined as

$$\boldsymbol{\epsilon}^T = \{\epsilon_{xx}, \epsilon_{yy}, \gamma_{xy}\}, \qquad \boldsymbol{\gamma}^T = \{\gamma_{xz}, \gamma_{yz}\}, \tag{7c}$$

$$\boldsymbol{\epsilon}^{0^T} = \left\{\left[u_{x,x} + \tfrac{1}{2}(u_{z,x})^2\right], \left[u_{y,y} + \tfrac{1}{2}(u_{z,y})^2\right], (u_{x,y} + u_{y,x} + u_{z,x}u_{z,y})\right\}, \tag{7d}$$

$$\boldsymbol{\kappa}^{0^T} = -\{u_{z,xx}, u_{z,yy}, 2u_{z,xy}\}, \quad \boldsymbol{\Gamma}^{0^T} = \{\Phi_{xz,x}, \Phi_{yz,y}, (\Phi_{xz,y} + \Phi_{yz,x})\}, \quad \boldsymbol{\Phi}^T = \{\Phi_{xz}, \Phi_{yz}\}. \tag{7e}$$

The prime mark in (7b) denotes differentiation with respect to the through-the-thickness coordinate z. The transverse normal strain, ϵ_{zz}, is zero-valued, consistent with assumption of a uniform through-the-thickness out-of-plane displacement specified by (1c). In addition, defining average transverse shearing strains γ_{xz}^0 and γ_{yz}^0 by

$$\boldsymbol{\gamma}^0 = \begin{Bmatrix} \gamma_{xz}^0 \\ \gamma_{yz}^0 \end{Bmatrix} = \frac{1}{h} \int_{-h/2}^{+h/2} \begin{Bmatrix} \gamma_{xz} \\ \gamma_{yz} \end{Bmatrix} dz, \tag{8}$$

where h denotes the uniform thickness of the plate, gives

$$\boldsymbol{\gamma}^0 = \frac{1}{h}\left(\Lambda\left(\frac{h}{2}\right) - \Lambda\left(-\frac{h}{2}\right)\right) \begin{Bmatrix} \Phi_{xz} \\ \Phi_{yz} \end{Bmatrix}. \tag{9}$$

Inspection of (7b) reveals that the transverse shearing strains vanish at the bounding surfaces of the plate given by $z = \pm h/2$ provided that

$$\Lambda'(h/2) = \Lambda'(-h/2) = 0. \tag{10}$$

The strain energy of a laminate is obtained by substituting the expressions for the strains in Equations (7) into the strain energy expression for a three-dimensional elastic solid and performing through-the-thickness integration of the resulting equations. This process yields the strain energy of a laminate as

$$U = \frac{1}{2} \int_A (N^T \epsilon^0 + M^T \kappa^0 + F^T \Gamma^0 + f^T \Phi) \, dx \, dy, \tag{11}$$

with

$$N^T = \{N_{xx}, N_{yy}, N_{xy}\}, \quad M^T = \{M_{xx}, M_{yy}, M_{xy}\}, \quad F^T = \{F_{xx}, F_{yy}, F_{xy}\}, \quad f^T = \{f_{xz}, f_{yz}\}, \tag{12}$$

where the definitions of the stress resultants appearing in this expression, N_{ij}, M_{ij}, and F_{ij} with $i, j = x, y$ and f_{iz} with $i = x, y$, are given in Appendix A. It is convenient to express (11) in the following compact form:

$$U = \frac{1}{2} \int_A s^T e \, dA, \tag{13}$$

where s and e are vectors of the stress and strain resultants given by

$$s^T = \{N^T, M^T, F^T, f^T\}, \tag{14a}$$

$$e^T = \{\epsilon^{0^T}, \kappa^{0^T}, \Gamma^{0^T}, \Phi^T\}. \tag{14b}$$

For the elastic materials considered herein, the stress resultant vector s is related to the strain resultant vector e through the constitutive matrix C as

$$s = Ce, \tag{15}$$

in which

$$C = \begin{bmatrix} A & B & E & 0 \\ & D & F & 0 \\ & & H & 0 \\ & & & G \end{bmatrix}. \tag{16}$$

The submatrices A, B, D, E, F, G, and H are explicitly defined in Appendix A. Substituting (15) into (13) yields the desired form of the laminate strain energy given by

$$U = \frac{1}{2} \int_A e^T C e \, dA. \tag{17}$$

As described in the preceding section, elastic extensional and rotational springs are employed to accommodate the enforcement of prescribed edge displacements ($\tilde{u}_x^*$, $\tilde{u}_y^*$, and $\tilde{u}_z^*$) and slopes ($\tilde{\vartheta}_x^*$ and $\tilde{\vartheta}_y^*$) defined in (6), along the boundary of the laminate, Γ_u. Associated with these displacements $\tilde{u}_x^*$, $\tilde{u}_y^*$, $\tilde{u}_z^*$ and with the slopes $\tilde{\vartheta}_x^*$, $\tilde{\vartheta}_y^*$ are the extensional and rotational spring stiffnesses S_x, S_y, S_z and $J_{\vartheta x}$, $J_{\vartheta y}$, respectively. As the concentrated loads P_x^* and P_y^* are applied to the rigid bar shown in Figure 1, the laminate undergoes the uniform edge displacements Δ_x and Δ_y. Associated with these uniform edge

displacements are the extensional spring stiffnesses, s_x and s_y. The potential energy that results from the elastic deformation of the springs, consistent with the $\{3, 0\}$-theory used herein, is given by

$$\Omega = \frac{1}{2} \int_{\Gamma_u} (\tilde{\boldsymbol{u}} - \tilde{\boldsymbol{u}}^*)^T \boldsymbol{k}_u (\tilde{\boldsymbol{u}} - \tilde{\boldsymbol{u}}^*) \, d\Gamma + \frac{1}{2} \int_{\Gamma_\Delta} (\tilde{\boldsymbol{u}} - \boldsymbol{\Delta})^T \boldsymbol{k}_u (\tilde{\boldsymbol{u}} - \boldsymbol{\Delta}) \, d\Gamma, \tag{18}$$

where the vectors $\tilde{\boldsymbol{u}}$, $\tilde{\boldsymbol{u}}^*$, and $\boldsymbol{\Delta}$, and the matrices $\boldsymbol{k}_u$ and $\boldsymbol{k}_\Delta$, are defined as

$$\tilde{\boldsymbol{u}}^T = \{\tilde{u}_x, \tilde{u}_y, \tilde{u}_z, \tilde{\vartheta}_x, \tilde{\vartheta}_y\}, \tag{19a}$$

$$\tilde{\boldsymbol{u}}^{*T} = \{\tilde{u}_x^*, \tilde{u}_y^*, \tilde{u}_z^*, \tilde{\vartheta}_x^*, \tilde{\vartheta}_y^*\}, \tag{19b}$$

$$\boldsymbol{\Delta}^T = \{\Delta_x, \Delta_y, 0, 0, 0\}, \tag{19c}$$

and

$$\boldsymbol{k}_u = \begin{bmatrix} S_x & & & & \\ & S_y & & & \\ & & S_z & & \\ & & & J_{\vartheta x} & \\ & & & & J_{\vartheta y} \end{bmatrix}, \qquad \boldsymbol{k}_\Delta = \begin{bmatrix} S_x & & & & \\ & S_y & & & \\ & & 0 & & \\ & & & 0 & \\ & & & & 0 \end{bmatrix}. \tag{19d}$$

The potential energy of the lateral pressure p^*, the external edge tractions (t_x^*, t_y^*, t_z^*), and the concentrated forces P_x^* and P_y^* acting on the rigid end-bar is given by

$$V = \int_{\Gamma_\sigma} \int_{-h/2}^{h/2} (t_x^* \tilde{U}_x + t_y^* \tilde{U}_y + t_z^* \tilde{U}_z) \, dz \, d\Gamma + \int_A p^* U_z \, dA + P_x^* \Delta_x + P_y^* \Delta_y. \tag{20}$$

Substituting (1), (2), and (5) into this expression and integrating through the thickness yields

$$V = \int_{\Gamma_\sigma} \left(N_x^* u_x + N_y^* u_y + N_z^* u_z - M_x^* \left(u_{z,x} - \frac{6}{5h} \Phi_{xz} \right) - M_y^* \left(u_{z,y} - \frac{6}{5h} \Phi_{yz} \right) \right) d\Gamma$$
$$+ \int_A p^* u_z \, dA + P_x^* \Delta_x + P_y^* \Delta_y, \tag{21a}$$

or

$$V = \int_{\Gamma_\sigma} \boldsymbol{T}^{*T} \tilde{\boldsymbol{u}} \, d\Gamma + \int_A p^* u_z \, dA + \boldsymbol{P}^{*T} \boldsymbol{\Delta}, \tag{21b}$$

in which the vector containing the resultant forces and moments acting along the boundary is given by

$$\boldsymbol{T}^{*T} = \{N_x^*, N_y^*, N_z^*, -M_x^*, -M_y^*\}, \tag{22a}$$

and the prescribed point forces acting on the rigid end-bar are defined as

$$\boldsymbol{P}^{*T} = \{P_x^*, P_y^*, 0, 0, 0\}. \tag{22b}$$

The explicit definitions of the stress and moment resultants (N_x^*, N_y^*, N_z^*) and (M_x^*, M_y^*) in (22) are given in Appendix A.

Equilibrium equations and boundary conditions. The nonlinear equilibrium equations and the corresponding boundary conditions are obtained by requiring the variation of the total potential energy of the laminate to vanish, that is,

$$\delta\pi = \delta U + \delta\Omega - \delta V = 0, \tag{23}$$

in which δU and $\delta\Omega$ represent the variation of strain energies of the laminate and the elastic edge supports (springs) due to the internal forces, and δV represents the variation of potential energy due to external boundary loads acting on the surface and around the boundary of the laminate. Their first variations are readily obtained from (17), (18), and (21) and are given explicitly in Appendix B. The resulting nonlinear partial differential equations and boundary conditions constitute a boundary-value problem that defines the stresses and displacements associated with stable and unstable deformation states in the realm of small strains and moderate rotations. The equations are applicable to laminates subjected to general loading conditions that exhibit anisotropy that couples all modes of deformation present in laminates with a general asymmetric lamination scheme. The equations needed to perform linear stress analysis can be obtained by direct linearization of the nonlinear plate equations. The specific form of these linearized equations is also given in Appendix B.

When a laminate is subjected to only in-plane loads, with monotonically increasing magnitudes, it may exhibit a flat stable equilibrium configuration for relatively small magnitudes of the loads. Then, a load level is reached at which a bent or buckled equilibrium configuration exists. This particular load level is obtained herein by linearizing the nonlinear plate equation with respect to the flat equilibrium configuration incipient to buckling [Brush and Almroth 1975]. The explicit forms of the resulting equations for buckling analyses are also given in Appendix B.

5. Solution method

Exact solutions for linear stress and buckling analyses of a composite laminate with a cutout are not mathematically tractable, especially when transverse shear deformations are included in the analyses. Therefore, a semianalytical approximate solution was constructed based on the principle of stationary potential energy.

In this approximate solution method, the midplane displacements $u_x(x, y)$, $u_y(x, y)$, and $u_z(x, y)$ and the higher-order in-plane deformation modes $\Phi_{xz}(x, y)$ and $\Phi_{yz}(x, y)$ are partitioned into global and local contributions. In particular,

$$u_i = \bar{u}_i + \bar{\bar{u}}_i \quad \text{with } i = x, y, z, \tag{24a}$$

and

$$\Phi_{iz} = \bar{\Phi}_{iz} + \bar{\bar{\Phi}}_{iz} \quad \text{with } i = x, y, \tag{24b}$$

where single and double overbars represent the global and local quantities, respectively. In the present formulation, no kinematic admissibility requirements on the local or global functions exist because of the presence of the elastic springs in the formulation. Robust, uniformly convergent Laurent series (used for doubly connected regions) are used for the local functions to enhance capturing steep stress gradients and deformations near a cutout, and complete sets of Chebyshev polynomials are used in series expansions primarily to capture the overall global response of the laminate. The global functions are defined to include all of the possible rigid-body modes associated with global translation and rotation

of the laminate. These rigid-body modes are eliminated in the analysis by enforcing the appropriate displacement boundary conditions. The Laurent series for the local quantities generally yield multivalued displacements. Therefore, single-valuedness of the local quantities must be enforced. This task is achieved by using Lagrange multipliers to enforce the required constraint conditions. The Lagrange multipliers can be viewed as the forces that are needed to enforce the corresponding constraints. The explicit form of the local and global quantities appearing in (24) and the constraint conditions are given in Appendix C.

In the solution method of the present study, the series expansions for the global and local quantities appearing in (24) are expressed in matrix form to yield

$$u_i = V_i^T q \qquad \text{with } i = x, y, z, \tag{25a}$$

$$\Phi_{iz} = V_{iz}^T q \qquad \text{with } i = x, y. \tag{25b}$$

In these expressions, the unknown coefficients of the local and global functions are arranged in the vector q, which is referred to herein as the vector of generalized coordinates. The explicit form for the vector of unknowns, q, and the known vector functions, V_i, are given in detail in Appendix C. Using (25), the total potential energy, π, of the laminate is expressed as

$$\pi(q, \Delta, \lambda) = U(q) + \Omega(q, \Delta) - V(q, \Delta) + W(q, \lambda), \tag{26}$$

in which U and Ω represent the strain energies of the laminate and the elastic edge supports (springs), and V represents the potential energy due to external boundary loads acting inside and around the boundary of the laminate. The vector Δ includes the unknown uniform edge-displacements that arise from the prescribed concentrated loads that are applied through the rigid end-bar. Because elastic edge supports are used as a means to relax the kinematic admissibility requirements on the assumed displacement functions, the potential energy of the constraint forces arising from the constraint equations must vanish. Therefore, the constraint equations are included in the total potential energy formulation by using Lagrange multipliers that produce zero potential energy; that is,

$$W(q, \lambda) = \lambda^T G_c q \equiv 0, \tag{27}$$

where W is the potential energy of constraint forces, G_c is the coefficient matrix of the constraint equations, and λ is a vector of Lagrange multipliers. The vector λ contains the unknown Lagrange multipliers of the constraint equations, and they represent the constraint forces. A detailed derivation is given in Appendix C.

Stress analysis. Under the presumption of infinitesimal displacement gradients, the potential energy is linearized by disregarding products of the displacement gradients. Thus, the vector of unknown generalized coordinates of the laminate, q, is associated only with the linear terms in the expression for total potential energy. The requirement that the first variation of the total potential vanish, $\delta\pi = 0$, yields the following equations for linear stress analysis:

$$\begin{bmatrix} K_{qq} + S_{qq} & G_c^T \\ G_c & 0 \end{bmatrix} \begin{Bmatrix} q \\ \lambda \end{Bmatrix} = \begin{Bmatrix} p_z^* + N^* - S_q^* \\ 0 \end{Bmatrix}, \tag{28}$$

in which the matrices K_{qq} and S_{qq} represent the stiffness of the laminate with a general stacking sequence and the stiffness of the springs associated with the deformation of the laminate, respectively. The vector S_q^* represents the loading that arises from displacements prescribed along the edges. The load vectors N^* and p_z^* are associated with the external tractions acting on the unrestrained edges of the laminate and the distributed loads acting over the surface of the laminate, respectively. The explicit forms of these matrices and vectors are given in Appendix D. Solving for the unknown vectors, q and λ, in (28) permits the calculation of the displacements, strains, and stresses at any point of the laminate under general loading conditions.

Buckling analysis. As mentioned previously, the equations needed to perform buckling analyses are obtained by linearizing the nonlinear field equations about the known flat, stable, equilibrium configuration incipient to buckling. To simplify the linearization process, the vector of generalized coordinates q, the uniform edge-displacement vector Δ, and the constraint force vector λ are combined into a single vector of unknowns, Q, given by

$$Q^T = \{q^T, \Delta^T, \lambda^T\}. \tag{29}$$

As part of the linearization procedure, the vector Q is expressed as

$$Q = Q^{(0)} + e\, Q^{(1)}, \tag{30}$$

where $Q^{(0)}$ and $Q^{(1)}$ correspond to the incipient prebuckling and adjacent equilibrium states, respectively, and e is a real number that can be made as small as required. The vector $Q^{(0)}$ is obtained from a linear stress analysis and is presumed known in the buckling equations. Next, (30) is used to express the total potential energy in the form

$$\pi(Q) = \pi^{(0)}(Q^{(0)}) + e\pi^{(1)}(Q^{(0)}, Q^{(1)}) + e^2\pi^{(2)}(Q^{(0)}, Q^{(1)}) + O(e^3), \tag{31}$$

where $\pi^{(0)}$, $\pi^{(1)}$, and $\pi^{(2)}$ are functionals that are defined explicitly in Appendix E. The equations governing the prebuckling state incipient to buckling are obtained by enforcing

$$\delta\pi^{(0)} = 0, \tag{32a}$$

and the equations that define the load level for which an adjacent equilibrium state exists are obtained from

$$\delta\pi^{(2)} = 0, \tag{32b}$$

which is referred to as Treftz's criterion [Brush and Almroth 1975]. The boundary conditions associated with (32b) are homogeneous. Hence, the extensional and rotational springs are utilized only to apply fixed kinematic boundary conditions in the buckling analysis.

Enforcing the variational statement given by (32a) yields the matrix equation

$$K Q^{(0)} = F \tag{33a}$$

for the prebuckling equilibrium states. The boundary conditions associated with (33a) are nonhomogeneous, so (33a) constitutes a well-posed linear boundary-value problem. In the solution of buckling problems, the applied loads are scaled proportionally by a loading parameter λ_c and, as a result, the

solution vector $Q^{(0)}$ depends on the loading parameter. Thus, every prebuckling equilibrium state corresponds to a different value of λ_c. The relationship between the loading parameter, the relative proportions of the applied loads acting on a plate, and the solution vector $Q^{(0)}$ can be expressed conveniently as

$$Q^{(0)} = \lambda_c \overline{Q}^{(0)}, \tag{33b}$$

where $\overline{Q}^{(0)}$ represents a known prebuckling reference state. Similarly, enforcing the variational statement given by (32b) and using (33b) yields the matrix equation

$$\left[K + \lambda_c H(\overline{Q}^{(0)}) \right] Q^{(1)} = 0, \tag{33c}$$

which constitutes a linear generalized eigenvalue problem in which the loading parameter λ_c is the eigenvalue. The smallest positive value of λ_c represents the smallest load level at which the laminate has a nonflat adjacent equilibrium state in the shape of the corresponding eigenvector.

The matrices appearing in (33a) and (33c) are given by

$$K = \begin{bmatrix} K_{qq} & -s_{q\Delta} & G_c^T \\ -s_{q\Delta}^T & s_{\Delta\Delta} & 0 \\ G_c & 0 & 0 \end{bmatrix}, \qquad H(Q^{(0)}) = \begin{bmatrix} H_s(Q^{(0)}) & 0 & 0 \\ 0 & 0 & 0 \\ 0 & 0 & 0 \end{bmatrix}, \tag{34}$$

with

$$K_{qq} = K_C + S_{qq}, \qquad F = \begin{Bmatrix} N^* \\ P^* \\ 0 \end{Bmatrix}. \tag{35}$$

The matrix K_C represents the stiffness of a symmetric laminate, as defined by (D7), and the matrix S_{qq} represents the stiffness of the springs associated with the deformation of the laminate, as defined in (D9a). The matrix H_S, whose explicit form is given in Appendix E, is the stress-induced geometric stiffness of the laminate. The matrices S_{qq}, $s_{\Delta\Delta}$, and $s_{q\Delta}$ represent the stiffness of the springs associated with the deformation of the laminate, the end-displacements, and their coupling, respectively. The derivation of these matrices is given in Appendix E. The load vectors N^* and P^* that appear in (35) are associated with the external tractions acting on the unrestrained edges of the laminate and the concentrated in-plane loads acting on the rigid end-bar, respectively. These vectors are defined as

$$N^{*T} = \{N_x^*, N_y^*, 0, 0, 0, 0, 0\}, \qquad P^{*T} = \{P_x^*, P_y^*, 0, 0, 0\}. \tag{36}$$

6. Numerical results

Results for two problems are presented in order to demonstrate the accuracy of the {3, 0}-plate theory for stress and buckling analyses. The first problem considered is the stress analysis of an angle-ply laminate with a centrally located circular cutout, subjected to a uniform lateral pressure load, as depicted in Figure 3 for a general rectangular laminate. The second problem considered is the buckling analysis of a square laminate that is subjected to uniform end-shortening and has a centrally located circular cutout. For both of these problems, the dimensions of the square laminate are given by $W = L = 10$ in and the cutout diameter is denoted by the symbol d. In addition, each ply is made of graphite-epoxy material with elastic lamina properties $E_{11} = 18.5 \times 10^6$ psi, $E_{22} = E_{33} = 1.6 \times 10^6$ psi, $G_{12} = G13 = 1.0 \times 10^6$ psi, $G_{23} = 0.64 \times 10^6$ psi, $\nu_{12} = \nu_{13} = 0.35$, and $\nu_{23} = 0.25$. Results are presented for several laminate

thickness-to-width ratios, h/W. As the value of this ratio changes, the ply thicknesses, t_k, are given by $t_k = h/20$.

Stress-analysis problem. For this problem, a square $[\pm\theta]_{5s}$ angle-ply laminate with a centrally located circular cutout is subjected to a uniform transverse pressure with a unit-magnitude intensity of $p_0 = 1$ psi, as depicted in Figure 3. The laminate is simply supported along the edges $x = 0$ and $x = W$, such that

$$\tilde{u}_z(x, y) = 0, \qquad \tilde{\vartheta}_y(x, y) = 0, \tag{37a}$$

and is clamped along the edges $y = 0$ and $y = W$, such that

$$\tilde{u}_x(x, y) = 0, \qquad \tilde{u}_y(x, y) = 0, \qquad \tilde{u}_z(x, y) = 0, \qquad \tilde{\vartheta}_x(x, y) = 0, \qquad \tilde{\vartheta}_y(x, y) = 0. \tag{37b}$$

Several results were obtained for this problem by using the analysis process of the present study. Corresponding results were also obtained from finite element analysis (FEA) based on the {1, 2}-plate theory of [Tessler and Saether 1991]. The finite element implementation of this theory was developed in [Tessler 1993] for linear analysis and extended to geometrically nonlinear analysis in [Barut et al. 1998]. The nonlinear element has three nodes with six degrees of freedom per node, and two additional element-dependent C^{-1} continuous fields that represent higher-order transverse displacement modes. As a result of a convergence study, the finite element model used consists of 6400 elements and 3360 nodes. In contrast, converged results were obtained with the present {3, 0}-plate theory by using Chebyshev polynomial series with 12 terms for the global displacement quantities and Laurent series with 6 terms for the local displacement quantities. The total number of unknowns in the solution vector, without the additional three constraint equations arising from the removal of the redundancy of the local kinematic field, is 575.

Critical in-plane stresses are expected to exist at the intersections of the cutout boundary with the cutout diameter that is parallel to the clamped edges. One of these points is labeled as A and located at the coordinates $(x, y, z) = (5 + d/2, 5, 0)$, where d is the cutout diameter. Similarly, critical transverse shear stresses are expected to occur at the midpoint of the straight laminate edges. These points are labeled B and C, and are located, respectively, at the coordinates $(10, 5, 0)$ and $(5, 10, 0)$. Therefore,
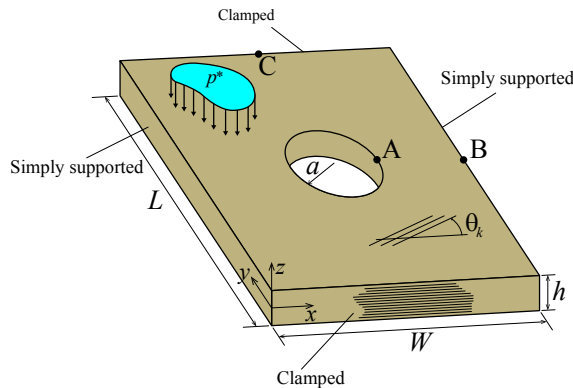

Figure 3. Square laminate with a central circular cutout, subjected to a uniform transverse pressure.

three points on the laminate midplane were selected for comparisons of selected stress variations obtained from the present analysis and the FEA.

Results are presented in Table 1 for $[\pm 45]_{5s}$ laminates with a fixed thickness-to-width ratio given by $h/W = 0.1$. In particular, values of the out-of-plane displacement at the point $(x, y, z) = (5 + d/2, 5, 0)$ are given for select cutout sizes in the range $0.2 \le d/W \le 0.6$. These results indicate small differences between the displacements predicted by the two analyses that range from 0.47% to 1.65% as the cutout size increases from $d/W = 0.2$ to 0.6. Additional results are presented in Table 2 for the $[\pm 45]_{5s}$ laminates with a fixed cutout size given by $d/W = 0.3$ and for select values of $0.05 \le h/W \le 0.2$. These results correspond to the point $(x, y, z) = (6.5, 5, 0)$ and also indicate small differences between the displacements predicted by the two analyses that range from 0.81% to 1.12% as the thickness-to-width ratio increases from $h/W = 0.05$ to 0.2. Similar results are presented in Table 3 for $[\pm \theta]_{5s}$

	u_z (in) $\times 10^5$		
d/W	Present: {3, 0}	FEA: {1, 2}	% Difference
0.2	4.25	4.23	0.47
0.3	3.86	3.84	0.52
0.4	3.23	3.21	0.62
0.5	2.52	2.49	1.19
0.6	1.82	1.79	1.65

Table 1. Out-of-plane displacement at $(x, y, z) = (5 + d/2, 5, 0)$ for $[\pm 45°]_{5s}$ laminates with $h/W = 0.1$ as a function of cutout size d/W.

	u_z (in) $\times 10^5$)		
h/W	Present: {3, 0}	FEA: {1, 2}	% Difference
0.05	19.79	19.63	0.81
0.10	3.234	3.208	0.80
0.15	1.285	1.274	0.86
0.20	0.717	0.709	1.12

Table 2. Out-of-plane displacement at $(x, y, z) = (6.5, 5, 0)$ for $[\pm 45°]_{5s}$ laminates with $d/W = 0.3$ as a function the thickness-to-width ratio h/W.

	u_z (in) $\times 10^5$)		
θ	Present: {3, 0}	FEA: {1, 2}	% Difference
0	8.243	8.200	0.52
30	4.144	4.099	1.09
60	2.905	2.879	0.90
90	3.085	3.070	0.49

Table 3. Out-of-plane displacement at $(x, y, z) = (6.5, 5, 0)$ for $[\theta/-\theta]_{5s}$ laminates with $d/W = 0.3$ and $h/W = 0.1$ as a function of the fiber angle θ.

Figure 4. Effect of cutout size on the through-the-thickness variation of σ_{yy} at point A for a square $[\pm45]_{5s}$ graphite-epoxy laminate with a central circular cutout, subjected to uniform pressure ($h/W = 0.1$).

laminates with a fixed thickness-to-width ratio given by $h/W = 0.1$ and a fixed cutout size given by $d/W = 0.3$. Specifically, results are given for select values of the ply orientation angle in the range $0 \leq \theta \leq 90$ degrees. These results also correspond to the point $(x, y, z) = (6.5, 5, 0)$ and indicate a very small effect of variations in the fiber angle.

Variations of through-the-thickness normal stress σ_{yy} at point A on the cutout edge, normalized by the magnitude of the applied pressure, are shown in Figure 4 for a $[\pm45]_{5s}$ laminate with a thickness-to-width ratio of $h/W = 0.1$. Similarly, distributions of the normalized transverse shearing stresses σ_{xz} at point B on the simply supported edge and σ_{yz} at point C on the clamped edge are shown for this laminate in Figure 5. Several curves are shown in each figure for values of cutout diameter-to-width ratios given by $d/W = 0.2, 0.3, 0.4, 0.5$, and 0.6. The black solid lines correspond to results from the present analysis

Figure 5. Effect of cutout size for a square $[\pm45]_{5s}$ graphite-epoxy laminate with a central circular cutout, subjected to uniform pressure ($h/W = 0.1$). Left: through-the-thickness variation of σ_{xz} at point B (simply supported edge). Right: through-the-thickness variation of σ_{yz} at point C (clamped edge).

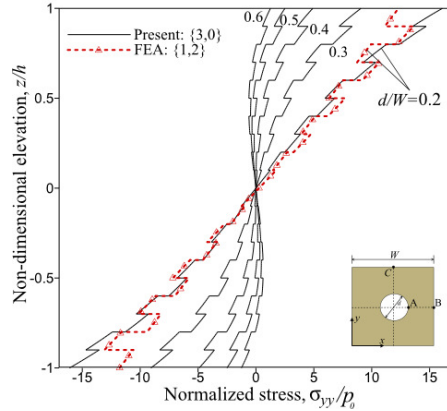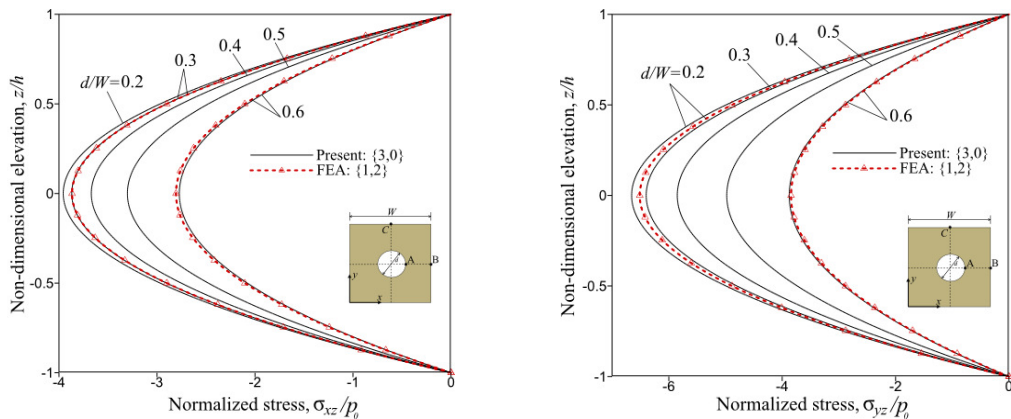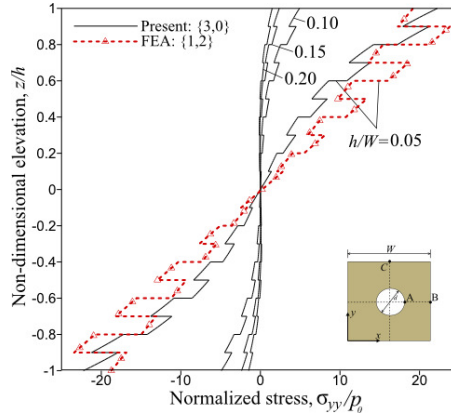**Figure 6.** Effect of the plate thickness-to-width ratio on the through-the-thickness variation of σ_{yy} at point A for a square $[\pm 45]_{5s}$ graphite-epoxy laminate with a central circular cutout, subjected to uniform pressure ($d/W = 0.3$).

and the red dashed lines with triangular symbols correspond to results from the FEA. Discontinuities in the point-wise slope of the curves are associated with the piecewise constant lamina properties that are used to calculate stresses based on continuous through-the-thickness strain distributions.

The results in Figure 4 indicate that the present analysis yields a nonlinear variation σ_{yy/p_0} at point A whereas the finite-element solution based on the {1, 2}-plate theory yields a linear variation. Although results from the two analyses are only shown for $d/W = 0.2$, similar results were obtained for the other values of d/W that show the same trend. The maximum difference in the stresses predicted by the two theories is 26%, in contrast to the maximum difference in the corresponding out-of-plane displacements, which is less than 2%.

The results in Figure 5 indicate that the present analysis and the FEA yield identical through-the-thickness transverse shear stress distributions at points B and C, with slightly different amplitudes. The largest difference in the transverse shear stresses for the two plate theories is 2%. In these figures, the red dashed lines with triangular symbols (FEA) are shown only for the two extreme cases of $d/W = 0.2$ and 0.6, for clarity. Altogether, the results in Figures 4 and 5 indicate that the variation of the in-plane and transverse shear stresses diminishes with increasing cutout size. This trend is expected because increasing the hole size decreases the extent of loading surface and, as a result, reduces the net force applied to the laminate. Reducing the net applied force reduces the magnitude and through-the-thickness variation of all the stresses.

Variations of through-the-thickness normal stress σ_{yy} at point A on the cutout edge, normalized by the magnitude of the applied pressure, are shown in Figure 6 for a $[\pm 45]_{5s}$ laminate with a cutout diameter-to-width ratio $d/W = 0.3$. Similarly, distributions of the normalized transverse shearing stresses σ_{xz} at point B on the simply supported edge and σ_{yz} at point C on the clamped edge are shown for this laminate in Figure 7. Several curves are shown in each figure for values of thickness-to-width ratios of $h/W = 0.05, 0.10, 0.15$, and 0.20. The black solid lines correspond to results from the present analysis and the red dashed lines with triangular symbols correspond to results from the FEA. Discontinuities in the point-wise slope of these curves are also associated with the piecewise constant lamina properties that are used to calculate stresses based on continuous through-the-thickness strain distributions.
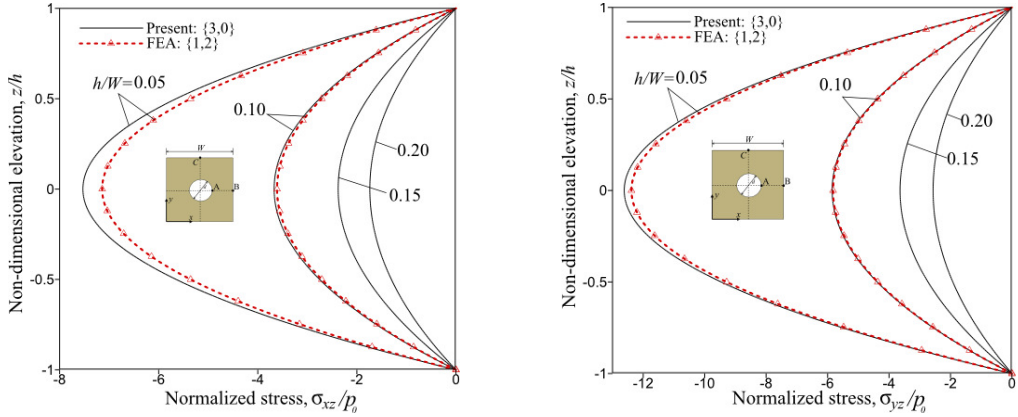
Figure 7. Effect of the plate thickness-to-width ratio for a square $[\pm45]_{5s}$ graphite-epoxy laminate with a central circular cutout, subjected to uniform pressure ($d/W = 0.3$). Left: through-the-thickness variation of σ_{xz} at point B (simply supported edge). Right: through-the-thickness variation of σ_{yz} at point C (clamped edge).

As expected, the results in Figure 6 also indicate that the present analysis yields a nonlinear variation σ_{yy}/p_0 at point A whereas the finite-element solution based on the {1, 2}-plate theory yields a linear variation. Although results from the two analyses are only shown for $h/W = 0.05$, similar results were obtained for the other values of h/W that show the same trend. Altogether, the maximum differences in the in-plane and transverse shear stresses predicted by the two theories for $h/W = 0.05$ and 0.1 are 29% and 4.8%, respectively. The results in Figures 6 and 7 also show an increase in stresses as h/W decreases. This increase in stresses is due to the reduction in bending stiffness with decreasing h/W and the fact that the laminate must carry the same applied load.

The effect of fiber angle, θ, on through-the-thickness variation σ_{yy} at point A located on the cutout edge is shown for $[\pm\theta]_{5s}$ laminates with $d/W = 0.3$ and $h/W = 0.1$ in Figure 8. The corresponding
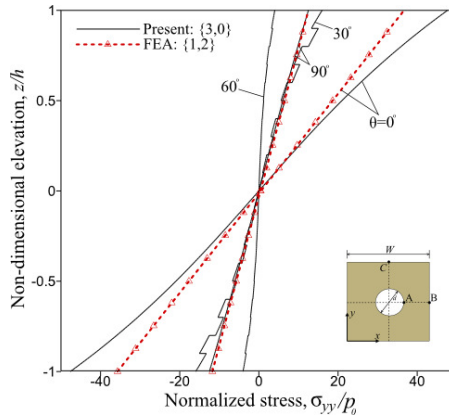
Figure 8. Effect of fiber angle on the through-the-thickness variation of σ_{yy} at point A for a square $[\pm\theta]_{5s}$ graphite-epoxy laminate with a central circular cutout, subjected to uniform pressure ($d/W = 0.3$, $h/W = 0.1$).
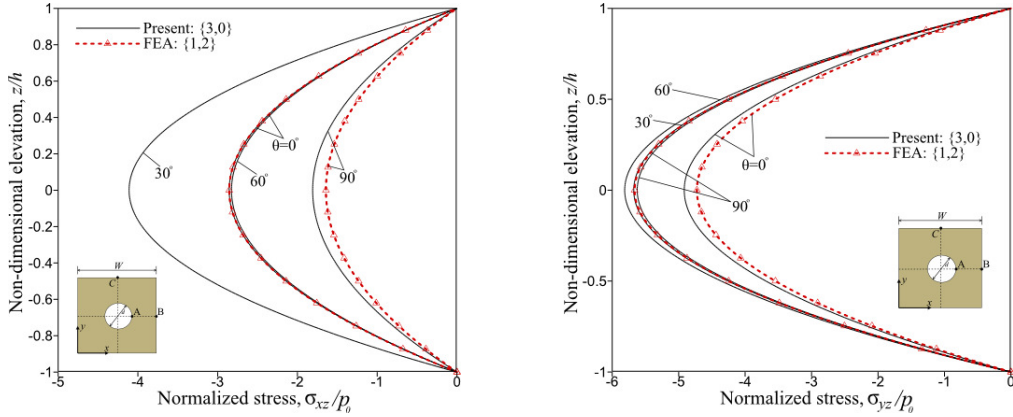
Figure 9. Effect of fiber angle for a $[\pm\theta]_{5s}$ graphite-epoxy laminate with a central circular cutout, subjected to uniform pressure ($d/W = 0.3$, $h/W = 0.1$). Left: through-the-thickness variation of σ_{xz} at point B (simply supported edge). Right: through-the-thickness variation of σ_{yz} at point C (clamped edge).

distributions of the normalized transverse shearing stresses σ_{xz} at point B (on the simply supported edge) and σ_{yz} at point C (on the clamped edge) are shown for this laminate in Figure 9. Several curves are shown in each figure for values of $\theta = 0, 30, 60$, and 90 degrees. The black solid lines correspond to results from the present analysis and the red dashed lines with triangular symbols for $\theta = 0$ and 90 degrees correspond to results from the FEA. Discontinuities in the point-wise slope of these curves are also associated with the piecewise constant lamina properties that are used to calculate stresses based on continuous through-the-thickness strain distributions.

The results in Figure 8 show that the largest variation in the in-plane stress σ_{yy} occurs for $\theta = 0$ degrees. Similarly, the results in Figure 9 show the largest variations in σ_{xz} and σ_{yz} for $\theta = 30$ and 60 degrees, respectively. The results in Figure 8 also show better agreement in predicted values of σ_{yy} at point A obtained from the two theories for $\theta = 90$ degrees than for $\theta = 0$ degrees. Likewise, the results in Figure 9, right, show better agreement in predicted values of σ_{yz} at point C for $\theta = 90$ degrees than for $\theta = 0$ degrees. In contrast, the results in Figure 9, left, show better agreement in predicted values of σ_{xz} at point B for $\theta = 0$ degrees than for $\theta = 90$ degrees.

Buckling-analysis problem. The second problem considered is buckling of a square $[+\theta_5/-\theta_5]_s$ laminate with a central circular cutout, subjected to uniform end-shortening, as shown in Figure 10. This pathological family of laminates was chosen because of the high degree of anisotropy that exists in the form of coupling between pure-bending and twisting deformations. The dimensions of this square laminate are also given by $W = L = 10$ in and the diameter of the cutout is specified as $d = 6$ in. The values of the thickness-to-width ratios considered for this problem are $h/W \leq 0.05$, and were chosen such that elastic buckling is likely to occur prior to a first-ply failure. This range of h/W values was determined by using the point-stress failure criteria of [Whitney and Nuismer 1974] with a critical strength value of $X = 320$ ksi. Two sets of boundary conditions are also considered. Specifically, the edges at $x = 0$ and $x = W$ are simply supported, and those at $y = 0$ and $y = L$ are either simply supported or clamped.
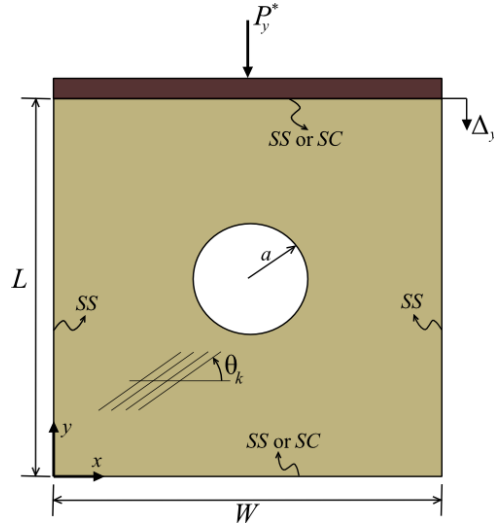
Figure 10. Square laminate with a circular cutout, subjected to uniform end-shortening.

The load is introduced into the laminate as a uniform end-shortening, Δ_y, that results from applying the concentrated force $-P_y^*$ to a rigid end-bar. In addition, the unloaded lateral edges are free to expand and contract. In particular, the two sets of boundary are specified and designated as follows.

- Two simply supported and two clamped opposite edges (SS-CL):

$$\tilde{u}_z = \tilde{\vartheta}_y = 0 \qquad\qquad \text{at } x = 0 \text{ and } x = W, \qquad (38a)$$

$$\tilde{u}_y = \tilde{u}_z = \tilde{\vartheta}_x = \tilde{\vartheta}_y = 0 \qquad\qquad \text{at } y = 0, \qquad (38b)$$

$$\tilde{u}_z = \tilde{\vartheta}_x = \tilde{\vartheta}_y = 0 \text{ and } \tilde{u}_y = \Delta_y \text{ through } - P_y^* \qquad \text{at } y = L. \qquad (38c)$$

- All edges simply supported (SS-SS):

$$\tilde{u}_z = \tilde{\vartheta}_y = 0 \qquad\qquad \text{at } x = 0 \text{ and } x = W, \qquad (39a)$$

$$\tilde{u}_y = \tilde{u}_z = \tilde{\vartheta}_x = 0 \qquad\qquad \text{at } y = 0, \qquad (39b)$$

$$\tilde{u}_z = \tilde{\vartheta}_x = 0 \text{ and } \tilde{u}_y = \Delta_y \text{ through } - P_y^* \qquad \text{at } y = L. \qquad (39c)$$

Several buckling predictions obtained by using the present analysis were compared with corresponding results obtained from the FEA based on a {1, 2}-order plate theory developed in [Barut et al. 1998]. In these analyses, converged solutions were obtained by using the finite element model with 6400 elements and 3360 nodes that was used in the stress analyses. Likewise, 12-term Chebyshev polynomial series and 6-term Laurent series were used in the present analysis. In addition, corresponding results were also obtained by using the semianalytical method developed in [Barut and Madenci 2001], which is based on classical laminated plate theory (CLPT) and formulated in a manner similar to the present analysis.

The buckling loads obtained by using the three analysis methods are presented in Tables 4 and 5 for $[+\theta_5/-\theta_5]_s$ laminates with $h/W = 0.035$ and $d/W = 0.6$. The results in Tables 4 and 5 are for laminates with SS-CL and SS-SS boundary conditions, respectively, and are given for select values of the fiber angle
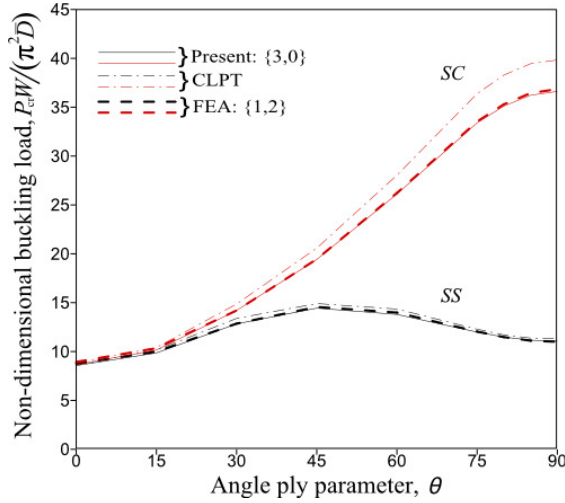
Figure 11. Effects of boundary conditions and transverse shear flexibility on the buckling resistance of $[+\theta_5/-\theta_5]_s$ angle-ply laminates with a central circular cutout, subjected to uniform end-shortening ($h/W = 0.035$, $d/W = 0.6$).

θ. These results are also shown in Figure 11, where the buckling load is given in nondimensional form as $P_{cr}W/(\pi^2\bar{D})$, and where $\bar{D}$ denotes the bending stiffness defined as $\bar{D} = E_T h^3/[12(1 - \nu_{LT}^2)]$ and P_{cr} is the value of the applied load at buckling. The results obtained from the present analysis are represented by the solid lines in the figures, FEA results are represented by the thick-dashed lines, and results based on CLPT are represented by the dash-dotted lines. Also, the red and black lines correspond to results for the SS-CL and SS-SS boundary conditions, respectively.

The results in these tables and in Figure 11 show very good agreement between the present analysis and the FEA. For all values of θ the differences in the buckling loads predicted by the two shear-deformation-based theories are less than 3%. The results also indicate maximum differences between the buckling loads obtained by using the present analysis and the CLPT analysis of approximately 6% and 9% for the

Fiber angle, θ (deg)	Buckling load (kips)		
	Present: {3, 0}	FEA: {1, 2}	CLPT
0	55.646	57.463	56.504
15	73.762	75.043	75.892
30	114.532	114.000	121.201
45	156.650	156.490	167.471
60	198.143	199.574	213.171
75	228.638	230.546	246.813
90	235.416	236.930	256.077

Table 4. Buckling loads of $[+\theta_5/-\theta_5]_s$ angle-ply laminates with a central circular cutout, subjected to uniform end-shortening, with SS-CL boundary conditions ($h/W = 0.035$, $d/W = 0.6$).
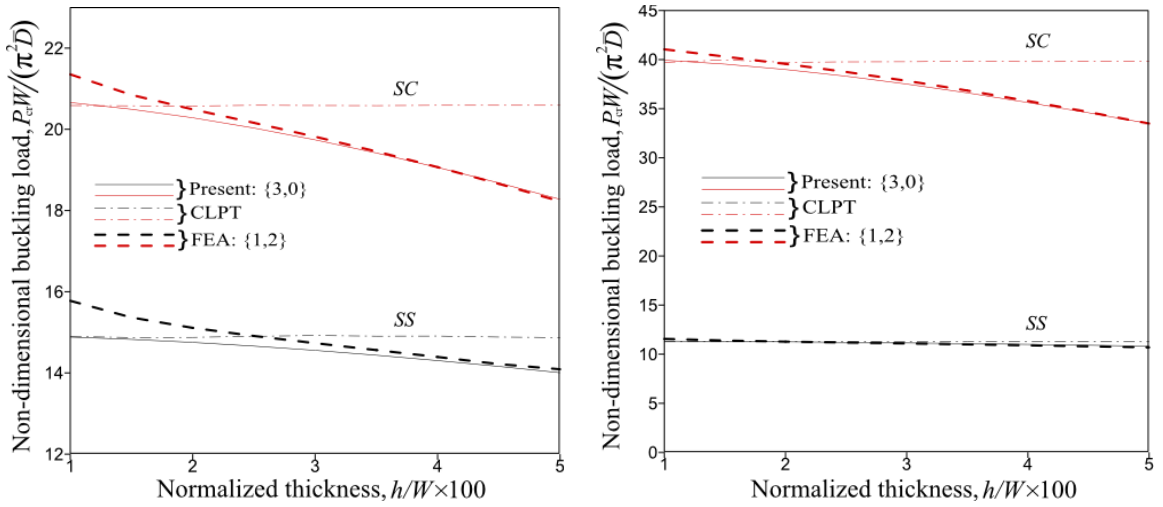
Figure 12. Effect of thickness-to-width ratio and transverse shear flexibility on the buckling resistance of angle-ply laminates with a central circular cutout, subjected to uniform end-shortening ($d/W = 0.6$). Left: $[+45^\circ_5/-45^\circ_5]_s$ laminate. Right: $[90^\circ]_{20}$ unidirectional laminate.

laminates with SS-SS and SS-CL boundary conditions, respectively. Moreover, the maximum difference occurred for $\theta = 30$ and 90 degrees for the laminates with SS-SS and SS-CL boundary conditions, respectively. The results in Figure 11 also indicate that the boundary conditions influence the importance of transverse shear flexibility in addition to how fiber angle affects buckling resistance.

The effects of the thickness-to-width ratio h/W on the buckling predictions for $[+\theta_5/-\theta_5]_s$ angle-ply laminates with $d/W = 0.6$ are shown in Figure 12 for $\theta = 45$ and 90 degrees. Laminates with $\theta = 45$ degrees have a very high degree of anisotropy in the form of coupling between pure-bending and twisting deformations. In contrast, laminates with $\theta = 90$ degrees are unidirectional, aligned with the loading direction, and have a very high degree of orthotropy. Two groups of curves, one red and one

	Buckling load (kips)		
Fiber angle, θ (deg)	Present: {3, 0}	FEA: {1, 2}	CLPT
0	55.012	56.270	55.523
15	63.399	64.226	65.254
30	82.521	82.667	86.091
45	92.826	93.636	96.268
60	88.736	89.926	92.261
75	77.121	77.438	78.997
90	71.160	70.701	72.464

Table 5. Buckling loads of $[+\theta_5/-\theta_5]_s$ angle-ply laminates with a central circular cutout, subjected to uniform end-shortening, with SS-SS boundary conditions ($h/W = 0.035$, $d/W = 0.6$).

black, are shown in each figure, corresponding to laminates with SS-SS and SS-CL boundary conditions, respectively. In each group of curves, the solid lines correspond to results obtained with the present analysis, while thick dashed and dash-dotted lines correspond to results obtained from the CLPT-based analysis and the FEA, respectively.

The results in Figure 12, left, for $\theta = 45$ degrees, generally show discrepancies between the results obtained by using all three analysis methods that are more pronounced for the SS-CL than for the SS-SS boundary condition. For the thinner laminates, the results obtained from the present analysis and the CLPT-based analysis are in very good agreement, but neither set of results agrees with the corresponding results obtained by using the FEA. For the thinner laminates, the FEA overpredicts the buckling loads. As the laminate thickness increases, the agreement between the results obtained from the present analysis and the FEA becomes very good, but neither set of results agrees with the corresponding results obtained by using the CLPT-based analysis. In addition, the CLPT results significantly overpredict the buckling loads for the larger values of h/W. In particular, the largest difference in the results obtained from the CLPT-based analysis and the two shear-deformation-based analyses is 11% for the SS-SS laminates and 5% in the case of SS-CL laminates, for the upper limit of $h/W = 0.05$ shown in the figure. The results in Figure 12, right, for $\theta = 90$ degrees, show the same trends for the SS-CL laminates; however, the results for the SS-SS laminates obtained from the three analysis methods are in very good agreement. The largest differences in the results obtained from the CLPT-based analysis and the two shear-deformation-based analyses are 15% for the SS-SS laminates and less than 2% in the case of SS-CL laminates, for the upper limit of $h/W = 0.05$ shown in Figure 12, left.

Typical buckling modes are shown in Figures 13 and 14 for the laminates with $\theta = 45$ and 90 degrees, respectively, and with $h/W = 0.035$ and $d/W = 0.6$. Two modes are shown in each figure that correspond to the SS-CL and SS-SS boundary conditions. The mode shapes shown in Figure 13 for the laminates with
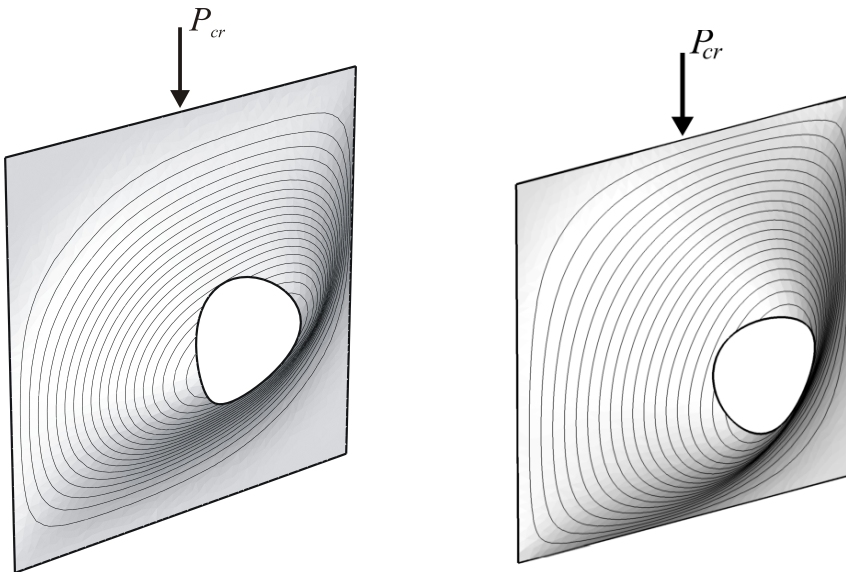

Figure 13. Buckling modes for a $[45^\circ_5/-45^\circ_5]_s$ laminate with $h/W = 0.035$ and $d/W = 0.6$: (a) SS-CL and (b) SS-SS boundary conditions.
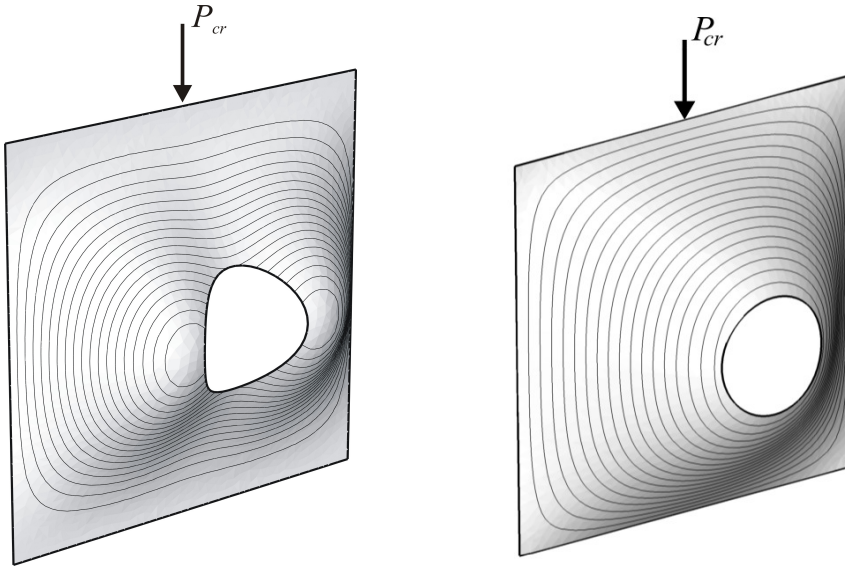
Figure 14. Buckling modes for a $[90°]_{20}$ laminate with $h/W = 0.035$ and $d/W = 0.6$: (a) SC and (b) SS-type boundary conditions.

$\theta = 45$ degrees are skewed for both boundary-condition cases, as a result of the high degree of bending-twisting anisotropy. In addition, the buckle pattern for the SS-CL boundary condition (Figure 13a) is flatter than that for the SS-SS boundary condition (Figure 13b), as expected. The buckle patterns shown in Figure 14 for the laminates with $\theta = 90$ degrees exhibit bilateral symmetry for both sets of boundary conditions. However, the buckle pattern for the unidirectional laminate with the clamped loaded edges exhibits three half waves in the horizontal x-direction (weak direction), as shown in Figure 14a, as compared to one half wave for the SS-SS laminate shown in Figure 14b. The buckling mode shown in Figure 14a for the SS-CL boundary conditions has the same features as the experimentally determined buckle pattern of a similar specially orthotropic plate that was presented in [Nemeth 1990].

7. Conclusions

A semianalytical solution method for predicting the bending and buckling behavior of a moderately thick laminate with a cutout has been presented. The analysis method has been validated for linear stress analyses of laminates with a cutout and subjected to uniform lateral pressure against corresponding results obtained from finite element analyses (FEA) based on a {1, 2} shear deformation plate theory appearing in the literature. The agreement between the present method and the FEA was found to be excellent. In all cases considered, the maximum difference in the out-of-plane displacements predicted by the two methods is less than 2%. Comparisons of the through-the-thickness stress variations also showed favorable agreement between the two approaches, despite the fact that the FEA are based on a plate theory that cannot capture nonuniform through-the-thickness variations of the in-plane stresses for thick plates.

The present method has also been validated for the buckling analyses of pathological highly orthotropic and highly anisotropic laminates with relatively large cutouts, subjected to uniform end-shortening. Comparisons of results obtained by the present method with the corresponding results obtained from the FEA and from a similar semianalytical solution method based on CLPT have been presented for two sets of boundary conditions. The comparisons with the FEA show close agreement between the two shear-deformation-based analyses, for the most part. Differences were found for relatively small values of the thickness-to-width ratio, h/W. In contrast, very good agreement between the present analysis and the FEA was found for the larger values of h/W. Results have also been presented that show the effects of laminate orthotropy and anisotropy, and boundary conditions, on the importance of including transverse shear flexibility in the analysis. Overall, the analysis method presented herein successfully captures the effects of transverse shear flexibility and represents boundary conditions adequately, which is problematic for some analyses based on a transverse shear deformation theory.

Appendix A: Stress resultants and constitutive equations

The stress resultants appearing in (12) are defined as

$$\begin{Bmatrix} N_{xx} \\ N_{yy} \\ N_{xy} \end{Bmatrix} = \int_{-h/2}^{+h/2} \begin{Bmatrix} \sigma_{xx} \\ \sigma_{yy} \\ \sigma_{xy} \end{Bmatrix} dz, \qquad\qquad \begin{Bmatrix} M_{xx} \\ M_{yy} \\ M_{xy} \end{Bmatrix} = \int_{-h/2}^{+h/2} \begin{Bmatrix} \sigma_{xx} \\ \sigma_{yy} \\ \sigma_{xy} \end{Bmatrix} z \, dz, \qquad\qquad \text{(A1a)}$$

$$\begin{Bmatrix} F_{xx} \\ F_{yy} \\ F_{xy} \end{Bmatrix} = \int_{-h/2}^{+h/2} \begin{Bmatrix} \sigma_{xx} \\ \sigma_{yy} \\ \sigma_{xy} \end{Bmatrix} \Lambda(z) \, dz, \qquad\qquad \begin{Bmatrix} q_{xz} \\ q_{yz} \end{Bmatrix} = \int_{-h/2}^{+h/2} \begin{Bmatrix} \sigma_{xz} \\ \sigma_{yz} \end{Bmatrix} \Lambda'(z) \, dz, \qquad\qquad \text{(A1b)}$$

where h is the plate thickness. In terms of the notation used in [Ray 2003],

$$\begin{Bmatrix} F_{xx} \\ F_{yy} \\ F_{xy} \end{Bmatrix} = \frac{3}{2h}\left(\begin{Bmatrix} M_{xx} \\ M_{yy} \\ M_{xy} \end{Bmatrix} - \frac{4}{3h^2}\begin{Bmatrix} P_{xx} \\ P_{yy} \\ P_{xy} \end{Bmatrix}\right), \qquad \begin{Bmatrix} f_{xz} \\ f_{yz} \end{Bmatrix} = \frac{3}{2h}\left(\begin{Bmatrix} Q_x \\ Q_y \end{Bmatrix} - \frac{4}{h^2}\begin{Bmatrix} R_x \\ R_y \end{Bmatrix}\right), \qquad \text{(A1c)}$$

where Q_x and Q_y are the transverse shear stress resultants of CLPT given by

$$\begin{Bmatrix} Q_{xz} \\ Q_{yz} \end{Bmatrix} = \int_{-h/2}^{+h/2} \begin{Bmatrix} \sigma_{xz} \\ \sigma_{yz} \end{Bmatrix} dz, \qquad\qquad \text{(A2a)}$$

and

$$\begin{Bmatrix} P_{xx} \\ P_{yy} \\ P_{xy} \end{Bmatrix} = \int_{-h/2}^{+h/2} \begin{Bmatrix} \sigma_{xx} \\ \sigma_{yy} \\ \sigma_{xy} \end{Bmatrix} z^3 \, dz, \qquad \begin{Bmatrix} R_x \\ R_y \end{Bmatrix} = \int_{-h/2}^{+h/2} \begin{Bmatrix} \sigma_{xz} \\ \sigma_{yz} \end{Bmatrix} z^2 \, dz. \qquad \text{(A2b)}$$

The constitutive equations used in the present theory are those for a plate made of one or more layers of linear elastic, specially orthotropic materials. As a result, the plate is generally inhomogeneous through the thickness. These equations, referred to the corresponding (x, y, z) plate coordinate system, are given

by

$$\left\{\begin{array}{c}\sigma_{xx}\\\sigma_{yy}\\\sigma_{xy}\end{array}\right\}=\begin{bmatrix}\bar{Q}_{11}&\bar{Q}_{12}&\bar{Q}_{16}\\\bar{Q}_{12}&\bar{Q}_{22}&\bar{Q}_{26}\\\bar{Q}_{16}&\bar{Q}_{26}&\bar{Q}_{66}\end{bmatrix}\left\{\begin{array}{c}\epsilon_{xx}\\\epsilon_{yy}\\\gamma_{xy}\end{array}\right\},\qquad\left\{\begin{array}{c}\sigma_{yz}\\\sigma_{xz}\end{array}\right\}=\begin{bmatrix}\bar{C}_{44}&\bar{C}_{45}\\\bar{C}_{45}&\bar{C}_{55}\end{bmatrix}\left\{\begin{array}{c}\gamma_{yz}\\\gamma_{xz}\end{array}\right\},\tag{A3}$$

where the subscripted σ_{ij} with $i, j = x, y, z$ are the stress components, $\bar{Q}_{ij} = \bar{Q}_{ij}(z)$ are the transformed, reduced stiffness matrix coefficients of CLPT, and $\bar{C}_{ij} = \bar{C}_{ij}(z)$ are the transformed transverse shearing stiffnesses of the FSDT [Jones 1975]. These equations reveal that, if the transverse shearing strains vanish on the bounding surfaces of a plate, the transverse shearing stresses also vanish on the bounding surfaces of the plate.

The submatrices in (16) are defined as

$$\boldsymbol{A}=\begin{bmatrix}A_{11}&A_{12}&A_{16}\\A_{12}&A_{22}&A_{26}\\A_{16}&A_{26}&A_{66}\end{bmatrix}=\int_{-h/2}^{+h/2}\begin{bmatrix}\bar{Q}_{11}&\bar{Q}_{12}&\bar{Q}_{16}\\\bar{Q}_{12}&\bar{Q}_{22}&\bar{Q}_{26}\\\bar{Q}_{16}&\bar{Q}_{26}&\bar{Q}_{66}\end{bmatrix}dz,\tag{A4a}$$

$$\boldsymbol{B}=\begin{bmatrix}B_{11}&B_{12}&B_{16}\\B_{12}&B_{22}&B_{26}\\B_{16}&B_{26}&B_{66}\end{bmatrix}=\int_{-h/2}^{+h/2}\begin{bmatrix}\bar{Q}_{11}&\bar{Q}_{12}&\bar{Q}_{16}\\\bar{Q}_{12}&\bar{Q}_{22}&\bar{Q}_{26}\\\bar{Q}_{16}&\bar{Q}_{26}&\bar{Q}_{66}\end{bmatrix}z\,dz,\tag{A4b}$$

$$\boldsymbol{D}=\begin{bmatrix}D_{11}&D_{12}&D_{16}\\D_{12}&D_{22}&D_{26}\\D_{16}&D_{26}&D_{66}\end{bmatrix}=\int_{-h/2}^{+h/2}\begin{bmatrix}\bar{Q}_{11}&\bar{Q}_{12}&\bar{Q}_{16}\\\bar{Q}_{12}&\bar{Q}_{22}&\bar{Q}_{26}\\\bar{Q}_{16}&\bar{Q}_{26}&\bar{Q}_{66}\end{bmatrix}z^2\,dz,\tag{A4c}$$

$$\boldsymbol{E}=\begin{bmatrix}E_{11}&E_{12}&E_{16}\\E_{12}&E_{22}&E_{26}\\E_{16}&E_{26}&E_{66}\end{bmatrix}=\int_{-h/2}^{+h/2}\begin{bmatrix}\bar{Q}_{11}&\bar{Q}_{12}&\bar{Q}_{16}\\\bar{Q}_{12}&\bar{Q}_{22}&\bar{Q}_{26}\\\bar{Q}_{16}&\bar{Q}_{26}&\bar{Q}_{66}\end{bmatrix}\Lambda(z)\,dz,\tag{A4d}$$

$$\boldsymbol{F}=\begin{bmatrix}F_{11}&F_{12}&F_{16}\\F_{12}&F_{22}&F_{26}\\F_{16}&F_{26}&F_{66}\end{bmatrix}=\int_{-h/2}^{+h/2}\begin{bmatrix}\bar{Q}_{11}&\bar{Q}_{12}&\bar{Q}_{16}\\\bar{Q}_{12}&\bar{Q}_{22}&\bar{Q}_{26}\\\bar{Q}_{16}&\bar{Q}_{26}&\bar{Q}_{66}\end{bmatrix}\Lambda(z)z\,dz,\tag{A4e}$$

$$\boldsymbol{H}=\begin{bmatrix}H_{11}&H_{12}&H_{16}\\H_{12}&H_{22}&H_{26}\\H_{16}&H_{26}&H_{66}\end{bmatrix}=\int_{-h/2}^{+h/2}\begin{bmatrix}\bar{Q}_{11}&\bar{Q}_{12}&\bar{Q}_{16}\\\bar{Q}_{12}&\bar{Q}_{22}&\bar{Q}_{26}\\\bar{Q}_{16}&\bar{Q}_{26}&\bar{Q}_{66}\end{bmatrix}(\Lambda(z))^2\,dz,\tag{A4f}$$

$$\boldsymbol{G}=\begin{bmatrix}G_{55}&G_{45}\\G_{45}&G_{44}\end{bmatrix}=\int_{-h/2}^{+h/2}\begin{bmatrix}\bar{C}_{55}&\bar{C}_{45}\\\bar{C}_{45}&\bar{C}_{44}\end{bmatrix}(\Lambda'(z))^2\,dz.\tag{A4g}$$

Substituting the strain expressions given by (7a) and (7b) into the stresses given by (A3) and performing the through-the-thickness integrations in (A1) yields the laminate constitutive equations as

$$\boldsymbol{N}=\boldsymbol{A}\boldsymbol{\epsilon}^0+\boldsymbol{B}\boldsymbol{\kappa}^0+\boldsymbol{E}\boldsymbol{\Gamma}^0,\qquad\boldsymbol{M}=\boldsymbol{B}\boldsymbol{\epsilon}^0+\boldsymbol{D}\boldsymbol{\kappa}^0+\boldsymbol{F}\boldsymbol{\Gamma}^0,\qquad\boldsymbol{F}=\boldsymbol{E}\boldsymbol{\epsilon}^0+\boldsymbol{F}\boldsymbol{\kappa}^0+\boldsymbol{H}\boldsymbol{\Gamma}^0,\tag{A5a}$$

$$\boldsymbol{f}=\boldsymbol{G}\boldsymbol{\Phi}.\tag{A5b}$$

For the laminated plates investigated in [Ray 2003], the expression

$$\Lambda(z)=\tfrac{3}{2}(z/h)-2(z/h)^3\tag{A6}$$

was used to obtain the laminate constitutive equations given by (A5a). In particular, using (A6) with (A5a) the constitutive equations reduce to

$$\boldsymbol{N} = \boldsymbol{A}\boldsymbol{\epsilon}^0, \qquad \boldsymbol{M} = \boldsymbol{D}\boldsymbol{\kappa}^0 + \boldsymbol{F}\boldsymbol{\Gamma}^0, \qquad \boldsymbol{F} = \boldsymbol{F}\boldsymbol{\kappa}^0 + \boldsymbol{H}\boldsymbol{\Gamma}^0, \tag{A7}$$

for symmetrically laminated plates. The first of these equations indicates that there is no coupling between membrane action and bending or transverse shearing actions. In contrast, the last two parts of (A7) indicate strong coupling between bending and/or transverse shearing actions.

The resultant forces and moments appearing in (22) that are associated with the applied edge tractions are defined as

$$N_x^* = \int_{-h/2}^{h/2} t_x^* \, dz, \qquad N_y^* = \int_{-h/2}^{h/2} t_y^* \, dz, \qquad N_z^* = \int_{-h/2}^{h/2} t_z^* \, dz, \tag{A8a}$$

$$M_x^* = \int_{-h/2}^{h/2} z t_x^* \, dz, \qquad M_y^* = \int_{-h/2}^{h/2} z t_y^* \, dz. \tag{A8b}$$

Appendix B: Nonlinear and linearized forms of equations for stress and buckling analyses

The first variations of the strain energies of the laminate, the elastic edge supports (springs) due to the internal forces, and the potential energy due to external boundary loads acting on the surface and around the boundary of the laminate, δU, $\delta \Omega$, and δV, respectively, are derived in the form

$$
\begin{aligned}
\delta U = -\int_A & \big\{ (N_{xx,x} + N_{xy,y})\delta u_x + (N_{yy,y} + N_{xy,x})\delta u_y \\
& + \big(M_{xx,xx} + 2M_{xy,xy} + M_{yy,yy} + [N_{xx}u_{z,x} + N_{xy}u_{z,y}]_{,x} + [N_{yy}u_{z,y} + N_{xy}u_{z,x}]_{,y} \big)\delta u_z \\
& + (F_{xx,x} + F_{xy,y} - q_{xz})\delta \Phi_{xz} + (F_{yy,y} + F_{xy,y} - q_{yz})\delta \Phi_{yz} \big\} \, dA \\
+ \int_\Gamma & \big\{ (N_{xx}n_x + N_{xy}n_y)\delta u_x + (N_{yy}n_y + N_{xy}n_x)\delta u_y \\
+ \big(M_{xx,x}n_x & + M_{yy,y}n_y + M_{xy,y}n_x + M_{xy,x}n_y + N_{xx}u_{z,x}n_x + N_{yy}u_{z,y}n_y + N_{xy}u_{z,x}n_y + N_{xy}u_{z,x}n_y \big)\delta u_z \\
- (M_{xx}n_x + M_{xy}n_y)\delta u_{z,x} & - (M_{yy}n_y + M_{xy}n_x)\delta u_{z,y} + (F_{xx}n_x + F_{xy}n_y)\delta \Phi_{xz} + (F_{yy}n_y + F_{xy}n_x)\delta \Phi_{yz} \big\} \, d\Gamma,
\end{aligned}
\tag{B1a}
$$

$$
\begin{aligned}
\delta \Omega = \int_{\Gamma_u} & \Big\{ S_x(u_x - \tilde{u}_x^*)\delta u_x + S_y(u_y - \tilde{u}_x^*)\delta u_y + S_z(u_z - \tilde{u}_x^*)\delta u_z \\
& + J_{\vartheta x}\Big(u_{z,x} - \frac{6}{5h}\Phi_{xz} - \tilde{\vartheta}_x^*\Big)\Big(\delta u_{z,x} - \frac{6}{5h}\delta \Phi_{xz}\Big) + J_{\vartheta y}\Big(u_{z,y} - \frac{6}{5h}\Phi_{yz} - \tilde{\vartheta}_y^*\Big)\Big(\delta u_{z,y} - \frac{6}{5h}\delta \Phi_{yz}\Big) \Big\} \, d\Gamma \\
& \qquad\qquad + \int_{\Gamma_\Delta} \big\{ s_x(u_x - \Delta_x)\delta(u_x - \Delta_x) + s_y(u_y - \Delta_y)\delta(u_y - \Delta_y) \big\} \, d\Gamma,
\end{aligned}
\tag{B1b}
$$

and

$$
\begin{aligned}
\delta V = \int_{\Gamma_\sigma} & N_x^*\delta u_x + N_y^*\delta u_y + N_z^*\delta u_z - M_x^*\delta u_{z,x} - M_y^*\delta u_{z,y} + \frac{5}{6h}M_x^*\delta \Phi_{xz} + \frac{5}{6h}M_y^*\delta \Phi_{yz} \, d\Gamma \\
& \qquad\qquad\qquad\qquad + \int_A p^*\delta u_z \, dA + P_x^*\Delta_x + P_y^*\Delta_y.
\end{aligned}
\tag{B1c}
$$

Substituting these expressions for δU, $\delta \Omega$, and δV into (23) and enforcing the fundamental theorem of the calculus of variations leads to the equilibrium equations

$$\left\{ \begin{array}{c} N_{xx,x} + N_{xy,y} \\ N_{xy,x} + N_{yy,y} \\ M_{xx,xx} + 2M_{xy,xy} + M_{yy,yy} + N_{xx}u_{z,xx} + 2N_{xy}u_{z,xy} + N_{yy}u_{z,yy} - p^* \\ F_{xx,x} + F_{xy,y} - f_{xz} \\ F_{xy,x} + F_{yy,y} - f_{yz} \end{array} \right\} = \mathbf{0}. \tag{B2}$$

For external forces and moments applied along the boundary Γ_σ, the boundary conditions are obtained as

$$(\boldsymbol{b}_x + \boldsymbol{b}_{1x})n_x + (\boldsymbol{b}_y + \boldsymbol{b}_{1y})n_y = \boldsymbol{f}^*, \tag{B3}$$

where

$$\begin{aligned}
\boldsymbol{b}_x^T &= \{N_{xx}, N_{xy}, (M_{xx,x} + M_{xy,y}), M_{xx}, M_{xy}, F_{xx}, F_{xy}\}, \\
\boldsymbol{b}_{1x}^T &= \{0, 0, (N_{xx}u_{z,x} + N_{xy}u_{z,y}), 0, 0, 0, 0\}, \\
\boldsymbol{b}_y^T &= \{N_{xy}, N_{yy}, (M_{xy,x} + M_{yy,y}), M_{xy}, M_{yy}, F_{xy}, F_{yy}\}, \\
\boldsymbol{b}_{1y}^T &= \{0, 0, 0, (N_{xy}u_{z,x} + N_{yy}u_{z,y}), 0, 0, 0\}, \\
\boldsymbol{f}^{*T} &= \left\{N_x^*, N_y^*, N_z^*, M_x^*, M_y^*, \frac{6}{5h}M_x^*, \frac{6}{5h}M_y^*\right\}.
\end{aligned} \tag{B4}$$

For prescribed displacements and rotations applied through the elastic springs along the boundary Γ_u, with unit normal $\boldsymbol{n}$, the boundary conditions are obtained as

$$(\boldsymbol{c}_x + \boldsymbol{c}_{1x})n_x + (\boldsymbol{c}_y + \boldsymbol{c}_{1y})n_y + \boldsymbol{c}_u + \boldsymbol{c}_\Delta = \boldsymbol{g}_u^* + \boldsymbol{g}_\Delta^*, \tag{B5}$$

where

$$\begin{aligned}
\boldsymbol{c}_x^T &= \{N_{xx}, N_{xy}, (M_{xx,x} + M_{xy,y}), -M_{xx}, -M_{xy}, F_{xx}, F_{xy}, 0, 0\}, \\
\boldsymbol{c}_{1x}^T &= \{0, 0, (N_{xx}u_{z,x} + N_{xy}u_{z,y}), 0, 0, 0, 0, 0, 0\}, \\
\boldsymbol{c}_y^T &= \{N_{xy}, N_{yy}, (M_{xy,x} + M_{yy,y}), -M_{xy}, -M_{yy}, F_{xy}, F_{yy}, 0, 0\}, \\
\boldsymbol{c}_{1y}^T &= \{0, 0, 0, (N_{xy}u_{z,x} + N_{yy}u_{z,y}), 0, 0, 0, 0, 0\}, \\
\boldsymbol{c}_u^T &= \Big\{S_x u_x, S_y u_y, S_z u_z, J_{\vartheta x}\Big(u_{z,x} - \frac{6}{5h}\Phi_{xz}\Big), J_{\vartheta y}\Big(u_{z,y} - \frac{6}{5h}\Phi_{yz}\Big), \\
&\qquad -\frac{6}{5h}J_{\vartheta x}\Big(u_{z,x} - \frac{6}{5h}\Phi_{xz}\Big), -\frac{6}{5h}J_{\vartheta y}\Big(u_{z,y} - \frac{6}{5h}\Phi_{yz}\Big), 0, 0\Big\}, \\
\boldsymbol{c}_\Delta^T &= \{s_x(u_x - \Delta_x), s_y(u_y - \Delta_y), 0, 0, 0, 0, 0, s_x(\Delta_x - u_x), s_y(\Delta_y - u_y)\}, \\
\boldsymbol{g}_u^{*T} &= \Big\{S_x \tilde{u}_x^*, S_y \tilde{u}_y^*, S_x \tilde{u}_z^*, J_{\vartheta x}\vartheta_x^*, J_{\vartheta y}\vartheta_y^*, -\frac{6}{5h}J_{\vartheta x}\vartheta_x^*, -\frac{6}{5h}J_{\vartheta y}\vartheta_y^*, 0, 0\Big\}, \\
\boldsymbol{g}_\Delta^{*T} &= \Big\{0, 0, 0, 0, 0, 0, 0, \frac{P_x^*}{L}, \frac{P_y^*}{L}\Big\}.
\end{aligned} \tag{B6}$$

Equations for stress analysis. The equations needed to perform a linear stress analysis are obtained by direct linearization of the nonlinear plate equations. Under the presumption of infinitesimal displacement gradients, the product terms appearing in the in-plane strains given by (7d) and the equilibrium equations given by (B2) are neglected. The resulting equilibrium equations are

$$
\left\{
\begin{array}{c}
N_{xx,x} + N_{xy,y} \\
N_{xy,x} + N_{yy,y} \\
M_{xx,xx} + 2M_{xy,xy} + M_{yy,yy} - p^* \\
F_{xx,x} + F_{xy,y} - f_{xz} \\
F_{xy,x} + F_{yy,y} - f_{yz}
\end{array}
\right\} = \mathbf{0}.
\tag{B7}
$$

Similarly, the boundary conditions on Γ_σ that are given by (B3) reduce to

$$
\boldsymbol{b}_x n_x + \boldsymbol{b}_y n_y = \boldsymbol{f}^*,
\tag{B8}
$$

where the vectors are defined as

$$
\begin{aligned}
\boldsymbol{b}_x^T &= \{N_{xx}, N_{xy}, (M_{xx,x} + M_{xy,y}), M_{xx}, M_{xy}, F_{xx}, F_{xy}\}, \\
\boldsymbol{b}_y^T &= \{N_{xy}, N_{yy}, (M_{xy,x} + M_{yy,y}), M_{xy}, M_{yy}, F_{xy}, F_{yy}\}, \\
\boldsymbol{f}^{*T} &= \left\{ N_x^*, N_y^*, N_z^*, M_x^*, M_y^*, \frac{6}{5h} M_x^*, \frac{6}{5h} M_y^* \right\}.
\end{aligned}
\tag{B9}
$$

For the boundary Γ_u, the boundary conditions given by (B5) reduce to

$$
\boldsymbol{c}_x n_x + \boldsymbol{c}_y n_y + \boldsymbol{c}_u + \boldsymbol{c}_\Delta = \boldsymbol{g}_u^* + \boldsymbol{g}_\Delta^*,
\tag{B10}
$$

where the vectors are defined as

$$
\begin{aligned}
\boldsymbol{c}_x^T &= \{N_{xx}, N_{xy}, (M_{xx,x} + M_{xy,y}), -M_{xx}, -M_{xy}, F_{xx}, F_{xy}, 0, 0\}, \\
\boldsymbol{c}_y^T &= \{N_{xy}, N_{yy}, (M_{xy,x} + M_{yy,y}), -M_{xy}, -M_{yy}, F_{xy}, F_{yy}, 0, 0\}, \\
\boldsymbol{c}_u^T &= \Big\{ S_x u_x, S_y u_y, S_z u_z, J_{\vartheta x}\Big(u_{z,x} - \frac{6}{5h}\Phi_{xz}\Big), J_{\vartheta y}\Big(u_{z,y} - \frac{6}{5h}\Phi_{yz}\Big), \\
&\qquad\qquad -\frac{6}{5h} J_{\vartheta x}\Big(u_{z,x} - \frac{6}{5h}\Phi_{xz}\Big), -\frac{6}{5h} J_{\vartheta y}\Big(u_{z,y} - \frac{6}{5h}\Phi_{yz}\Big), 0, 0 \Big\}, \\
\boldsymbol{c}_\Delta^T &= \{s_x(u_x - \Delta_x), s_y(u_y - \Delta_y), 0, 0, 0, 0, 0, s_x(\Delta_x - u_x), s_y(\Delta_y - u_y)\}, \\
\boldsymbol{g}_u^{*T} &= \Big\{ S_x \tilde{u}_x^*, S_y \tilde{u}_y^*, S_x \tilde{u}_z^*, J_{\vartheta x}\vartheta_x^*, J_{\vartheta y}\vartheta_y^*, -\frac{6}{5h} J_{\vartheta x}\vartheta_x^*, -\frac{6}{5h} J_{\vartheta y}\vartheta_y^*, 0, 0 \Big\}, \\
\boldsymbol{g}_\Delta^{*T} &= \Big\{ 0, 0, 0, 0, 0, 0, 0, \frac{P_x^*}{L}, \frac{P_y^*}{L} \Big\}.
\end{aligned}
\tag{B11}
$$

These equations constitute a linear boundary-value problem that defines the stresses and displacements associated with stable deformations. Typically, this boundary-value problem has nonhomogeneous partial differential equations and nonhomogeneous boundary conditions.

Equations for buckling analysis. In a classical linear bifurcation analysis, the displacement field is linearized about a stable, initially flat prebuckling state. In particular, each dependent kinematic variable is partitioned into a linear prebuckling part plus an infinitesimal increment. The displacement expansions

are then substituted into the nonlinear strain-displacement relations, the linear constitutive equations, the nonlinear equilibrium equations, the boundary conditions, and the potential energy. By collecting like terms and retaining only terms that are linear in the infinitesimal increments of the dependent kinematic variables, the field equations are separated into two groups. The first group is a set of linear equations that are a subset of the equations used for the linear stress analysis in which only in-plane loads are considered and out-of-plane displacements are negligible. This linear boundary-value problem defines the in-plane stresses and displacements associated with the initial, stable prebuckling state and is referred to as the prebuckling problem.

The second group of equations, associated with infinitesimal increments in the kinematic variables, consists of homogeneous linear differential equations and homogeneous boundary conditions. Thus, these equations constitute a linear boundary-eigenvalue problem, which is referred to as the buckling problem. This type of analysis presumes that the initial prebuckling configuration of the laminate is flat, which places requirements on the nature of the applied loads. For a general in-plane loading state and multiply connected domain, the prebuckling stress state is nonuniform, with respect to the in-plane coordinates. This nonuniformity manifests itself as variable coefficients in the differential equations that define the buckling kinematic variables (incremental kinematic variables). Moreover, it is these variable coefficients that relate the buckling displacement to the magnitude of the in-plane loads.

The stable prebuckling equilibrium state of the plate is denoted by the superscript (0) while the incremental state, just after buckling occurs, is denoted by the superscript (1). It is assumed that the plate is symmetrically laminated ($\boldsymbol{B} = \boldsymbol{0}$) and remains flat prior to buckling. During the linearization procedure, no out-of-plane displacement and transverse shear deformations occur during the prebuckling state; thus, $u_z^{(0)} = 0$ and $\Phi_{xz}^{(0)} = \Phi_{yz}^{(0)} = 0$. Also, the out-of-plane displacement component in the incremental state is moderately large as compared to the incremental in-plane displacements (von Kármán assumptions are applied), that is, $u_z^{(1)} \gg u_x^{(1)}, u_y^{(1)}, \Phi_x z^{(1)}, \Phi_y z^{(1)}$. During transition to an adjacent equilibrium state, the external loads do not change and the prebuckling in-plane stresses are much higher than those in the incremental state, that is, $N_{\alpha\beta}^{(0)} \gg N_{\alpha\beta}^{(1)}$.

Prebuckling equations. In the linearization process, the terms with only superscript (0) are associated with flat stable equilibrium states and are isolated to obtain the equilibrium equations

$$\left\{ \begin{array}{c} N_{xx,x}^{(0)} + N_{xy,y}^{(0)} \\ N_{yy,y}^{(0)} + N_{xy,x}^{(0)} \end{array} \right\} = 0, \tag{B12}$$

and the boundary conditions

$$\boldsymbol{b}_{0x} n_x + \boldsymbol{b}_{0y} n_y = \boldsymbol{f}_0^*, \tag{B13}$$

on the boundary, Γ_σ, in which

$$\boldsymbol{b}_{0x}^T = \left\{ N_{xx}^{(0)}, N_{xy}^{(0)} \right\}, \qquad \boldsymbol{b}_{0y}^T = \left\{ N_{xy}^{(0)}, N_{yy}^{(0)} \right\}, \qquad \boldsymbol{f}_0^{*T} = \{ N_x^*, N_y^* \}. \tag{B14}$$

Likewise, linearization gives the boundary conditions

$$\boldsymbol{c}_{0x} n_x + \boldsymbol{c}_{0y} n_y + \boldsymbol{c}_{0u} + \boldsymbol{c}_{0\Delta} = \boldsymbol{g}_{0u}^* + \boldsymbol{g}_{0\Delta}^* \tag{B15}$$

on the boundary, Γ_u, in which

$$c_{0x}^T = \{N_{xx}^{(0)}, N_{xy}^{(0)}, 0, 0\}, \qquad c_{0y}^T = \{N_{xy}^{(0)}, N_{yy}^{(0)}, 0, 0\}, \qquad c_{0s}^T = \{S_x u_x^{(0)}, S_y u_y^{(0)}, 0, 0\}, \qquad \text{(B16a)}$$

$$c_{0\Delta}^T = \{s_x(u_x^{(0)} - \Delta_x^{(0)}), s_y(u_y^{(0)} - \Delta_y^{(0)}), s_x(\Delta_x^{(0)} - u_x^{(0)}), s_y(\Delta_y^{(0)} - u_y^{(0)})\}, \qquad \text{(B16b)}$$

$$g_{0u}^{*\,T} = \{S_x \tilde{u}_x^{*(0)}, S_y \tilde{u}_y^{*(0)}, 0, 0\}, \qquad g_{0\Delta}^{*\,T} = \left\{0, 0, \frac{P_x^*}{L}, \frac{P_y^*}{L}\right\}, \qquad \text{(B16c)}$$

where L represents the length of the edge mounted to the rigid bar.

Buckling equations. In the linearization process, the terms involving only superscript (1) correspond to the adjacent equilibrium state, and products of these small terms are neglected. The equilibrium equations obtained are

$$\begin{Bmatrix} N_{xx,x}^{(1)} + N_{xy,y}^{(1)} \\ N_{yy,y}^{(1)} + N_{xy,x}^{(1)} \\ M_{xx,xx}^{(1)} + 2M_{xy,xy}^{(1)} + M_{yy,yy}^{(1)} + N_{xx}^{(0)} u_{z,xx}^{(1)} + 2N_{xy}^{(0)} u_{z,xy}^{(1)} + N_{yy}^{(0)} u_{z,yy}^{(1)} \\ F_{xx,x}^{(1)} + F_{xy,y}^{(1)} - f_{xz}^{(1)} \\ F_{yy,y}^{(1)} + F_{xy,x}^{(1)} - f_{yz}^{(1)} \end{Bmatrix} = \mathbf{0}, \qquad \text{(B17)}$$

and the boundary conditions on the edge Γ_σ are

$$(\boldsymbol{b}_x + \boldsymbol{b}_{1x})n_x + (\boldsymbol{b}_y + \boldsymbol{b}_{1y})n_y = \mathbf{0}, \qquad \text{(B18)}$$

where

$$\begin{aligned}
\boldsymbol{b}_x^T &= \{N_{xx}^{(1)}, N_{xy}^{(1)}, (M_{xx,x}^{(1)} + M_{xy,y}^{(1)}), M_{xx}^{(1)}, M_{xy}^{(1)}, F_{xx}^{(1)}, F_{xy}^{(1)}\}, \\
\boldsymbol{b}_y^T &= \{N_{xy}^{(1)}, N_{yy}^{(1)}, (M_{xy,x}^{(1)} + M_{yy,y}^{(1)}), M_{xy}^{(1)}, M_{yy}^{(1)}, F_{xy}^{(1)}, F_{yy}^{(1)}\}, \\
\boldsymbol{b}_{1x}^T &= \{0, 0, (N_{xx}^{(0)} u_{z,x}^{(1)} + N_{xy}^{(0)} u_{z,y}^{(1)}), 0, 0, 0, 0\}, \\
\boldsymbol{b}_{1y}^T &= \{0, 0, 0, (N_{xy}^{(1)} u_{z,x}^{(1)} + N_{yy}^{(1)} u_{z,y}^{(1)}), 0, 0, 0\}.
\end{aligned} \qquad \text{(B19)}$$

Similarly, the boundary conditions on the edges Γ_u and Γ_Δ obtained from linearization are

$$(\boldsymbol{c}_x + \boldsymbol{c}_{1x})n_x + (\boldsymbol{c}_y + \boldsymbol{c}_{1y})n_y + \boldsymbol{c}_u + \boldsymbol{c}_\Delta = \mathbf{0}, \qquad \text{(B20)}$$

where

$$\begin{aligned}
\boldsymbol{c}_x^T &= \{N_{xx}^{(1)}, N_{xy}^{(1)}, (M_{xx,x}^{(1)} + M_{xy,y}^{(1)}), -M_{xx}^{(1)}, -M_{xy}^{(1)}, F_{xx}^{(1)}, F_{xy}^{(1)}, 0, 0\}, \\
\boldsymbol{c}_{1x}^T &= \{0, 0, (N_{xx}^{(0)} u_{z,x}^{(1)} + N_{xy}^{(0)} u_{z,y}^{(1)}), 0, 0, 0, 0, 0, 0\}, \\
\boldsymbol{c}_y^T &= \{N_{xy}^{(1)}, N_{yy}^{(1)}, (M_{xy,x}^{(1)} + M_{yy,y}^{(1)}), -M_{xy}^{(1)}, -M_{yy}^{(1)}, F_{xy}^{(1)}, F_{yy}^{(1)}, 0, 0\}, \\
\boldsymbol{c}_{1y}^T &= \{0, 0, 0, (N_{xy}^{(0)} u_{z,x}^{(1)} + N_{yy}^{(0)} u_{z,y}^{(1)}), 0, 0, 0, 0, 0\}, \\
\boldsymbol{c}_u^T &= \Big\{S_x u_x^{(1)}, S_y u_y^{(1)}, S_z u_z^{(1)}, J_{\vartheta x}\Big(u_{z,x}^{(1)} - \frac{6}{5h}\Phi_{xz}^{(1)}\Big), J_{\vartheta y}\Big(u_{z,y}^{(1)} - \frac{6}{5h}\Phi_{yz}^{(1)}\Big), \\
&\qquad -\frac{6}{5h}J_{\vartheta x}\Big(u_{z,x}^{(1)} - \frac{6}{5h}\Phi_{xz}^{(1)}\Big), -\frac{6}{5h}J_{\vartheta y}\Big(u_{z,y}^{(1)} - \frac{6}{5h}\Phi_{yz}^{(1)}\Big), 0, 0\Big\}, \\
\boldsymbol{c}_\Delta^T &= \{S_x(u_x^{(1)} - \Delta_x^{(1)}), S_y(u_y^{(1)} - \Delta_y^{(1)}), 0, 0, 0, 0, 0, S_x(\Delta_x^{(1)} - u_x^{(1)}), S_y(\Delta_y^{(1)} - u_y^{(1)})\}.
\end{aligned} \qquad \text{(B21)}$$

Appendix C: Representation of the displacement quantities

The local displacement quantities $\bar{u}_i$ and $\bar{\Phi}_{iz}$ that appear in (24) are specified in the form of Laurent series

$$\bar{u}_\alpha = 2h(\rho)\,\mathrm{Re}\sum_{\substack{n=-N\\n\neq 0}}^{N} \bar{a}_n^{(\alpha)}\xi^n, \quad \bar{u}_z = 2h(\rho)\,\mathrm{Re}\sum_{\substack{n=-N\\n\neq 0}}^{N} \bar{a}_n^{(z)}\int \xi^n\,d\bar{z}, \quad \bar{\Phi}_{\alpha z} = 2h(\rho)\,\mathrm{Re}\sum_{\substack{n=-N\\n\neq 0}}^{N} \bar{a}_n^{(\alpha z)}\xi^n$$

$$(\alpha = x, y), \quad \text{(C1)}$$

where $\bar{a}_n^{(\alpha)}$ and $\bar{a}_n^{(\alpha z)}$ are complex-valued unknown coefficients and the complex variable $\bar{z}$ is defined as $\bar{z} = x' + iy'$ with respect to the local x'-y' coordinate system shown in Figure 1. In (C1), all the series expansions are defined in terms of a complex variable ξ that is analytic outside of a unit circle and related to the complex variable $\bar{z}$ through a mapping function $\omega(\bar{z})$ as

$$\bar{z} = \omega^{-1}(\bar{z}) = r\xi - \frac{s}{\xi}. \quad \text{(C2)}$$

In this mapping, r and s are real-valued constants defined in terms of the cutout geometry as

$$r = \tfrac{1}{2}(a+b), \quad \text{(C3a)}$$

and

$$s = \tfrac{1}{2}(a-b). \quad \text{(C3b)}$$

The mapping function, $\omega(\bar{z})$, transforms the complex plane, $\bar{z}$, with an elliptic cutout to another complex plane, ξ, with an internal boundary as a unit-radius circle while the external boundaries preserve their 90 degree angles [Bowie 1956], thus enabling use of Laurent series. Furthermore, a domain-of-influence function $h(\rho)$ is defined as the fifth-order polynomial

$$h(\rho) = \begin{cases} 1 - 10\left(\dfrac{\rho}{\rho_0}\right)^3 + 15\left(\dfrac{\rho}{\rho_0}\right)^4 - 6\left(\dfrac{\rho}{\rho_0}\right)^5 & \text{if } 0 \leq \rho \leq \rho_0, \\ 0 & \text{if } \rho \geq \rho_0, \end{cases} \quad \text{(C4)}$$

in which $\rho = \sqrt{x'^2 + y'^2}$ and ρ_0 is the radius of influence of $h(\rho)$ outside the cutout (that is, $\rho_0 > \max[a, b]$). Note that the function $h(\rho)$ and its derivatives vanish for $\rho \geq \rho_0$.

The global displacement quantities $\bar{\bar{u}}_i$ and $\bar{\bar{\Phi}}_{\alpha z}$ are specified as Chebyshev series in the form

$$\bar{\bar{u}}_\alpha = \sum_{m=0}^{M}\sum_{n=0}^{m} c_{mn}^{(\alpha)} T_m(s_1)T_n(s_2), \qquad \bar{\bar{\Phi}}_{\alpha z} = \sum_{m=0}^{M}\sum_{n=0}^{m} c_{mn}^{(\alpha z)} T_m(s_1)T_n(s_2) \qquad (\alpha = x, y), \quad \text{(C5)}$$

where T_k is the kth term of the Chebyshev series with $T_{k+1}(x) = 2xT_k(x) - T_{k-1}(x)$ while $T_0(x) = 1$ and $T_1(x) = x$. The nondimensional coordinates s_1 and s_2 are defined as $s_1 = 2x/W$ and $s_2 = 2y/L$, where W and L are the characteristic width and length of the plate, respectively.

The vector of unknown generalized coordinates $\boldsymbol{q}$ that appears in (25) contains all the unknown real and complex-valued constants that appear in (C1) and (C5). Specifically,

$$\boldsymbol{q}^T = \{\bar{\boldsymbol{q}}_x^T, \bar{\boldsymbol{q}}_y^T, \bar{\boldsymbol{q}}_z^T, \bar{\boldsymbol{q}}_{xz}^T, \bar{\boldsymbol{q}}_{yz}^T, \bar{\bar{\boldsymbol{q}}}_x^T, \bar{\bar{\boldsymbol{q}}}_y^T, \bar{\bar{\boldsymbol{q}}}_z^T, \bar{\bar{\boldsymbol{q}}}_{xz}^T, \bar{\bar{\boldsymbol{q}}}_{yz}^T\}, \quad \text{(C6)}$$

where

$$\bar{q}_\alpha^T = \left\{ a_{-N}^{(\alpha)\,T}, a_{-N+1}^{(\alpha)\,T}, \dots, a_{-1}^{(\alpha)\,T}, a_{1}^{(\alpha)\,T}, \dots, a_{N-1}^{(\alpha)\,T}, a_{N}^{(\alpha)\,T} \right\},$$

$$\bar{q}_{\alpha z}^T = \left\{ a_{-N}^{(\alpha z)\,T}, a_{-N+1}^{(\alpha z)\,T}, \dots, a_{-1}^{(\alpha z)\,T}, a_{1}^{(\alpha z)\,T}, \dots, a_{N-1}^{(\alpha z)\,T}, a_{N}^{(\alpha z)\,T} \right\},$$

$$\bar{\bar{q}}_\alpha^T = \left\{ c_{00}^{(\alpha)\,T}, c_{10}^{(\alpha)\,T}, c_{01}^{(\alpha)\,T}, \dots, c_{M0}^{(\alpha)\,T}, c_{(M-1)1}^{(\alpha)\,T}, c_{(M-2)2}^{(\alpha)\,T}, \dots, c_{1(M-1)}^{(\alpha)\,T}, c_{0M}^{(\alpha)\,T} \right\},$$

$$\bar{\bar{q}}_{\alpha z}^T = \left\{ c_{00}^{(\alpha z)\,T}, c_{10}^{(\alpha z)\,T}, c_{01}^{(\alpha z)\,T}, \dots, c_{M0}^{(\alpha z)\,T}, c_{(M-1)1}^{(\alpha z)\,T}, c_{(M-2)2}^{(\alpha z)\,T}, \dots, c_{1(M-1)}^{(\alpha z)\,T}, c_{0M}^{(\alpha z)\,T} \right\},$$

$$(\alpha = x, y, z).$$

(C7)

The corresponding vectors of known functions, V_i and $V_{\alpha z}$ ($i = x, y, z$; $\alpha = x, y$) in (25) for all displacement quantities are defined as

$$V_x^T = \{ \bar{V}_0^T, 0^T, 0^T, 0^T, 0^T, \bar{\bar{V}}_0^T, 0^T, 0^T, 0^T, 0^T \},$$

$$V_y^T = \{ 0^T, \bar{V}_0^T, 0^T, 0^T, 0^T, 0^T, \bar{\bar{V}}_0^T, 0^T, 0^T, 0^T \},$$

$$V_y^T = \{ 0^T, 0^T, \bar{V}_z^T, 0^T, 0^T, 0^T, 0^T, \bar{\bar{V}}_0^T, 0^T, 0^T \},$$

$$V_{xz}^T = \{ 0^T, 0^T, 0^T, \bar{V}_0^T, 0^T, 0^T, 0^T, 0^T, \bar{\bar{V}}_0^T, 0^T \},$$

$$V_{yz}^T = \{ 0^T, 0^T, 0^T, 0^T, \bar{V}_0^T, 0^T, 0^T, 0^T, 0^T, \bar{\bar{V}}_0^T \},$$

(C8)

where the vectors $\bar{V}_0$, $\bar{V}z$, and $\bar{\bar{V}}_0$ are defined in the form

$$\bar{V}_\beta^T = \left\{ \bar{V}_{\beta(-N)}^T, \bar{V}_{\beta(-N+1)}^T, \dots, \bar{V}_{\beta(-1)}^T, \bar{V}_{\beta(1)}^T, \dots, \bar{V}_{\beta(N-1)}^T, \bar{V}_{\beta(N)}^T \right\} \quad (\beta = 0, z),$$

(C9)

with

$$\bar{V}_{0(n)}^T = \{ 2 \operatorname{Re}[\xi^n h(\rho)], -2 \operatorname{Im}[\xi^n h(\rho)] \},$$

(C10a)

$$\bar{V}_{z(n)}^T = \left\{ 2 \operatorname{Re}\left[\left(\int \xi^n \, d\bar{z} \right) h(\rho) \right], -2 \operatorname{Im}\left[\left(\int \xi^n \, d\bar{z} \right) h(\rho) \right] \right\},$$

(C10b)

and

$$\bar{\bar{V}}_0^T = \{ T_0(s_1) T_0(s_2), T_1(s_1) T_0(s_2), T_0(s_1) T_1(s_2), \dots, T_M(s_1) T_0(s_2),$$

$$T_{M-1}(s_1) T_1(s_2), \dots, T_1(s_1) T_{M-1}(s_2), T_0(s_1) T_M(s_2) \}. \quad \text{(C11)}$$

The integral term, $\int \xi^n \, d\bar{z}$, in (C10b) is expressed as

$$\int \xi^n \, d\bar{z} = \begin{cases} r \dfrac{\xi^{n+1}}{n+1} - s \dfrac{\xi^{n-1}}{n-1} & \text{if } |n| > 1, \\[2mm] r \ln \xi + s \dfrac{\xi^{-2}}{2} & \text{if } n = -1, \\[2mm] r \dfrac{\xi^2}{2} - s \ln \xi & \text{if } n = 1. \end{cases}$$

(C12)

The functions chosen for representing the local displacement quantities produce multivalued modes, because of the presence of the logarithmic terms in (C12), and must be made single-valued to obtain

unique representations. In matrix form, the single-valuedness conditions are expressed as

$$G_c q = 0,$$ (C13)

in which G_c is the coefficient matrix of the constraint equations and is defined as

$$G_c = \begin{bmatrix} G_r \\ G_s \end{bmatrix},$$ (C14)

where

$$G_r^T = \{ 0^T, 0^T, \dots, 0^T, g_{(-1)}, 0^T, 0^T, \dots, 0^T, 0^T \},$$ (C15a)
$$G_s^T = \{ 0^T, 0^T, \dots, 0^T, 0^T, g_{(1)}, 0^T, \dots, 0^T, 0^T \},$$ (C15b)

with

$$g_{(-1)}^T = \{0, r\},$$ (C16a)

and

$$g_{(1)}^T = \{0, s\}.$$ (C16b)

Note that the subscripts (-1) and (1) denote the locations of the terms in the local series. Finally, the matrix constraint equations in (C13) are integrated into the total potential energy formulation via Lagrange multipliers, producing zero potential energy, in the form

$$W = \lambda^T G_c q \equiv 0,$$ (C17)

where W is the potential energy of constraint forces, and λ denotes the vector of unknown Lagrange multipliers given by

$$\lambda^T = \{\lambda_r, \lambda_s\},$$ (C18)

where λ_r and λ_s denote the unknown constraint forces (Lagrange multipliers) that enforce the conditions in (C13).

Appendix D: Details of the solution method

Using the representations of the displacement fields in (25), the linearized form of the vector of strain quantities, e, given by (14b), is expressed in terms of the unknown generalized coordinates as

$$e = Bq,$$ (D1)

where the matrix B is defined as

$$B = \begin{bmatrix} B^\epsilon \\ B^\kappa \\ B^\Gamma \\ B^\Phi \end{bmatrix},$$ (D2)

and the coefficient matrices $\boldsymbol{B}^\epsilon$, $\boldsymbol{B}^\kappa$, $\boldsymbol{B}^\Gamma$, and $\boldsymbol{B}^\Phi$ are defined as

$$\boldsymbol{B}^\epsilon = \begin{bmatrix} \boldsymbol{V}_{x,x}^T \\ \boldsymbol{V}_{y,y}^T \\ \boldsymbol{V}_{x,y}^T + \boldsymbol{V}_{y,x}^T \end{bmatrix}, \quad \boldsymbol{B}^\kappa = \begin{bmatrix} -\boldsymbol{V}_{z,xx}^T \\ -\boldsymbol{V}_{z,yy}^T \\ -2\boldsymbol{V}_{z,xy}^T \end{bmatrix}, \quad \boldsymbol{B}^\Gamma = \begin{bmatrix} \boldsymbol{V}_{xz,x}^T \\ \boldsymbol{V}_{yz,y}^T \\ \boldsymbol{V}_{xz,y}^T + \boldsymbol{V}_{yz,x}^T \end{bmatrix}, \quad \boldsymbol{B}^\Phi = \begin{bmatrix} \boldsymbol{V}_{xz}^T \\ \boldsymbol{V}_{yz}^T \end{bmatrix}. \tag{D3}$$

The weighted-average boundary displacement vector (19a) is also expressed in terms of the unknown generalized coordinates as

$$\tilde{\boldsymbol{u}} = \tilde{\boldsymbol{V}}_B \boldsymbol{q}, \tag{D4}$$

where the matrix $\tilde{\boldsymbol{V}}_B$ is defined as

$$\tilde{\boldsymbol{V}}_B = \begin{bmatrix} \boldsymbol{V}_x^T \\ \boldsymbol{V}_y^T \\ \boldsymbol{V}_z^T \\ \boldsymbol{V}_{z,x}^T - \frac{6}{5}\boldsymbol{V}_{xz}^T \\ \boldsymbol{V}_{z,y}^T - \frac{6}{5}\boldsymbol{V}_{yz}^T \end{bmatrix}. \tag{D5}$$

Substituting the matrix representation of $\boldsymbol{e}$ given by (D1) into the strain energy expression for the laminate defined by (17) and rearranging the terms, the linearized form of the strain energy is expressed in terms of the unknown generalized coordinates as

$$U = \frac{1}{2}\boldsymbol{q}^T \boldsymbol{K}_C \boldsymbol{q}, \tag{D6}$$

where the matrix $\boldsymbol{K}_C$ is defined as

$$\boldsymbol{K}_C = \int_A \boldsymbol{B}^T \boldsymbol{C} \boldsymbol{B} \, dA. \tag{D7}$$

Substituting (D4) for the boundary displacement vector $\tilde{\boldsymbol{u}}$ into the strain energy of the elastic spring supports, given by (18) and rearranging the terms, the linearized form of the strain energy Ω is expressed in terms of the unknown generalized coordinates as

$$\Omega = \tfrac{1}{2}\boldsymbol{q}^T \boldsymbol{S}_{qq}\boldsymbol{q} - \boldsymbol{q}^T \boldsymbol{S}_q^* + \Omega^*, \tag{D8}$$

where the matrix $\boldsymbol{S}_{qq}$ and the vector $\boldsymbol{S}_q^*$ are defined as

$$\boldsymbol{S}_{qq} = \int_{\Gamma_u} \tilde{\boldsymbol{V}}_B^T \boldsymbol{k}_u \tilde{\boldsymbol{V}}_B \, d\Gamma \tag{D9a}$$

and

$$\boldsymbol{S}_q^* = \int_{\Gamma_u} \tilde{\boldsymbol{V}}_B^T \boldsymbol{k}_u \tilde{\boldsymbol{u}}^* \, d\Gamma. \tag{D9b}$$

The strain energy of the elastic spring arising from the applied displacement constraints Ω^* is written as

$$\Omega^* = \frac{1}{2}\int_{\Gamma_u} \tilde{\boldsymbol{u}}^{*T} \boldsymbol{k}_u \tilde{\boldsymbol{u}}^* \, d\Gamma. \tag{D10}$$

Substituting (D4) and the transverse displacement u_z given by (25a) into the potential energy of external loads given by (21) and rearranging the terms, the linearized form of the potential energy V is expressed

in terms of the unknown generalized coordinates as

$$V = -\boldsymbol{q}^T \boldsymbol{N}^* - \boldsymbol{q}^T \boldsymbol{p}_z^*, \tag{D11}$$

where the vectors $\boldsymbol{N}^*$ and $\boldsymbol{p}_z^*$ are defined as

$$\boldsymbol{N}^* = \int_{\Gamma^{(\sigma)}} \tilde{\boldsymbol{V}}_B^T \boldsymbol{T}^* \, d\Gamma, \qquad \boldsymbol{p}_z^* = \int_A p^* \boldsymbol{V}_z \, dA. \tag{D12}$$

Appendix E: Details of the bifurcation analysis

In the bifurcation analysis, the displacement vector $\boldsymbol{u}$, weighted-average boundary displacement vector $\tilde{\boldsymbol{u}}$, vector of generalized coordinates $\boldsymbol{q}$, uniform-edge-displacement vector $\boldsymbol{\Delta}$, and constraint force vector $\boldsymbol{\lambda}$ are expressed as

$$\boldsymbol{u} = \boldsymbol{u}^{(0)} + e\boldsymbol{u}^{(1)}, \tag{E1a}$$

$$\tilde{\boldsymbol{u}} = \tilde{\boldsymbol{u}}^{(0)} + e\tilde{\boldsymbol{u}}^{(1)}, \tag{E1b}$$

$$\boldsymbol{q} = \boldsymbol{q}^{(0)} + e\boldsymbol{q}^{(1)}, \tag{E1c}$$

$$\boldsymbol{\Delta} = \boldsymbol{\Delta}^{(0)} + e\boldsymbol{\Delta}^{(1)}, \tag{E1d}$$

$$\boldsymbol{\lambda} = \boldsymbol{\lambda}^{(0)} + e\boldsymbol{\lambda}^{(1)}. \tag{E1e}$$

By using these expressions, the terms appearing in the potential energy expansion given by (31) are obtained as

$$\pi^{(0)}\big(\boldsymbol{Q}^{(0)}\big) = U^{(0)}\big(\boldsymbol{q}^{(0)}\big) + \Omega^{(0)}\big(\boldsymbol{q}^{(0)}, \boldsymbol{\Delta}^{(0)}\big) + V^{(0)}\big(\boldsymbol{q}^{(0)}, \boldsymbol{\Delta}^{(0)}\big) + W^{(0)}\big(\boldsymbol{q}^{(0)}, \boldsymbol{\lambda}^{(0)}\big), \tag{E2a}$$

$$\begin{aligned} \pi^{(1)}\big(\boldsymbol{Q}^{(0)}, \boldsymbol{Q}^{(1)}\big) = U^{(1)}\big(\boldsymbol{q}^{(0)}, \boldsymbol{q}^{(1)}\big) + \Omega^{(1)}\big(\boldsymbol{q}^{(0)}, \boldsymbol{\Delta}^{(0)}, \boldsymbol{q}^{(1)}, \boldsymbol{\Delta}^{(1)}\big) \\ + V^{(1)}\big(\boldsymbol{q}^{(0)}, \boldsymbol{\Delta}^{(0)}, \boldsymbol{q}^{(1)}, \boldsymbol{\Delta}^{(1)}\big) + W^{(1)}\big(\boldsymbol{q}^{(0)}, \boldsymbol{\lambda}^{(0)}, \boldsymbol{q}^{(1)}, \boldsymbol{\lambda}^{(1)}\big), \end{aligned} \tag{E2b}$$

$$\pi^{(2)}\big(\boldsymbol{Q}^{(0)}, \boldsymbol{Q}^{(1)}\big) = U^{(1)}\big(\boldsymbol{q}^{(0)}, \boldsymbol{q}^{(1)}\big) + \Omega^{(1)}\big(\boldsymbol{q}^{(1)}, \boldsymbol{\Delta}^{(1)}\big) + W^{(1)}\big(\boldsymbol{q}^{(1)}, \boldsymbol{\lambda}^{(1)}\big). \tag{E2c}$$

The corresponding displacement vectors for the prebuckling and adjacent equilibrium states, $\boldsymbol{u}^{(0)}$ and $\boldsymbol{u}^{(1)}$, are given by

$$\boldsymbol{u}^{(0)T} = \big\{u_x^{(0)}, u_y^{(0)}, 0, 0, 0, 0, 0\big\}, \tag{E3}$$

$$\boldsymbol{u}^{(1)T} = \big\{u_x^{(1)}, u_y^{(1)}, u_z^{(1)}, \Phi_{xz}^{(1)}, \Phi_{yz}^{(1)}, u_{z,x}^{(1)}, u_{z,y}^{(1)}\big\}. \tag{E4}$$

The zero values in (E3) indicate an absence of bending deformations in the prebuckling equilibrium state. The strain vector $\boldsymbol{e}$, defined by (14b), becomes

$$\boldsymbol{e}(x, y) = \boldsymbol{e}^{(0)}(x, y) + e\boldsymbol{e}^{(1)}(x, y) + e^2\boldsymbol{e}^{(2)}(x, y) + O(e^3), \tag{E5}$$

where third-order terms in the parameter e are disregarded. The first three terms in (E5) are given by

$$e^{(0)T} = \{u_{x,x}^{(0)}, u_{y,y}^{(0)}, u_{x,y}^{(0)} + u_{y,x}^{(0)}, 0, 0, 0, 0, 0, 0, 0, 0\}, \tag{E6a}$$

$$e^{(1)T} = \{u_{x,x}^{(1)}, u_{y,y}^{(1)}, u_{x,y}^{(1)} + u_{y,x}^{(1)}, -u_{z,xx}^{(1)}, -u_{z,yy}^{(1)}, -2u_{z,xy}^{(1)}, \Phi_{xz,x}^{(1)}, \Phi_{yz,y}^{(1)}, \Phi_{xz,y}^{(1)} + \Phi_{yz,x}^{(1)}, \Phi_{xz}^{(1)}, \Phi_{yz}^{(1)}\}, \tag{E6b}$$

$$e^{(2)T} = \tfrac{1}{2}\{(u_{z,x}^{(1)})^2, (u_{z,y}^{(1)})^2, 2u_{z,x}^{(1)}u_{z,y}^{(1)}, 0, 0, 0, 0, 0, 0, 0, 0\}. \tag{E6c}$$

Applying the bifurcation procedure to (25), the displacement quantities u_i $(i = x, y, z)$ and Φ_{iz} $(i = x, y)$ for each state are found to be

$$u_i^{(k)} = V_i^T q^{(k)} \quad \text{with } i = x, y, z, \qquad \Phi_{iz}^{(k)} = V_{iz}^T q^{(k)} \quad \text{with } i = x, y, \tag{E7}$$

in which $k = 0, 1$. Using these representations, the strain vectors $e^{(0)}$, $e^{(1)}$, and $e^{(2)}$ are rewritten in matrix form in terms of the unknown generalized coordinates as

$$e^{(0)} = B_L q^{(0)}, \qquad e^{(1)} = B q^{(1)}, \qquad e_N^{(1)} = B_N q^{(1)}, \tag{E8}$$

where the matrices B_L and B_N are defined as

$$B_L = \begin{bmatrix} B^\epsilon \\ 0 \\ 0 \\ 0 \end{bmatrix}, \qquad B_N = \begin{bmatrix} B_N^\epsilon \\ 0 \\ 0 \\ 0 \end{bmatrix}, \tag{E9}$$

and the coefficient matrix B_N^ϵ is defined as

$$B_N^\epsilon = \begin{bmatrix} V_{z,x}^T \\ V_{z,y}^T \end{bmatrix}. \tag{E10}$$

Substituting (E5) into the constitutive equations given by (15) yields

$$s(x, y) = s^{(0)}(x, y) + e s^{(1)}(x, y) + e^2 s^{(2)}(x, y) + O(e^3), \tag{E11}$$

where

$$s^{(0)} = Ce^{(0)}, \qquad s^{(1)} = Ce^{(1)}, \qquad s^{(2)} = Ce^{(2)}, \tag{E12}$$

and C is for symmetrically laminated plates, that is,

$$C = \begin{bmatrix} A & 0 & 0 & 0 \\ 0 & D & F & 0 \\ 0 & F & H & 0 \\ 0 & 0 & 0 & G \end{bmatrix}. \tag{E13}$$

Thus, the stress resultant vector for each state becomes

$$s^{(0)T} = \{N_{xx}^{(0)}, N_{yy}^{(0)}, N_{xy}^{(0)}, 0, 0, 0, 0, 0, 0, 0, 0\}, \tag{E14a}$$

$$s^{(1)T} = \{N_{xx}^{(1)}, N_{yy}^{(1)}, N_{xy}^{(1)}, M_{xx}^{(1)}, M_{yy}^{(1)}, M_{xy}^{(1)}, F_{xx}^{(1)}, F_{yy}^{(1)}, F_{xy}^{(1)}, q_{xz}^{(1)}, q_{yz}^{(1)}\}, \tag{E14b}$$

and $s^{(2)}$ involves only the contribution of the matrix A and the nonlinear components of the in-plane strains appearing in (E6c).

Next, substituting (E5) and (E11) into (13) and noting that $s^{(k)T}e^{(j)} = s^{(j)T}e^{(k)}$ gives the strain energy expansion

$$U = U^{(0)} + eU^{(1)} + e^2 U^{(2)} + O(e^3),\tag{E15}$$

where

$$
\begin{aligned}
U^{(0)} &= \frac{1}{2} \iint_A e^{(0)T} C e^{(0)} \, dx \, dy, \\
U^{(1)} &= \iint_A s^{(1)T} e^{(0)} \, dx \, dy, \\
U^{(2)} &= \iint_A \left(\frac{1}{2} e^{(1)T} C e^{(1)} + s^{(0)T} e^{(2)} \right) dx \, dy.
\end{aligned}
\tag{E16}
$$

The terms $U^{(1)}$ and $U^{(2)}$ represent the first and second variations of the strain energy, respectively. It is convenient to represent the second term of $U^{(2)}$ as the quadratic form

$$s^{(0)T} e^{(2)} = e_N^{(1)T} N^{(0)} e_N^{(1)},\tag{E17}$$

where

$$e_N^{(1)T} = \{u_{z,x}^{(1)}, u_{z,y}^{(1)}\}, \qquad N^{(0)} = \begin{bmatrix} N_{xx}^{(0)} & N_{xy}^{(0)} \\ N_{xy}^{(0)} & N_{yy}^{(0)} \end{bmatrix},\tag{E18}$$

leading to

$$U^{(2)} = \iint_A \left(\frac{1}{2} e^{(1)T} C e^{(1)} + e_N^{(1)T} N^{(0)} e_N^{(1)} \right) dx \, dy.\tag{E19}$$

Substituting for the matrix representation of the strain resultant vectors $e^{(k)}$ ($k = 0, 1, 2$) given by (E8) into the strain energy expression given by (E16) and rearranging the terms, the expressions for $U^{(k)}$ ($k = 0, 1, 2$) are expressed in terms of the unknown generalized coordinates as

$$
\begin{aligned}
U^{(0)} &= \tfrac{1}{2} q^{(0)T} K_{L0} q^{(0)}, \qquad U^{(1)} = -\tfrac{1}{2} q^{(0)T} K_{L01} q^{(1)} - \tfrac{1}{2} q^{(0)T} K_{L01}^T q^{(1)}, \\
U^{(2)} &= \tfrac{1}{2} q^{(1)T} K_{L1} q^{(1)} + \tfrac{1}{2} q^{(1)T} H q^{(1)},
\end{aligned}
\tag{E20}
$$

where the matrices K_{L0}, K_{L1}, K_{L01}, and H are defined as

$$
\begin{aligned}
K_{L0} &= \int_A B_{L0}^T C B_{L0} \, dA, \qquad K_{L1} = \int_A B_{L1}^T C B_{L1} \, dA, \\
K_{L01} &= \int_A B_{L0}^T C B_{L1} \, dA, \qquad H = \int_A B_N^T N^{(0)} B_N \, dA.
\end{aligned}
\tag{E21}
$$

Similarly, substituting (E1b) into the expression for the strain energy of the elastic spring supports given by (18) results in

$$\Omega = \Omega^{(0)} + e\Omega^{(1)} + e^2 \Omega^{(2)},\tag{E22}$$

where

$$\Omega^{(0)} = \frac{1}{2} \int_{\Gamma_u} \left(\tilde{\boldsymbol{u}}^{(0)} - \tilde{\boldsymbol{u}}^* \right)^T \boldsymbol{k}_u \left(\tilde{\boldsymbol{u}}^{(0)} - \tilde{\boldsymbol{u}}^* \right) d\Gamma + \frac{1}{2} \int_{\Gamma_\Delta} \left(\tilde{\boldsymbol{u}}^{(0)} - \boldsymbol{\Delta}^{(0)} \right)^T \boldsymbol{k}_u \left(\tilde{\boldsymbol{u}}^{(0)} - \boldsymbol{\Delta}^{(0)} \right) d\Gamma, \qquad \text{(E23a)}$$

$$\Omega^{(1)} = \int_{\Gamma_u} \left(\tilde{\boldsymbol{u}}^{(0)} - \tilde{\boldsymbol{u}}^* \right)^T \boldsymbol{k}_u \tilde{\boldsymbol{u}}^{(1)} d\Gamma + \int_{\Gamma_\Delta} \left(\tilde{\boldsymbol{u}}^{(1)} - \boldsymbol{\Delta}^{(1)} \right)^T \boldsymbol{k}_u \left(\tilde{\boldsymbol{u}}^{(0)} - \boldsymbol{\Delta}^{(0)} \right) d\Gamma, \qquad \text{(E23b)}$$

$$\Omega^{(2)} = \frac{1}{2} \int_{\Gamma_u} \tilde{\boldsymbol{u}}^{(1)T} \boldsymbol{k}_u \tilde{\boldsymbol{u}}^{(1)} d\Gamma + \frac{1}{2} \int_{\Gamma_\Delta} \left(\tilde{\boldsymbol{u}}^{(1)} - \boldsymbol{\Delta}^{(1)} \right)^T \boldsymbol{k}_u \left(\tilde{\boldsymbol{u}}^{(1)} - \boldsymbol{\Delta}^{(1)} \right) d\Gamma. \qquad \text{(E23c)}$$

Substituting for the vector representation of the weighted-average boundary displacement field $\tilde{\boldsymbol{u}}$, given by (D4), the expressions for $\Omega^{(k)}$ are rewritten as

$$\Omega^{(0)} = \tfrac{1}{2} \boldsymbol{q}^{(0)T} \boldsymbol{S}_{qq} \boldsymbol{q}^{(0)} - \boldsymbol{q}^{(0)T} \boldsymbol{S}_q^* + \Omega^* + \tfrac{1}{2} \boldsymbol{\Delta}^{(0)T} \boldsymbol{s}_{\Delta\Delta} \boldsymbol{\Delta}^{(0)} \qquad \text{(E24a)}$$

$$- \tfrac{1}{2} \boldsymbol{\Delta}^{(0)T} \boldsymbol{s}_{q\Delta}^T \boldsymbol{q}^{(0)} - \tfrac{1}{2} \boldsymbol{q}^{(0)T} \boldsymbol{s}_{q\Delta} \boldsymbol{\Delta}^{(0)} + \tfrac{1}{2} \boldsymbol{q}^{(0)T} \boldsymbol{S}_{\Delta\Delta} \boldsymbol{q}^{(0)}, \qquad \text{(E24b)}$$

$$\Omega^{(1)} = \boldsymbol{q}^{(0)T} \boldsymbol{S}_{qq} \boldsymbol{q}^{(1)} - \boldsymbol{q}^{(1)T} \boldsymbol{S}_q^* + \boldsymbol{\Delta}^{(1)T} \boldsymbol{s}_{\Delta\Delta} \boldsymbol{\Delta}^{(0)} - \boldsymbol{\Delta}^{(1)T} \boldsymbol{s}_{q\Delta}^T \boldsymbol{q}^{(0)} - \boldsymbol{q}^{(1)T} \boldsymbol{s}_{q\Delta} \boldsymbol{\Delta}^{(0)} + \boldsymbol{q}^{(1)T} \boldsymbol{S}_{\Delta\Delta} \boldsymbol{q}^{(0)}, \qquad \text{(E24c)}$$

$$\Omega^{(2)} = \tfrac{1}{2} \boldsymbol{q}^{(1)T} \boldsymbol{S}_{qq} \boldsymbol{q}^{(1)} + \tfrac{1}{2} \boldsymbol{\Delta}^{(1)T} \boldsymbol{s}_{\Delta\Delta} \boldsymbol{\Delta}^{(1)} - \tfrac{1}{2} \boldsymbol{\Delta}^{(1)T} \boldsymbol{s}_{q\Delta}^T \boldsymbol{q}^{(1)} - \tfrac{1}{2} \boldsymbol{q}^{(1)T} \boldsymbol{s}_{q\Delta} \boldsymbol{\Delta}^{(1)} + \tfrac{1}{2} \boldsymbol{q}^{(1)T} \boldsymbol{S}_{\Delta\Delta} \boldsymbol{q}^{(1)}, \qquad \text{(E24d)}$$

where the matrices $\boldsymbol{S}_{\Delta\Delta}$, $\boldsymbol{s}_{\Delta\Delta}$, and $\boldsymbol{s}_{q\Delta}$ are defined as

$$\boldsymbol{S}_{\Delta\Delta} = \int_{\Gamma_\Delta} \tilde{\boldsymbol{V}}_B^T \boldsymbol{k}_\Delta \tilde{\boldsymbol{V}}_B \, d\Gamma, \qquad \boldsymbol{s}_{\Delta\Delta} = \int_{\Gamma_\Delta} \boldsymbol{k}_\Delta \, d\Gamma, \qquad \boldsymbol{s}_{q\Delta} = \int_{\Gamma_\Delta} \tilde{\boldsymbol{V}}_B^T \boldsymbol{k}_\Delta \, d\Gamma. \qquad \text{(E25)}$$

In these integrals, Γ_Δ represents the boundary segment having extensional springs that remain between the laminate boundary and the rigid bar.

Substituting (E1a) into the potential energy given by (21) with only the in-plane external forces acting along the edges of the laminate included gives

$$V = \left(V_\sigma^{(0)} + e V_\sigma^{(1)} \right) + \left(V_\Delta^{(0)} + e V_\Delta^{(1)} \right), \qquad \text{(E26)}$$

where

$$V_\sigma^{(0)} = \int_{\Gamma_\sigma} \boldsymbol{T}^{*T} \tilde{\boldsymbol{u}}^{(0)} \, d\Gamma, \qquad V_\sigma^{(1)} = \int_{\Gamma_\sigma} \boldsymbol{T}^{*T} \tilde{\boldsymbol{u}}^{(1)} \, d\Gamma, \qquad \text{(E27)}$$

and

$$V_\Delta^{(k)} = \boldsymbol{P}^{*T} \boldsymbol{\Delta}^{(k)} \quad \text{on } \Gamma_\Delta \text{ with } k = 0, 1. \qquad \text{(E28)}$$

In these integrals, $\boldsymbol{T}^{*T} = \{N_x^*, N_y^*, 0, 0, 0\}$. Note that only the in-plane loads, N_x^* and N_y^*, are included in vector $\boldsymbol{T}^*$ in order to avoid bending deformations in the prebuckling state. Substituting the vector representation of the weighted-average boundary displacement field $\tilde{\boldsymbol{u}}$ into (E27), the linearized forms of the potential energy of elastic restraints, $V_\sigma^{(k)}$, are rewritten as

$$V_\sigma^{(k)} = \boldsymbol{q}^{(k)T} \boldsymbol{N}^* \quad \text{with } k = 0, 1. \qquad \text{(E29)}$$

The vector $\boldsymbol{N}^*$ is defined as

$$\boldsymbol{N}^{*T} = \int_{\Gamma_\sigma} \tilde{\boldsymbol{V}}_B^T \boldsymbol{T}^* \, d\Gamma. \qquad \text{(E30)}$$

The zeroth, first, and second variations of the constraint forces are obtained by substituting the vector of unknown generalized coordinates given by (E1c) and (E1e) into (C17) and rearranging the terms. This process yields

$$W^{(0)} = \boldsymbol{\lambda}^{(0)T} \boldsymbol{G}_c \boldsymbol{q}^{(0)}, \qquad W^{(1)} = \boldsymbol{\lambda}^{(0)T} \boldsymbol{G}_c \boldsymbol{q}^{(1)} + \boldsymbol{\lambda}^{(1)T} \boldsymbol{G}_c \boldsymbol{q}^{(0)}, \qquad W^{(2)} = \boldsymbol{\lambda}^{(1)T} \boldsymbol{G}_c \boldsymbol{q}^{(1)}. \tag{E31}$$

References

[Altenbach 1998] H. Altenbach, "Theories for laminated and sandwich plates: a review", *Mech. Compos. Mater.* **34**:3 (1998), 243–252.

[Barut and Madenci 2001] A. Barut and E. Madenci, "A complex potential-variational formulation for buckling analysis of flat laminates with multiple cutouts", in *42nd AIAA/ASME/ASCE/AHS/ASC Structures, Structural Dynamics, and Materials Conference* (Seattle, WA, 2001), AIAA, Reston, VA, 2001. AIAA Paper 2001-1547.

[Barut et al. 1998] A. Barut, E. Madenci, and A. Tessler, "Analysis of composite sandwich panels via a triangular shell element based on higher-order theory", pp. 263–278 in *Sandwich construction 4: proceedings of the Fourth International Conference on Sandwich Construction* (Stockholm, 1998), edited by K.-A. Olsson, Engineering Materials Advisory Services, Cradley Heath, 1998.

[Barut et al. 2002] A. Barut, E. Madenci, T. Anderson, and A. Tessler, "Equivalent single-layer theory for a complete stress field in sandwich panels under arbitrarily distributed loading", *Compos. Struct.* **58**:4 (2002), 483–495.

[Bosia et al. 2002] F. Bosia, T. Gmür, and J. Botsis, "Deformation characteristics of composite laminates, II: An experimental/numerical study on equivalent single-layer theories", *Compos. Sci. Technol.* **62**:1 (2002), 55–66.

[Bowie 1956] O. L. Bowie, "Analysis of an infinite plate containing radial cracks originating at the boundary of an internal circular hole", *J. Math. Phys.* (*MIT*) **35** (1956), 60–71.

[Brush and Almroth 1975] D. O. Brush and B. O. Almroth, *Buckling of bars, plates and shells*, McGraw-Hill, New York, 1975.

[Demasi and Yu 2009] L. Demasi and W. Yu, "Assess the accuracy of the variational asymptotic plate and shell analysis (VAPAS) using the generalized unified formulation (GUF)", in *50th AIAA/ASME/ASCE/AHS/ASC Structures, Structural Dynamics, and Materials Conference* (Palm Springs, CA, 2009), AIAA, Reston, VA, 2009. AIAA Paper 2009-2417.

[Fung and Tong 2001] F. C. Fung and P. Tong, *Classical and computational solid mechanics*, World Scientific, River Edge, NJ, 2001.

[Ghugal and Shimpi 2002] Y. M. Ghugal and R. P. Shimpi, "A review of refined shear deformation theories of isotropic and anisotropic laminated plates", *J. Reinf. Plast. Compos.* **21**:9 (2002), 775–813.

[Iyengar and Chakraborty 2004] N. G. R. Iyengar and A. Chakraborty, "Study of interaction curves for composite laminate subjected to in-plane uniaxial and shear loadings", *Compos. Struct.* **64**:3–4 (2004), 307–315.

[Jones 1975] R. M. Jones, *Mechanics of composite materials*, McGraw-Hill, Washington, DC, 1975.

[Krishna Murty 1987] A. V. Krishna Murty, "Flexure of composite plates", *Compos. Struct.* **7**:3 (1987), 161–177.

[Liu and Li 1996] D. Liu and X. Li, "An overall view of laminate theories based on displacement hypothesis", *J. Compos. Mater.* **30**:14 (1996), 1539–1561.

[Nemeth 1990] M. P. Nemeth, "Buckling and postbuckling behavior of square compression-loaded graphite-epoxy plates with circular cutouts", NASA Technical Paper 3007, Langley Research Center, Hampton, VA, 1990, Available at http://ntrs.nasa.gov/search.jsp?R=19900016761.

[Noor and Malik 2000] A. K. Noor and M. Malik, "An assessment of five modeling approaches for thermo-mechanical stress analysis of laminated composite panels", *Comput. Mech.* **25**:1 (2000), 43–58.

[Ramm 2000] E. Ramm, "From Reissner plate theory to three dimensions in large deformation shell analysis", *Z. Angew. Math. Mech.* **80**:1 (2000), 61–68.

[Ray 2003] M. C. Ray, "Zeroth-order shear deformation theory for laminated composite plates", *J. Appl. Mech.* (*ASME*) **70**:3 (2003), 374–380.

[Reddy 1984] J. N. Reddy, "A simple higher-order theory for laminated composite plates", *J. Appl. Mech.* (*ASME*) **51**:4 (1984), 745–752.

[Reddy 1987] J. N. Reddy, "A small strain and moderate rotation theory of elastic anisotropic plates", *J. Appl. Mech.* (*ASME*) **54**:3 (1987), 623–626.

[Reddy 1990] J. N. Reddy, "A general non-linear third-order theory of plates with moderate thickness", *Int. J. Non-Linear Mech.* **25**:6 (1990), 677–686.

[Reddy 1997] J. N. Reddy, *Mechanics of laminated composite plates*, CRC Press, Boca Raton, FL, 1997.

[Reissner 1944] E. Reissner, "On the theory of bending of elastic plates", *J. Math. Phys.* (*MIT*) **23** (1944), 184–191.

[Reissner 1945] E. Reissner, "The effect of transverse shear deformation on the bending of elastic plates", *J. Appl. Mech.* (*ASME*) **12** (1945), A69–A77.

[Rohwer et al. 2001] K. Rohwer, R. Rolfes, and H. Sparr, "Higher-order theories for thermal stresses in layered plates", *Int. J. Solids Struct.* **38**:21 (2001), 3673–3687.

[Senthilnathan et al. 1987] N. R. Senthilnathan, S. P. Lim, K. H. Lee, and S. T. Chow, "Buckling of shear-deformable plates", *AIAA J.* **25**:9 (1987), 1268–1271.

[Shi 2007] G. Shi, "A new simple third-order shear deformation theory of plates", *Int. J. Solids Struct.* **44**:13 (2007), 4399–4417.

[Shimpi 1999] R. C. Shimpi, "Zeroth-order shear deformation theory for plates", *AIAA J.* **37**:4 (1999), 524–526.

[Shu and Sun 1994] X. Shu and L. Sun, "Thermomechanical buckling of laminated composite plates with higher-order transverse shear deformation", *Comput. Struct.* **53**:1 (1994), 1–7.

[Singh et al. 1994] G. Singh, G. Venkateswara Rao, and N. G. R. Iyengar, "Geometrically nonlinear flexural response characteristics of shear deformable unsymmetrically laminated plates", *Comput. Struct.* **53**:1 (1994), 69–81.

[Soldatos and Timarci 1993] K. P. Soldatos and T. Timarci, "A unified formulation of laminated composite, shear deformable, five-degrees-of-freedom cylindrical shell theories", *Compos. Struct.* **25**:1–4 (1993), 165–171.

[Sun and Hsu 1990] L. X. Sun and T. R. Hsu, "Thermal buckling of laminated composite plates with transverse shear deformation", *Comput. Struct.* **36**:5 (1990), 883–889.

[Tessler 1993] A. Tessler, "An improved plate theory of {1, 2}-order for thick composite laminates", *Int. J. Solids Struct.* **30**:7 (1993), 981–1000.

[Tessler and Saether 1991] A. Tessler and E. Saether, "A computationally viable higher-order theory for laminated composit plates", *Int. J. Numer. Methods Eng.* **31**:6 (1991), 1069–1086.

[Tessler et al. 2009] A. Tessler, M. Di Sciuva, and M. Gherlone, "A refined zigzag beam theory for composite and sandwich beams", *J. Compos. Mater.* **43**:9 (2009), 1051–1081.

[Timarci and Aydogdu 2005] T. Timarci and M. Aydogdu, "Buckling of symmetric cross-ply square plates with various boundary conditions", *Compos. Struct.* **68**:4 (2005), 381–389.

[Voyiadjis and Shi 1991] G. Z. Voyiadjis and G. Shi, "A refined two-dimensional theory for thick cylindrical shells", *Int. J. Solids Struct.* **27**:3 (1991), 261–282.

[Whitney and Nuismer 1974] J. M. Whitney and R. J. Nuismer, "Stress fracture criteria for laminated composites containing stress concentrations", *J. Compos. Mater.* **8**:3 (1974), 253–265.

[Yu and Hodges 2004] W. Yu and D. H. Hodges, "Asymptotic approach for thermoelastic analysis of laminated composite plates", *J. Eng. Mech.* (*ASCE*) **130**:5 (2004), 531–540.

ATILA BARUT: atila@email.arizona.edu
Department of Aerospace and Mechanical Engineering, The University of Arizona, Tucson, AZ 85721, United States

ERDOGAN MADENCI: madenci@email.arizona.edu
Department of Aerospace and Mechanical Engineering, The University of Arizona, Tucson, AZ 85721, United States

MICHAEL P. NEMETH: michael.p.nemeth@nasa.gov
Structural Mechanics and Concepts Branch, NASA Langley Research Center, Hampton, VA 23681-2199, United States

msp

ELECTROTHERMOMECHANICAL BEHAVIOR OF A RADIALLY POLARIZED ROTATING FUNCTIONALLY GRADED PIEZOELECTRIC CYLINDER

ALI GHORBANPOUR ARANI, ABBAS LOGHMAN,
ALI ABDOLLAHITAHERI AND VAHID ATABAKHSHIAN

A hollow circular cylinder made of exponentially graded piezoelectric material, such as PZT_4, is considered. Loading is composed of internal and external pressures, a distributed temperature field due to steady state heat conduction with convective boundary condition, an inertia body force due to rotation with constant angular velocity and a constant electric potential difference between its inner and outer surfaces. The material properties except Poisson's ratio and thermal conduction coefficient are assumed to be exponentially distributed along radius. The governing equation in polarized form is shown to reduce to a second-order ordinary differential equation with variable coefficients for the radial displacement. In this article, a closed form solution is presented for this ODE by employing hypergeometric functions such as Whittaker's M and W functions. Also we have considered four different sets of boundary conditions. The electrothermomechanical induced stresses and the electric potential distributions are investigated for the piezoceramic PZT_4 cylinder. It is concluded that the inhomogeneity exponent μ plays a substantial role in radial and circumferential stress distributions. Therefore, the results of this investigation can contribute to the design of EGPM rotating thick-walled circular cylinders.

A list of symbols can be found on page 881.

1. Introduction

In recent years there has been a resurgence of interest in piezoelectricity, due to advances in the intelligent structures technology. It is well known that piezoelectric materials experience mechanical deformations when placed in an electric field, and become electrically polarized under mechanical loads and in fact they exhibit electromechanical coupling. Piezoelectric materials have been used for a long time to make many electromechanical devices. One of the first applications of the piezoelectric effect was an ultrasonic submarine detector developed during the First World War. Other applications include transducers for converting electrical energy to mechanical energy or vice versa, resonators and filters for frequency control and selection for telecommunication and precise timing and synchronization, and acoustic wave sensors. To amend the structure of piezoelectric material and the application of these materials in various environments, functionally graded piezoelectric materials (FGPM) have been created. The mechanical and thermal properties of FGPM are similar to FGM, varying continuously in terms of the spatial coordinate system.

For homogeneous piezoelectric media, Ghorbanpour et al. [2006] investigated the stress distribution of dielectric potential fields in piezoelectric hollow spheres. Their results showed that an existing mechanical hoop stress distribution can be neutralized by a suitably applied electric field. Saadatfar and Razavi

Keywords: EGPM, rotating cylinder, hypergeometric function, electrothermomechanical stress, electric potential.

[2009] analyzed the stress in piezoelectric hollow cylinder with thermal gradient. An analytic solution to the axisymmetric problem of an infinitely long, radially polarized, radially orthotropic piezoelectric hollow circular cylinder was developed in [Galic and Horgan 2002].

For a special inhomogeneous case, Lu et al. [2005] derived the exact three-dimensional analytical solutions for a rectangular laminate with piezoelectric layers of exponentially graded material properties along thickness, and under simply supported boundary conditions along two opposite edges. They discussed some properties of the mechanical and electric responses of the FGPM plates under mechanical and/or electrical forces, and they also showed the influence of material gradients by numerical examples based on the exact solutions.

Zhong and Shang [2003] presented an exact solution of a simply supported functionally gradient piezoelectric rectangular plate based on three-dimensional electroelasticity theory. The obtained exact solution was valid for arbitrary mechanical and electric loads applied on the upper and lower surfaces of the plate and could serve as a benchmark result to assess other approximate methodologies or as a basis for establishing simplified FGPM plate theories.

The three-dimensional exact solutions of a simply supported FGPM plate/laminate were obtained based on an alternative approach in [Lu et al. 2006], which compared the exact solutions with the solutions obtained in [Zhong and Shang 2003], and concluded that their exact solutions may be more convenient for further treatments of both analytical and numerical studies.

Pan and Han [2005] also presented an exact solution for a multilayered rectangular plate made of anisotropic and functionally graded magneto-electroelastic materials. The plate is simply supported along its edges, and both mechanical and electric loads are applied on the top surface. Their numerical results showed the influence of the exponential factor, magneto-electroelastic properties, stacking sequence and loading types on the induced magneto-electroelastic fields, which should be of interest to the design of smart structures.

The static analysis of a single-layered functionally graded piezoelectric plate, in both sensor and actuator configuration was investigated in [Brischetto and Carrera 2009], which compared refined theories with classical ones, to demonstrate the effectiveness of these theories in the case of FGPMs.

Recently, Li et al. [2010] analyzed an axisymmetric electroelastic problem of hollow radially polarized piezoceramic cylinders made of FGMs as sensors and actuators. For two typical cases of sensors and actuators, the response of the radial and circumferential stresses as well as the electric potential was shown graphically by them. Their derived results for the distribution of hoop and radial stresses as well as the electric response are useful in designing hollow cylindrical FG piezoelectric sensors/ actuators.

The elastic and piezoelectric properties vary as a power-function along radius, Khoshgoftar et al. [2009] studied thermopiezoelectric behavior of a thick-walled cylinder made of FGMs subjected to a temperature gradient and inner and outer pressures.

Babaei and Chen [2008] presented the analytical solution for a radially piezoelectric functionally graded rotating hollow shaft. The analytical solution of a functionally graded piezothermoelastic hollow cylinder was presented in [Chen and Shi 2005]. This article assumed that only the piezoelectric coefficient was varying quadratically in the radial direction while the other material parameters were assumed to be constants. They neglected other inhomogeneity parameters such as thermal conduction coefficient and modulus of elasticity. Because of this incompleteness and more accordance of exponential form of
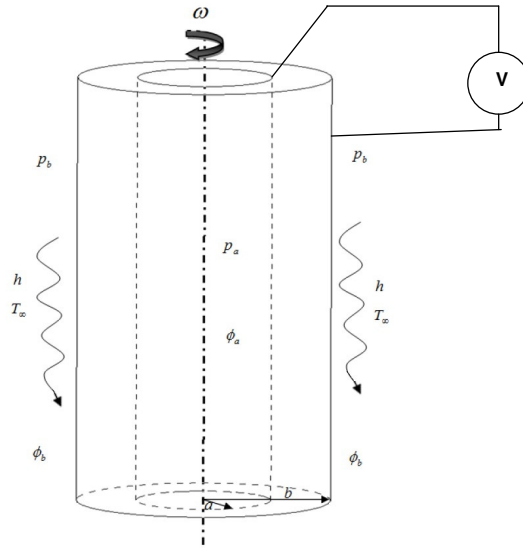
Figure 1. Configuration of an EGPM rotating hollow circular cylinder.

properties with new practical model, the effect of the entire material inhomogeneity on the piezothermo-electroelastic behavior of an EGPM hollow rotating cylinder is studied in the present paper.

In this study a thick-walled rotating cylinder of radially polarized anisotropic piezoelectric material, such as PZT_4, is assumed. The cylinder is subjected to mechanical and thermal loads, together with a potential difference induced by electrodes attached to the inner and outer surfaces (Figure 1). All the mechanical, thermal and piezoelectric properties of the EGPM rotating hollow cylinder, except Poisson's ratio, are assumed to be radial dependent and they are expressed as exponential functions of r. The governing equations of exponentially graded piezoelectric cylindrically structure in radially polarized form are reduced to a second-order inhomogeneous differential equation in terms of displacement with variable coefficients and is solved using hypergeometric functions and Simpson's integrating method. Finally, numerical results and the associated data are presented for four different sets of boundary conditions to illustrate electroelastic stresses, electric potential, radial displacement and thermal distributions for piezoceramic, PZT_4.

2. Heat conduction problem

In this section, the axisymmetric, steady state, heat conduction equation in the cylindrical coordinate system with the thermal boundary condition is given as (see [Hosseini et al. 2007])

$$
\begin{aligned}
&\frac{1}{r}\frac{\partial}{\partial r}\left[rk(r)\frac{\partial T(r)}{\partial r}\right]=0, \quad (a \leq r \leq b),\\
&T(r)|_{r=a}=T_0,\\
&\left[\frac{\partial T(r)}{\partial r}+hT(r)\right]\Bigg|_{r=b}=0,
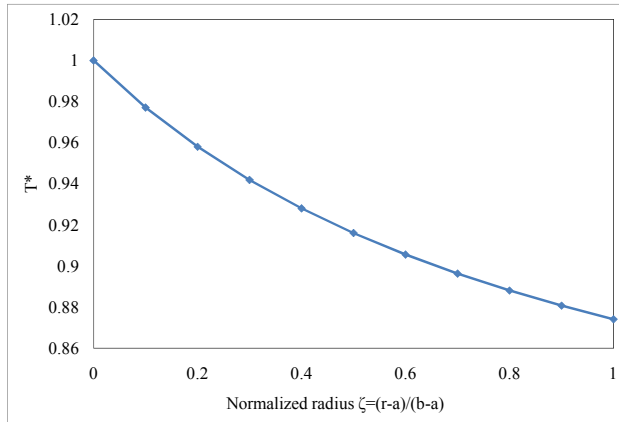\end{aligned}
\tag{1}
$$

Figure 2. Temperature distribution versus normalized radius for $\beta = 1$.

where h is the ratio of convective heat transfer coefficient and $k(r)$ is the thermal conduction coefficient, which is assumed to be a power function of r as

$$k(r) = k_0 r^\beta, \tag{2}$$

Substituting (2) into the heat conduction equation (1) one can obtain

$$\frac{1}{r} \frac{\partial}{\partial r} \left[r^{\beta+1} \frac{\partial T(r)}{\partial r} \right] = 0, \tag{3}$$

the general solution for the temperature distribution is obtained by integrating (3), as

$$T(r) = D_1 r^{-\beta} + D_2, \tag{4}$$

where D_1 and D_2 are obtained from the thermal boundary conditions as follows:

$$D_1 = \frac{hT_0}{\beta b^{-(\beta+1)} + h(a^{-\beta} - b^{-\beta})}, \quad D_2 = \frac{T_0[\beta b^{-(\beta+1)} - hb^{-\beta}]}{\beta b^{-(\beta+1)} + h(a^{-\beta} - b^{-\beta})}. \tag{5}$$

The temperature distribution thus obtained is illustrated in Figure 2.

3. Basic formulation

In this section, the general differential equation of a rotating hollow cylinder with inhomogeneous material properties is obtained. The material properties are exponentially variable along the radial direction as follows:

$$c_{ij}(r) = c_{ij0} \exp\left(\mu \frac{r-a}{b-a}\right), \quad e_{1i}(r) = e_{1i0} \exp\left(\mu \frac{r-a}{b-a}\right), \quad g_{11}(r) = g_{110} \exp\left(\mu \frac{r-a}{b-a}\right),$$
$$p_{11}(r) = p_{110} \exp\left(\mu \frac{r-a}{b-a}\right), \quad \rho(r) = \rho_0 \exp\left(\mu \frac{r-a}{b-a}\right), \tag{6}$$

where c_{ij} $(i, j = 1, 2)$, e_{1i} $(i = 1, 2)$, g_{11}, p_{11} and $\rho(r)$ are elastic constants, piezoelectric constants, dielectric constant, pyroelectric coefficient and mass density, respectively. The constants c_{ij0}, e_{1i0}, g_{110}, p_{110} and ρ_0 are the material properties of the inner surface, while μ is the material inhomogeneity parameter.

In this study, we can assume the cylinder is long enough to guarantee a plane strain condition.

Thus, for this case all the field variables are the function of radial coordinate r and circumferential displacement u_θ is zero as

$$u_r = u_r(r), \quad u_z = 0, \quad u_\theta = 0, \quad \phi = \phi(r), \tag{7a}$$

where ϕ is the electric potential.

The radial and circumferential strains and the relation between electric field and electric potential are written as

$$\varepsilon_r = \frac{\partial u}{\partial r}, \quad \varepsilon_\theta = \frac{u}{r}, \quad E_r = -\frac{\partial \phi(r)}{\partial r}. \tag{7b}$$

The constitutive relations of stresses and displacement in radially polarized piezoelectric cylinder and the component of radial electric displacement vector are written as (see [Dai et al. 2010])

$$\sigma_r = c_{11}\frac{\partial u}{\partial r} + c_{12}\frac{u}{r} + e_{11}\frac{\partial \phi(r)}{\partial r} - \lambda_1 T(r), \tag{8a}$$

$$\sigma_\theta = c_{12}\frac{\partial u}{\partial r} + c_{22}\frac{u}{r} + e_{12}\frac{\partial \phi(r)}{\partial r} - \lambda_2 T(r), \tag{8b}$$

$$D_r = e_{11}\frac{\partial u}{\partial r} + e_{12}\frac{u}{r} + g_{11}\frac{\partial \phi(r)}{\partial r} + p_{11}T(r), \tag{8c}$$

where σ_r, σ_θ are radial and circumferential stresses, D_r is the radial electric displacement and the thermal modulus λ_1, λ_2 are given by

$$\lambda_1 = c_{11}\alpha_1 + c_{12}\alpha_2, \quad \lambda_2 = c_{12}\alpha_1 + c_{22}\alpha_2. \tag{9}$$

The equation of equilibrium and the charge equation of rotating cylinder are expressed as (see [Tiersten 1969; Fung 1965])

$$\frac{\partial \sigma_r}{\partial r} + \frac{\sigma_r - \sigma_\theta}{r} + \rho r \omega^2 = 0, \tag{10a}$$

$$\frac{\partial D_r}{\partial r} + \frac{D_r}{r} = 0. \tag{10b}$$

4. Solution procedure

By solving the differential equation (10b) the electrical displacement is obtained as

$$D_r(r) = \frac{A_1}{r}, \tag{11}$$

Substituting (11) into (8c) the following equation is obtained for potential gradient as

$$\frac{\partial \phi(r)}{\partial r} = \frac{1}{g_{110}}\left[e_{110}\frac{\partial u}{\partial r} + e_{120}\frac{u}{r} + p_{110}T(r) - \frac{A_1}{r}\exp\left(-\mu\frac{r-a}{b-a}\right)\right], \tag{12}$$

where A_1 is a constant.

Substituting (12) into (8a) and (8b), the radial and hoop stresses can be rewritten as

$$
\sigma_r = e^{\xi(r-a)} \left[w_1 \frac{\partial u}{\partial r} + w_2 \frac{u}{r} + w_3 T(r) \right] - \frac{w_4 A_1}{r},
$$
$$
\sigma_\theta = e^{\xi(r-a)} \left[w_2 \frac{\partial u}{\partial r} + w_5 \frac{u}{r} + w_6 T(r) \right] - \frac{w_7 A_1}{r}.
$$
(13)

Substituting (13) into (10a) the governing differential equation for the problem in terms of radial displacement u and temperature distribution $T(r)$ is derived as

$$
r^2 \frac{\partial^2 u}{\partial r^2} + (1+\xi r) r \frac{\partial u}{\partial r} + \frac{\xi w_2 r - w_5}{w_1} u
$$
$$
= -\frac{\xi w_3 r^2 + r(w_3 - w_6)}{w_1} T(r) - \frac{w_3}{w_1} r^2 \frac{\partial T(r)}{\partial r} - \frac{\rho_0 \omega^2}{w_1} r^3 - \frac{w_7 A_1}{w_1} e^{-\xi(r-a)}, \quad (14)
$$

where

$$
w_1 = c_{110} + \frac{e_{110}^2}{g_{110}}, \quad w_2 = c_{120} + \frac{e_{110} e_{120}}{g_{110}}, \quad w_3 = \frac{e_{110}}{g_{110}} - c_{110}\alpha_{10} - c_{120}\alpha_{20},
$$
$$
w_4 = \frac{e_{110}}{g_{110}}, \quad\quad w_5 = c_{220} + \frac{e_{120}^2}{g_{110}}, \quad w_6 = \frac{e_{120} p_{110}}{g_{110}} - c_{120}\alpha_{10} - c_{220}\alpha_{20},
$$
$$
w_7 = \frac{e_{120}}{g_{110}}, \quad\quad\quad \xi = \frac{\mu}{b-a}.
$$
(15)

Substituting the temperature distribution (4) into (14) yields

$$
r^2 \frac{\partial^2 u}{\partial r^2} + (1+\xi r) r \frac{\partial u}{\partial r} + \frac{\xi w_2 r - w_5}{w_1} u = F(r).
$$
(16)

The inhomogeneous term on the right-hand-side of (16) is denoted by $F(r)$ as follows

$$
F(r) = -D_2 \frac{\xi w_3 r^2 + r(w_3 - w_6)}{w_1} - D_1 \frac{\xi w_3 r + w_3 - w_6 - w_3 \beta}{w_1} r^{1-\beta} - \frac{\sigma_0 \omega^2}{w_1} r^3 - \frac{w_7 A_1}{w_1} e^{-\xi(r-a)}. \quad (17)
$$

The general solution of (16) is assumed to be in the form

$$
u(r) = C_1 P(r) + C_2 Q(r) + R(r),
$$
(18)

where C_1 and C_2 are arbitrary integration constants, $P(r)$ and $Q(r)$ are homogenous solutions, and $R(r)$ is the particular solution.

A particular solution can be developed by employing the variation of parameter method:

$$
R(r) = -P(r) \int_a^r \frac{Q(r) F(r)}{W(r)} \, dr + Q(r) \int_a^r \frac{P(r) F(r)}{W(r)} \, dr.
$$
(19)

where $W(r)$ is the Wronskian of $P(r)$, $Q(r)$, defined by

$$
W(r) = P(r) \frac{dQ}{dr} + Q(r) \frac{dP}{dr}.
$$
(20)

The homogeneous solution of the corresponding differential equation (16) is obtained using Maple as

$$P(r) = \frac{e^{-\xi r/2}\,{}^W\!W\left(\frac{2w_2-w_1}{2w_1},\sqrt{\frac{w_5}{w_1}},\xi r\right)}{\sqrt{r}}, \quad Q(r) = \frac{e^{-\xi r/2}\,{}^W\!M\left(\frac{2w_2-w_1}{2w_1},\sqrt{\frac{w_5}{w_1}},\xi r\right)}{\sqrt{r}}, \quad (21)$$

where the Whittaker functions ${}^W\!M$ and ${}^W\!W$ are defined in the sidebar below (for details see [Abramowitz and Stegun 1965] or [Brischetto and Carrera 2009], for instance). A particular solution is obtained by the method of variation of parameters; defining

$$\Delta = -\left(D_1 r^{1-\beta}\xi w_3 - ((\beta-1)w_3 + w_6)D_1 r^{-\beta} + D_2(1+\xi r)w_3 - w_6 D_2 + \rho_0 r^2 \omega^2\right)e^{\xi r/2},$$

we can write

$$\begin{aligned}
R(r) = \frac{e^{-\xi r/2}}{\sqrt{r}}\Bigg[&{}^W\!M\left(\frac{2w_2-w_1}{2w_1},\sqrt{\frac{w_5}{w_1}},\xi r\right)\int_a^r {}^W\!W\left(\frac{2w_2-w_1}{2w_1},\sqrt{\frac{w_5}{w_1}},\xi r\right)\sqrt{r}\,\Delta\,\frac{dr}{W(r)} \\
&- {}^W\!W\left(\frac{2w_2-w_1}{2w_1},\sqrt{\frac{w_5}{w_1}},\xi r\right)\int_a^r {}^W\!M\left(\frac{2w_2-w_1}{2w_1},\sqrt{\frac{w_5}{w_1}},\xi r\right)\sqrt{r}\,\Delta\,\frac{dr}{W(r)} \\
&+ w_7 A_1\,{}^W\!M\left(\frac{2w_2-w_1}{2w_1},\sqrt{\frac{w_5}{w_1}},\xi r\right)\int_a^r {}^W\!W\left(\frac{2w_2-w_1}{2w_1},\sqrt{\frac{w_5}{w_1}},\xi r\right)\frac{e^{\xi(a-r/2)}}{\sqrt{r}\,W(r)}\,dr \\
&- w_7 A_1\,{}^W\!W\left(\frac{2w_2-w_1}{2w_1},\sqrt{\frac{w_5}{w_1}},\xi r\right)\int_a^r {}^W\!M\left(\frac{2w_2-w_1}{2w_1},\sqrt{\frac{w_5}{w_1}},\xi r\right)\frac{e^{\xi(a-r/2)}}{\sqrt{r}\,W(r)}\,dr\Bigg].
\end{aligned}$$

Substituting (18) into (12) and integrating, the electric potential $\phi(r)$ is obtained:

$$\phi(r) = \frac{1}{g_{110}}\left[e_{110}u(r) + e_{120}\int_a^r \frac{u(r)}{r} + p_{110}T(r) - \int_a^r \frac{A_1}{r}\exp\left(-\mu\frac{r-a}{b-a}\right)\right] + A_2. \quad (22)$$

The Whittaker functions ${}^W\!M$ and ${}^W\!W$ are defined by

$$\begin{aligned}
{}^W\!M(k,u,z) &= e^{-z/2}z^{u+\frac{1}{2}}\,{}^K\!M\left(u-k+\tfrac{1}{2},1+2y;z\right), \\
{}^W\!W(k,u,z) &= e^{-z/2}z^{u+\frac{1}{2}}\,{}^K\!U\left(u-k+\tfrac{1}{2},1+2y;z\right),
\end{aligned} \quad (23)$$

where ${}^K\!M$ and ${}^K\!U$, known as Kummer functions, are certain generalized hypergeometric series. With the notation $(\alpha)_n = \alpha(\alpha+1)(\alpha+2)\cdots(\alpha+n-1)$, we have

$$\begin{aligned}
{}^K\!M(\alpha,\beta,z) &= \sum_{n=0}^{\infty} \frac{(\alpha)_n z^n}{(\beta)_n n!}, \\
{}^K\!U(\alpha,\beta,z) &= \frac{\Gamma(1-\beta)}{\Gamma(\alpha-\beta+1)}\,{}^K\!M(\alpha,\beta,z) + \frac{\Gamma(\beta-1)}{\Gamma(\alpha)}z^{1-\beta}\,{}^K\!M(\alpha-\beta+1,2-\beta,z),
\end{aligned} \quad (24)$$

where Γ denotes the usual gamma function.

Substituting the general solution (18) into (13), the radial and circumferential stresses are obtained as

$$\sigma_r(r) = e^{\xi(r-a)}\left[w_1\frac{\partial u(r)}{\partial r} + w_2\frac{u(r)}{r} + w_3T(r)\right] - \frac{w_4A_1}{r},$$
(25)

$$\sigma_\theta(r) = e^{\xi(r-a)}\left[w_2\frac{\partial u(r)}{\partial r} + w_5\frac{u(r)}{r} + w_6T(r)\right] - \frac{w_7A_1}{r},$$
(26)

where σ_r, σ_θ and ϕ are radial stress, hoop stress and electric potential, respectively.

Four unknown constants A_1, C_1, C_2 and A_2 are determined by the boundary conditions as

$$\sigma_r(a) = -P_a, \quad \sigma_r(b) = -P_b, \qquad \phi(a) = \phi_a, \quad \phi(b) = \phi_b.$$
(27)

5. Numerical results and discussion

In this section, numerical results are presented graphically for Electric displacement, electrothermoelastic stresses and electric potential of the EGPM rotating hollow cylinder in four cases of boundary conditions as follows:

$$\text{Case 1:} \quad \sigma_r(a) = -P_a, \quad \sigma_r(b) = 0, \qquad \phi(a) = 0, \qquad \phi(b) = 0.$$
(28)

$$\text{Case 2:} \quad \sigma_r(a) = 0, \qquad \sigma_r(b) = 0, \qquad \phi(a) = \phi_a, \quad \phi(b) = 0.$$
(29)

$$\text{Case 3:} \quad \sigma_r(a) = 0, \qquad \sigma_r(b) = -P_b, \quad \phi(a) = 0, \qquad \phi(b) = 0.$$
(30)

$$\text{Case 4:} \quad \sigma_r(a) = -P_a, \quad \sigma_r(b) = -P_b, \quad \phi(a) = \phi_a, \quad \phi(b) = 0.$$
(31)

The cylinders are assumed to be made of PZT_4, whose properties are listed in the Table 1.

For all cases, the following data for geometry, material properties, boundary and loading conditions are considered: $a = 0.1$ m, $b = 0.2$ m, $\omega = 400\ rad/s$, $P_a = 3 \cdot 10^7$ (Pa), $\phi_a = 1000$ (W/A), $T_0 = 20°C$, $\beta = 1$, $\mu = -2, -1, 0, 1, 2$.

The results are reported based on the normalized variables

$$\zeta = \frac{r-a}{b-a}, \quad \sigma_i^* = \frac{\sigma_i}{P_a}\ (i = r, \theta), \quad U^* = \frac{u(r)}{a}, \quad \Phi^* = \frac{\phi}{\phi_a}, \quad T^* = \frac{T(r)}{T_0}.$$
(32)

Case 1. In Figure 3 results are shown for case 1, where internal pressure is applied. Figure 3, top left, depicts the distribution of radial stress along the radius for different values of μ. It is seen from the figure that the radial stresses satisfy the mechanical boundary conditions. The distributions of the hoop stresses for different values of μ are displayed in Figure 3, top right. In this figures we can easily observe a reference stress point at $\zeta = 0.2$ in which the hoop stress is identical for all material properties except

c_{110}	139 GPa	g_{110}	$6.46 \cdot 10^{-9}$ C^2/Nm^2
c_{120}	74 GPa	p_{110}	$-2.5 \cdot 10^{-5}$ C/m^{2}K
c_{220}	115 GPa	α_{10}	$7.41 \cdot 10^{-6}$ 1/K
e_{110}	15.1 C/m^2	α_{20}	$2.11 \cdot 10^{-6}$ 1/K
e_{120}	-5.2 C/m^2	ρ_0	7500 kg/m^3

Table 1. Mechanical and electrical properties for PZT_4.
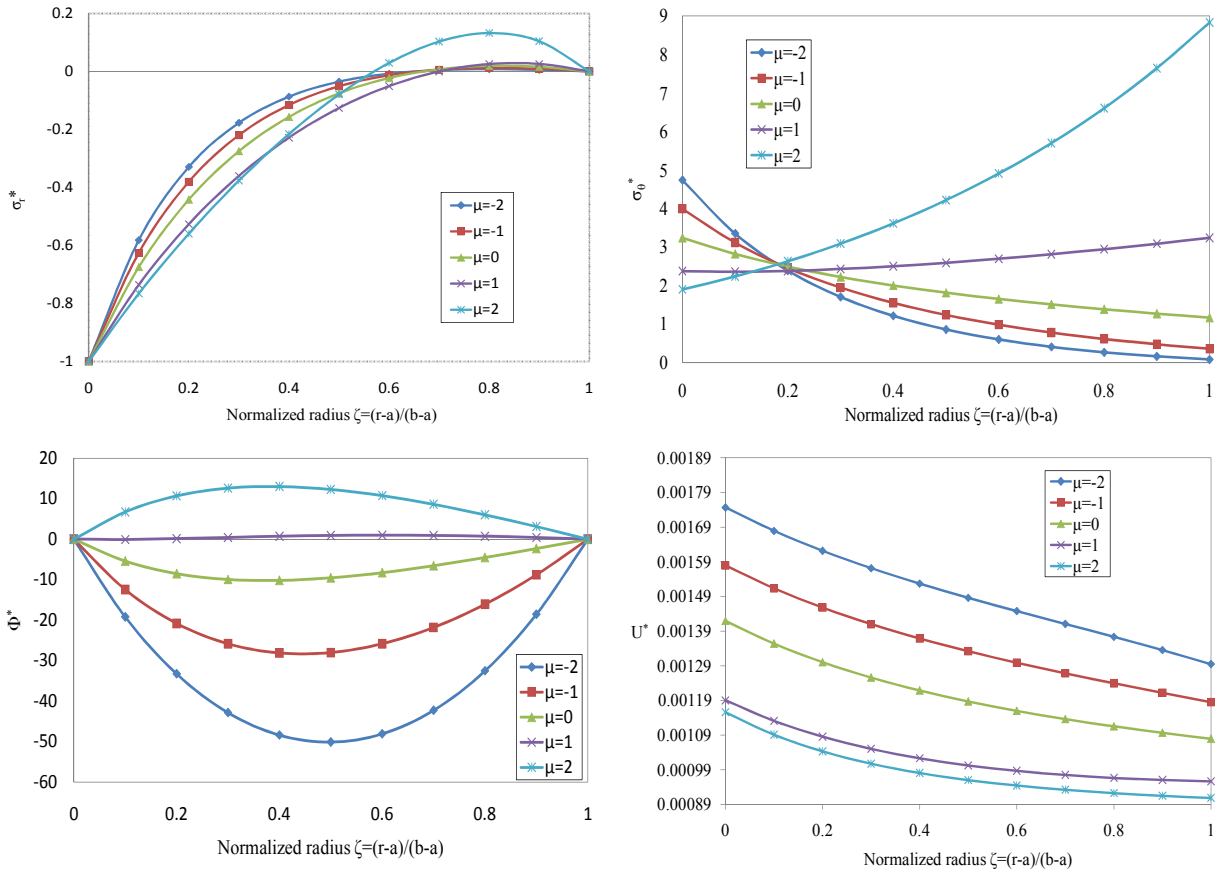
Figure 3. Case 1: Distribution of (normalized) radial stress σ_r^*, circumferential stress σ_θ^*, electric potential Φ^*, and radial displacement U^* for different values of μ.

for $\mu = 1$. Furthermore, this figure shows that the hoop stresses are increasing at the outer surface and decreasing at the inner surface with increasing the material inhomogeneity exponent μ.

Although for the first case no electric potential is imposed however an induced electric potential distribution satisfying the zero potential boundary condition is obtained in which the minimum potential distribution belongs to the material identified by $\mu = -2$ and the maximum distribution belongs to $\mu = 2$. It is concluded from Figure 3, bottom left, that the material inhomogeneity exponent μ significantly affects the induced electric potential.

The radial displacement distributions for different values of the inhomogeneity material μ are demonstrated in Figure 3, bottom right. It is seen from this figure that the radial displacement decreases with increasing μ and its maximum value is located at the inner radius of the cylinder.

Case 2. Figures 4 show the results of case 2, in which purely electric potential is imposed. The tensile radial and hoop stresses are induced in the thickness of the cylinder. The top two graphs of Figure 4 show that the material inhomogeneity exponent significantly affect the induced stresses throughout the thickness. Radial induced stresses satisfy the free-free boundary conditions of the cylinder. Radial and
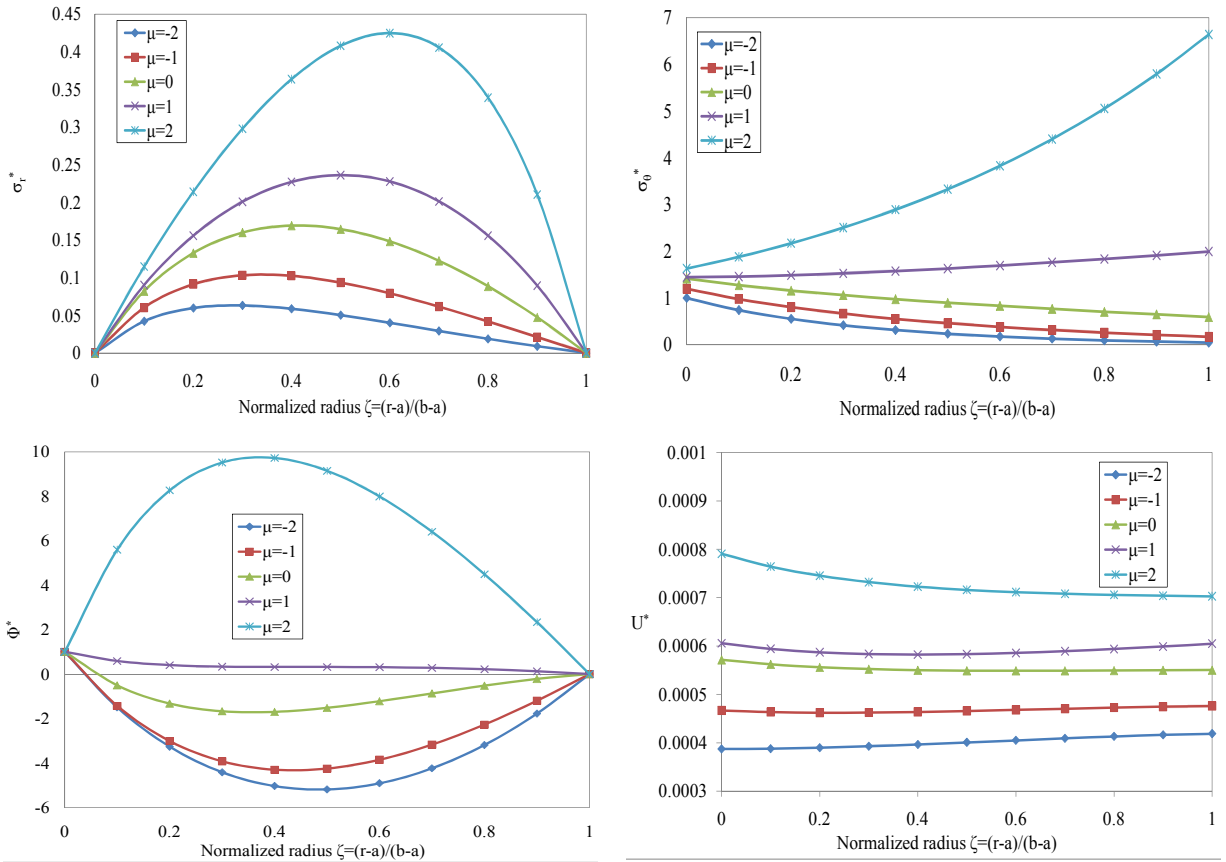
Figure 4. Case 2: Distribution of (normalized) radial stress σ_r^*, circumferential stress σ_θ^*, electric potential Φ^*, and radial displacement U^* for different values of μ.

hoop induced stresses increase when the exponent μ rises. It is clear from Figure 4, top right, that for nonpositive values of the index μ, the hoop stresses are decreased and for positive values of the index μ, the hoop stresses are increased throughout the thickness.

The electric potential distributions satisfy the boundary conditions of this case is shown in Figure 4, bottom left. The electric potential distribution is significantly affected by the material exponent μ so that for positive values of μ is positive throughout the thickness and for negative values of μ is almost negative throughout the thickness. The minimum electric potential belongs to material identified by $\mu = -2$ and the maximum electric potential belongs to $\mu = 2$.

Variation of displacement along radius is shown in Figure 4, bottom right. It is almost a uniform distribution throughout the thickness however its value is affected by the material exponent μ so that as μ increases displacement also increases.

Case 3. In case 3 (Figure 5), the EGPM rotating hollow cylinder is subjected to an external uniform pressure, zero electric potential difference between the inner and outer surfaces and free mechanical boundary condition at the inner surface. The compressive radial stresses for different values of μ are
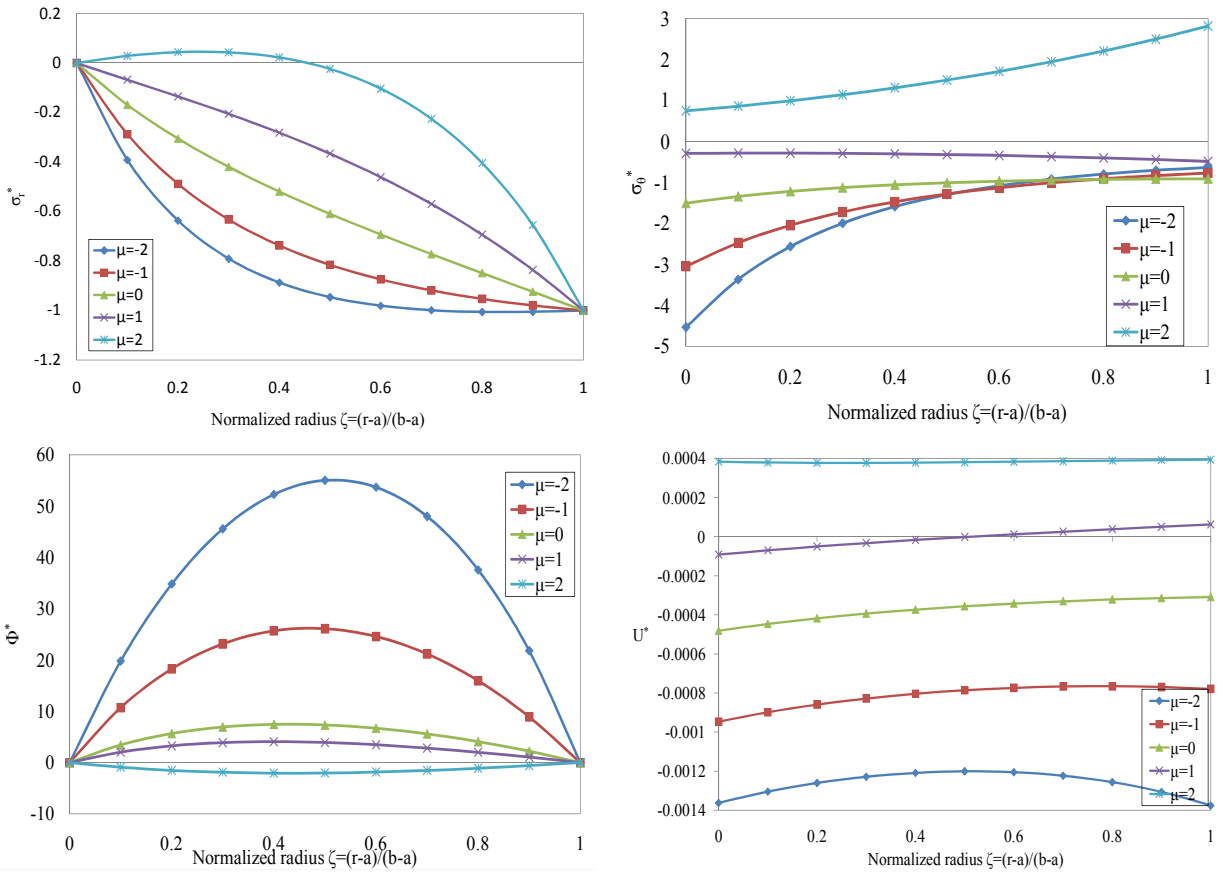
Figure 5. Case 3: Distribution of (normalized) radial stress σ_r^*, circumferential stress σ_θ^*, electric potential Φ^*, and radial displacement U^* for different values of μ.

shown in Figure 5, top left. It is clear that the radial stresses satisfy the boundary conditions. The material inhomogeneity exponent μ significantly affects the radial stresses throughout the thickness. It is also obvious from this figure that the radial stress increases with increasing exponent μ. The hoop stresses are illustrated in Figure 5, top right. Hoop stresses are increasing by increasing the exponent μ. However except for the exponent $\mu = 2$ the hoop stresses approaches almost the same value at the outer surface of the cylinder.

Although for this case no electric potential is imposed however an electric potential distribution satisfying the zero potential boundary condition is induced in which the minimum potential distribution belongs to the material identified by $\mu = 2$ and the maximum distribution belongs to $\mu = -2$. It is concluded from Figure 5, bottom left, that the material inhomogeneity exponent μ significantly affects the induced electric potential. Comparing the induced electric potential in this case with the case in which the cylinder is subjected to an internal pressure a fully reverse potential distribution can be identified.

Variation of displacement along radius is shown in Figure 5, bottom right. It is almost a uniform distribution throughout the thickness however its absolute value is affected by the material exponent μ so that as μ increases the absolute value of displacement decreases.
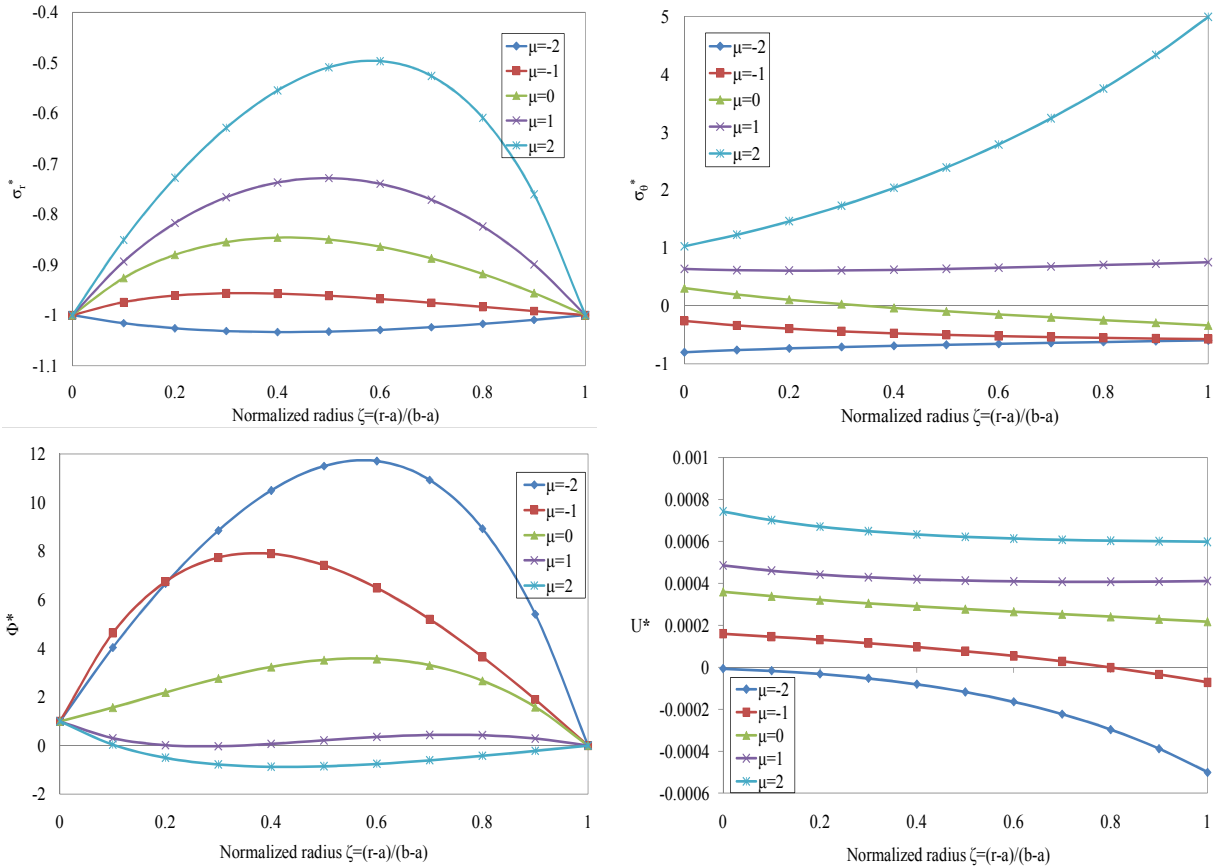
Figure 6. Case 4: Distribution of (normalized) radial stress σ_r^*, circumferential stress σ_θ^*, electric potential Φ^*, and radial displacement U^* for different values of μ.

Case 4. In case 4 (Figure 6) superposition of cases 1, 2 and 3 is investigated. Distribution of radial and hoop stresses along the radius for different values of exponent μ are shown in the top two graphs fo Figure 6. It is obvious from these figures that the inhomogeneity parameter μ has a major effect on the electrothermoelastic stresses. Electric potential and radial displacement distributions in the bottom two graphs of Figure 6 are indeed superposition of previous cases 1, 2 and 3.

6. Conclusions

Using the hypergeometric function, closed form solution for EGPM rotating hollow cylinder, is presented with four different sets of boundary conditions. The analytical solution of homogeneous piezoelectric rotating hollow cylinder is fully covered by setting the material inhomogeneity $\mu = 0$, our results for the homogeneous PZT_4 hollow cylinder are almost the same as those in [Galic and Horgan 2003]. The correctness of the present solution is then verified in this respect.

It is concluded from the present result that the inhomogeneity exponent μ significantly affects the radial and hoop stress distributions. This implies that the electrothermomechanical fields in EGP cylindrical

structures can be optimized for specific applications by selecting a suitable inhomogeneity parameter. Moreover, the inhomogeneous constants presented in the present study are useful parameters from a design point of view in that they can be tailored for special applications to control the distributions of electrothermoelastic stresses.

The technological implications of this study are significant, e.g., the amount of hoop stress resulting from thermomechanical loads in an EGPM rotating hollow cylinder can be reduced or neutralized by a suitably applied electric potential field and material inhomogeneity. Henceforward, our results can help engineers to design a rotating piezoelectric pressure vessel made of EGPM with an optimum distribution of stresses.

List of symbols

a, b	Inner and outer radius [m]	C_{ij} $(i, j = 1, 2)$	Elastic constant [N/m^2]
r	Radial variable [m]	e_{1i} $(i = 1, 2)$	Piezoelectric coefficient [C/m^2]
u_r	Radial displacement [m]	g_{11}	Dielectric constant [C^2/Nm^2]
β, μ	Inhomogeneity parameters	p_{11}	Pyroelectric coefficient [C/m^{2}K]
σ_θ, σ_r	Components of stresses [N/m^2]	φ	Electric potential [W/A]
α_1, α_2	Thermal expansion coefficients [1/K]	D_r	Radial electric displacement [C/m^2]
λ_1, λ_2	Thermal modulus [N/m^{2}K]	ω	Angular velocity [rad/s]
$T(r)$	Temperature distribution [K]	ρ	Mass density [kg/m^3]
h	Ratio of the convective heat-transfer coefficient [W/K]		
k	Thermal conduction coefficient [W/mK]		

Nondimensional quantities:

$$T^* = \frac{T(r)}{T_0}, \quad \zeta = \frac{r - a}{b - a}, \quad \sigma_i^* = \frac{\sigma_i}{P_a}(i = r, \theta), \quad U^* = \frac{u(r)}{a}, \quad \Phi^* = \frac{\phi}{\phi_a}$$

Acknowledgment

References

[Abramowitz and Stegun 1965] M. Abramowitz and I. A. Stegun (editors), *Handbook of Mathematical Functions*, Dover, New York, 1965.

[Babaei and Chen 2008] M. Babaei and Z. Chen, "Analytical solution for the electromechanical behavior of a rotating functionally graded piezoelectric hollow shaft", *Arch. Appl. Mech.* **78** (2008), 489–500.

[Brischetto and Carrera 2009] S. Brischetto and E. Carrera, "Refined 2D models for the analysis of functionally graded piezoelectric plates", *J. Intelligent Mater. Syst. Struct.* **20**:15 (2009), 1783–1797.

[Chen and Shi 2005] Y. Chen and Z.-f. Shi, "Analysis of a functionally graded piezothermoelastic hollow cylinder", *J. Zhejiang Univ. Sci. A* **6** (2005), 956–961.

[Dai et al. 2010] H.-L. Dai, L. Hong, Y.-M. Fu, and X. Xiao, "Analytical solution for electromagnetothermoelastic behaviors of a functionally graded piezoelectric hollow cylinder", *Appl. Math. Model.* **34**:2 (2010), 343 – 357.

[Fung 1965] Y. C. Fung, *Foundations of solid mechanics*, Prentice-Hall, New York, 1965.

[Galic and Horgan 2002] D. Galic and C. Horgan, "Internally pressurized radially polarized piezoelectric cylinders", *J. Elasticity* **66** (2002), 257–272.

[Galic and Horgan 2003] D. Galic and C. O. Horgan, "The Stress Response of Radially Polarized Rotating Piezoelectric Cylinders", *J. Appl. Mech. (ASME)* **70**:3 (2003), 426–435.

[Ghorbanpour et al. 2006] A. Ghorbanpour, S. Golabi, and M. Saadatfar, "Stress and electric potential fields in piezoelectric smart spheres", *J. Mech. Sci. Tech. (Korea)* **20** (2006), 1920–1933.

[Hosseini et al. 2007] S. Hosseini, M. Akhlaghi, and M. Shakeri, "Transient heat conduction in functionally graded thick hollow cylinders by analytical method", *Heat and Mass Transfer* **43** (2007), 669–675.

[Khoshgoftar et al. 2009] M. J. Khoshgoftar, A. G. Arani, and M. Arefi, "Thermoelastic analysis of a thick walled cylinder made of functionally graded piezoelectric material", *Smart Mater. Struct.* **18**:11 (2009), 115007.

[Li et al. 2010] X.-F. Li, X.-L. Peng, and K. Y. Lee, "Radially polarized functionally graded piezoelectric hollow cylinders as sensors and actuators", *Eur. J. Mech. A Solids* **29**:4 (2010), 704 – 713.

[Lu et al. 2005] P. Lu, H. Lee, and C. Lu, "An exact solution for functionally graded piezoelectric laminates in cylindrical bending", *Int. J. Mech. Sci.* **47**:3 (2005), 437 – 458.

[Lu et al. 2006] P. Lu, H. Lee, and C. Lu, "Exact solutions for simply supported functionally graded piezoelectric laminates by Stroh-like formalism", *Compos. Struct.* **72**:3 (2006), 352 – 363.

[Pan and Han 2005] E. Pan and F. Han, "Exact solution for functionally graded and layered magneto-electro-elastic plates", *Int. J. Eng. Sci.* **43**:3-4 (2005), 321 – 339.

[Saadatfar and Razavi 2009] M. Saadatfar and A. Razavi, "Piezoelectric hollow cylinder with thermal gradient", *J. Mech. Sci. Tech. (Korea)* **23** (2009), 45–53.

[Tiersten 1969] H. F. Tiersten, *Linear piezoelectric plate vibrations*, Plenum Press, New York, 1969.

[Zhong and Shang 2003] Z. Zhong and E. T. Shang, "Three-dimensional exact analysis of a simply supported functionally gradient piezoelectric plate", *Int. J. Solids Struct.* **40**:20 (2003), 5335 – 5352.

ALI GHORBANPOUR ARANI: aghorban@kashanu.ac.ir
Mechanical Engineering Department, University of Kashan, Kilometre 6 Bolvar Ghotb Ravandi, POBox 87317-51167, Kashan, Iran

ABBAS LOGHMAN: aloghman@kashanu.ac.ir
Mechanical Engineering Department, University of Kashan, Kilometre 6 Bolvar Ghotb Ravandi, POBox 87317-51167, Kashan, Iran

ALI ABDOLLAHITAHERI: abdollahitaheri@grad.kashanu.ac.ir
Mechanical Engineering Department, University of Kashan, Kilometre 6 Bolvar Ghotb Ravandi, POBox 87317-51167, Kashan, Iran

VAHID ATABAKHSHIAN: v.atabakhshian@gmail.com
Mechanical Engineering Department, University of Kashan, Kilometre 6 Bolvar Ghotb Ravandi, POBox 87317-51167, Kashan, Iran

msp

LARGE-AMPLITUDE DYNAMIC ANALYSIS OF STIFFENED PLATES WITH FREE EDGES

ANIRBAN MITRA, PRASANTA SAHOO AND KASHINATH SAHA

Large-amplitude free-vibration analysis of stiffened plates subjected to uniformly distributed transverse loading with free flexural boundary conditions is presented. The free edge is taken with different combinations of clamped and simply supported end conditions for three types of stiffened plates classified according to number and orientation of stiffeners. The computational domain is divided into an adequate number of subdomains based on the number, orientation, and location of stiffeners to generate the appropriate grid of computation points. Nonlinear strain displacement relations are considered in the formulation but the effects of shear deformation have been neglected. The analysis involves two steps. First the static displacement field of the system is solved for. The second step takes up the free-vibration analysis on the basis of the known static displacement field. The mathematical formulation of the static problem is based on the principle of minimum potential energy, whereas Hamilton's principle has been applied for the dynamic analysis. The results are validated with the published results of other researchers. The dynamic behavior is presented in the form of backbone curves in a dimensionless frequency-amplitude plane. Three-dimensional mode shape plots are also presented along with contour plots in a few specific cases.

A list of symbols can be found on page 911.

1. Introduction

In marine construction and aerospace structures stiffened plates are extensively used due to their enhanced stiffness and stability characteristics. They also have widespread application in many branches of modern civil, mechanical, and structural engineering. Hence, investigation of the dynamic behavior of stiffened plates has always been an area of immense interest to researchers. Research work on the dynamic characteristics of stiffened plates has a long history as different researchers have employed different methodologies to perform dynamic analysis of such structures. The comprehensive review [Mukherjee and Mukhopadhyay 1986] documents different numerical and analytical tools used in earlier years to study the dynamic behavior of stiffened plates.

Aksu and Ali [1976] developed a variational technique in conjunction with finite difference formulation to obtain natural frequencies and mode shapes of eccentrically stiffened rectangular plates having a single stiffener. Their formulation considered in-plane displacements and inertia in the direction of the stiffener and the total energy of the system was minimized with respect to discretized displacement components. This free-vibration analysis was later extended to cross-stiffened plates thus taking into account

in-plane inertia effects for two directions in [Aksu 1982]. In [Prathap and Varadan 1978] large-amplitude, free flexural vibrations of simply supported and clamped thin elastic orthotropic stiffened plates with immovable and movable in-plane edges were studied. The governing dynamic equations were derived in terms of nondimensional parameters and solved on the basis of a single-term vibration mode shape by making use of Galerkin's method. Varadan and Pandalai [1979] obtained modal equations for nonlinear free vibration of eccentrically stiffened elastic rectangular plates through Lagrange's equation and an approximate analytical solution based on one-term transverse displacement was determined. They analyzed plates having clamped boundary conditions with movable in-plane edges and observed hardening-type nonlinearity.

Mukherjee and Mukhopadhyay [1988] performed free-vibration analysis of eccentrically stiffened plates using an isoparametric quadratic stiffened plate bending element. They included the effect of shear deformation in the formulation and studied the effects of eccentricity, shape, and torsional stiffness on the natural frequencies and mode shapes of the system. In [Koko and Olson 1992] free-vibration analysis of rectangular plates with discrete stiffeners was carried out utilizing the superelements and including the effects of bending and in-plane effects as well as beam torsion and lateral bending motion. In [Rao et al. 1993b] a large-amplitude free flexural vibration study of eccentrically stiffened plates incorporating in-plane and shear deformation effects was presented. Harik and Guo [1993] introduced a compound finite element model based on small deflection and thin plate theory to examine eccentrically stiffened plates in free vibration. Their formulation considered membrane forces for the plate and axial forces in the stiffener. In [Chen et al. 1994] a spline compound strip method was proposed, where the plate was discretized in only one direction, for analyzing the free-vibration problem of stiffened plates. Bedair and Troitsky [1997] analyzed eccentrically and concentrically stiffened simply supported plates on the basis of energy formulation and mathematical programming techniques and studied the effect of variation in plate and stiffener geometric parameters on the fundamental frequency of the system.

Although substantial research has been carried out in the field of vibrations of stiffened plates, interest in this field has not diminished. Vibration analysis of stiffened plates using hierarchical finite elements with a set of local trigonometric interpolation functions was presented in [Barrette et al. 2000]. In [Zeng and Bert 2001] a differential quadrature analysis of the free vibration of eccentrically stiffened plates having simply supported or clamped boundaries at all edges was implemented. In [Peng et al. 2006] free vibration and stability analysis of stiffened plates via the first-order shear deformable theory and mesh-free Galerkin method was performed. Sapountzakis and Mokos [2008] developed an improved model and obtained eigenfrequencies as a general solution for dynamic analysis of plates stiffened by arbitrarily positioned parallel beams. In [Dozio and Ricciardi 2009] a computationally efficient combined analytical-numerical method was presented for low-frequency free-vibration analysis of thin rectangular plates stiffened by a small number of light stiffeners.

A general method taking into account the nonuniform torsional response of the stiffener for free vibration of plates and shells stiffened by beams of arbitrary cross-section was introduced in [Vörös 2009]. In [Xu et al. 2010] an analytical method was put forward for the vibration analysis of plates stiffened by any number of beams of arbitrary lengths and placement angles considering coupling at an interface of plate and beam. In [Deb Nath et al. 2010] an analytical solution of elastic fields for a stiffened plate subjected to axial tension and pure bending was obtained using an alternative displacement potential approach.

The majority of the dynamic studies are confined to stiffened plates with simply supported or clamped boundaries; only in few cases are a combination of simply supported and clamped-end conditions considered. Works on stiffened plates having free boundaries are also limited. In [Bapu Rao et al. 1978] an experimental study was carried out to determine the resonant frequencies and mode shapes of rib-stiffened skew cantilever plates by holographic interferometry. In [Irie et al. 1982] a stiffened trapezoidal cantilever plate with a clamped end and three free boundaries was analyzed and the natural frequencies and mode shapes were numerically calculated. However, some works considering unstiffened plates with free edges are available in literature. In [Rossi et al. 1998] small-amplitude transverse vibration of a rectangular orthotropic plate with a free edge and a concentrated mass was considered. In [Shuyu 2001] an analytical method was presented to predict the natural frequency of flexural vibration of rectangular thin plates with free boundary conditions. In [Wang and Xu 2010] discrete singular convolution was utilized to determine nondimensional frequency parameters for clamped (CCCC), clamped with one free edge (CFCC), and free (FFFF) rectangular plates.

A review of the existing literature reveals that studies are primarily focused on free-vibration analysis of stiffened plates with simply supported, clamped, and a combination of both boundary conditions, whereas studies on stiffened plates with free edges are limited. It is also noted that the emphasis is mainly on developing different methodologies to obtain the natural frequencies compared to studying the variations in the dynamic behavior corresponding to changes in system geometry and boundary conditions. Works on large-amplitude dynamic behavior, specifically the effect of loaded vibration amplitude on the natural frequency of stiffened plates, are also rare. We investigate large-amplitude dynamic behavior of stiffened plates for various boundary conditions including a single free edge. It also looks into the effect of vibration amplitude on loaded natural frequency. The results for large-amplitude behavior are presented in terms of backbone curves in the dimensionless amplitude-frequency plane. These results have been documented for the first six vibration modes of stiffened plates under uniformly distributed transverse loading. Vibration mode shapes are also provided corresponding to the minimum and maximum amplitudes of vibration. Unlike in finite element analysis (FEA), where the physical domain is discretized into smaller finite elements, the present semianalytical formulation is associated with the whole domain, that is, the assumed displacement field is a function of the whole physical domain. As a result, the number of algebraic equations to be solved is substantially reduced compared to FEA.

2. Mathematical formulation

A thin rectangular plate ($a \times b \times t_p$) orthogonally stiffened by eccentric stiffeners parallel to the edges of the plate is shown in Figure 1, which also depicts the significant dimensions of the system and the coordinate system for the present analysis. It is assumed that the stiffeners are rigidly attached to the plate such that no relative motion can take place and no field discontinuity can occur between the two. Although the figure shows only one stiffener along each of the coordinate directions, the mathematical formulation is carried out for multiple stiffeners having generalized location in both directions. The number of stiffeners in the x and y-directions are represented by ns_x and ns_y, respectively, and the location of the q-th stiffener along the y-direction and the p-th stiffener along the x-direction are denoted by x_{stf}^q and y_{stf}^p. The eccentricity (e_x^p, e_y^q) of the stiffeners is quantified by the perpendicular distance between the centroid (CG) of the stiffener cross-section and the midplane of the plate. Only rectangular stiffener
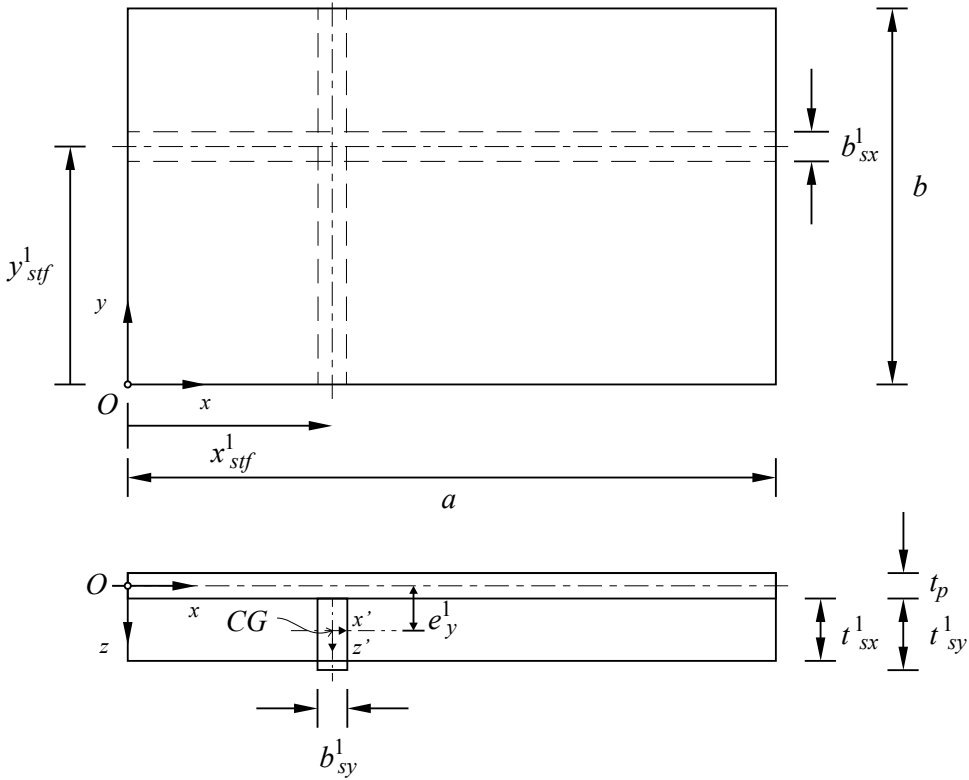
Figure 1. Stiffened plate with significant dimensions and coordinate system.

cross-sections are considered: $(b_{sx}^p \times t_{sx}^p)$ for the p-th stiffener parallel to the x-axis and $(b_{sy}^q \times t_{sy}^q)$ for the q-th stiffener along the y-axis. The mathematical formulation is further based on the assumptions that the plate and stiffener materials are isotropic, homogeneous, and linearly elastic and the plate thickness (t_p) is small enough compared to its lateral dimensions (a and b) so that the effects of shear deformation and rotary inertia can be ignored.

The physical domain in the x-y coordinate system as shown in Figure 1 is converted to the computational domain by normalizing the midplane coordinates as $\xi = x/a$ and $\eta = y/b$. In this ξ-η computational plane, Gauss points are generated along the two orthogonal coordinate directions and constant ξ and constant η lines are drawn through the generated Gauss points. Intersections of these constant ξ and constant η lines provide a grid of reference points for computations. However, a stiffener can be placed at any location inside the domain and as the locations of the Gauss points are fixed, there may not be a sufficient number of computation points around a stiffener. Hence, depending on the number, orientation, and location of the stiffeners the domain is decomposed into subdomains, which have their own Gauss points spaced in the same ratio as the original domain. This technique helps to have an adequate number of computation points around the location of stiffeners and boundaries of the plate so that the displacement field can be captured accurately. Such decomposed domains with modified grids corresponding to different types of plates having different stiffener orientations and positions are shown in Figure 2.
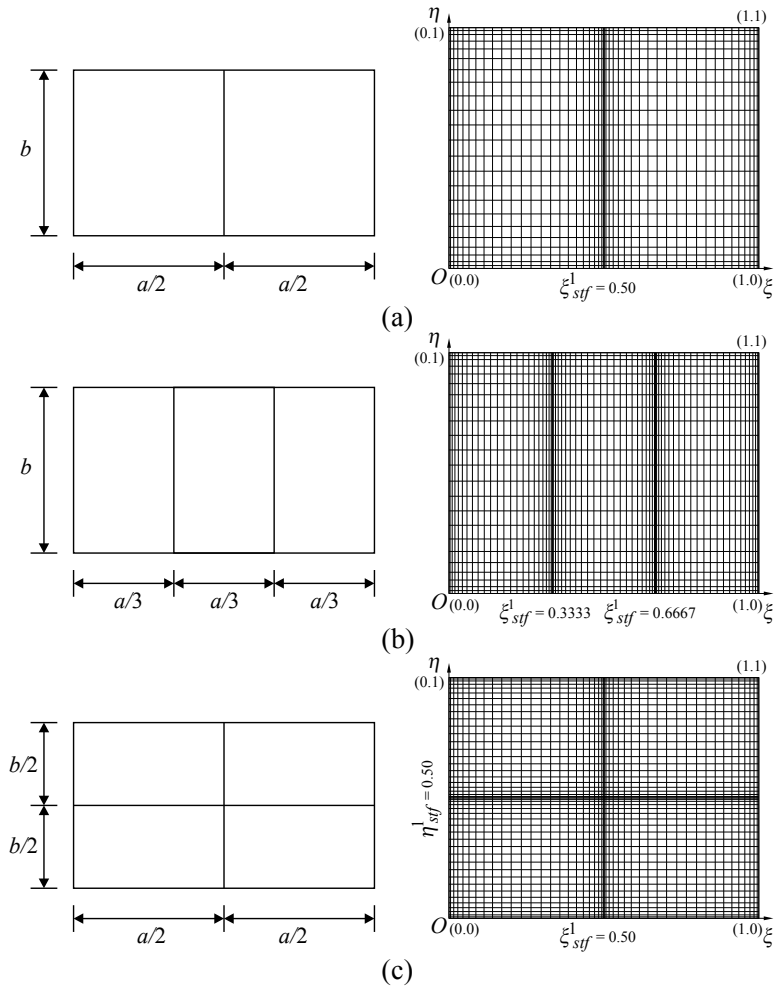
Figure 2. Decomposed computational domain along with schematic representations for (a) uniaxially single stiffened (UASS), (b) uniaxially double stiffened (UADS), and (c) biaxially cross stiffened (BACS) plates.

In nonlinear vibration, frequency is a function of the vibration amplitude and the nature of the deflected profile [Bikri et al. 2003; Das et al. 2009]; moreover, the amplitude of vibration at a point within a vibrating continuous system depends on the location. In studying the effect of vibration amplitude on the dynamic behavior of stiffened plates, the maximum amplitude of vibration is taken as representative of the amplitude. The deflection profile of a system is dependent on the boundary conditions of the system and the nature of loading to which it is subjected. Different boundary conditions may arise from the different combinations of clamped, simply supported, and free end conditions of a plate. However, the present paper only deals with combinations of simply supported and clamped boundary conditions with a single free edge, under transverse uniformly distributed loading (UDL).

Large-amplitude free-vibration analysis of a nonlinear system is essentially the same as free-vibration analysis of the system subjected to a static load producing such large-amplitude deflection [Crandall

1956]. Here, the system is assumed to execute small-amplitude vibration about the statically deflected equilibrium configuration as opposed to large-amplitude vibration about its undeformed equilibrium position. Hence, the present large-amplitude free-vibration analysis of stiffened plates is performed in two steps. First, large displacement is statically imposed by applying uniform transverse loading on the stiffened plate and then the free-vibration analysis is performed as an eigenvalue problem to identify the loaded natural frequency. The static analysis yields the initial deflection profile, which is used in the subsequent free-vibration analysis. As the dynamic problem is solved on the basis of the solution of the static displacement field, the effect of a statically imposed large amplitude of vibration is incorporated into the dynamic system. The mathematical formulation for both the static and dynamic problems is based on the variational form of the energy principle. Nonlinear strain displacement relations are considered in order to incorporate geometric nonlinearity in the system.

2.1. *Static analysis.* The principle of minimum potential energy [Reddy 2002] can be mathematically expressed as

$$\delta(U + V) = 0. \tag{1}$$

Here, V is the work function or potential of the external forces and U is the total strain energy stored in the system. For a stiffened plate under an externally applied uniformly distributed load of intensity p, the total potential energy is given by

$$V = -(ab) \int_0^1 \int_0^1 (pw)\, d\xi\, d\eta. \tag{2}$$

The total strain energy (U) of the system consists of two components, namely the strain energy of the plate (U_p) and the total strain energy stored in all the stiffeners (U_s). In the case of large-displacement analysis of plates, both bending and stretching effects are taken into consideration. So, the strain energy of the plate (U_p) also consists of two parts: strain energy due to pure bending (U_b) and strain energy due to stretching (U_m) of its midplane. The expressions of U_b and U_m are well-known for rectangular plates [Saha et al. 2004] and are indicated here for ready reference:

$$U_b = \frac{D}{2}(ab) \int_0^1 \int_0^1 \left[\left\{ \frac{1}{a^2}(w,_{\xi\xi}) + \frac{1}{b^2}(w,_{\eta\eta}) \right\}^2 + 2(1-v)\frac{1}{a^2 b^2}\{(w,_{\xi\eta})^2 - (w,_{\xi\xi})(w,_{\eta\eta})\} \right] d\xi\, d\eta,$$

$$U_m = \frac{E_p t_p}{2(1-v^2)}(ab) \int_0^1 \int_0^1 \left[\frac{1}{a^2}(u,_{\xi})^2 + \frac{1}{a^3}(u,_{\xi})(w,_{\xi})^2 + \frac{1}{b^2}(v,_{\eta})^2 + \frac{1}{b^3}(v,_{\eta})(w,_{\eta})^2 \right.$$
$$+ \frac{1}{4}\left\{ \frac{1}{a^2}(w,_{\xi})^2 + \frac{1}{b^2}(w,_{\eta})^2 \right\}^2 + 2v\left\{ \frac{1}{ab}(u,_{\xi})(v,_{\eta}) + \frac{1}{2a^2 b}(v,_{\eta})(w,_{\xi})^2 + \frac{1}{2ab^2}(u,_{\xi})(w,_{\eta})^2 \right\} \tag{3}$$
$$\left. + \frac{1-v}{2}\left\{ \frac{1}{b^2}(u,_{\eta})^2 + \frac{2}{ab}(u,_{\eta})(v,_{\xi}) + \frac{1}{a^2}(v,_{\xi})^2 + \frac{2}{ab^2}(u,_{\eta})(w,_{\xi})(w,_{\eta}) + \frac{2}{a^2 b}(v,_{\xi})(w,_{\xi})(w,_{\eta}) \right\} \right] d\xi\, d\eta,$$

where E_p, v, and $D\ (= E_p t_p^3/12(1-v^2))$ are the elastic modulus, Poisson's ratio, and the flexural rigidity of the plate, respectively. The displacement fields of the plate along the x, y, and z-directions are represented by u, v, and w, respectively. The expression for strain energy stored in the stiffeners (U_s) can be written as $U_s = \sum_{p=1}^{ns_x} U_{sx}^p + \sum_{q=1}^{ns_y} U_{sy}^q$, where U_{sx}^p and U_{sy}^q are strain energies stored in the p-th stiffener along the x-direction and the q-th stiffener along the y-direction, respectively. In order to derive the expressions for strain energies of the individual stiffeners a compatible strain distribution at the line

joining the plate and the stiffener is assumed. Hence, the axial strain of a stiffener along the x-direction is derived from the expression $\varepsilon_{sx}^p = \varepsilon_{px}|_{z=t_p/2} - (z - t_p/2)w_{,xx} - y_s v_{,xx}$, where the plate strain at $z = t_p/2$ is denoted by $\varepsilon_{px}|_{z=t_p/2}$ and y_s denotes the distance from the local minor axis. Substituting for the plate strain, $\varepsilon_{px}|_{z=t_p/2} = u_{,x} + 0.5(w_{,x})^2 - (t_p/2)w_{,xx}$, the expression for the total strain of an x-direction stiffener is obtained as $\varepsilon_{sx}^p = u_{,x} + 0.5(w_{,x})^2 - zw_{,xx} - y_s v_{,xx}$. So, the axial strain of a stiffener along the x-direction includes axial strain due to bending action about the major axis, stretching of the neutral axis, and bending action about the minor axis. It should be pointed out that the effect of shear deformation due to direct shear and torsion has not been taken into consideration while calculating the total axial strain. Substituting the total strain in the generalized expression of strain energy, $U_{sx}^p = (E_s/2)\int_{vol}(\varepsilon_{sx}^p)^2 dV$, the final expression of the strain energy stored in a x-direction stiffener is obtained. Similarly, the strain energy expression of a y-direction stiffener can be obtained and the final expression of total stiffener strain energy (U_s) is given by

$$
\begin{aligned}
U_s = \sum_{p=1}^{ns_x} \frac{E_s a}{2} \int_0^1 & \left[\frac{(I_y^p + A_y^p e_x^{p2})}{a^4}(w_{,\xi\xi})^2 + \frac{(I_{yz}^p + A_y^p (b\eta_{\text{stf}}^p)^2)}{a^4}(v_{,\xi\xi})^2 \right. \\
& \left. - Q_y^p \left\{ \frac{2}{a^3}(u_{,\xi})(w_{,\xi\xi}) + \frac{1}{a^4}(w_{,\xi\xi})(w_{,\xi})^2 \right\} + A_y^p \left\{ \frac{1}{a^2}(u_{,\xi})^2 + \frac{1}{4a^4}(w_{,\xi})^4 + \frac{1}{a^3}(u_{,\xi})(w_{,\xi})^2 \right\} \right] d\xi \\
+ \sum_{q=1}^{ns_y} \frac{E_s b}{2} \int_0^1 & \left[\frac{(I_x^q + A_x^q e_y^{q2})}{b^4}(w_{,\eta\eta})^2 + \frac{(I_{xz}^q + A_x^q (a\xi_{\text{stf}}^q)^2)}{b^4}(u_{,\eta\eta})^2 - Q_x^q \left\{ \frac{2}{b^3}(v_{,\eta})(w_{,\eta\eta}) \right. \right. \\
& \left. \left. + \frac{1}{b^4}(w_{,\eta\eta})(w_{,\eta})^2 \right\} + A_x^q \left\{ \frac{1}{b^2}(v_{,\eta})^2 + \frac{1}{4b^4}(w_{,\eta})^4 + \frac{1}{b^3}(v_{,\eta})(w_{,\eta})^2 \right\} \right] d\eta. \quad (4)
\end{aligned}
$$

Here, E_s is the elastic modulus of the stiffener material. $I_x^q \ (= b_{sy}^q t_{sy}^{q\,3}/12)$, $I_y^p \ (= b_{sx}^p t_{sx}^{p\,3}/12)$ and I_{xz}^q $(= b_{sy}^{q\,3} t_{sy}^q/12)$, $I_{yz}^p \ (= b_{sx}^{p\,3} t_{sx}^p/12)$ are moments of inertia about the major and minor axes of the stiffener cross-section. $Q_y^p \ (= A_x^q e_y^q)$, $Q_x^q \ (= A_y^p e_x^p)$ are the first moment of area about the plate midplane and A_y^p, A_x^q are the cross-sectional areas of the p-th x and q-th y-direction stiffeners, respectively. In the expressions of the energy functionals ξ and η are the dimensionless forms of the midplane coordinates which are associated with the computational domain.

2.1.1. *Approximate displacement fields.* The plate displacement fields (w, u, and v) can be approximately expressed as linear combinations of unknown coefficients d_i as:

$$
w(\xi, \eta) = \sum_{i=1}^{nw} d_i \phi_i(\xi, \eta), \quad u(\xi, \eta) = \sum_{i=nw+1}^{nw+nu} d_i \alpha_{i-nw}(\xi, \eta), \quad v(\xi, \eta) = \sum_{i=nw+nu+1}^{nw+nu+nv} d_i \beta_{i-nw-nu}(\xi, \eta), \quad (5)
$$

where $\phi(\xi, \eta)$, $\alpha(\xi, \eta)$, and $\beta(\xi, \eta)$ are sets of orthogonal functions for w, u, and v, respectively. The functions $\phi_i(\xi, \eta)$ are associated with displacements due to bending, whereas $\alpha_i(\xi, \eta)$ and $\beta_i(\xi, \eta)$ describe stretching of the midplane of the plate. Appropriate start functions for these orthogonal sets are selected in such a way that they satisfy the flexural and membrane boundary conditions of the plate. The two-dimensional (2D) start functions are generated from one-dimensional (1D) functions corresponding to the two coordinate directions. The 1D starting functions for transverse displacement are taken to be the beam deflection functions, derived from the static deflection shape of the beam under uniform loading,
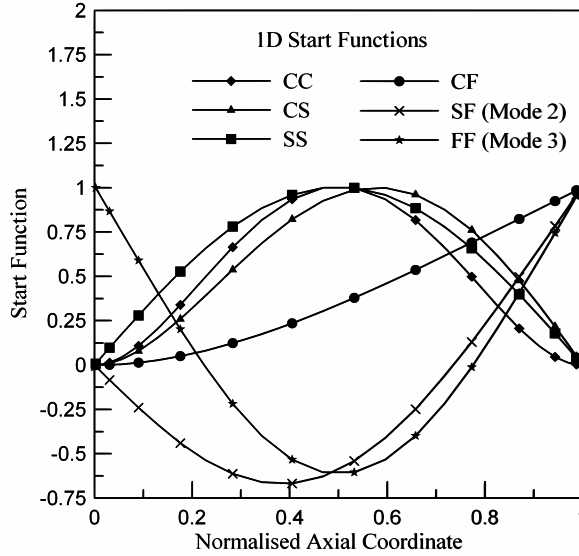
Figure 3. Plots of 1D beam functions.

corresponding to the boundary condition of the plate along the particular coordinate axis. A complete set with 21 different boundary conditions may arise from the different combinations of clamped (C), simply supported (S), and free (F) end conditions of a plate. But it is found that six basic beam functions, represented as CC, CS, CF, SS, SF, and FF, are sufficient to generate 2D start functions corresponding to all the classical boundary conditions possible for a plate. Both transcendental and polynomial functions are used to describe these 1D beam functions [Blevins 1981] and they are graphed in Figure 3.

As per the requirements of the numerical scheme, all the functions are described numerically within the computational domain at the selected Gauss points. The higher-order 1D functions are generated through a numerical implementation of the Gram–Schmidt orthogonalization procedure. However, the necessary rigid body modes for SF and FF beams are incorporated by inserting appropriate functions into the corresponding sets of orthogonal functions. The 2D functions are obtained through ordered multiplication of the 1D functions for two orthogonal directions and are specified for various boundary conditions involving a single free edge in Table 1. The notation for the boundary conditions of the plate has been specified through its edge conditions, starting from the edge $x = 0$ and proceeding counterclockwise.

Boundary condition	Start function for $w(\phi_1(\xi, \eta))$
CCCF	$\xi^2(1-\xi)^2\big(\cosh(A\eta) - \cos(A\eta) + B\{\sinh(A\eta) - \sin(A\eta)\}\big)$
CCSF	$\xi^2(3 - 5\xi + 2\xi^2)\big(\cosh(A\eta) - \cos(A\eta) + B\{\sinh(A\eta) - \sin(A\eta)\}\big)$
CSCF	$\xi^2(1-\xi)^2\big(\cosh(C(1-\eta)) - \cos(C(1-\eta)) + D\{\sinh(C(1-\eta)) - \sin(C(1-\eta))\}\big)$
CSSF	$\xi^2(3 - 5\xi + 2\xi^2)\big(\cosh(C(1 - \eta)) - \cos(C(1 - \eta))$ $+ D\{\sinh(C(1 - \eta)) - \sin(C(1 - \eta))\}\big)$
SCSF	$\sin(\pi\xi)\big(\cosh(A\eta) - \cos(A\eta) + B\{\sinh(A\eta) - \sin(A\eta)\}\big)$
SSSF	$\sin(\pi\xi)\big(\cosh(C(1 - \eta)) - \cos(C(1 - \eta)) + D\{\sinh(C(1 - \eta)) - \sin(C(1 - \eta))\}\big)$

Table 1. Start functions for assumed displacement fields w.

The start functions for stretching displacement of the plate (u and v) come from in-plane or membrane boundary conditions and zero displacement is assumed at the edges ($u = 0$ at $\xi = 0$, 1 and $v = 0$ at $\eta = 0$, 1) to obtain the 1D starting polynomial functions. It should be pointed out that at the free end of the plate the transverse displacements are unrestricted, but the in-plane boundary condition is immovable, that is, displacements are restricted at all the ends including the free edge. Similar to the previous case, the 2D base functions are generated by multiplying the 1D start functions for the two orthogonal directions; these functions are given by $\alpha_1(\xi, \eta) = \{\xi(1-\xi)\}.\{\eta(1-\eta)\}$ and $\beta_1(\xi, \eta) = \{\xi(1-\xi)\}.\{\eta(1-\eta)\}$. However, in this case the higher-order functions are generated from the start functions following a two-dimensional implementation of the Gram–Schmidt orthogonalization scheme. The Gram–Schmidt orthogonalization principle and its two-dimensional implementation have been discussed in detail in [Saha et al. 2004; Das et al. 2009]. It should be noted that the generated functions are for the total domain and they need to be broken down in terms of the subdomains. These sets of functions for the subdomains are derived by carrying out interpolation operations on the total functions and are represented by ϕ_i^{mn}, α_i^{mn}, β_i^{mn}, where $m = 1, \ldots, ns_y + 1$ and $n = 1, \ldots, ns_x + 1$.

2.1.2. *Governing system of equations.* Substituting the complete energy expressions and the approximate displacement fields into (1), the set of system governing equations in matrix form is obtained as

$$[K(\{d\})]\{d\} = \{f\}. \tag{6}$$

Here, $[K]$, $\{d\}$, and $\{f\}$ are stiffness matrix, vector of unknown coefficients, and load vector, respectively. The total stiffness matrix $[K]$ of the system is given by $[K] = [K_b] + [K_m] + \sum_{p=1}^{ns_x}[K_{sx}]^p + \sum_{q=1}^{ns_y}[K_{sy}]^q$, where $[K_b]$ and $[K_m]$ are contributions from the bending and stretching action of the plate, and $[K_{sx}]^p$ and $[K_{sy}]^q$ represent the stiffness matrices of the p-th stiffener along the x-direction and the q-th stiffener along the y-direction, respectively. The details of the elements of the stiffness matrices and load vector are furnished in the Appendix.

2.1.3. *Solution methodology for static displacement field.* As large displacement induced by geometric nonlinearity is taken into consideration, the stiffness matrix $[K]$ includes elements that contain the unknown coefficients $\{d\}$, to be determined subsequently. The stiffness matrices for the stiffeners also include some terms containing the unknown coefficients. As a result the system of governing equations presented in (6) becomes nonlinear in nature and cannot be solved directly. Hence, the solution methodology specially adopted to solve the set of nonlinear equations employs an iterative procedure utilizing a direct substitution technique with a successive relaxation scheme [Cook et al. 1989]. At the start of the solution procedure necessary parameters that cater to the iterative scheme, for example, the relaxation parameter (λ), error limit (ε), etc., are chosen along with a starting load value. The linear component of the stiffness matrix $[K_b]$ is computed and an initial guess (generally taken as 0) for the unknown coefficients is assumed. The total stiffness matrix $[K]$ is calculated on the basis of the assumed values and a new set of unknown coefficients is determined from the expression $\{d\}^{(n+1)} = [K(\{d\}^{(n)})]^{-1}\{f\}$, where n denotes the iteration counter. A comparison between the calculated values and the corresponding values in the previous iteration is carried out to determine the error. If the error comes out to be within the predefined limit of tolerance, convergence is achieved. Otherwise, if the error is outside the specified value the next iteration is performed with modified values of the unknown coefficients, computed by the relation $\{d\} = \{d\}_{old} + \lambda(\{d\} - \{d\}_{old})$. Once convergence is achieved for a particular load step, an

increment is provided to the load and the present solution is taken as the initial guess for the next load step.

2.2. Dynamic analysis. The governing set of equations for the dynamic analysis is derived following Hamilton's principle, which is expressed as

$$\delta\left(\int_{\tau_1}^{\tau_2}(T-U)d\tau\right)=0. \tag{7}$$

According to Hamilton's principle a dynamic system can be characterized by two energy functionals, kinetic energy and potential energy. In the case of a free vibration analysis the potential energy is made up of only the strain energy of the system, as the potential of the external forces is reduced to zero. So, in the mathematical expression T and U represent the total kinetic energy of the system and the total strain energy stored in the system. The variational operator and time coordinate are denoted by δ and τ, respectively. The total kinetic energy (T) is a summation of the plate kinetic energy (T_p) and stiffener kinetic energy (T_s), that is,

$$T=T_p+T_s, \quad \text{where } T_s=\sum_{p=1}^{ns_x}T_{sx}^p+\sum_{q=1}^{ns_y}T_{sy}^q. \tag{8}$$

T_{sx}^p and T_{sy}^q are kinetic energies of the p-th stiffener along the x-direction and the q-th stiffener along the y-direction, respectively. The expressions for the kinetic energies of plate and individual stiffeners are, in terms of dynamic displacement fields,

$$T_p=\tfrac{1}{2}\rho_p t_p(ab)\int_0^1\int_0^1(\dot{w}^2+\dot{u}^2+\dot{v}^2)d\xi d\eta,$$

$$T_{sx}^p=\tfrac{1}{2}\rho_s t_{sx}^p(ab_{sx}^p)\int_0^1(\dot{w}^2+\dot{u}^2+\dot{v}^2)d\xi, \tag{9}$$

$$T_{sy}^q=\tfrac{1}{2}\rho_s t_{sy}^q(bb_{sy}^q)\int_0^1(\dot{w}^2+\dot{u}^2+\dot{v}^2)d\eta,$$

where ρ_p and ρ_s are the densities of the plate and stiffener materials. The expressions of strain energies for the plate (U_b and U_m) and stiffeners (U_s) are identical to those given by (3) and (4). These energy functionals are determined from the assumed transverse ($w(\xi,\eta,\tau)$) and in-plane ($u(\xi,\eta,\tau)$ and $v(\xi,\eta,\tau)$) dynamic displacement fields, which are associated with the midplane of the plate. The assumed dynamic displacements are separable in space and time and can be approximately represented by finite linear combinations of orthogonal admissible functions and a new set of unknown coefficients, denoted by $\{c\}$:

$$w(\xi,\eta,\tau)=\sum_{i=1}^{nw}c_i\phi_i e^{i\omega\tau},$$

$$u(\xi,\eta,\tau)=\sum_{i=nw+1}^{nw+nu}c_i\alpha_{i-nw}e^{(i-nw)\omega\tau}, \tag{10}$$

$$v(\xi,\eta,\tau)=\sum_{i=nw+nu+1}^{nw+nu+nv}c_i\beta_{i-nw-nu}e^{(i-nw-nu)\omega\tau}.$$

In these expressions ω is the natural frequency of the system and $\{c\}$ denotes the eigenvectors in matrix form which represent the contribution of the individual space functions in a particular vibration frequency mode. The spatial functions $\phi_i(\xi, \eta)$, $\alpha_i(\xi, \eta)$, and $\beta_i(\xi, \eta)$ are identical to those for the static analysis in (5). Substitution of the kinetic (T) and strain energy (U) expressions along with the dynamic displacement fields gives the governing equation of the dynamic system in the following form:

$$-\omega^2[M]\{c\} + [K]\{c\} = 0, \tag{11}$$

where $[K]$ is the stiffness matrix of the system at the deflected configuration. This implies that the unknown parameters obtained from the converged static solution are used to compute the starting values for solving the dynamic problem. In the above expression, $[M]$ is the mass matrix that includes contributions from the plate $([M_p])$ and the x and y-direction stiffeners $([M_{sx}]$ and $[M_{sy}])$. So, the final expression for the total mass matrix is obtained as $[M] = [M_p] + [M_{sx}] + [M_{sy}]$. The form of $[M]$ is given by

$$[M] = \begin{bmatrix} M_{11} & 0 & 0 \\ 0 & M_{22} & 0 \\ 0 & 0 & M_{33} \end{bmatrix},$$

where

$$[M_{11}] = \rho_p t_p(ab) \sum_{j=1}^{nw} \sum_{i=0}^{nw} \int_0^1 \int_0^1 \phi_i\phi_j \, d\xi d\eta + \sum_{p=1}^{ns_x} \left[\rho_s t_{sx}^p(ab_{sx}^p) \sum_{j=1}^{nw} \sum_{i=1}^{nw} \int_0^1 \phi_i\phi_j \, d\xi \right]$$
$$+ \sum_{q=1}^{ns_y} \left[\rho_s t_{sy}^q(bb_{sy}^q) \sum_{j=1}^{nw} \sum_{i=1}^{nw} \int_0^1 \phi_i\phi_j \, d\eta \right],$$

$$[M_{22}] = \rho_p t_p(ab) \sum_{j=nw+1}^{nw+nu} \sum_{i=nw+1}^{nw+nu} \int_0^1 \int_0^1 \alpha_{i-nw}\alpha_{j-nw} \, d\xi d\eta$$
$$+ \sum_{p=1}^{ns_x} \left[\rho_s t_{sx}^p(ab_{sx}^p) \sum_{j=nw+1}^{nw+nu} \sum_{i=nw+1}^{nw+nu} \int_0^1 \alpha_{i-nw}\alpha_{j-nw} \, d\xi \right]$$
$$+ \sum_{q=1}^{ns_y} \left[\rho_s t_{sy}^q(bb_{sy}^q) \sum_{j=nw+1}^{nw+nu} \sum_{i=nw+1}^{nw+nu} \int_0^1 \alpha_{i-nw}\alpha_{j-nw} \, d\eta \right],$$

$$[M_{33}] = \rho_p t_p(ab) \sum_{j=nw+nu+1}^{nw+nu+nv} \sum_{i=nw+nu+1}^{nw+nu+nv} \int_0^1 \int_0^1 \beta_{i-nw-nu}\beta_{j-nw-nu} \, d\xi d\eta$$
$$+ \sum_{p=1}^{ns_x} \left[\rho_s t_{sx}^p(ab_{sx}^p) \sum_{j=nw+nu+1}^{nw+nu+nv} \sum_{i=nw+nu+1}^{nw+nu+nv} \int_0^1 \beta_{i-nw-nu}\beta_{j-nw-nu} \, d\xi \right]$$
$$+ \sum_{q=1}^{ns_y} \left[\rho_s t_{sy}^q(bb_{sy}^q) \sum_{j=nw+nu+1}^{nw+nu+nv} \sum_{i=nw+nu+1}^{nw+nu+nv} \int_0^1 \beta_{i-nw-nu}\beta_{j-nw-nu} \, d\eta \right].$$

The governing equation of the dynamical system (11) can be alternatively written as

$$[[M]^{-1}[K]]\{c\} = \omega^2\{c\}.$$

This is a standard eigenvalue problem which is solved numerically through IMSL routines. The square roots of the computed eigenvalues give the free vibration frequencies at the statically deflected configuration of the stiffened plate and are called the loaded natural frequencies. The amplitude of free vibration is obtained from the transverse displacement fields associated with the eigenvalues. The plot of the loaded natural frequencies against the corresponding amplitudes in a nondimensional plane represents the backbone curve of the system. The eigenvectors corresponding to the eigenvalues are utilized to determine the mode shapes of the vibrating system.

3. Results and discussion

Our analysis is carried out for three different types of stiffened plates — uniaxially single stiffened, uniaxially double stiffened, and biaxially cross stiffened — under a uniformly distributed load. The classification is according to the number and orientation of the stiffeners, as shown schematically in Figure 2, which also presents the decomposed computational domains that provide an improved grid corresponding to the three different types of stiffened plates. As stated earlier, for each of the three types of plates, six classical flexural boundary conditions are considered: CCCF, CCSF, CSCF, CSSF, SCSF, and SSSF, each letter indicating an edge condition, moving counterclockwise beginning with the edge $x = 0$. Thus there is a single free edge, always at $y = b$, and the other edges are variously clamped or simply supported. These flexural boundary conditions dictate the choice of start functions for the definition of transverse deflection (w). The base functions for the in-plane displacement (u and v) of the plate are derived from the membrane boundary conditions, which are modeled as immovable edges in all cases.

The process of generation of start functions for both transverse and deformation displacement has been discussed in Section 2.1.1, and Table 1 presents base functions for individual cases of flexural end conditions. The Gram–Schmidt orthogonalization principle is utilized to generate a complete set of higher-order functions and adequate measures are taken to insert rigid body modes wherever necessary. The number of functions for each of the plate displacements (u, v, and w) is taken as 25 (5×5), where the numbers in the parentheses indicate the number of functions corresponding to the two orthogonal directions. Due to the general nature of the formulation any other classical flexural boundary conditions can be handled through this method. It should also be mentioned that the present methodology can be applied for any other transverse loading pattern, mathematically expressible in terms of the coordinates.

The analysis is based on determining the static displacement field first and subsequently computing the eigenvalues of the corresponding dynamic problem based on the known static displacement field. The solution methodology of the static problem involves an iterative numerical scheme using successive relaxation due to presence of nonlinearity in the stiffness matrix. The tolerance value of the error limit (ε) for the numerical iterative scheme is fixed at 0.50% and the relaxation parameter (λ) is taken as 0.50. The solution of the dynamic problem is obtained using IMSL routines.

To determine the number of Gauss points to be used for generation of results a convergence study is carried out on a uniaxially single stiffened plate under uniformly distributed transverse loading. The details of the plate and stiffener geometry, material properties, and boundary conditions are provided in the figure's legend. For a transverse load of 100 kPa intensity, the normalized maximum deflection ($w_{\max}/t_p$) of the system is plotted against a number of Gauss points (ng) in Figure 4. A choice of 24 Gauss points for the present work is made from the convergence study. The initial choice of number of Gauss
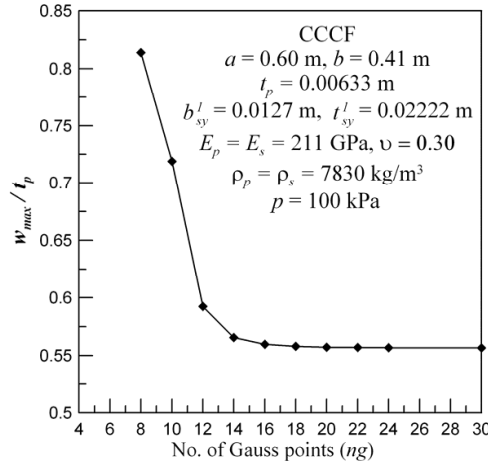
Figure 4. Convergence study for selection of a number of Gauss points.

points dictates the grid density of the computational domain after applying the domain decomposition technique. However, with increase in the stiffener number, the number of subdomains increases and as each subdomain has a grid of $ng \times ng$ reference points, the computations become extensive.

3.1. *Validation study.* The formulation and solution methodology used in the present work are validated through comparison with results available in the existing literature. The load-deflection curve obtained from the static analysis incorporating geometric nonlinearity is compared with the results of [Koko and Olson 1992; Rao et al. 1993a; Sheikh and Mukhopadhyay 2000]. A clamped (CCCC) stiffened plate, whose geometry and dimensions (in mm) are provided in Figure 5, left, under uniformly distributed transverse pressure is analyzed and the comparison plots at two different locations on the plate, A and B, are presented in Figure 5, right. Fairly good agreement with the results of other researchers is observed.
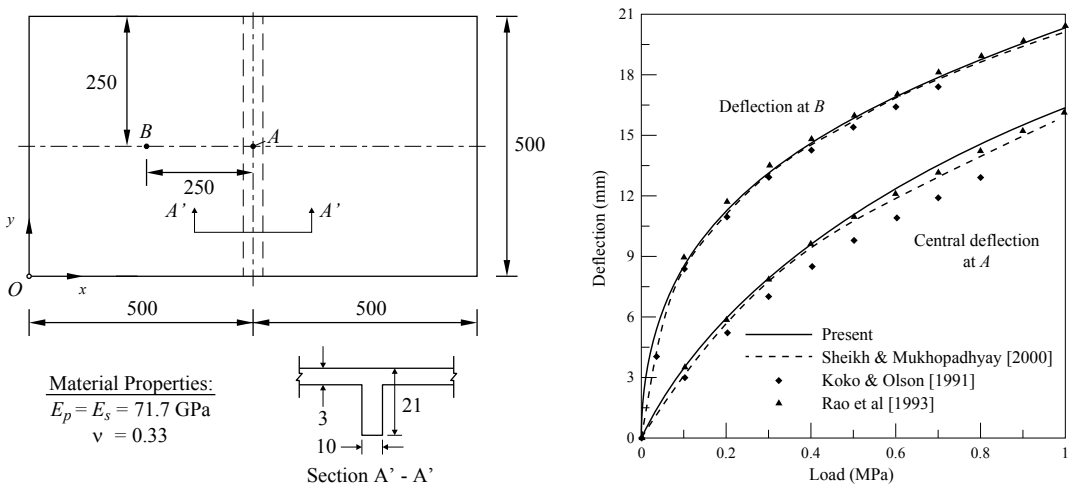

Figure 5. Left: detailed geometry and dimensions of clamped (CCCC) stiffened plate used for validation purpose. Right: comparison of load deflection behavior of clamped stiffened plate at selected points.
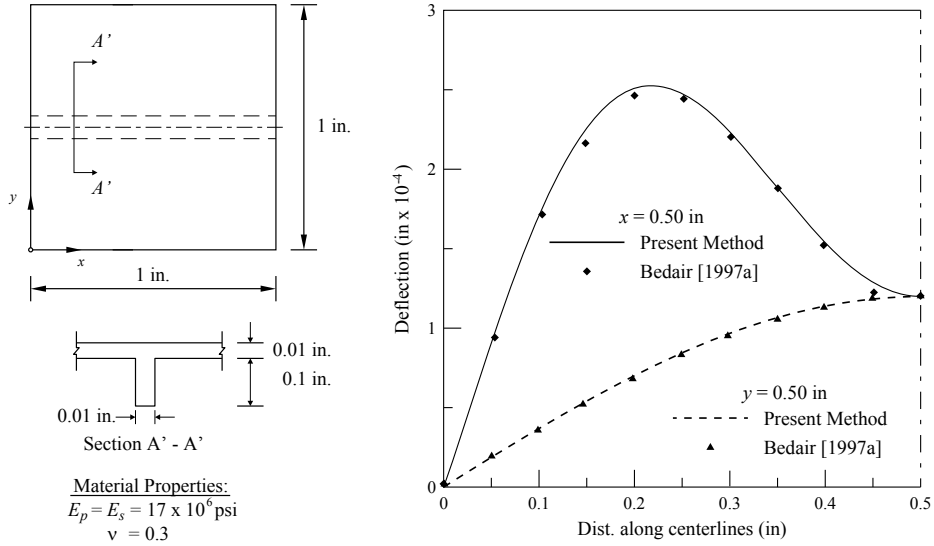
Figure 6. Deflected profile of simply supported square stiffened plate under UDL.

A comparison of the deflected shape of a simply supported (SSSS) square plate with one stiffener under UDL generated through the present method is carried out with results furnished by [Bedair 1997a]. The details of the plate geometry and the material properties are furnished in Figure 6, left, and the results are generated for a uniformly distributed load of 1.0 psi. The comparative plot in Figure 6, right, shows that deflected profiles have identical natures and agreement between the two sets of results is excellent.

The dynamic problem is validated by comparing the linear free vibration frequencies of different modes for a system with reduced complexity. Table 2 shows the free vibration frequency parameters $\omega a^2 \sqrt{\rho t_p / D}$ for the first six modes of an unstiffened square plate with various boundary conditions,

Boundary condition	Mode =	1	2	3	4	5	6
CCCC	[Leissa 1973]	24.012	40.029	63.471	76.745	80.704	116.799
	Present	23.939	40.029	63.280	78.031	80.668	118.035
CCSF	[Leissa 1973]	17.621	36.044	52.060	71.182	74.339	106.294
	Present	17.546	36.045	51.851	71.167	75.668	106.324
CSCF	[Leissa 1973]	23.469	35.604	63.135	66.809	77.495	108.985
	Present	23.401	35.606	62.964	67.303	77.496	109.981
CSSF	[Leissa 1973]	16.870	31.128	51.620	64.040	67.637	101.197
	Present	16.806	31.138	51.465	64.563	67.656	102.248
SCSF	[Leissa 1973]	12.679	33.068	41.685	63.005	72.398	90.614
	Present	12.687	33.079	41.715	63.079	73.756	91.115
SSSF	[Leissa 1973]	11.669	27.764	41.193	59.072	61.867	90.278
	Present	11.687	27.772	41.235	59.162	62.391	90.886

Table 2. Comparison of linear dimensionless frequency parameter for an unstiffened plate.
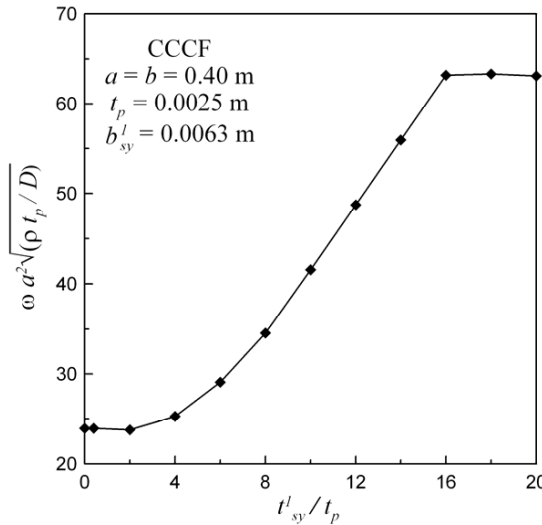
Figure 7. Variation of dimensionless free vibration frequency parameter for the first mode with change in plate-to-stiffener thickness ratio.

comparing them with the results of [Leissa 1973]. For this particular vibration study the stiffener dimensions are taken as zero and good agreement is observed for all the cases. Figure 7 depicts the variation of frequency parameter for the fundamental mode with change in stiffener-to-plate thickness ratio for a square CCCF plate having a single centrally placed eccentric stiffener along the y-direction. The material properties used in this case are as follows: $E_p = E_s = 210$ GPa, $\rho_p = \rho_s = 7850$ kg/m^3, and $\nu = 0.30$. It is seen that the frequency parameter decreases with decrease in stiffener thickness and as the thickness becomes negligibly small the parameter value converges towards that of an unstiffened plate. The dimensionless frequency parameter of the unstiffened square plate with CCCF boundary is obtained through the present method as 23.939 and, as shown in Table 2, it is in close agreement with the value presented by [Leissa 1973]. The convergence of the frequency parameter towards the value corresponding to an unstiffened plate with decreasing stiffener dimension provides an indirect validation of the present method. Figure 7 also indicates that the dimensionless frequency parameter attains a constant value beyond a particular thickness ratio. At this critical thickness ratio the stiffener divides the plate into two panels of equal width that vibrate with the same natural frequency as the plate. In [Bedair 1997b] a similar trend is observed for simply supported stiffened plates.

3.2. *Large-amplitude dynamic behavior.* The present study is undertaken with an objective of investigating the effect of large displacement on the dynamic behavior of stiffened plates and to study the influence of different flexural boundary conditions on the system behavior. The results are presented for a rectangular stiffened plate with $a = 0.60$ m, $b = 0.41$ m, and $t_p = 0.00633$ m, having stiffeners of rectangular cross-section (0.0127 m $\times 0.02222$ m). The following material properties are used to generate the results: $E_p = E_s = 211$ GPa, $\rho_p = \rho_s = 7830$ kg/m^3, and $\nu = 0.30$. The nonlinear frequency amplitude relationships of the three different types of stiffened plates (as shown in Figure 2) having typical combinations of boundary conditions are shown graphically as backbone curves in Figures 8–10. These backbone curves have been presented for the first six vibration modes in a nondimensional plane. The
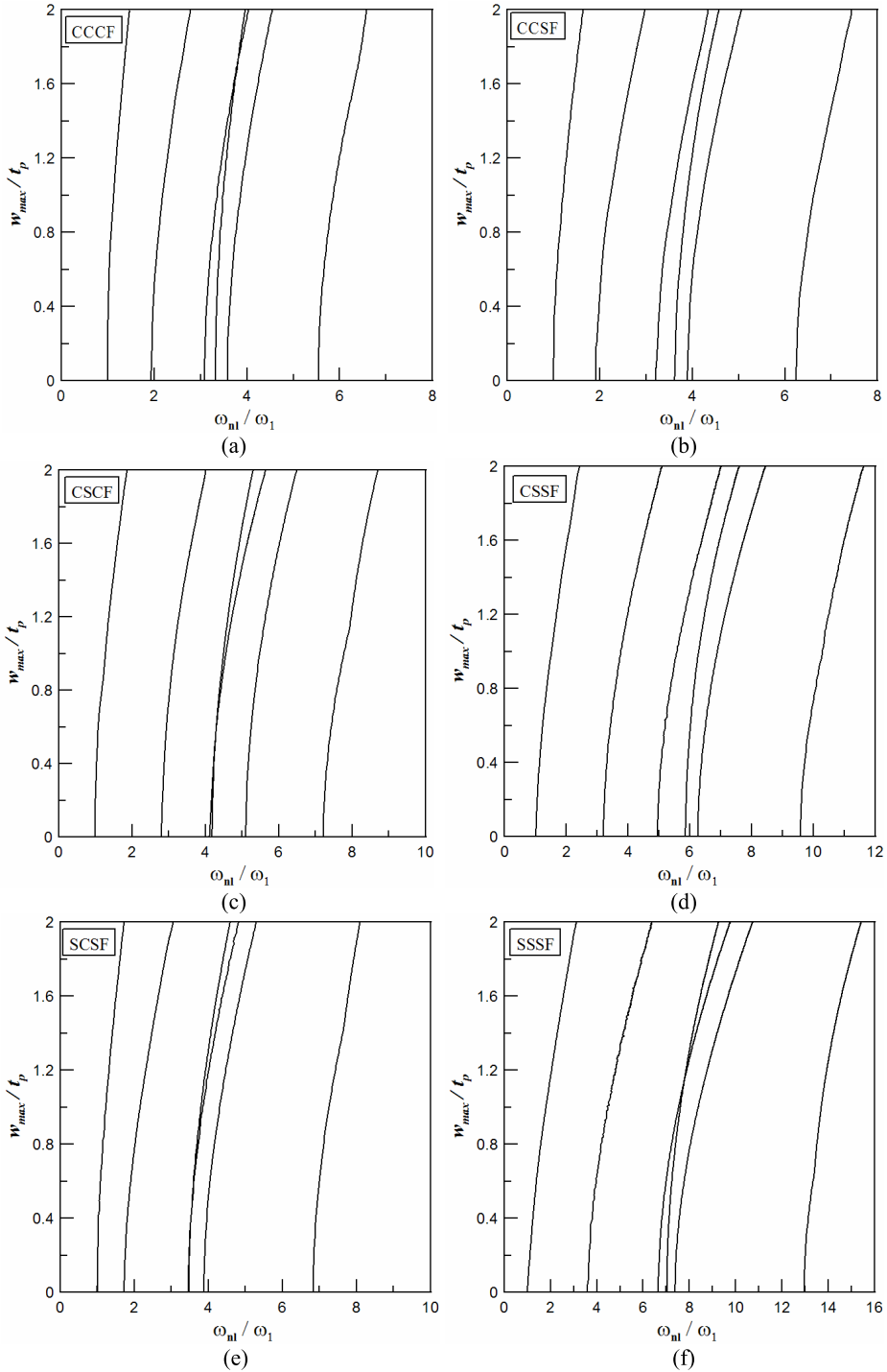
Figure 8. Backbone curves for uniaxially single stiffened rectangular plate under UDL for different boundary conditions with one free edge: (a) CCCF, (b) CCSF, (c) CSCF, (d) CSSF, (e) SCSF, and (f) SSSF.

Type of stiffened plate	Boundary condition					
	CCCF	CCSF	CSCF	CSSF	SCSF	SSSF
Uniaxially single stiffened	148.682	127.015	101.197	72.486	114.094	52.549
Uniaxially double stiffened	154.653	139.136	99.929	84.069	129.423	58.083
Biaxially cross stiffened	199.061	160.732	190.063	144.228	138.142	103.736

Table 3. Fundamental linear frequency (ω_1) in Hz for the three types of stiffened plates with different boundary conditions.

ratio of the maximum transverse deflection to plate thickness is taken as the dimensionless amplitude ($w_{\max}/t_p$) while the nonlinear frequency (ω_{nl}) is normalized by the corresponding fundamental linear frequency (ω_1) to obtain the dimensionless frequency. The results are generated up to a maximum value of dimensionless amplitude ($w_{\max}/t_p$), which is taken as 2.0. The backbone curves for uniaxially single stiffened, uniaxially double stiffened, and biaxially cross stiffened rectangular plates under uniformly distributed transverse load are shown for different boundary conditions, namely CCCF, CCSF, CSCF, CSSF, SCSF, and SSSF, in Figures 8, 9, and 10, respectively. These figures indicate that for a given plate and stiffener geometry the natural frequencies increase as the deflection of the stiffened plate increases for all the cases. In other words, the system exhibits hardening-type nonlinearity. The increase in nonlinear frequency is caused by stiffening of the plate with increasing deflection due to geometric nonlinearity. It is also observed from Figures 8 and 9 that a decrease in rigidity of the boundary conditions, due to introduction of simply supported ends in place of clamped ends, causes the backbone curves for different modes to spread apart in the nondimensional plane. Thus it can be stated that systems with different boundary conditions possess different degrees of nonlinearity.

Mode switching has been observed in a few boundary condition cases for the three types of stiffened plates. Figure 8 shows that for uniaxially single stiffened plates with CCCF, CSCF, SCSF, and SSSF boundary conditions switching occurs between the third (ω_3) and fourth (ω_4) modes. However, a closer inspection reveals that there is also mode switching between the sixth (ω_6) and seventh (ω_7) backbone curves for the cases mentioned above, evident from the slight change in direction of the sixth curve. The absence of the seventh mode gives the sixth curve a broken appearance. In the case of uniaxially double stiffened plates mode switching is absent for all the boundary conditions except SCSF boundaries as shown by Figure 9. From Figure 9e it is clear that first a switch between the fifth (ω_5) and sixth (ω_6) modes takes place and then the fourth (ω_4) and fifth (ω_5) backbone curves intersect each other indicating a further switch. Finally, from the different sets of backbone curves of biaxially cross stiffened plates shown in Figure 10 it is evident that mode switching occurs between fourth (ω_4) and fifth (ω_5) backbone curves for CSCF and SSSF boundaries, whereas no mode switching is observed for the case of CCCF, CCSF, and CSSF conditions. At first glance it seems that this phenomenon is absent in the case of the SCSF boundary condition also. But the discontinuous appearance of the sixth mode indicates that there is indeed a switch between the sixth and seventh backbone curves. The occurrence of mode switching and the modes between which switching occurs depend on parameters such as plate aspect ratio, plate-to-stiffener thickness ratio, stiffener position, stiffener orientation, type of loading, and boundary conditions.

For all the backbone curves, the fundamental linear frequency (ω_1) is used as the normalizing parameter, so its values are provided separately for the three types of stiffened plates with different boundary
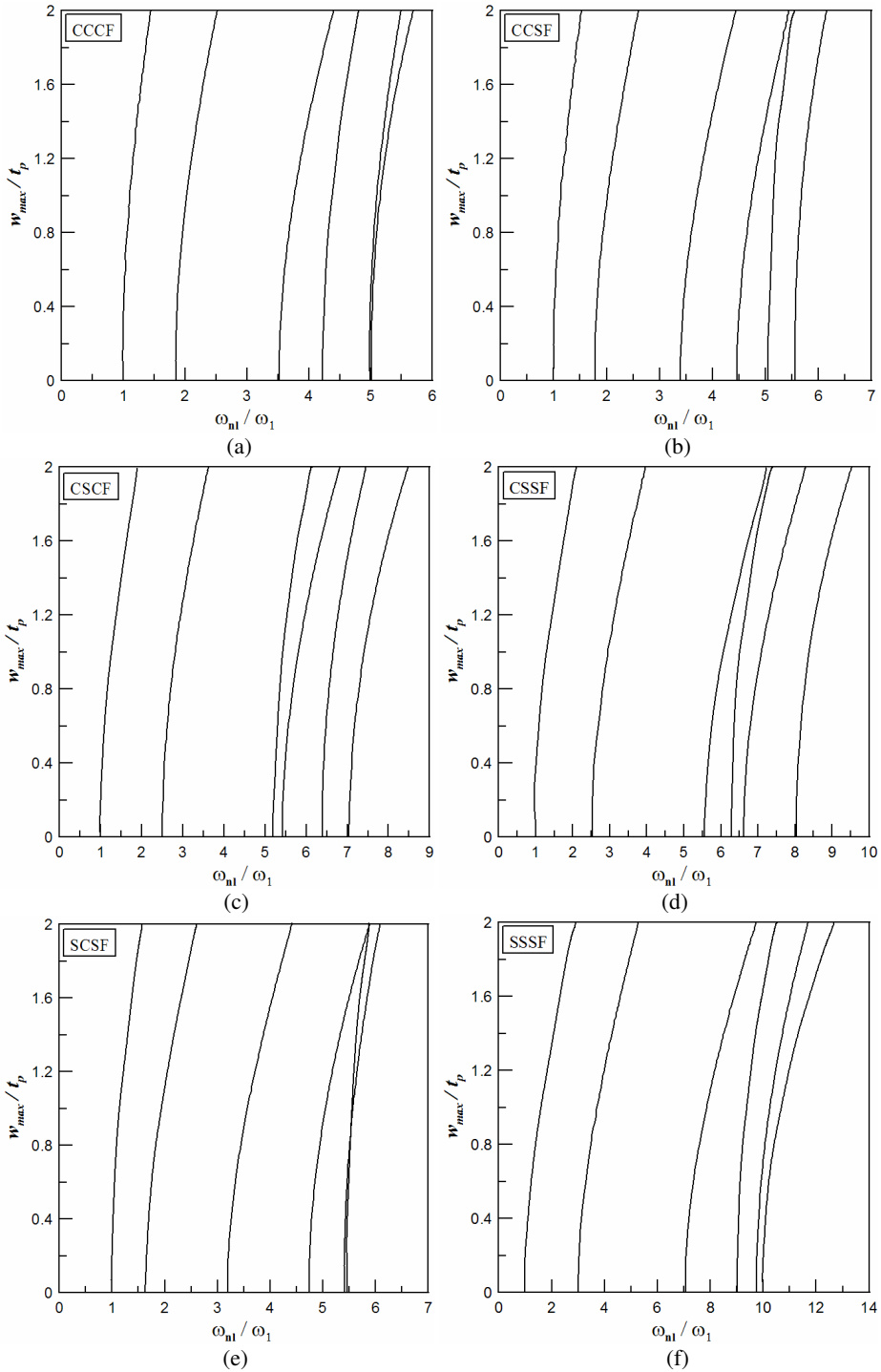
Figure 9. Backbone curves for uniaxially double stiffened rectangular plate under UDL for different boundary conditions with one free edge: (a) CCCF, (b) CCSF, (c) CSCF, (d) CSSF, (e) SCSF, and (f) SSSF.
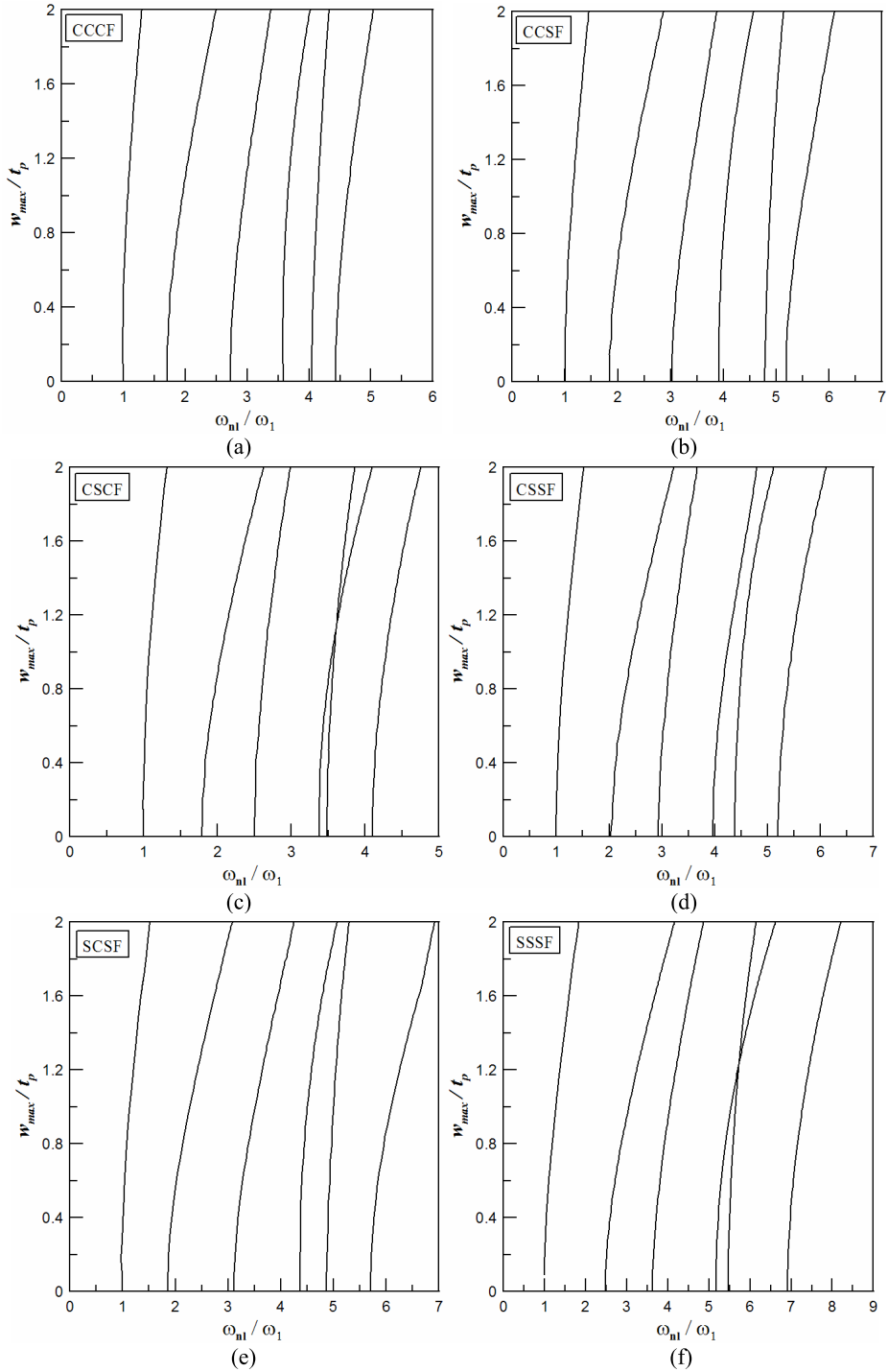
Figure 10. Backbone curves for biaxially cross stiffened rectangular plate under UDL for different boundary conditions with one free edge: (a) CCCF, (b) CCSF, (c) CSCF, (d) CSSF, (e) SCSF, and (f) SSSF.

Type of plate	$w_{\max}/t_p$	Mode = 1	2	3	4	5	6
				ω_{nl}/ω_l			
	0.0	1.000	1.943	3.092	3.329	3.584	5.548
UASS	1.0	1.126	2.176	3.355	3.474	3.867	5.862
	2.0	1.460	2.776	3.958	4.032	4.550	6.581
	0.0	1.000	1.859	3.522	4.230	4.992	5.015
UADS	1.0	1.101	2.020	3.764	4.385	5.098	5.158
	2.0	1.443	2.515	4.396	4.804	5.494	5.691
	0.0	1.000	1.708	2.725	3.588	4.045	4.430
BACS	1.0	1.684	1.954	2.951	3.658	4.141	4.621
	2.0	1.293	2.489	3.379	4.011	4.323	5.037

Table 4. Normalized nonlinear frequency (ω_{nl}/ω_l) for the six modes at $w_{\max}/t_p = 0.0$, 1.0, and 2.0 points on the backbone curve of uniaxially single stiffened (UASS), uni-axially double stiffened (UADS), and biaxially cross stiffened (BACS) plates with the CCCF boundary condition.

conditions in Table 3. It is observed from Table 3 that for a particular type of plate the fundamental linear frequency is highest for the CCCF boundary condition, whereas it is lowest for the SSSF condition. This clearly indicates that clamped-end conditions provide greater rigidity compared to simply supported ends. As a result of the increased stiffness of the system due to end rigidity a higher fundamental frequency is obtained. In the case of uniaxially stiffened plates having a single simply supported end along with the free edge, adjacent clamped ends correspond to a higher fundamental frequency, but for biaxially stiffened plates an opposite trend manifests. Similarly for uniaxially stiffened plates having a single clamped end in addition to the free edge, adjacent simply supported ends correspond to a lower fundamental frequency, but for biaxially stiffened plates the situation is reversed. The table also reveals that the highest stiffness and thus highest fundamental frequency corresponds to cross stiffened plates. Table 4 presents numerical values of normalized nonlinear frequency (ω_{nl}/ω_1) at specific points ($w_{\max}/t_p = 0.0$, 1.0, and 2.0) on the backbone curves for the six modes of three different types of plates having the CCCF boundary condition (shown in Figures 8a, 9a, and 10a).

3.3. *Mode shape plots.* To highlight the effect of vibration amplitude on the dynamic behavior in greater detail the mode shape plots for all six vibration modes are presented for the three types of plates in Figures 11–13. For each mode of vibration, two mode shape plots corresponding to linear ($w_{\max}/t_p = 0$) and nonlinear ($w_{\max}/t_p = 2.00$) frequencies are given. In each of these figures, the surface plot and its corresponding contour plot for the vibrating stiffened plate have been presented. The amplitude of vibration is normalized by the absolute difference between the two extremities of the displacement amplitudes. The first six mode shapes for a CCCF uniaxially single stiffened plate under uniform transverse loading are given in Figure 11. Interchange of the linear and nonlinear mode shapes described in Figures 11c and 11d appropriately supports the case of switching between the third and fourth mode. It is also observed from Figure 11f that the linear and nonlinear mode shape plots are totally different, which corroborates that switching occurs between the sixth and seventh modes. The mode shape plots along
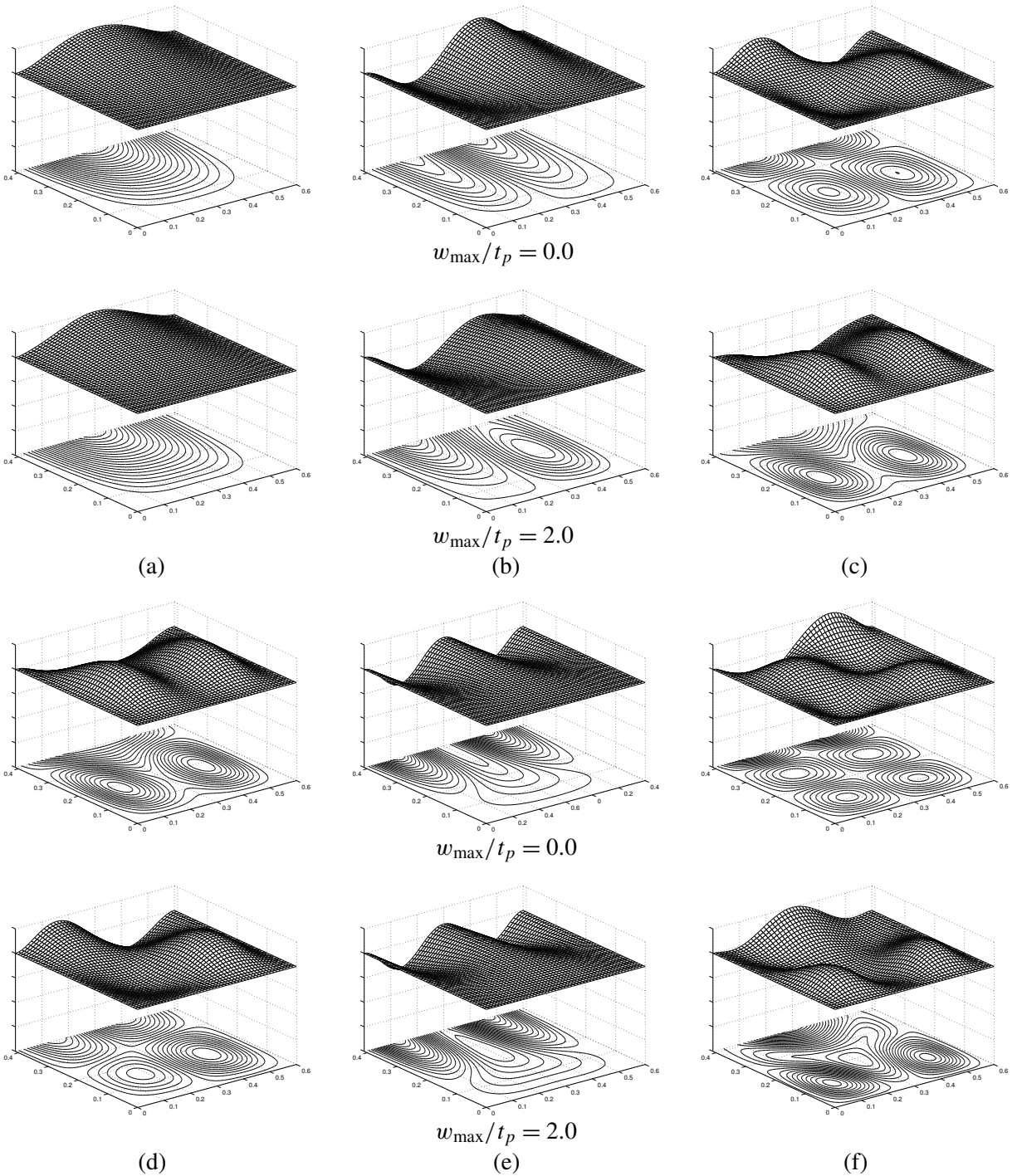
Figure 11. Mode shape plots for uniaxially single stiffened rectangular plate with CCCF boundary condition under UDL: (a) mode 1, (b) mode 2, (c) mode 3, (d) mode 4, (e) mode 5, and (f) mode 6.
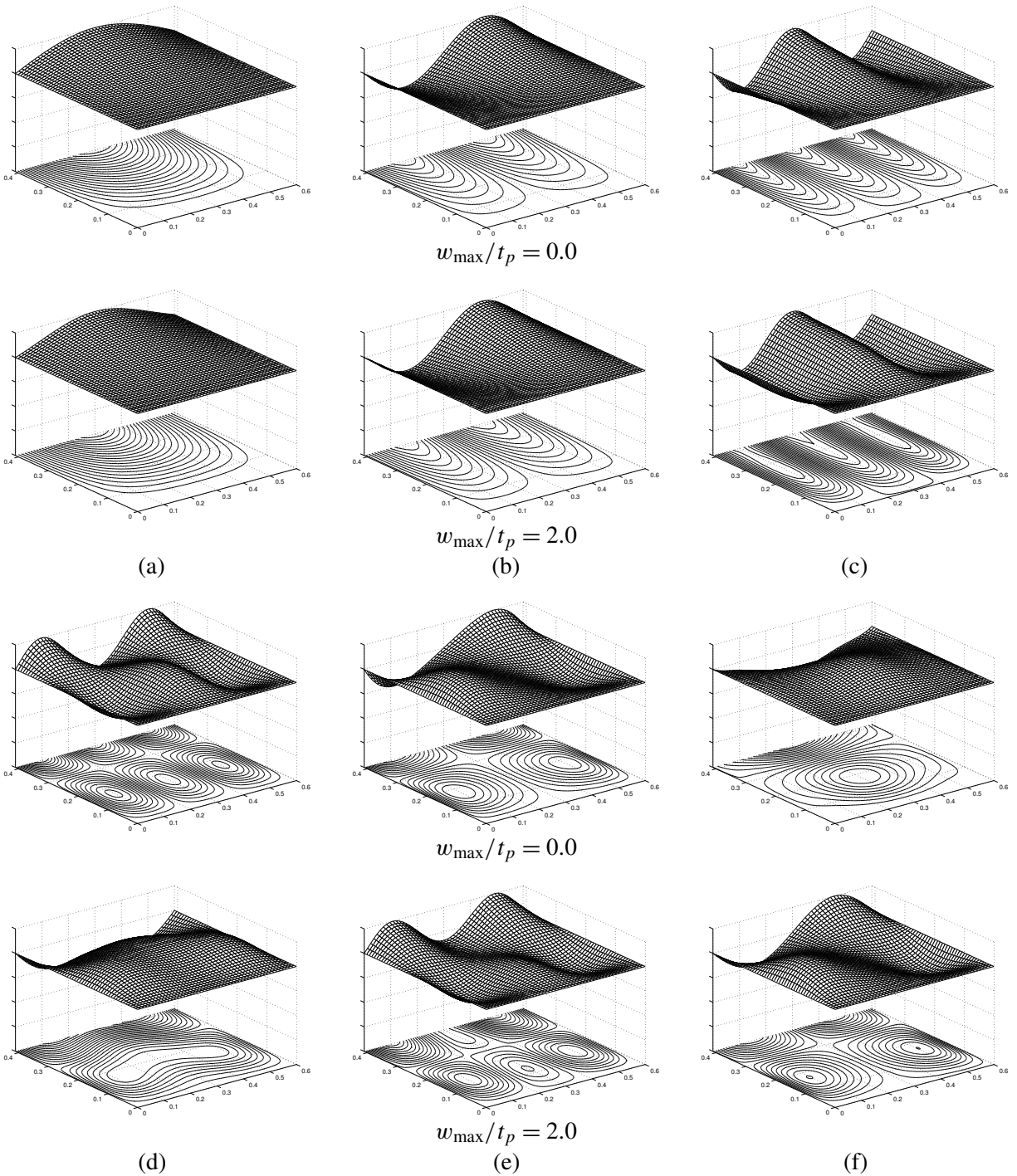
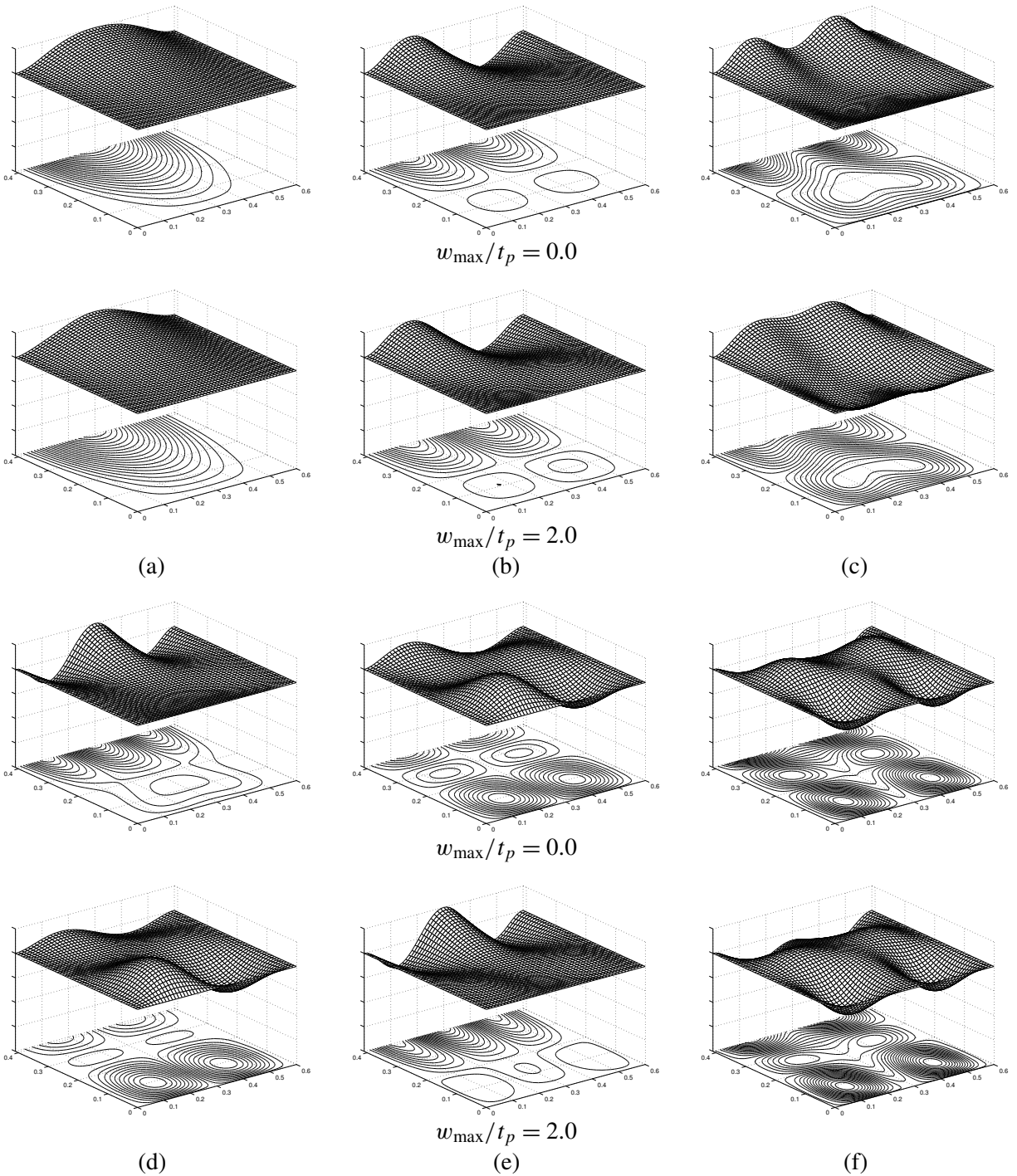$w_{max}/t_p = 0.0$

$w_{max}/t_p = 2.0$

(a) (b) (c)

$w_{max}/t_p = 0.0$

$w_{max}/t_p = 2.0$

(d) (e) (f)

Figure 12. Mode shape plots for uniaxially double stiffened rectangular plate with SCSF boundary condition under UDL: (a) mode 1, (b) mode 2, (c) mode 3, (d) mode 4, (e) mode 5, and (f) mode 6.

$w_{\max}/t_p = 0.0$

$w_{\max}/t_p = 2.0$

(a)   (b)   (c)

$w_{\max}/t_p = 0.0$

$w_{\max}/t_p = 2.0$

(d)   (e)   (f)

Figure 13. Mode shape plots for biaxially cross stiffened rectangular plate with CSCF boundary condition under UDL: (a) mode 1, (b) mode 2, (c) mode 3, (d) mode 4, (e) mode 5, and (f) mode 6.

with contour plots for all six vibration modes for a uniaxially double stiffened plate are presented in
Figure 12, corresponding to SCSF boundary condition (Figure 9e). As expected the mode shape plots
in Figure 12d–f support the case of double mode switching. It is clearly seen that the linear mode shape
plot in Figure 12d corresponds to the nonlinear mode shape in Figure 12e, the linear mode shape plot
in Figure 12e corresponds to the nonlinear mode shape in Figure 12f, and the linear mode shape of
Figure 12f is similar to the nonlinear mode shape in Figure 12d. Figure 13 gives the linear and nonlinear
mode shape plots for biaxially cross stiffened plates with CSCF boundary conditions. Here interchange
of mode shapes between the fourth and fifth modes is observed.

3.4. *Effect of stiffener position on dynamic behavior.* The backbone curves of a uniaxially single stiff-
ened plate with CCCF boundary conditions are presented in Figure 14 corresponding to two different
stiffener positions, $\eta_{stf}^1 = 1.0$ and $\eta_{stf}^1 = 0.5$, that is, the stiffener is placed parallel to the free edge. In one
case the stiffener is positioned at the free edge spanning the length of the plate, whereas for the other the
stiffener is at the center of the plate along the x-direction. The figure shows that the general trends of the
backbone curves remain identical to those discussed in the preceding section. The effect of shifting the
stiffener position on the dynamic behavior of the system is apparent from the changes in the backbone
curves of the two cases. For example, switching between the second and third modes of vibration takes
place for the central stiffener position as shown in Figure 14b, but the phenomenon is absent for the
stiffener placed at the free edge ($\eta_{stf}^1 = 1.0$). The fundamental linear frequencies for the $\eta_{stf}^1 = 1.0$ and
$\eta_{stf}^1 = 0.5$ positions of the stiffeners are found as 200.493 and 155.704 Hz, respectively. This indicates
that a higher stiffness of the system corresponds to plates with stiffeners at the free edge.

Mode shape plots for the first six vibration modes for a CCCF plate with the stiffener positioned at
the free edge are presented in Figure 15. Two mode shape plots corresponding to linear and nonlinear
frequencies are provided along with the corresponding contour plots for the vibrating system. Similar to
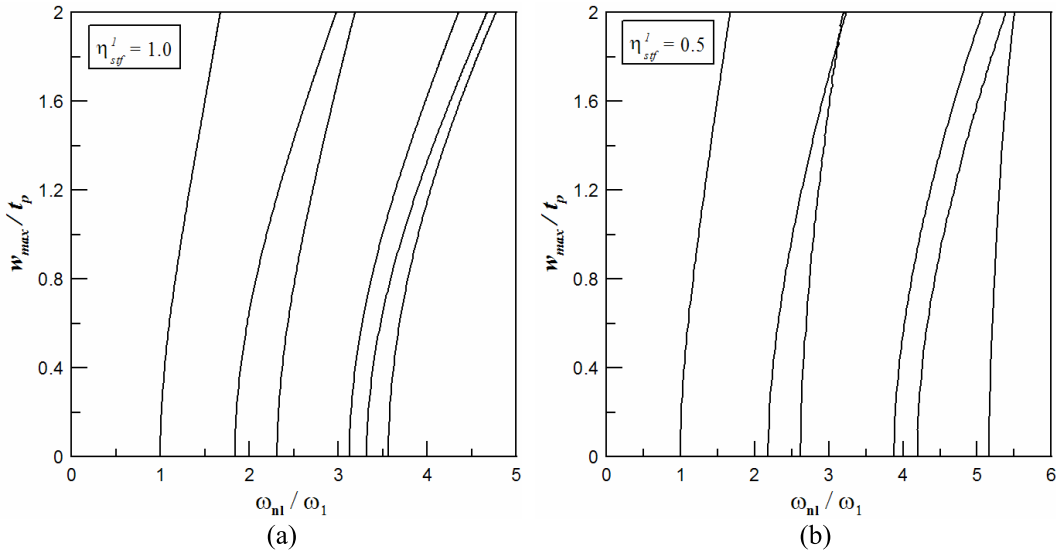

Figure 14. Backbone curves of uniaxially single stiffened rectangular plate with CCCF
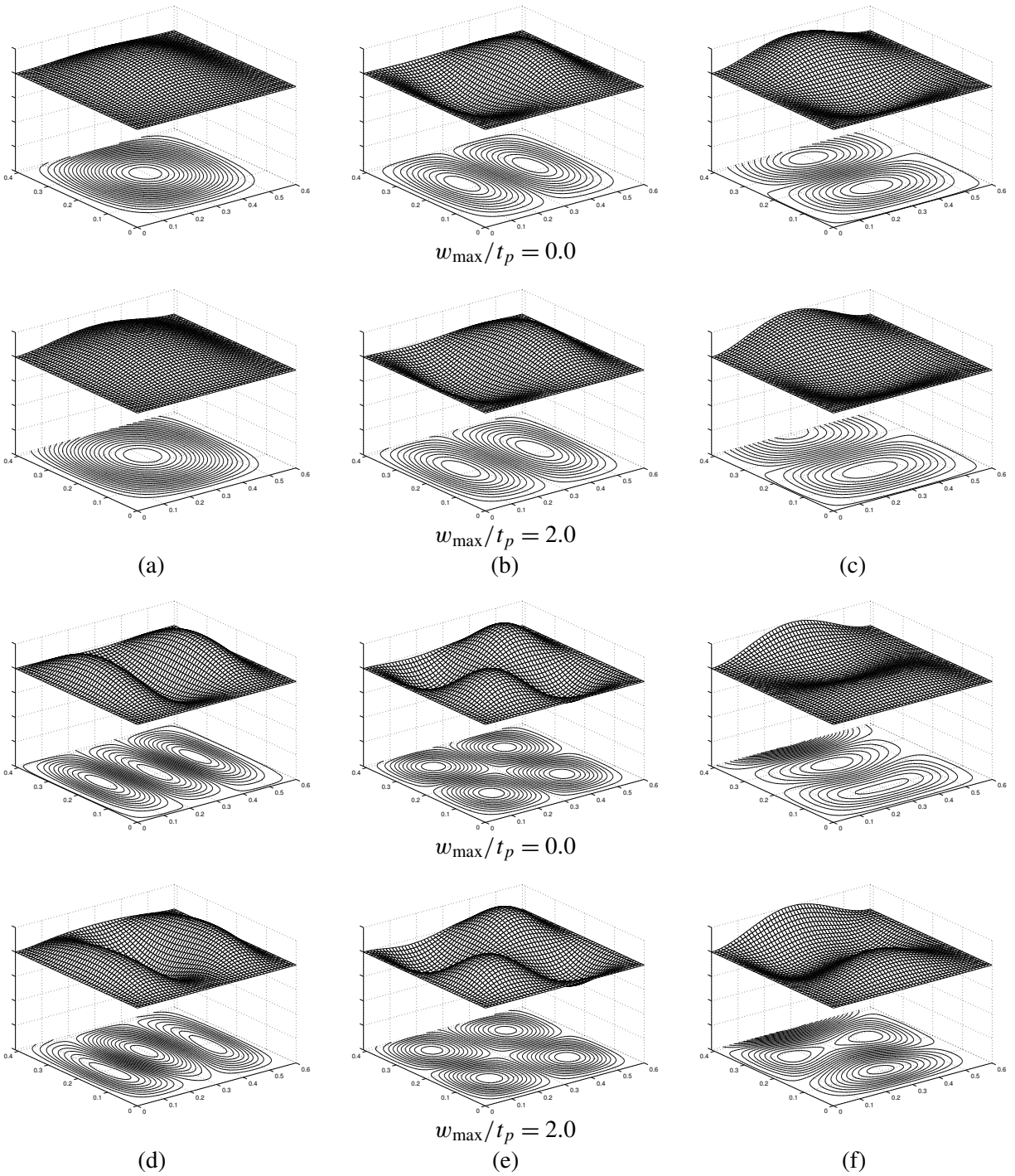boundaries for different stiffener positions: (a) $\eta_{stf}^1 = 1.0$ and (b) $\eta_{stf}^1 = 0.5$.

$w_{\max}/t_p = 0.0$

$w_{\max}/t_p = 2.0$

(a)   (b)   (c)

$w_{\max}/t_p = 0.0$

$w_{\max}/t_p = 2.0$

(d)   (e)   (f)

Figure 15. Mode shape plots for uniaxially single stiffened rectangular plate with the stiffener along the free edge, that is, $\eta_{\text{stf}}^1 = 1.0$, having CCCF boundary condition: (a) mode 1, (b) mode 2, (c) mode 3, (d) mode 4, (e) mode 5, and (f) mode 6.

Figures 11–13, here also the amplitude of vibration for the surface plots is normalized by the difference between the extremities of the displacement amplitude. It is found that the mode shape plots for linear and nonlinear frequencies are similar in nature. However, minor variations in these mode shape plots are apparent from the contour plots and point to the fact that the amplitude of vibration influences the mode shapes of the system.

4. Conclusion

The present work deals with large-amplitude free-vibration analysis of stiffened plates with various flexural boundary conditions that include a single free edge. The stiffened plates are classified into three categories, by number and orientation of the stiffeners: uniaxially single stiffened, uniaxially double stiffened, and biaxially cross stiffened. A domain decomposition technique is applied to generate the appropriate grid of computation points for the various types of plates. The analysis involves two steps, the first being solution of the static displacement field of the system produced due to a uniformly distributed transverse loading. The second step takes up the free-vibration analysis as an eigenvalue problem on the basis of known static displacement field. The square roots of the computed eigenvalues provide the loaded natural frequencies of the system. The mathematical formulation of the static problem is based on the principle of minimum potential energy, whereas Hamilton's principle has been applied for the dynamic analysis. The results of both static and dynamic analyses are validated with the published results of other researchers and good agreement is observed in almost all the cases. The large-amplitude dynamic behavior has been presented as backbone curves in a dimensionless frequency-amplitude plane. The general trend of the backbone curves indicates hardening-type nonlinearity. Mode switching has been observed for some specific boundary conditions and geometries of the system and the results are adequately backed up by three-dimensional mode shape plots presented along with contour plots in a few specific cases.

Appendix: Details of stiffness matrices and load vector

The form of $[K_b]$ is

$$[K_b] = \begin{bmatrix} k_{11}^b & 0 & 0 \\ 0 & 0 & 0 \\ 0 & 0 & 0 \end{bmatrix},$$

where

$$[k_{11}^b] = D(ab) \sum_{j=1}^{nw} \sum_{i=1}^{nw} \int_0^1 \int_0^1 \left[\left\{ \frac{1}{4}(\phi_{i,\xi\xi})(\phi_{j,\xi\xi}) + \frac{1}{b^4}(\phi_{i,\eta\eta})(\phi_{j,\eta\eta}) + \frac{1}{a^2b^2}(\phi_{i,\xi\xi})(\phi_{j,\eta\eta}) \right. \right.$$
$$\left. + \frac{1}{a^2b^2}(\phi_{i,\eta\eta})(\phi_{j,\xi\xi}) \right\} - \frac{(1-\nu)}{a^2b^2} \{(\phi_{i,\xi\xi})(\phi_{j,\eta\eta}) + (\phi_{i,\eta\eta})(\phi_{j,\xi\xi}) - 2(\phi_{i,\xi\eta})(\phi_{j,\xi\eta})\} \Bigg] d\xi d\eta.$$

The form of $[K_m]$ is

$$[K_m] = \begin{bmatrix} k_{11}^m & 0 & 0 \\ k_{21}^m & k_{22}^m & k_{23}^m \\ k_{31}^m & k_{32}^m & k_{33}^m \end{bmatrix},$$

where

$$
[k_{11}^m] = \frac{E_p t_p}{2(1-\nu^2)}(ab) \sum_{j=1}^{nw} \sum_{i=1}^{nw} \int_0^1 \int_0^1 \left[\frac{1}{a^4}\Big(\sum_{i=1}^{nw} d_i\phi_{i,\xi}\Big)^2 (\phi_{i,\xi})(\phi_{j,\xi}) + \frac{1}{b^4}\Big(\sum_{i=1}^{nw} d_i\phi_{i,\eta}\Big)^2 (\phi_{i,\eta})(\phi_{j,\eta}) \right.
$$
$$
+ \frac{1}{a^2b^2}\Big(\sum_{i=1}^{nw} d_i\phi_{i,\xi}\Big)^2 (\phi_{i,\eta})(\phi_{j,\eta}) + \frac{1}{a^2b^2}\Big(\sum_{i=1}^{nw} d_i\phi_{i,\eta}\Big)^2 (\phi_{j,\xi})(\phi_{j,\xi})
$$
$$
+ \frac{2}{a^3}\Big(\sum_{i=nw+1}^{nw+nu} d_i\alpha_{i-nw,\xi}\Big)(\phi_{i,\xi})(\phi_{j,\xi}) + \frac{2}{b^3}\Big(\sum_{i=nw+nu+1}^{nw+nu+nv} d_i\beta_{i-nw-nu,\eta}\Big)(\phi_{i,\eta})(\phi_{j,\eta})
$$
$$
+ \frac{2\nu}{a^2b}\Big(\sum_{i=nw+nu+1}^{nw+nu+nv} d_i\beta_{i-nw-nu,\eta}\Big)(\phi_{i,\xi})(\phi_{j,\xi}) + \frac{2\nu}{ab^2}\Big(\sum_{i=nw+1}^{nw+nu} d_i\alpha_{i-nw,\xi}\Big)(\phi_{i,\eta})(\phi_{j,\eta})
$$
$$
+ \frac{(1-\nu)}{ab^2}\Big\{ \Big(\sum_{i=nw+1}^{nw+nu} d_i\alpha_{i-nw,\eta}\Big)(\phi_{i,\xi})(\phi_{j,\eta}) + \Big(\sum_{i=nw+1}^{nw+nu} d_i\alpha_{i-nw,\eta}\Big)(\phi_{i,\eta})(\phi_{j,\xi}) \Big\}
$$
$$
\left. + \frac{(1-\nu)}{a^2b}\Big\{ \Big(\sum_{i=nw+nu+1}^{nw+nu+nv} d_i\beta_{i-nw-nu,\xi}\Big)(\phi_{i,\xi})(\phi_{j,\eta}) + \Big(\sum_{i=nw+nu+1}^{nw+nu+nv} d_i\beta_{i-nw-nu,\xi}\Big)(\phi_{i,\eta})(\phi_{j,\xi}) \Big\} \right] d\xi d\eta,
$$

$$
[k_{21}^m] = \frac{E_p t_p}{2(1-\nu^2)}(ab) \sum_{j=nw+1}^{nw+nu} \sum_{i=1}^{nw} \int_0^1 \int_0^1 \left[\frac{1}{a^3}\Big(\sum_{i=1}^{nw} d_i\phi_{i,\xi}\Big)(\phi_{i,\xi})(\alpha_{j-nw,\xi}) \right.
$$
$$
\left. + \frac{\nu}{ab^2}\Big(\sum_{i=1}^{nw} d_i\phi_{i,\eta}\Big)(\phi_{i,\eta})(\alpha_{j-nw,\xi}) + \frac{(1-\nu)}{ab^2}\Big(\sum_{i=1}^{nw} d_i\phi_{i,\xi}\Big)(\phi_{i,\eta})(\alpha_{j-nw,\eta}) \right] d\xi d\eta,
$$

$$
[k_{22}^m] = \frac{E_p t_p}{2(1-\nu^2)}(ab) \sum_{j=nw+1}^{nw+nu} \sum_{i=nw+1}^{nw+nu} \int_0^1 \int_0^1 \left[\frac{2}{a^2}(\alpha_{i-nw,\xi})(\alpha_{j-nw,\xi}) \right.
$$
$$
\left. + \frac{(1-\nu)}{b^2}(\alpha_{i-nw,\eta})(\alpha_{j-nw,\eta}) \right] d\xi d\eta,
$$

$$
[k_{23}^m] = \frac{E_p t_p}{2(1-\nu^2)} \sum_{j=nw+1}^{nw+nu} \sum_{i=nw+nu+1}^{nw+nu+nv} \int_0^1 \int_0^1 \left[2\nu(\beta_{i-nw-nu,\eta})(\alpha_{j-nw,\xi}) \right.
$$
$$
\left. + (1-\nu)(\beta_{i-nw-nu,\xi})(\alpha_{j-nw,\eta}) \right] d\xi d\eta,
$$

$$
[k_{31}^m] = \frac{E_p t_p}{2(1-\nu^2)}(ab) \sum_{j=nw+nu+1}^{nw+nu+nv} \sum_{i=1}^{nw} \int_0^1 \int_0^1 \left[\frac{1}{b^3}\Big(\sum_{i=1}^{nw} d_i\phi_{i,\eta}\Big)(\phi_{i,\eta})(\beta_{j-nw-nu,\eta}) \right.
$$
$$
\left. + \frac{\nu}{a^2b}\Big(\sum_{i=1}^{nw} d_i\phi_{i,\xi}\Big)(\phi_{i,\xi})(\beta_{j-nw-nu,\eta}) + \frac{(1-\nu)}{a^2b}\Big(\sum_{i=1}^{nw} d_i\phi_{i,\xi}\Big)(\phi_{i,\eta})(\beta_{j-nw-nu,\xi}) \right] d\xi d\eta,
$$

$$
[k_{32}^m] = \frac{E_p t_p}{2(1-\nu^2)} \sum_{j=nw+nu+1}^{nw+nu+nv} \sum_{i=nw+1}^{nw+nu} \int_0^1 \int_0^1 \left[2\nu(\alpha_{i-nw,\xi})(\beta_{j-nw-nu,\eta}) \right.
$$
$$
\left. + (1-\nu)(\alpha_{i-nw,\eta})(\beta_{j-nw-nu,\xi}) \right] d\xi d\eta,
$$

$$[k_{33}^m] = \frac{E_p t_p}{2(1-v^2)}(ab) \sum_{j=nw+nu+1}^{nw+nu+nv} \sum_{i=nw+nu+1}^{nw+nu+nv} \int_0^1 \int_0^1 \left[\frac{2}{b^2}(\beta_{i-nw-nu,\eta})(\beta_{j-nw-nu,\eta}) \right. $$
$$\left. + \frac{(1-v)}{a^2}(\beta_{i-nw-nu,\xi})(\beta_{j-nw-nu,\xi}) \right] d\xi d\eta.$$

The form of $[K_{sx}]$ is

$$[K_{sx}] = \begin{bmatrix} k_{11}^{sx} & k_{12}^{sx} & 0 \\ k_{21}^{sx} & k_{22}^{sx} & 0 \\ 0 & 0 & k_{33}^{sx} \end{bmatrix},$$

where

$$[k_{11}^{sx}] = \sum_{p=1}^{ns_x} \left[\frac{E_s a}{2} \sum_{j=1}^{nw} \sum_{i=1}^{nw} \int_0^1 \left\{ \frac{2(I_y^p + A_y^p e_x^{p2})}{a^4}(\phi_{i,\xi\xi})(\phi_{j,\xi\xi}) - Q_y^p \frac{2}{a^4}\left(\sum_{i=1}^{nw} d_i \phi_{i,\xi}\right)^2 (\phi_{i,\xi\xi})(\phi_{j,\xi}) \right.\right.$$
$$\left.- Q_y^p \frac{1}{a^4}\left(\sum_{i=1}^{nw} d_i \phi_{i,\xi}\right)(\phi_{i,\xi})(\phi_{j,\xi\xi}) + A_y^p \frac{1}{a^4}\left(\sum_{i=1}^{nw} d_i \phi_{i,\xi}\right)^2 (\phi_{i,\xi})(\phi_{j,\xi})\right.$$
$$\left.\left. + A_y^p \frac{2}{a^3}\left(\sum_{i=nw+1}^{nw+nu} d_i \alpha_{i-nw,\xi}\right)^2 (\phi_{i,\xi})(\phi_{j,\xi}) \right\} d\xi \right],$$

$$[k_{12}^{sx}] = \sum_{p=1}^{ns_x} \left[\frac{E_s a}{2} \sum_{j=1}^{nw} \sum_{i=nw+1}^{nw+nu} \int_0^1 \left\{ -Q_y^p \frac{2}{a^3}(\alpha_{i-nw,\xi})(\phi_{j,\xi\xi}) \right\} d\xi \right],$$

$$[k_{21}^{sx}] = \sum_{p=1}^{ns_x} \left[\frac{E_s a}{2} \sum_{j=nw+1}^{nw+nu} \sum_{i=1}^{nw} \int_0^1 \left\{ -Q_y^p \frac{2}{a^3}(\phi_{i,\xi\xi})(\alpha_{j-nw,\xi}) + A_y^p \frac{1}{a^3}\left(\sum_{i=1}^{nw} d_i \phi_{i,\xi}\right)(\phi_{i,\xi})(\alpha_{j-nw,\xi}) \right\} d\xi \right],$$

$$[k_{22}^{sx}] = \sum_{p=1}^{ns_x} \left[\frac{E_s a}{2} \sum_{j=nw+1}^{nw+nu} \sum_{i=nw+1}^{nw+nu} \int_0^1 \left\{ A_y^p \frac{2}{a^2}(\alpha_{i-nw,\xi})(\alpha_{j-nw,\xi}) \right\} d\xi \right],$$

$$[k_{33}^{sx}] = \sum_{p=1}^{ns_x} \left[\frac{E_s a}{2} \sum_{j=nw+nu+1}^{nw+nu+nv} \sum_{i=nw+nu+1}^{nw+nu+nv} \int_0^1 \left\{ \frac{2(I_{yz}^p + A_y^p (b\eta_{stf}^p)^2)}{a^4}(\beta_{i-nw-nu,\xi})(\beta_{j-nw-nu,\xi}) \right\} d\xi \right].$$

The form of $[K_{sy}]$ is

$$[K_{sy}] = \begin{bmatrix} k_{11}^{sy} & 0 & k_{13}^{sy} \\ 0 & k_{22}^{sy} & 0 \\ k_{31}^{sy} & 0 & k_{33}^{sy} \end{bmatrix},$$

where

$$[k_{11}^{sy}] = \sum_{q=1}^{ns_y} \left[\frac{E_s b}{2} \sum_{j=1}^{nw} \sum_{i=1}^{nw} \int_0^1 \left\{ \frac{2(I_x^q + A_x^q e_y^{q2})}{b^4}(\phi_{i,\eta\eta})(\phi_{j,\eta\eta}) - Q_x^q \frac{2}{b^4}\left(\sum_{i=1}^{nw} d_i \phi_{i,\eta}\right)^2 (\phi_{i,\eta\eta})(\phi_{j,\eta}) \right.\right.$$
$$\left.- Q_x^q \frac{1}{b^4}\left(\sum_{i=1}^{nw} d_i \phi_{i,\eta}\right)(\phi_{i,\eta})(\phi_{j,\eta\eta}) + A_x^q \frac{1}{b^4}\left(\sum_{i=1}^{nw} d_i \phi_{i,\eta}\right)^2 (\phi_{i,\eta})(\phi_{j,\eta})\right.$$
$$\left.\left. + A_x^q \frac{2}{b^3}\left(\sum_{i=nw+1}^{nw+nu} d_i \beta_{i-nw,\eta}\right)^2 (\phi_{i,\eta})(\phi_{j,\eta}) \right\} d\eta \right],$$

$$[k_{22}^{sy}] = \sum_{q=1}^{ns_y} \left[\frac{E_s b}{2} \sum_{j=nw+1}^{nw+nu} \sum_{i=nw+1}^{nw+nu} \int_0^1 \left\{ \frac{2(I_{xz}^q + A_x^q (a\xi_{stf}^q)^2)}{b^4} (\alpha_{i-nw,\eta\eta})(\alpha_{j-nw,\eta\eta}) \right\} d\eta \right],$$

$$[k_{33}^{sy}] = \sum_{q=1}^{ns_y} \left[\frac{E_s b}{2} \sum_{j=nw+nu+1}^{nw+nu+nv} \sum_{i=nw+nu+1}^{nw+nu+nv} \int_0^1 \left\{ A_x^q \frac{2}{b^2} (\beta_{i-nw-nu,\eta})(\beta_{j-nw-nu,\eta}) \right\} d\eta \right],$$

$$[k_{31}^{sy}] = \sum_{q=1}^{ns_y} \left[\frac{E_s b}{2} \sum_{j=nw+nu+1}^{nw+nu+nv} \sum_{i=1}^{nw} \int_0^1 \left\{ -Q_x^q \frac{2}{b^3} (\phi_{i,\eta\eta})(\beta_{j-nw-nu,\eta}) \right. \right.$$
$$\left. \left. + A_x^q \frac{1}{b^3} \left(\sum_{i=1}^{nw} d_i \phi_{i,\eta} \right)(\phi_{i,\eta})(\beta_{j-nw-nu,\eta}) \right\} d\eta \right],$$

$$[k_{13}^{sy}] = \sum_{q=1}^{ns_y} \left[\frac{E_s b}{2} \sum_{j=1}^{nw} \sum_{i=nw+nu+1}^{nw+nu+nv} \int_0^1 \left\{ -Q_x^q \frac{2}{b^3} (\beta_{i-nw-nu,\eta})(\phi_{j,\eta\eta}) \right\} d\eta \right].$$

The load vector $\{f\}$ is of the form $\{f\} = \{f_{11} \ f_{12} \ f_{13}\}^T$, where $\{f_{11}\} = p(ab) \sum_{j=1}^{nw} \int_0^1 \int_0^1 \phi_j \, d\xi d\eta$, $\{f_{12}\} = \{f_{13}\} = 0$. In the present analysis, results are individually generated for uniformly distributed load $\left(\{f_{11}\} = p(ab) \sum_{j=1}^{nw} \int_0^1 \int_0^1 \phi_j \, d\xi d\eta \right)$.

List of symbols

a, b	length and width of the plate
b_{sx}^p, b_{sy}^p	width of p-th stiffener along the x- and y-directions
$\{d\}$	vector of unknown coefficients
e_x^p, e_y^p	eccentricity of p-th stiffener along the x- direction and y-directions
E_p	elastic modulus of the plate material
E_s	elastic modulus of the stiffener material
$\{f\}$	load vector
$[K]$	stiffness matrix
$[K_b]$	stiffness matrix due to bending
$[K_m]$	stiffness matrix due to stretching
$[K_{sx}]^p, [K_{sy}]^p$	stiffness matrices of the p-th stiffener along the x- and y-directions
$[M]$	mass matrix
$[M_p]$	mass matrix for plate
$[M_{sx}], [M_{sy}]$	mass matrix for the x and y-direction stiffeners
ns_x, ns_y	number of stiffeners in the x and y-directions
nw, nu, nv	number of constituent functions for w, u, and v
p	uniformly distributed transverse load
P	concentrated transverse load
t_p	thickness of the plate
t_{sx}^p, t_{sy}^p	thickness of p-th stiffener along the x- and y-directions
T	total kinetic energy of the system

T_p	kinetic energy of the plate
T_s	total kinetic energy of the stiffeners
T_{sx}^p, T_{sy}^p	kinetic energy of the p-th stiffener along the x- and y-directions
u, v, w	displacement along the x, y, and z-directions
U	total strain energy of the system
U_b	strain energy due to bending of the plate
U_m	strain energy due to stretching of the plate
U_p	strain energy of the plate
U_s	strain energy of the stiffeners
U_{sx}^p, U_{sy}^p	strain energy of the p-th stiffener along the x- and y-directions
V	work potential
$x_{\text{stf}}^p, y_{\text{stf}}^p$	position of p-th stiffener along the x- and y-directions
α_i	set of functions defining approximate displacement field u
β_i	set of functions defining approximate displacement field v
δ	variational operator
ε	predefined value of error limit for the iteration scheme
ϕ_i	set of functions defining approximate displacement field w
η	normalized coordinates in the y-direction
λ	relaxation parameter
ρ_p, ρ_s	density of the plate and stiffener material
τ	time coordinate
ν	Poisson's ratio
ω	natural frequency of the system
ω_1	first linear natural frequency
ω_{nl}	nonlinear frequency
ξ	normalized coordinates in the x-direction

References

[Aksu 1982] G. Aksu, "Free vibration analysis of stiffened plates by including the effect of inplane inertia", *J. Appl. Mech.* (*ASME*) **49**:1 (1982), 206–212.

[Aksu and Ali 1976] G. Aksu and R. Ali, "Free vibration analysis of stiffened plates using finite difference method", *J. Sound Vib.* **48**:1 (1976), 15–25.

[Bapu Rao et al. 1978] M. N. Bapu Rao, P. Guruswamy, M. V. Rao, and S. Pavithran, "Studies on vibration of some rib-stiffened cantilever plates", *J. Sound Vib.* **57**:3 (apr 1978), 389–402.

[Barrette et al. 2000] M. Barrette, A. Berry, and O. Beslin, "Vibration of stiffened plates using hierarchical trigonometric functions", *J. Sound Vib.* **235**:5 (2000), 727–747.

[Bedair 1997a] O. K. Bedair, "Analysis of stiffened plates under lateral loading using sequential quadratic programming (SQP)", *Comput. Struct.* **62**:1 (1997), 63–80.

[Bedair 1997b] O. K. Bedair, "Fundamental frequency determination of stiffened plates using sequential quadratic programming", *J. Sound Vib.* **199**:1 (1997), 87–106.

[Bedair and Troitsky 1997] O. K. Bedair and M. S. Troitsky, "A study of the fundamental frequency characteristics of eccentrically and concentrically simply supported stiffened plates", *Int. J. Mech. Sci.* **39**:11 (1997), 1257–1272.

[Bikri et al. 2003] K. E. Bikri, R. Benamar, and M. Bennouna, "Geometrically non-linear free vibrations of clamped simply supported rectangular plates. Part I: the effects of large vibration amplitudes on the fundamental mode shape", *Comput. Struct.* **81**:20 (2003), 2029–2043.

[Blevins 1981] R. D. Blevins, *Formulas for the Natural Frequency and Mode Shape*, Van Nostrand, New York, 1981.

[Chen et al. 1994] C. J. Chen, W. Liu, and S. M. Chern, "Vibration analysis of stiffened plates", *Comput. Struct.* **50**:4 (1994), 471–480.

[Cook et al. 1989] R. D. Cook, D. S. Malkus, and M. E. Plesha, *Concepts and Applications of Finite Element Analysis*, Wiley, 1989.

[Crandall 1956] S. H. Crandall, *Engineering Analysis: A Survey of Numerical Procedures*, McGrawMHill, 1956.

[Das et al. 2009] D. Das, P. Sahoo, and K. Saha, "Nonlinear vibration analysis of clamped skew plates by a variational method", *J. Vib. Control* **15**:7 (2009), 985–1017.

[Deb Nath et al. 2010] S. K. Deb Nath, S. R. Ahmed, and S.-G. Kim, "Analytical solution of a stiffened orthotropic plate using alternative displacement potential approach", *J. Aerospace Eng.* **224**:1 (2010), 89–99.

[Dozio and Ricciardi 2009] L. Dozio and M. Ricciardi, "Free vibration analysis of ribbed plates by a combined analytical-numerical method", *J. Sound Vib.* **319**:1-2 (2009), 681–697.

[Harik and Guo 1993] I. E. Harik and M. Guo, "Finite element analysis of eccentrically stiffened plates in free vibration", *Comput. Struct.* **49**:6 (1993), 1007–1015.

[Irie et al. 1982] T. Irie, G. Yamada, and H. Ida, "Free vibration of a stiffened trapezoidal cantilever plate", *J. Acoust. Soc. Am.* **72** (1982), 1508–1513.

[Koko and Olson 1992] T. S. Koko and M. D. Olson, "Vibration analysis of stiffened plates by super elements", *J. Sound Vib.* **158**:1 (1992), 149–167.

[Leissa 1973] A. W. Leissa, "The free vibration of rectangular plates", *J. Sound Vib.* **31**:3 (1973), 257–293.

[Mukherjee and Mukhopadhyay 1986] A. Mukherjee and M. Mukhopadhyay, "A review of dynamic behavior of stiffened plates", *Shock Vib. Digest* **18**:6 (1986), 3–8.

[Mukherjee and Mukhopadhyay 1988] A. Mukherjee and M. Mukhopadhyay, "Finite element free vibration of eccentrically stiffened plates", *Comput. Struct.* **30**:6 (1988), 1303–1317.

[Peng et al. 2006] L. X. Peng, K. M. Liew, and S. Kitipornchai, "Buckling and free vibration analyses of stiffened plates using the FSDT mesh-free method", *J. Sound Vib.* **289**:3 (2006), 421–449.

[Prathap and Varadan 1978] G. Prathap and T. K. Varadan, "Large amplitude flexural vibration of stiffened plates", *J. Sound Vib.* **57**:4 (1978), 583–593.

[Rao et al. 1993a] D. V. Rao, A. H. Sheikh, and M. Mukhopadhyay, "A finite element large displacement analysis of stiffened plates", *Comput. Struct.* **47**:6 (1993), 987–993.

[Rao et al. 1993b] S. R. Rao, A. H. Sheikh, and M. Mukhopadhyay, "Large-amplitude finite element flexural vibration of plates/stiffened plates", *J. Acoust. Soc. Am.* **93** (1993), 3250–3257.

[Reddy 2002] J. N. Reddy, *Energy principles and variational methods in applied mechanics*, John Wiley & Sons Inc, 2002.

[Rossi et al. 1998] R. E. Rossi, D. V. Bambill, and P. A. A. Laura, "Vibrations of a rectangular orthotropic plate with a free edge: A comparison of analytical and numerical results", *Ocean Eng.* **25**:7 (1998), 521–527.

[Saha et al. 2004] K. N. Saha, D. Misra, G. Pohit, and S. Ghosal, "Large amplitude free vibration study of square plates under different boundary conditions through a static analysis", *J. Vib. Control* **10**:7 (2004), 1009–1028.

[Sapountzakis and Mokos 2008] E. J. Sapountzakis and V. G. Mokos, "An improved model for the dynamic analysis of plates stiffened by parallel beams", *Eng. Struct.* **30**:6 (2008), 1720–1733.

[Sheikh and Mukhopadhyay 2000] A. H. Sheikh and M. Mukhopadhyay, "Geometric nonlinear analysis of stiffened plates by the spline finite strip method", *Comput. Struct.* **76**:6 (2000), 765–785.

[Shuyu 2001] L. Shuyu, "Study on the flexural vibration of rectangular thin plates with free boundary conditions", *J. Sound Vib.* **239**:5 (2001), 1063–1071.

[Varadan and Pandalai 1979] T. K. Varadan and K. A. V. Pandalai, "Large amplitude flexural vibration of eccentrically stiffened plates", *J. Sound Vib.* **67**:3 (1979), 329–340.

[Vörös 2009] G. M. Vörös, "Buckling and free vibration analysis of stiffened panels", *Thin-Walled Struct.* **47**:4 (2009), 382–390.

[Wang and Xu 2010] X. Wang and S. Xu, "Free vibration analysis of beams and rectangular plates with free edges by the discrete singular convolution", *J. Sound Vib.* **329**:10 (2010), 1780–1792.

[Xu et al. 2010] H. Xu, J. Du, and W. L. Li, "Vibrations of rectangular plates reinforced by any number of beams of arbitrary lengths and placement angles", *J. Sound Vib.* **329**:18 (2010), 3759–3779.

[Zeng and Bert 2001] H. Zeng and C. W. Bert, "A differential quadrature analysis of vibration for rectangular stiffened plates", *J. Sound Vib.* **241**:2 (2001), 247–252.

ANIRBAN MITRA: samik893@gmail.com
Department of Mechanical Engineering, Jadavpur University, Kolkata 700 032, India

PRASANTA SAHOO: psjume@gmail.com
Department of Mechanical Engineering, Jadavpur University, Kolkata 700 032, India

KASHINATH SAHA: kashinathsaha@gmail.com
Department of Mechanical Engineering, Jadavpur University, Kolkata 700 032, India
http://www.jaduniv.edu.in/profile.php?uid=490

msp

DYNAMIC BEHAVIOR OF MAGNETOSTRICTIVE/PIEZOELECTRIC LAMINATE CYLINDRICAL SHELLS DUE TO ELECTROMAGNETIC FORCE

B. BIJU, N. GANESAN AND K. SHANKAR

The effect of electromagnetic force on the dynamic response of magnetostrictive/piezoelectric laminate cylindrical shells is addressed using a semianalytical finite element method. The electric field is represented using electric scalar potential and the magnetic field by magnetic vector potentials. The electric field acting on the charged particles of a moving conductor is derived from the Lorentz force. The mechanical force generated by the interaction of the derived current density with the magnetic field is accounted for in the successive load steps using an iterative solution technique. The Terfenol-D/PZT configuration of the laminate is analyzed for the first circumferential harmonics of the shell structure with a clamped-free boundary condition. The effect of electromagnetic force on the dynamic response is marginal at normal operating conditions but numerical studies suggest that the magnetoelectric effect is significantly influenced by a small increase in magnetic potential at increased velocities of the shell.

1. Introduction

Magnetostrictive/piezoelectric laminates have attracted attention for their magnetoelectric effects, originating from the electroelastic and magnetoelastic couplings inherent in the material. The composite consists of a piezoelectric phase, showing a coupling between the mechanical and electric fields, and a piezomagnetic phase, showing a coupling between the mechanical and magnetic fields. In addition, a magnetoelectric coupling effect, which is absent in the constituent phases, is exhibited by this class of materials. This unique feature allows magnetic control of electric polarization, electric control of magnetization, and control of electric and magnetic fields with mechanical stress, which make the material suitable for a wide range of applications such as magnetic field probes, medical ultrasound imaging, sensors, actuators, and so on.

The magnetoelectric properties of laminate composites of magnetostrictive/piezoelectric materials were investigated in [Ryu et al. 2001]. In [Sunar et al. 2002] the finite element modeling of a fully coupled thermopiezomagnetic medium using a thermodynamic potential was presented. A magnetic vector potential is needed to derive the elemental matrices using the above formulation. An analytical solution for the transient response of a magnetoelectroelastic hollow cylinder was presented in [Hou and Leung 2004], where a plain strain condition with axisymmetric loading was used so that radial displacement only was considered to derive the solution. In [Dai and Wang 2006] an analytical solution was presented for the transient response of a magnetoelectroelastic hollow cylinder placed in an axial magnetic field subjected to thermal shock, mechanical load, and transient electric excitation. The finite element formulation of MEE cylindrical shells using the magnetic vector potential in cylindrical coordinates was done in [Biju et al. 2010]. In [Shindo et al. 2010] the nonlinear electromagnetomechanical

behavior of a magnetostrictive/piezoelectric laminate under a magnetic field was studied both numerically and experimentally.

The effect of electromagnetic force on the dynamic response of magnetostrictive/piezoelectric laminate cylindrical shells is addressed using a semianalytical finite element method in this paper. Dynamic loading will generate time-changing electric and magnetic fields in multifunctional smart materials. The electric field is represented using the electric scalar potential and modeling of the magnetic field is done using the magnetic vector potential in cylindrical coordinates. The current density acting on the charged particles of a moving conductor is evaluated using Ohm's law. The mechanical force generated by the interaction of the derived current density with the magnetic field is calculated using the Lorentz force equation and accounted for in the successive load steps using an iterative solution technique. Magneto-strictive Terfenol-D ($Tb_{0.3}Dy_{0.7}Fe_2$) and piezoelectric PZT ($Pb(Zr,Ti)O_3$) layers are used for modeling the axisymmetric cylindrical shell.

2. Theoretical formulation

2.1. *Constitutive equations.* The constitutive equations for the magnetostrictive/piezoelectric laminate in a cylindrical coordinate system (r, θ, z) relating stress σ_j, electric displacement D_l, and magnetic field intensity H_l to strain S_k, electric field E_m, and magnetic flux density B_m, exhibiting linear coupling between magnetic, electric, and elastic fields, can be written as (see [Shindo et al. 2010])

$$\sigma_j = C_{jk}S_k - e_{jm}E_m, \quad D_l = e_{lj}S_k - \epsilon_{lm}E_m, \tag{1}$$

for piezoelectric behavior and

$$\sigma_j = C_{jk}S_k - d_{jm}B_m, \quad H_l = -d_{lj}S_k - \mu_{lm}^{-1}B_m, \tag{2}$$

for magnetostrictive behavior. C_{jk}, ϵ_{lm}, and μ_{lm} are elastic, dielectric, and magnetic permeability coefficients, respectively, and e_{jl} and d_{jl} are the piezoelectric and piezomagnetic material coefficients ($d_{jl} = q_{jl}\mu_{lm}^{-1}$). Here $j, k = 1, \ldots, 6$ and $l, m = 1, \ldots, 3$.

2.2. *Finite element modeling of electric and magnetic fields.* The mechanical displacements, electric scalar potential, and magnetic vector potentials are expressed using Fourier series in the circumferential direction:

$$u_r = \sum u_r^n \cos n\theta, \qquad u_\theta = \sum u_\theta^n \sin n\theta, \qquad u_z = \sum u_z^n \cos n\theta, \qquad \phi = \sum \phi^n \cos n\theta, \quad \text{(3a)}$$

$$A_r = \sum A_r^n \cos n\theta, \qquad A_\theta = \sum A_\theta^n \sin n\theta, \qquad A_z = \sum A_z^n \cos n\theta, \tag{3b}$$

where u_r, u_θ, and u_z are the radial, circumferential, and axial displacements, ϕ is the electric scalar potential, and A_r, A_θ, and A_z are the radial, circumferential, and axial components of the magnetic vector potential as nodal variables, respectively. Superscript n denotes the symmetric components of the primary variables: thus u_r^n, u_θ^n, u_z^n, ϕ^n, A_r^n, A_θ^n, and A_z^n.

The displacements $\{u\} = \{u_r, u_\theta, u_z\}^T$, electric potential ($\phi$), and magnetic potential $\{A\} = \{A_r, A_\theta, A_z\}^T$ within the element can be expressed in terms of suitable shape functions:

$$\{u\} = [N_u]\{u^e\}, \quad \phi = [N_\phi]\{\phi^e\}, \quad \{A\} = [N_A]\{A^e\}. \tag{4}$$

The strains can be related to the nodal degree of freedom by the following expression:

$${S} = [Bu]{u^e},\tag{5}$$

where $[B_u]$, the strain displacement matrix, can be written as

$$[B_u] = \begin{bmatrix} \dfrac{\partial N_1}{\partial r} & 0 & 0 & \cdots \\[2mm] \dfrac{N_1}{r} & \dfrac{nN_1}{r} & 0 & \cdots \\[2mm] 0 & 0 & \dfrac{\partial N_1}{\partial z} & \cdots \\[2mm] 0 & \dfrac{\partial N_1}{\partial z} & -\dfrac{nN_1}{r} & \cdots \\[2mm] \dfrac{\partial N_1}{\partial z} & 0 & \dfrac{\partial N_1}{\partial r} & \cdots \\[2mm] -\dfrac{nN_1}{r} & \dfrac{\partial N_1}{\partial r} - \dfrac{N_1}{r} & 0 & \cdots \end{bmatrix}.\tag{6}$$

Using the Maxwell's relation, the electric field vector can be expressed as

$$\begin{Bmatrix} E_r \\ E_\theta \\ E_z \end{Bmatrix} = \begin{Bmatrix} -\dfrac{\partial \phi}{\partial r} \\[2mm] -\dfrac{1}{r}\dfrac{\partial \phi}{\partial \theta} \\[2mm] -\dfrac{\partial \phi}{\partial z} \end{Bmatrix} - \begin{Bmatrix} \dot{A}_r \\ \dot{A}_\theta \\ \dot{A}_z \end{Bmatrix}, \quad {E} = -[\nabla N_\phi]{\phi_e} - [N_A]{\dot{A}_e} = [B_\phi]{\phi^e} - [N_A]{\dot{A}_e}.\tag{7}$$

The derivative of the shape function matrix $[B_\phi]$ matrix is written as

$$[B_\phi] = \begin{bmatrix} -\dfrac{\partial N_1}{\partial r} & -\dfrac{\partial N_2}{\partial r} & -\dfrac{\partial N_3}{\partial r} & -\dfrac{\partial N_4}{\partial r} \\[2mm] \dfrac{nN_1}{r} & \dfrac{nN_2}{r} & \dfrac{nN_3}{r} & \dfrac{nN_4}{r} \\[2mm] -\dfrac{\partial N_1}{\partial z} & -\dfrac{\partial N_2}{\partial z} & -\dfrac{\partial N_3}{\partial z} & -\dfrac{\partial N_4}{\partial z} \end{bmatrix}.\tag{8}$$

Recalling Maxwell's relations,

$$B = \nabla \times A, \quad \nabla \times H = J_0 + \frac{\partial D}{\partial t},\tag{9}$$

where J_0 is the current supplied by an external source and $\partial D/\partial t$ is the displacement current. When dynamic mechanical loading is present, including the effect of the motion of the conductor, Ohm's law can be written as

$$J = \sigma\left\{E + \frac{\partial u}{\partial t} \times B\right\} + J_0,\tag{10}$$

where J is the total current density and σ is the electrical conductivity of the material.

In cylindrical coordinates

$$\nabla \times A = \hat{r}\left(\frac{1}{r}\frac{\partial A_z}{\partial \theta} - \frac{\partial A_\theta}{\partial z}\right) + \hat{\theta}\left(\frac{1}{r}\frac{\partial A_r}{\partial z} - \frac{\partial A_z}{\partial r}\right) + \hat{z}\frac{1}{r}\left(\frac{\partial r A_\theta}{\partial r} - \frac{\partial A_r}{\partial \theta}\right).\tag{11}$$

The magnetic flux density vector can be expressed as

$$
\begin{Bmatrix} B_r \\ B_\theta \\ B_z \end{Bmatrix} = \begin{Bmatrix} \dfrac{1}{r}\dfrac{\partial A_z}{\partial \theta} - \dfrac{\partial A_\theta}{\partial z} \\[2mm] \dfrac{1}{r}\dfrac{\partial A_r}{\partial z} - \dfrac{\partial A_z}{\partial r} \\[2mm] \dfrac{1}{r}\left(\dfrac{\partial r A_\theta}{\partial r} - \dfrac{\partial A_r}{\partial \theta}\right) \end{Bmatrix}, \quad \{B\} = [B_A]\{A_e\},
\tag{12}
$$

where the derivative of shape function matrix $[B_A]$ is written as

$$
B_A = \begin{bmatrix} 0 & \dfrac{\partial N_1}{\partial z} & \dfrac{nN_1}{r} & \cdots \\[3mm] \dfrac{\partial N_1}{\partial z} & 0 & -\dfrac{\partial N_1}{\partial r} & \cdots \\[3mm] \dfrac{nN_1}{r} & \dfrac{1}{r}\dfrac{\partial (rN_1)}{\partial r} & 0 & \cdots \end{bmatrix}.
\tag{13}
$$

3. Evaluation of elemental matrices

The finite element equations for magnetostrictive/piezoelectric laminate cylindrical shell can be written as

$$
[M_{uu}^e]\{\ddot{u}^e\} + [C_{uu}^e]\{\dot{u}^e\} + [C_{uA}^e]\{\dot{A}^e\} + [K_{uu}^e]\{u^e\} + [K_{u\phi}^e]\{\phi^e\} - [K_{uA}^e]\{A^e\} = \{F^e\},
$$
$$
[K_{\phi u}^e]\{u^e\} - [K_{\phi\phi}^e]\{\phi^e\} = \{G^e\}, \quad -[K_{Au}^e]\{u^e\} - [C_{\phi A}^e]\{\dot{A}^e\} + [K_{AA}^e]\{A^e\} = \{M^e\},
\tag{14}
$$

where $\{F^e\}$, $\{G^e\}$, and $\{M^e\}$ correspond to elemental load vectors of applied mechanical force, electric charge, and magnetic current, respectively. Different elemental matrices in (14) for the n-th harmonic are defined as

$$
[M_{uu}^e] = P\int_A [N_u]^T[\rho][N_u]\, r\, dr\, dz, \qquad [C_{uA}^e] = P\int_A [B_u]^T[e][N_A]\, r\, dr\, dz,
$$
$$
[C_{\phi A}^e] = P\int_A [B_\phi]^T[\epsilon][N_A]\, r\, dr\, dz, \qquad [K_{uu}^e] = P\int_A [B_u]^T[c][B_u]\, r\, dr\, dz,
$$
$$
[K_{u\phi}^e] = P\int_A [B_u]^T[e][B_\phi]\, r\, dr\, dz, \qquad [K_{uA}^e] = P\int_A [B_u]^T[d][B_A]\, r\, dr\, dz,
$$
$$
[K_{\phi\phi}^e] = P\int_A [B_\phi]^T[\epsilon][B_\phi]\, r\, dr\, dz, \qquad [K_{AA}^e] = P\int_A [B_A]^T[\mu]^{-1}[B_A]\, r\, dr\, dz,
\tag{15}
$$

where $P = 2\pi$ for $n = 0$ and $P = \pi$ for $n > 0$, and n is the circumferential harmonic number. When electric and magnetic loading are absent, (14) can be written in coupled form as

$$
\begin{bmatrix} M_{uu} & 0 & 0 \\ 0 & 0 & 0 \\ 0 & 0 & 0 \end{bmatrix} \begin{Bmatrix} \ddot{u} \\ \ddot{\phi} \\ \ddot{A} \end{Bmatrix} + \begin{bmatrix} C_{uu} & 0 & C_{uA} \\ 0 & 0 & -C_{\phi A} \\ 0 & 0 & 0 \end{bmatrix} \begin{Bmatrix} \dot{u} \\ \dot{\phi} \\ \dot{A} \end{Bmatrix} + \begin{bmatrix} K_{uu} & K_{u\phi} & -K_{uA} \\ K_{\phi u} & -K_{\phi\phi} & 0 \\ -K_{Au} & 0 & K_{AA} \end{bmatrix} \begin{Bmatrix} u \\ \phi \\ A \end{Bmatrix} = \begin{Bmatrix} F(t) \\ 0 \\ 0 \end{Bmatrix}.
\tag{16}
$$

The magnetic field generated due to mechanical loading will generate current density within the electrically conductive magnetostrictive layer. The finite element equation for current density can be written as

$$
\{J^e\} = P\int_A [N]^T \left\{ \sigma\left(\frac{\partial u}{\partial t} \times B\right) + J_0 \right\} r\, dr\, dz.
\tag{17}
$$

The vector of nodal Lorentz force can be written as

$$\{F^e\} = P \int_A [N]^T \{J \times B\} r \, dr \, dz. \tag{18}$$

This Lorentz force will generate an additional force vector in the equation of motion for the mechanical field. Simultaneous solution of (16) and (18) will account for the effect of the electromagnetic force on the dynamic response of the shell structure.

4. Results and discussions

4.1. *Validation.* Computer code has been developed to study the effect of electromagnetic force on electric and magnetic response of the structure. The dimensions of the cylinder used for the analysis are $L = 4.0$ m, $R_i = 0.5$ m, and the Terfenol-D and PZT-5A layers are 0.005 m each in thickness. A perfect bonding is assumed between layers and potential noise effects are neglected. The system of equations is solved using the Newmark-beta solution technique. The damping is assumed to be proportional and the damping matrix is derived as $[C_{uu}] = \alpha[M_{uu}] + \beta[K_{uu}]$ where α and β are the proportional damping coefficients depending on natural frequencies of the structure. Damping ratios of 1% and 2% are assumed for first and second modes, respectively, and the values of the proportional damping constants α and β are calculated accordingly.

A rectangular wave made up of a fundamental frequency and its combined odd and even harmonics is used as the load cycle. Each load step, the time increment is applied at 10 equal time intervals. The cylinder is subjected to a uniform internal pressure of $1 \, \text{N/m}^2$ with a clamped-free boundary condition. The electric and magnetic potentials are assumed to be zero at the clamped end. The load vectors corresponding to applied electric charge and magnetic current are also assumed to be zero. The absolute values of nodal velocity and magnetic flux density at the end of first load step are used for calculating the load vector for successive iterations. The results presented below are for the first circumferential harmonics of the shell structure ($n = 1$). A node near the clamped end of the shell giving maximum response is chosen for showing the results. The study is carried out for the Terfenol-D/PZT configuration of the laminate.

The commercial finite element package ANSYS 12.0 is used for the validation studies. The material properties of PZT-5A and Terfenol-D used for the analysis are shown in Tables 1 and 2. ANSYS cannot model fully coupled piezomagnetic material behavior and hence the present code is validated neglecting the piezomagnetic coupling. The response for the validation studies is calculated for the axisymmetric

Elastic constants ($\times 10^9 \, \text{N/m}^2$)					Density (kg/m^3)
C_{11}	C_{12}	C_{23}	$C_{22} = C_{33}$	$C_{44} = C_{66}$	ρ
94.23	40.38	40.38	94.23	26.92	9250
Magnetic permeability ($\times 10^{-6} \, \text{Ns}^2/\text{C}^2$)		Piezomagnetic constants (N/Am)			Electric conductivity ($\times 10^{10}\text{S/m}$)
μ_{11}	$\mu_{22} = \mu_{33}$	q_{11}	q_{12}	q_{35}	σ
6.29	6.29	400	−200	167.67	1.67

Table 1. Material properties of Terfenol-D [Olabi and Grunwald 2008] for radial plane of symmetry.
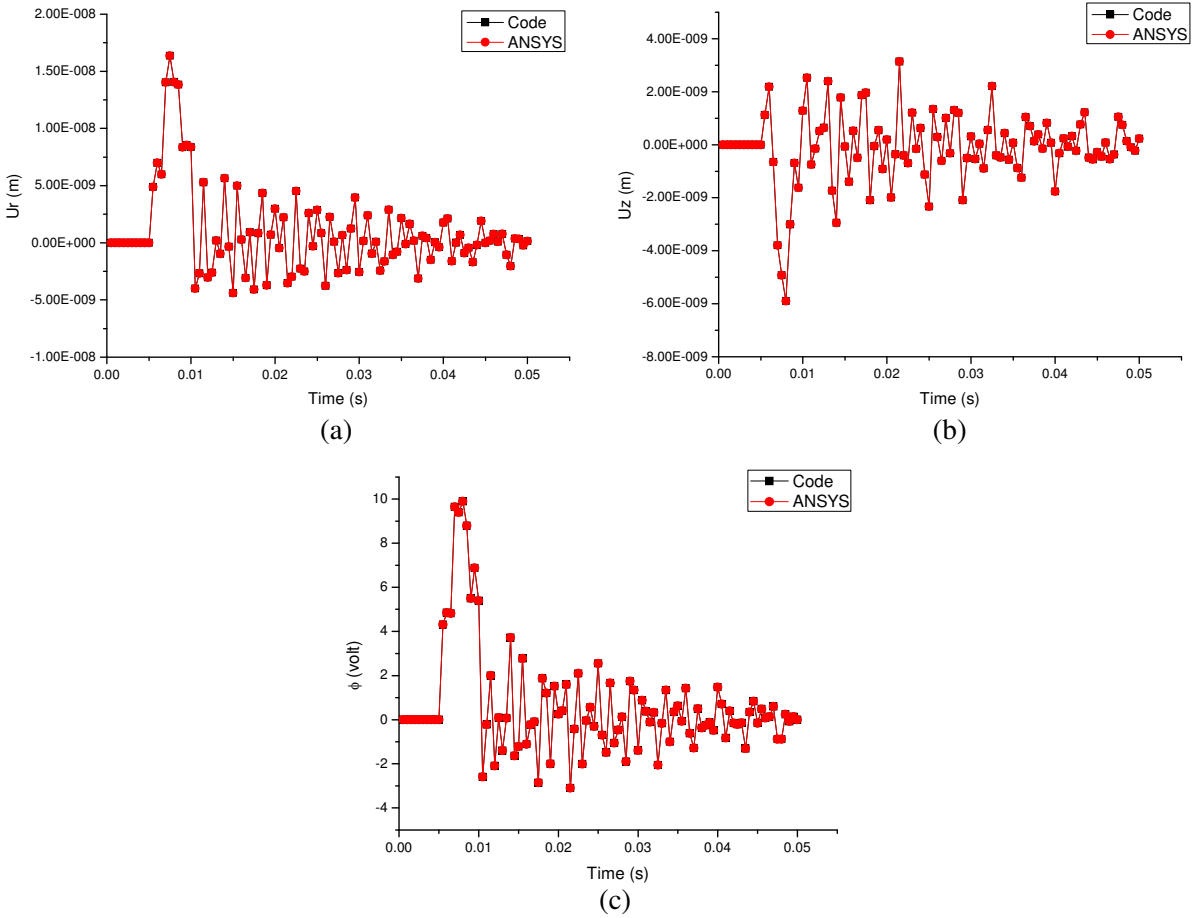
Figure 1. Validation of code for (a) radial displacement u_r, (b) axial displacement u_z, and (c) electric potential ϕ using code and ANSYS.

mode ($n = 0$) of the shell structure. The time harmonic response of the Terfenol-D/PZT laminate shell using our code and ANSYS is shown in Figure 1. It is seen that the result is in good agreement and hence the code is extended to study the dynamic response of fully coupled Terfenol-D/PZT laminate.

Elastic constants ($\times 10^9$ N/m^2)					Density (kg/m^3)
C_{11}	C_{12}	C_{23}	$C_{22} = C_{33}$	$C_{44} = C_{66}$	ρ
86.85	54.01	50.77	99.2	21.1	7750
Dielectric constants ($\times 10^{-9}$C/Vm)			Piezoelectric constants (C/m^2)		
ϵ_{11}	$\epsilon_{22} = \epsilon_{33}$		e_{11}	e_{12}	e_{35}
1.5	1.53		15.0	-7.2	12.32

Table 2. Material properties of PZT-5A [Chen et al. 2007] for radial plane of symmetry.
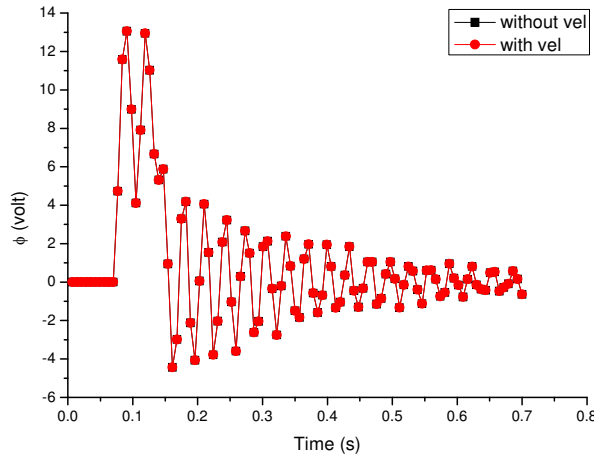
Figure 2. Variation of electric potential ϕ without and with consideration of the velocity effect.

4.2. *Dynamic response of clamped-free Terfenol-D/PZT shell.* The time harmonic response is calculated without considering the velocity effect and with the velocity effect after the first duty cycle of mechanical loading. Figure 2 represents the variation of electric potential (ϕ) of a node near the clamped end of the shell with and without considering the effect of velocity and the derived electromagnetic force. It is seen that there is no significant variation in the response when the dynamic electromagnetic force is accounted for. This is because the magnetic field generated due to piezomagnetic coupling of Terfenol-D is too small to influence the dynamic response.

Figure 3 shows the variation of the magnetic vector potential in the radial (A_r), circumferential (A_θ), and axial (A_z) directions without and with considering the effect of velocity in the dynamic response. It is seen that the axial component of the magnetic vector potential is the dominant component, so its influence on the electric field will be more in the axial direction.

The magnetic flux density generated in the radial (B_r), circumferential (B_θ), and axial (B_z) directions is shown in Figure 4a. The absolute value of the magnetic flux density in all directions is very small and among the three components, the circumferential component is the significant one. The nodal velocity variation in three directions is shown in Figure 4b.

Numerical studies are carried out by varying the nodal velocities and magnetic vector potentials, in order to understand the influence of velocity on generated electric potential. The nodal velocity and magnetic vector potential are increased independently and as a combination to study the influence of electromagnetic force on dynamic response. Figure 5a shows the variation of electric potential (ϕ) when the nodal velocity is increased from the initial value obtained in a transient analysis. A significant increase in electric potential is noticed when the nodal velocity reaches approximately 3.0 times the initial value. Similarly Figure 5b shows the variation of electric potential (ϕ) when the magnetic vector potential is increased; when the potential reaches 1.74 times the initial value, there is a marked increase. A combination of increase in velocity and magnetic potential is done on a trial and error basis and the variation of electric potential (ϕ) which is relevant in the present study is shown in Figure 5c. It is seen that when the nodal velocity is increased to 2.5 times the initial velocity, a 10% increase in magnetic vector potential will significantly increase the generated electric potential.
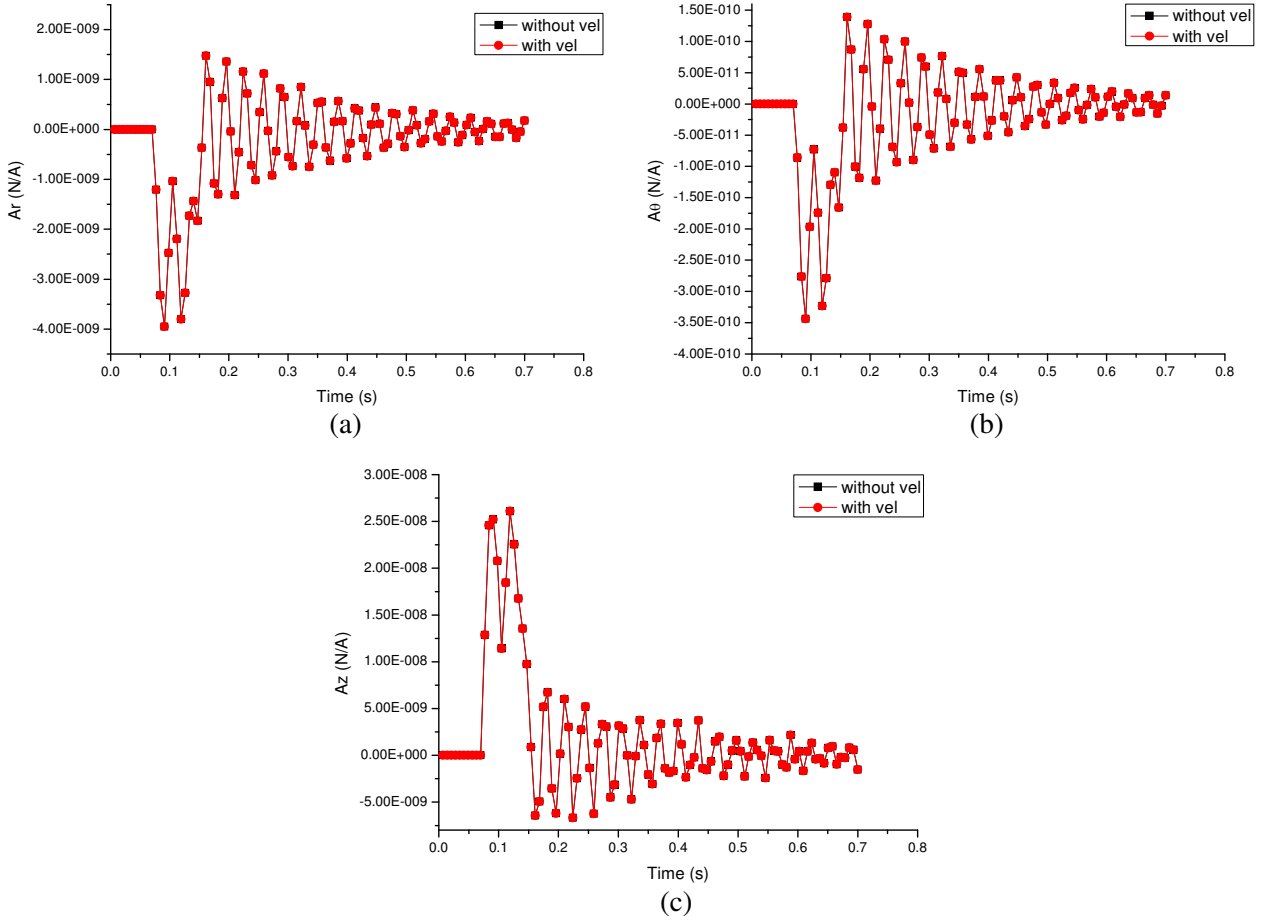
Figure 3. Variation of magnetic vector potential in (a) radial A_r, (b) circumferential A_θ, and (c) axial A_z directions without and with considering velocity effect.
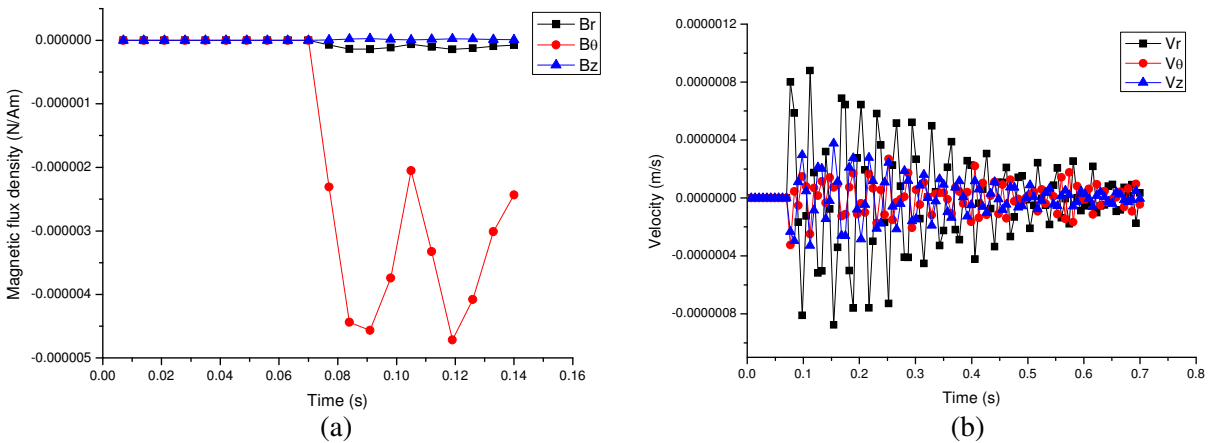

Figure 4. Variation of (a) magnetic flux density and (b) nodal velocity in radial, circumferential, and axial directions.
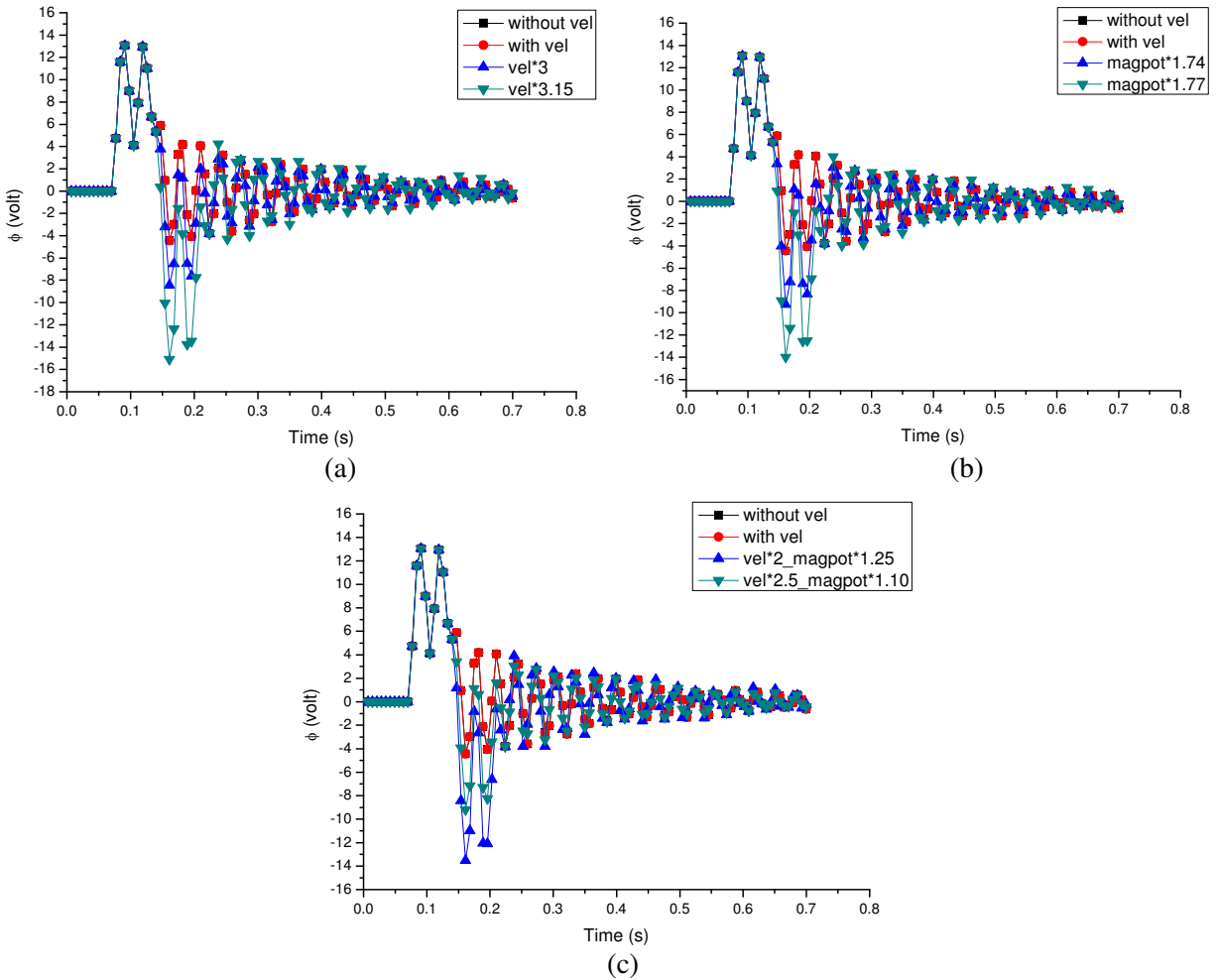
Figure 5. Variation of electric potential ϕ with (a) increased nodal velocity, (b) increased magnetic vector potential, and (c) a combination of both.

5. Conclusions

The dynamic response of magnetostrictive/piezoelectric laminate cylindrical shells subjected to uniform internal pressure is studied using a semianalytical finite element method. The Terfenol-D/PZT configuration of the laminate is analyzed for the first circumferential harmonics of the shell structure with a clamped-free boundary condition. Numerical studies are also carried out by varying the nodal velocities and magnetic vector potentials for understanding the influence of velocity on the generated electric potential. The effect of the electromagnetic Lorentz force on dynamic response is marginal at normal operating conditions, but numerical studies suggest that the magnetoelectric effect is significantly influenced by a small increase in magnetic potential at an increased velocity of the shell.

References

[Biju et al. 2010] B. Biju, N. Ganesan, and K. Shankar, "Finite element formulation using magnetic vector potential approach: effects of displacement current in magneto-electro-elastic cylindrical shells", *Smart Mater. Struct.* **19**:1 (2010), 015009.

[Chen et al. 2007] J. Chen, E. Pan, and H. Chen, "Wave propagation in magneto-electro-elastic multilayered plates", *Int. J. Solids Struct.* **44**:3–4 (2007), 1073–1085.

[Dai and Wang 2006] H. L. Dai and X. Wang, "Magneto-thermo-electro-elastic transient response in a piezoelectric hollow cylinder subjected to complex loadings", *Int. J. Solids Struct.* **43**:18–19 (2006), 5628–5646.

[Hou and Leung 2004] P.-F. Hou and A. Y. T. Leung, "The transient responses of magneto-electro-elastic hollow cylinders", *Smart Mater. Struct.* **13**:4 (2004), 762–776.

[Olabi and Grunwald 2008] A. G. Olabi and A. Grunwald, "Design and application of magnetostrictive materials", *Mater. Des.* **29**:2 (2008), 469–483.

[Ryu et al. 2001] J. Ryu, A. V. Carazo, K. Uchino, and H.-E. Kim, "Piezoelectric and magnetoelectric properties of lead zirconate titanate/Ni-ferrite particulate composites", *J. Electroceram.* **7**:1 (2001), 17–24.

[Shindo et al. 2010] Y. Shindo, K. Mori, and F. Narita, "Electromagneto-mechanical fields of giant magnetostrictive/piezoelectric laminates", *Acta Mech.* **212**:3–4 (2010), 253–261.

[Sunar et al. 2002] M. Sunar, A. Z. Al-Garni, M. H. Ali, and R. Kahraman, "Finite element modeling of thermopiezomagnetic smart structures", *AIAA J.* **40**:9 (2002), 1846–1851.

B. Biju: bbiju@rediffmail.com
Machine Design Section, Department of Mechanical Engineering, Indian Institute of Technology Madras, Chennai 600 036, India

N. Ganesan: nganesan@iitm.ac.in
Machine Design Section, Department of Mechanical Engineering, Indian Institute of Technology Madras, Chennai 600 036, India

K. Shankar: skris@iitm.ac.in
Machine Design Section, Department of Mechanical Engineering, Indian Institute of Technology Madras, Chennai 600 036, India

msp

GEOMETRICALLY NONLINEAR THERMOMECHANICAL RESPONSE OF CIRCULAR SANDWICH PLATES WITH A COMPLIANT CORE

YEOSHUA FROSTIG AND OLE THOMSEN

The geometrically nonlinear response of a circular sandwich plate that consists of two face sheets and a compliant ("soft") core with mechanical properties that may be either independent or dependent of temperature and subjected to both mechanical loads and thermal induced deformations, but remain elastic linear throughout the loading process, is presented. The mathematical formulation follows the principles of the high-order sandwich panel theory (HSAPT) and includes the vertical flexibility of the core in addition to the temperature dependency of the mechanical properties of the core material. The mathematical formulation outlines the set of governing partial differential equations as well the appropriate boundary conditions for a general sandwich layout. The particular case of an axisymmetric circular sandwich plate subjected to axisymmetric mechanical and thermal loads, and with axisymmetric boundary conditions is studied analytically and numerically. The numerical study includes an interaction of mechanical and thermal loads which is presented through results within the plate for various load levels of various structural quantities as well as equilibrium curves of temperatures versus these structural quantities. The results reveal that the combination of mechanical and thermal loads along with a compliant core material with mechanical properties that degrade with increasing temperatures shifts the behavior from a linear and stable (strength controlled) response into a strongly nonlinear response with limit point behavior and associated loss of stability, when large displacements and large rotations (geometrical nonlinearity) are included in the modeling.

1. Introduction

Lightweight sandwich structures are being used increasingly in the aerospace, naval and transportation industries due to their excellent stiffness-to-weight and strength-to-weight ratios. Typical sandwich structures are often composed of a low stiffness/strength (compliant or "soft") core material made of a polymeric foam or a Nomex® honeycomb that is flexible in the thickness direction, and laminated composite or metallic face sheets. The core usually provides the shear resistance/stiffness to the sandwich structure, as well as vertical (through-thickness) support to the face sheets that is associated with core vertical normal stresses. The use of compliant foam or Nomex core materials is often associated with localized effects such as indentation in case of localized, concentrated or line loads, abrupt geometrical changes or changes of mechanical properties as well as in the vicinity of stiff points such as inserts or supports. Thus, the low core through-thickness stiffness may be detrimental to the safety of a sandwich structure, either because of strength constraints such as stress allowables or due to loss of stability.

Sandwich structures are typically exposed to mechanical load as well as to aggressive environment

that may be associated with elevated temperature conditions. Traditionally, a typical design process of such structures examines separately the responses due to the mechanical and thermal loads, i.e., the deformations induced by thermal sources. However, the interaction between the mechanical and thermal loads may lead to an unsafe response with loss of stability and structural integrity, especially when the deformations are large and the mechanical properties such as stiffness and strength degrade as the temperature level is raised. This thermal degradation of the mechanical properties is especially pronounced for polymer foam core materials, where significant degradation of the mechanical properties may occur well within the operational temperature range. For example, PVC foams such as Divinycell® (see [DIAB 2003]) lose all stiffness and strength at about 80–100°C, while PMI (polymethacrylimide) foams such as Rohacell® (see [Rohacell 2004]) lose heat distortion resistance at about 200°C.

The effects of this degradation on the load-thermal interaction response are not well understood by researchers and industry. At the same time there is growing concern within the wind turbine blade, marine and aeronautical sectors that the simultaneous action of mechanical loads and elevated temperatures may compromise the structural integrity under certain circumstances. Hence, reliable computational models are needed for the accurate prediction of the load response of sandwich structures subjected to combine mechanical and thermal loads, including the thermal degradation of material properties as well as the nonlinear interactions between the mechanical and thermal loads. In the present paper such a model based on the principles of the high-order sandwich panel theory (HSAPT) is proposed for the case of circular sandwich plates.

Generally, two main categories are presented in the literature to describe the load response of sandwich structures. The first category assumes the sandwich structures to be compressible in the through-thickness direction, and the other category of models is based on the assumption of through-thickness incompressibility, i.e., infinite stiffness in the through-thickness direction, which is also known as antiplane core conditions; see [Allen 1969]. The majority of structural models assume that the core is incompressible; see for example the textbooks and review articles [Allen 1969; Plantema 1966; Zenkert 1995; Vinson 1999; Noor et al. 1996; Librescu and Hause 2000; Hohe and Librescu 2004]. However, in reality a sandwich structure is a layered structure with two face sheets and a core that compressible (has finite stiffness). The effect of the through-thickness core compressibility has been considered in through the use of the HSAPT models, and by others as well; see for example [Petras and Sutcliffe 2000]. A large number of computational models have been proposed based on the assumption of incompressible sandwich panels, and in most of these the layered sandwich assembly is replaced with an equivalent single layer (ESL); see for example [Mindlin 1951; Reddy 1984].

The same two categories of models — with compressible or incompressible core — have been proposed for circular sandwich plates. Computational models for sandwich plates with an incompressible core using the ESL approach have been considered for both static and dynamic applications by many researchers, including Selke [1971], who used the Reissner approach to analyze a mirror made of an annular sandwich plate resting on a ring; Montrey [1973], who used the split rigidities approach of [Allen 1969] to investigate the linear static response of a load introduced through an insert to a circular sandwich plate; Gupta and Sharma [1982], who used the zigzag approach of [Allen 1969]; and Wang [1995a; 1995b], who used Reissner–Mindlin first-order shear deformable theory for the analysis of radially symmetric circular plates. In all the references mentioned the core is assumed to be incompressible, and in most cases the problem considered is radially symmetric. Thermal effects have been considered by Kao [1970]

assuming that the core is incompressible, the face sheets are membranes, and the through-thickness shear is being carried by the core only.

Vibration analyses of circular sandwich plates been considered by many researchers, including Gupta and Jain [1982], who used first-order shear deformable plate theory (FOSDPT) to determine the dynamic response of a circular sandwich plate with a variable thickness assuming polynomial type of modes; Sherif [1992], who used a similar approach for the nonlinear dynamic problem where the core is viscoelastic and the modes are of polynomial type; and Du [1994] and Du and Li [2000] who discussed the radially symmetric large amplitude free vibration of circular sandwich plates assuming that the face sheets are membranes. Notice that the quoted models are limited to axisymmetric or isotropic plate behavior, to membrane action with no bending effects in the face sheets, and to incompressible cores. Zhou and Stronge [2006] used the FOSDPT approach assuming some special modes to deal with the vibration of a circular sandwich plate of a general layout.

The effect of the out of plane flexibility of the compressible core for circular plates has been considered in [Thomsen 1995; 1997; Thomsen and Rits 1998] using an elastic foundation and the HSAPT approaches, respectively. Rabinovitch and Frostig [2002a] used the HSAPT approach to investigate the response of a circular sandwich plates that are either fully bonded or debonded, and they used a similar approach to study the response of an reinforced concrete (RC) circular plate strengthened with a circular patch with an axisymmetric layup [2002b], with a general non-axisymmetric layout [2004a], and a with a delaminated patch [2004b]. In all these cases the computational models are limited to linear, small deformations. Recently, Santiuste et al. [2011] investigated the thermal-mechanical response of circular sandwich plates including thermal degradation of the core properties, large displacements and rotations and assuming axially symmetric loads and boundary condition. The paper emphasizes on the nonlinear finite element analysis of such structures with some comparison with the axisymmetric HSAPT model results.

The literature survey reveals that most references address computational models that are usually limited to an incompressible core, while ignoring all the localized effects involved as a result of the out of plane flexibility of the core. For all the static cases discussed geometrically linear analyses are considered, while for the dynamic cases nonlinear vibration analyses have been considered but still assuming an incompressible core and specific vibration modes.

In this paper, the principles of the HSAPT approach are used to determine the geometrically nonlinear response of a circular sandwich plate when subjected to a combination of mechanical and thermal loads, where the mechanical properties of the core material change with temperature. The computational model is based on the assumption of large displacements and moderate rotations with negligible shear deformations and linear constitutive relations for the face sheets. The core is modeled as a 3D small deformation linear elastic continuum with shear and vertical normal rigidities that are assumed to be of finite value, while the in-plane radial, circumferential and shear rigidities are neglected; see [Frostig et al. 1992] and the study in [Santiuste et al. 2011]. In addition, the loads are applied to the face sheets only, while the thermal loads is applied to all constituents. Finally, the face sheets and core are assumed to be fully bonded, and the face-core interfaces are able to transfer both shear and vertical normal stresses accordingly.

The mathematical formulation presents first the field and governing equations along with the appropriate boundary conditions and the closed-form solutions for the core displacement and stress fields of

a circular sandwich plate with a general construction layout. This is followed by the formulation for the special case of a radially symmetric sandwich plate. Finally, a numerical study of the response of circular sandwich plates subjected to axisymmetric combined mechanical and thermal loads is presented. This includes response curves within the sandwich plate and equilibrium curves of temperature versus selected structural variables/quantities.

2. Mathematical formulation

The field equations and the boundary conditions are derived following the steps of the HSAPT approach. They are derived using the variational principle of extremum of the total potential energy as follows:

$$\delta(U + V) = 0 \tag{1}$$

where U is in the internal potential strain energy, V is is the potential energy of the external loads, and δ is the variational operator.

The internal potential energy of the circular sandwich plate expressed in polar coordinates reads:

$$
\begin{aligned}
\delta U = \sum_{j=t,b} \Bigg(& \int_0^{2\pi} \int_{R_i}^{R_o} \int_{-\frac{1}{2}d_j}^{\frac{1}{2}d_j} \big(\sigma_{rrj}(r,\theta,z_j)\delta\epsilon_{rrj}(r,\theta,z_j) + \sigma_{\theta\theta j}(r,\theta,z_j)\delta\epsilon_{\theta\theta j}(r,\theta,z_j) \\
& \qquad\qquad\qquad\qquad + \tau_{r\theta j}(r,\theta,z_j)\delta\gamma_{r\theta j}(r,\theta,z_j)\big)r\,dz_j\,dr\,d\theta \Bigg) \\
& + \int_0^{2\pi} \int_{R_i}^{R_o} \int_0^c \big(\tau_{rzc}(r,\theta,z_c)\delta\gamma_{rzc}(r,\theta,z_c) + \tau_{\theta zc}(r,\theta,z_c)\delta\gamma_{\theta zc}(r,\theta,z_c) \\
& \qquad\qquad\qquad\qquad + \sigma_{zzc}(r,\theta,z_c)\delta\epsilon_{zzc}(r,\theta,z_c)\big)r\,dz_c\,dr\,d\theta, \tag{2}
\end{aligned}
$$

where $\sigma_{rrj}(r,\theta,z_j)$ and $\sigma_{\theta\theta j}(r,\theta,z_j)$ $(j=t,b)$ are the normal stresses in the radial and circumferential directions of the upper and the lower face sheets, respectively; $\epsilon_{rrj}(r,z_j)$ and $\epsilon_{\theta\theta j}(r,\theta,z_j)$ $(j=t,b)$ are the normal strains in the radial and circumferential directions of the face sheets, respectively; $\tau_{jzc}(r,\theta,z_c)$, and $\gamma_{jzc}(r,\theta,z_c)$ $(j=r,\theta)$ are the vertical shear stresses and the shear angle on the radial and circumferential faces of the core, respectively; $\sigma_{zzc}(r,\theta,z_c)$, and $\epsilon_{zzc}(r,\theta,z_c)$ are the vertical normal stresses and strains in the core, respectively; $R_j(j=i,o)$ are the inner and outer radii of the plate; c is the height of the core; $z_k(k=t,b,c)$ are the vertical coordinates of the face sheets measured from their centroid planes, and of the core measured from upper the face-core interface, respectively; r is the radial coordinate measured from center of plate, and finally θ is the circumferential coordinate measured positive in the counterclockwise direction. For geometry, sign conventions, coordinates, deformations and internal resultants, see Figure 1.

The variation of the potential energy of the external loads reads:

$$
\begin{aligned}
\delta V = -\int_0^{2\pi} \Bigg(& \sum_{j=t,b} \bigg(\int_{R_i}^{R_o} \big(n_{rr_j}(r,\theta)\delta u_{0j}(r,\theta) + n_{\theta\theta_j}(r,\theta)\delta v_{0j}(r.\theta) + q_j(r,\theta)\delta w_j(r,\theta)\big)r\,dr \bigg) \\
& + \sum_{R_e=R_i}^{R_o} \big(N_{rre_j}(R_e,\theta)\delta u_{0j}(R_e,\theta) + N_{r\theta e_j}(R_e,\theta)\delta v_{0j}(R_i,\theta) + P_{e_j}(R_e,\theta)\delta w_j(R_e,\theta) \\
& \qquad\qquad + M_{rre_j}(R_e,\theta)\delta w_{j,r}(R_e,\theta) + M_{r\theta e_j}(R_e,\theta)\delta w_{j,\theta}(R_e,\theta)\big)R_e \Bigg) d\theta, \tag{3}
\end{aligned}
$$

where n_{kk_j} and q_j ($k = r, \theta$; $j = t, b$) are the external distributed loads in-plane and the vertical distributed load, respectively, at the upper and the lower face sheets; u_{0j}, v_{0j} and w_j ($j = t, b$) are the in-plane displacements in the radial and circumferential directions, and the vertical displacements, respectively of the upper and lower face sheets, respectively; $D_m f(r, \theta)$ ($m = r, \theta$) denotes a derivative of the function $f(r, \theta)$ with respect to the m-th variable or a derivative at a specified location; N_{ne_j}, P_{ne_j} and M_{ne_j} ($n = rr, r\theta$ and $j = t, b$) are the external concentrated loads in the radial and circumferential directions, in the vertical direction and the external bending moments in the radial and circumferential directions at the upper and lower face sheets. For sign conventions and definitions of loads see Figure 1.

The displacement distributions through the face sheet thicknesses there are assumed to follow the Euler–Bernoulli assumption of negligible through-thickness shear deformations and they read ($j = t, b$):

$$u_j(r, \theta, z_j) = u_{0j}(r, \theta) - z_j \frac{\partial}{\partial r} w_j(r, \theta),$$

$$v_j(r, \theta, z_j) = v_{0j}(r, \theta) - z_j \frac{\partial}{\partial \theta} w_j(r, \theta),$$

(4)
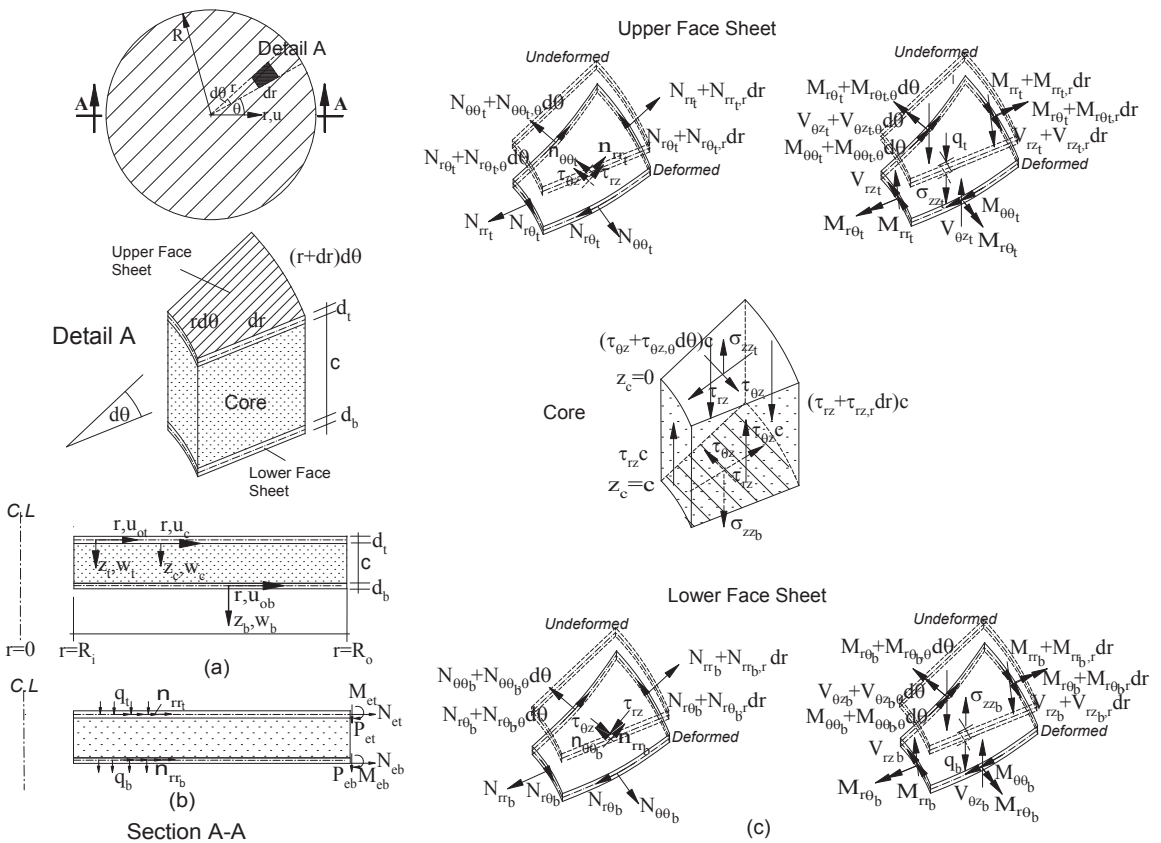
Figure 1. A typical circular sandwich plate: (a) plate layout, geometry and sign convention; (b) loads; (c) stress resultants in face sheets and core.

where u_{0j} and v_{0j} are the radial and circumferential displacements, respectively, of the mid-plane of the face sheets. Adopting the kinematic relations corresponding to moderately large deformations (von Kármán class of deformations), the radial and circumferential normal strains and the in-plane shear angle read ($j = t, b$):

$$\epsilon_{rrj}(r, \theta) = \epsilon_{rroj}(r, \theta) + z_j \chi_{rr_j}(r, \theta) - \alpha_j T_j(r, \theta, z_j),$$

$$\epsilon_{rroj}(r, \theta) = \frac{\partial}{\partial r} u_{0j}(r, \theta) + \frac{1}{2}\left(\frac{\partial}{\partial r} w_j(r, \theta)\right)^2,$$

$$\chi_{rj}(r, \theta) = -\frac{\partial^2}{\partial r^2} w_j(r, \theta),$$

$$\epsilon_{\theta\theta j}(r, \theta) = \epsilon_{\theta\theta oj}(r, \theta) + z_j \chi_{\theta\theta_j}(r, \theta) - \alpha_j T_j(r, \theta, z_j),$$

$$\epsilon_{\theta\theta oj}(r, \theta) = \frac{1}{r} u_{0j}(r, \theta) + \frac{1}{r}\frac{\partial}{\partial\theta} v_{0j}(r, \theta) + \frac{1}{2r^2}\left(\frac{\partial}{\partial\theta} w_j(r, \theta)\right)^2, \tag{5}$$

$$\chi_{\theta\theta_j}(r, \theta) = -\frac{1}{r}\frac{\partial}{\partial r} w_j(r, \theta) - \frac{1}{r^2}\frac{\partial^2}{\partial\theta^2} w_j(r, \theta),$$

$$\gamma_{r\theta_j}(r, \theta) = \gamma_{r\theta oj}(r, \theta) + z_j \chi_{r\theta_j}(r, \theta),$$

$$\gamma_{r\theta oj}(r, \theta) = \frac{1}{r}\frac{\partial}{\partial\theta} u_{0j}(r, \theta) - \frac{1}{r} v_{0j}(r, \theta) + \frac{\partial}{\partial r} v_{0j}(r, \theta) + \frac{1}{r}\frac{\partial}{\partial r} w_j(r, \theta)\frac{\partial}{\partial\theta} w_j(r, \theta),$$

$$\chi_{r\theta_j}(r, \theta) = -\frac{2}{r}\frac{\partial^2}{\partial\theta\,\partial r} w_j(r, \theta) + \frac{2}{r^2}\frac{\partial}{\partial\theta} w_j(r, \theta),$$

where ϵ_{kko_j} ($k = r, \theta$) denotes the mid-plane strains in the radial and circumferential directions, $\gamma_{r\theta o_j}$ ($j = t, b$) the in-plane shear angles of the top and bottom face sheets, χ_{kl_j} ($k, l = r, \theta$) the radial, circumferential and twist curvatures, the temperature distribution through the depth of the (top or bottom) face sheet reads,

$$T_j(r, \theta, z_j) = \frac{1}{2}\left(T_{jb}(r, \theta) + T_{jt}(r, \theta)\right) + \frac{z_j}{h}\left(T_{jb}(r, \theta) - T_{jt}(r, \theta)\right) \quad (j = t, b), \tag{6}$$

and α_j ($j = t, b$) the coefficient of thermal expansion of the face sheet.

The kinematic relations of the core material are derived assuming small displacements and rotations, and they read

$$\gamma_{rzc}(r, \theta, z_c) = \frac{\partial}{\partial z_c} u_c(r, \theta, z_c) + \frac{\partial}{\partial r} w_c(r, \theta, z_c),$$

$$\gamma_{\theta zc}(r, \theta, z_c) = \frac{\partial}{\partial z_c} v_c(r, \theta, z_c) + \frac{\partial}{\partial\theta} w_c(r, \theta, z_c), \tag{7}$$

$$\epsilon_{zzc}(r, \theta, z_c) = \frac{\partial}{\partial z_c} w_c(r, \theta, z_c) - \alpha_c T(r, \theta, z_c),$$

where $u_c(r, \theta, z_c)$, $v_c(r, \theta, z_c)$ and $w_c(r, \theta, z_c)$ are the radial, circumferential and vertical core displacements, respectively.

The compatibility conditions corresponding to perfect bonding between the face sheets and the core require that the following conditions are fulfilled:

$$u_c(r, \theta, z_{cj}) = u_{0j}(r, \theta) + \tfrac{1}{2}(-1)^k d_j \frac{\partial}{\partial r} w_j(r, \theta),$$

$$v_c(r, \theta, z_{cj}) = v_{0j}(r, \theta) + \tfrac{1}{2}(-1)^k d_j \frac{\partial}{\partial \theta} w_j(r, \theta), \qquad (8)$$

$$w_c(r, \theta, z_{cj}) = w_j(r, \theta),$$

where $k = 1$ when $j = t$, $k = 0$ when $j = b$, and z_{cj} $(j = t, b)$ are the vertical coordinates at the upper and the lower face-core interfaces, respectively; thus $z_{ct} = 0$ and $z_{cb} = c$. See Figure 1 for coordinate definitions for the core.

The field equations and the boundary conditions are derived using the variational principle (1), the variational energies (2) and (3), the kinematic relations (5)–(7) of the face sheets and the core, the compatibility requirements (8), and the stress resultants (see Figure 1).

Hence, after integration by parts and some algebraic manipulations, the field equations for the face sheets $(j = t, b)$ read:

$$-\frac{\partial}{\partial \theta} N_{r\theta_j}(r, \theta) + N_{\theta\theta_j}(r, \theta) - N_{rr_j}(r, \theta) - r\frac{\partial}{\partial r} N_{rr_j}(r, \theta) - rn_{rr_j}(r, \theta) + (-1)^k r \tau_{rz_j}(r, \theta) = 0,$$

$$-2N_{r\theta_j}(r, \theta) - \frac{\partial}{\partial \theta} N_{\theta\theta_j}(r, \theta) - rn_{\theta\theta_j}(r, \theta) - r\frac{\partial}{\partial r} N_{r\theta_j}(r, \theta) + (-1)^k r \tau_{\theta z_j}(r, \theta) = 0,$$

$$r\frac{\partial}{\partial \theta} m_{\theta\theta_j}(r, \theta) + \frac{\partial}{\partial r} M_{\theta\theta_j}(r, \theta) - \frac{2}{r}\frac{\partial}{\partial \theta} M_{r\theta_j}(r, \theta) - \frac{d_j}{2}\left(r\frac{\partial}{\partial \theta}\tau_{\theta zc_j}(r, \theta) + r\frac{\partial}{\partial r}\tau_{rzc_j}(r, \theta) + \tau_{rzc_j}(r, \theta)\right)$$

$$+ \left((-1)^{k-1} r \tau_{rzc_j}(r, \theta) + rn_{rr_j}(r, \theta) - N_{\theta\theta_j}(r, \theta)\right)\frac{\partial}{\partial r} w_j(r, \theta)$$

$$+ \left((-1)^{k-1} \tau_{\theta zc_j}(r, \theta) + n_{\theta\theta_j}(r, \theta) + \frac{2}{r} N_{r\theta_j}(r, \theta)\right)\frac{\partial}{\partial \theta} w_j(r, \theta)$$

$$- 2N_{r\theta_j}(r, \theta)\frac{\partial^2}{\partial \theta \partial r} w_j(r, \theta) - rq_j(r, \theta) + (-1)^k r \sigma_{zzj}(r, \theta) - \frac{1}{r}\frac{\partial^2}{\partial \theta^2} M_{\theta\theta_j}(r, \theta) - r\frac{\partial^2}{\partial r^2} M_{rr_j}(r, \theta)$$

$$- rN_{rr_j}(r, \theta)\frac{\partial^2}{\partial r^2} w_j(r, \theta) - \frac{1}{r} N_{\theta\theta_j}(r, \theta)\frac{\partial^2}{\partial \theta^2} w_j(r, \theta) - 2\frac{\partial^2}{\partial \theta \partial r} M_{r\theta_j}(r, \theta) - 2\frac{\partial}{\partial r} M_{rr_j}(r, \theta) = 0, \quad (9)$$

where $k = 1, 2$ indicate the upper and the lower face-core interfaces, respectively; N_{rr_j}, $N_{\theta\theta_j}$ and $N_{r\theta_j}$ $(j = t, b)$ are respectively the in-plane stress resultants in the radial and circumferential directions and the in-plane shear stress resultants of the face sheets; M_{rr_j}, $M_{\theta\theta_j}$ and $M_{r\theta_j}$ $(j = t, b)$ are the bending moment resultants in the radial and circumferential directions and the torsion moment resultants of the face sheets; τ_{rzc_j} and $\tau_{\theta zc_j}$ $(j = t, b)$ are the radial and circumferential core shear stresses at the upper and the interfaces of the core, respectively, and σ_{zzcj} are the vertical normal stresses at the upper and the lower face core interfaces, respectively. It should be noticed that the core shear stresses in the circumferential direction are null when no in-plane distributed loads are applied; see second equation in (9).

The field equations for the core read:

$$\frac{\partial}{\partial z_c}\tau_{rzc}(r,\theta,z_c)=0, \qquad \frac{\partial}{\partial z_c}\tau_{\theta zc}(r,\theta,z_c)=0,$$

$$r\frac{\partial}{\partial z_c}\sigma_{zzc}(r,\theta,z_c)+r\frac{\partial}{\partial r}\tau_{rzc}(r,\theta,z_c)+\tau_{rzc}(r,\theta,z_c)-r\frac{\partial}{\partial\theta}\tau_{\theta zc}(r,\theta,z_c)=0. \tag{10}$$

It should be noticed that due to the geometrical nonlinearities of the face sheets, the equilibrium conditions on each differential segment of the face sheets and the core, which equal to the field equations, should be conducted on the deformed shape of the face sheets, and the undeformed shape of the core; see Figure 1.

The boundary conditions at the inner and outer edges of the face sheets and the core (i.e., at $r=R_i$ and R_o) of the circular sandwich plate are given below.

The boundary conditions for the face sheets ($j=t,b$) read:

$$\lambda N_{rr_j}(R_k,\theta)-N_{re_j}(R_k,\theta)=0 \qquad \text{or} \qquad u_{0j}(R_k,\theta)-u_{0e_j}(R_k,\theta)=0,$$

$$\lambda N_{r\theta_j}(R_e,\theta)-N_{r\theta e_j}(R_e,\theta)=0 \qquad \text{or} \qquad v_{0j}(R_k,\theta)-v_{0e_j}(R_k,\theta)=0,$$

$$-M_{re_j}(R_k,\theta)-\lambda M_{rr_j}(R_k,\theta)=0 \qquad \text{or} \qquad Dw_j(R_k,\theta)-Dw_{ej}(R_k,\theta)=0,$$

$$\lambda\big(R_eN_{rr_j}(R_e,\theta)D_rw_j(R_e,\theta)+D_rM_{rr_j}(R_e,\theta)R_e$$
$$+\tfrac{1}{2}d_j\tau_r(R_e,\theta)R_e+N_{r\theta_j}(R_e,\theta)D_\theta(w_j)(R_e,\theta)$$
$$+2D_\theta(M_{r\theta_j})(R_e,\theta)-M_{\theta\theta_j}(R_e,\theta)+M_{rr_j}(R_e,\theta)\big)$$
$$+D_\theta(M_{r\theta e_j})(R_e,\theta)R_e-P_{e_j}(R_e,\theta)R_e=0 \qquad \text{or} \qquad w_j(R_k,\theta)-w_{e_j}(R_k,\theta)=0, \tag{11}$$

where $\lambda=1$ when $r=R_o$ and $\lambda=-1$ when $r=R_i$; $k=o$ or i; u_{0e_j}, v_{0e_j}, Dw_{e_j} and w_{e_j} ($j=t,b$) are the prescribed radial, circumferential, radial rotations and vertical displacements at the edges of the upper and the lower face sheet, respectively; N_{re_j}, $N_{r\theta e_j}$ ($j=t,b$)are the external imposed radial and circumferential loads (stress resultants); M_{re_j} and $M_{r\theta e_j}$ ($j=t,b$) are the bending and twist moment resultants in the radial and circumferential directions, respectively, imposed at the edges of the face sheets; and

$$D_k(f)(R_l,\theta)=\frac{\partial}{\partial k}f(r,\theta)|_{r=R_l} \quad (k=r,\theta;\ l=i,o)$$

is the derivative of the function f at the edge of the panel.

The boundary conditions for the core read:

$$\tau_{rzc}(R_k,\theta)=0 \quad \text{or} \quad w_c(R_k,\theta,z_c)-w_{ec}(R_k,\theta,z_c)=0, \tag{12}$$

where $w_{ec}(R_k,\theta,z_c)$ are the prescribed vertical core displacements at the edge of the sandwich plate with a specified distribution through the depth of the core.

In order to express the governing equations in explicit form, the core stress and displacement fields must be defined first. This will be derived next for a core with uniform mechanical properties that are temperature-independent (TI).

3. Core fields — uniform mechanical properties (TI)

The explicit formulation of the isotropic core stress and displacement fields is achieved by using the kinematic relations (7), the compatibility conditions (8) and the constitutive relations

$$
\epsilon_{zzc}(r, \theta, z_c) = \frac{\sigma_{zzc}(r, \theta, z_c)}{E_{zc}} + \alpha_c T_c(r, \theta, z_c),
$$

$$
\gamma_{rzc}(r, \theta, z_c) = \frac{\tau_{rzc}(r, \theta)}{G_{rzc}}, \quad \gamma_{\theta zc}(r, \theta, z_c) = \frac{\tau_{\theta zc}(r, \theta)}{G_{\theta zc}},
$$

(13)

where E_{zc}, G_{rzc} and $G_{\theta zc}$ are the vertical modulus of elasticity and the shear moduli of the core in the radial and circumferential directions, respectively; and $T_c(r, \theta, z_c)$ is the temperature field within the core imposed throughout the sandwich plate.

The stress field within the core is derived through the solution of the field equations (10) of the core. Hence they read:

$$
\tau_{rzc}(r, \theta, z_c) = \tau_r(r, \theta), \qquad \tau_{\theta zc}(r, \theta, z_c) = \tau_\theta(r, \theta),
$$

$$
\sigma_{zzc}(r, \theta, z_c) = -z_c \frac{\partial}{\partial r} \tau_r(r, \theta) - z_c \frac{1}{r} \tau_r(r, \theta) - z_c \frac{\partial}{\partial \theta} \tau_\theta(r, \theta) + C_{w1}(r, \theta),
$$

(14)

where $C_{w1}(r, \theta)$ is a coefficient of integration to be determined through the compatibility conditions at the face-core interfaces; see third equation in (8).

The displacements fields of the core in the radial and circumferential directions are determined through the constitutive relations (13), and by enforcing four compatibility conditions (8); in the radial and circumferential directions at the upper face-core interface, respectively, and in the vertical direction at the upper and the lower interfaces, respectively. The temperature field is assumed to be radially symmetric for simplicity and linear through the depth of the core.

After some algebraic manipulations the explicit description of the radial stress and displacements fields in the core read:

$$
\sigma_{zzc}(r, \theta) = -\tfrac{1}{2} E_{zc} \big(T_{cb}(r) + T_{ct}(r)\big) \alpha_c + \frac{1}{c} E_{zc} \big(w_b(r, \theta) - w_t(r, \theta)\big)
$$
$$
+ \tfrac{1}{2}(-2z_{cj} + c)\Big(\frac{\partial}{\partial r} \tau_r(r, \theta) + \frac{\partial}{\partial \theta} \tau_\theta(r, \theta) + \frac{1}{r} \tau_r(r, \theta)\Big),
$$

$$
w_c(r, \theta, z_c) = -\frac{z_c}{2c}(-z_c + c)\big(T_{cb}(r) - T_{ct}(r)\big) \alpha_c + \frac{z_c}{c} w_b(r, \theta) + \Big(1 - \frac{z_c}{c}\Big) w_t(r, \theta)
$$
$$
+ \frac{1}{2E_{zc}} z_c(-z_c + c)\Big(\frac{\partial}{\partial r} \tau_r(r, \theta) + \frac{\partial}{\partial \theta} \tau_\theta(r, \theta) + \frac{1}{r} \tau_r(r, \theta)\Big),
$$

$$
u_c(r, \theta, z_c) = -\frac{z_c^2(3c - 2z_c)}{12c} \frac{d}{dr}\big(T_{ct}(r) - T_{cb}(r)\big) \alpha_c - \frac{z_c^2}{2c} \frac{\partial}{\partial r} w_b(r, \theta) + \Big(\frac{z_c^2}{2c} - z_c - \frac{d_t}{2}\Big) \frac{\partial}{\partial r} w_t(r, \theta)
$$
$$
- \frac{z_c^2(3c - 2z_c)}{12 E_{zc} r^2}\Big(r^2 \frac{\partial^2}{\partial r^2} \tau_r(r, \theta) + r^2 \frac{\partial^2}{\partial \theta \partial r} \tau_\theta(r, \theta) + r \frac{\partial}{\partial r} \tau_r(r, \theta) - \tau_r(r, \theta)\Big) + \frac{z_c}{G_{rzc}} \tau_r(r, \theta) + u_{0t}(r, \theta),
$$

$$
v_c(r, \theta, z_c) = -\frac{z_c^2}{2c} \frac{\partial}{\partial \theta} w_b(r, \theta) + \Big(\frac{z_c^2}{2c} - z_c - \frac{d_t}{2}\Big) \frac{\partial}{\partial \theta} w_t(r, \theta)
$$
$$
- \frac{z_c^2(3c - 2z_c)}{12 E_{zc} r}\Big(r \frac{\partial^2}{\partial \theta^2} \tau_\theta(r, \theta) + \frac{\partial}{\partial \theta} \tau_r(r, \theta) + r \frac{\partial^2}{\partial \theta \partial r} \tau_r(r, \theta)\Big) + \frac{z_c}{G_{\theta zc}} \tau_\theta(r, \theta) + v_{0t}(r, \theta), \quad (15)
$$

Notice that the distribution, through the depth of the core, of the vertical normal stresses is linear, that of the vertical displacement is quadratic and those of the radial and circumferential displacements are cubic. In addition, the circumferential displacements are shown to be independent of the temperature due to the assumption of a radially symmetric thermal field.

4. Nonlinear governing equations

The governing equations are derived assuming that the face sheets are linear elastic and isotropic, and that the core is linear, elastic and orthotropic. Hence, the nonlinear stress resultant-displacement relations for the face sheets ($j = t, b$) can be expressed in the form:

$$N_{rr_j}(r,\theta) = \mathbb{A}_j\left(\frac{\partial}{\partial r}u_{0j}(r,\theta) + \frac{1}{2}\left(\frac{\partial}{\partial r}w_j(r,\theta)\right)^2 - \frac{1}{2}\alpha_j(1+\mu_j)\big(T_{jt}(r)+T_{jb}(r)\big)\right.$$
$$\left. + \mu_j\left(\frac{1}{r}u_{0j}(r,\theta) + \frac{1}{r}\frac{\partial}{\partial\theta}v_{0j}(r,\theta) + \frac{1}{2r^2}\left(\frac{\partial}{\partial\theta}w_j(r,\theta)\right)^2\right)\right),$$

$$N_{\theta\theta_j}(r,\theta) = \mathbb{A}_j\left(\frac{1}{r}u_{0j}(r,\theta) + \frac{1}{r}\frac{\partial}{\partial\theta}v_{0j}(r,\theta) + \frac{1}{2r^2}\left(\frac{\partial}{\partial\theta}w_j(r,\theta)\right)^2\right.$$
$$\left. - \frac{1}{2}\alpha_j(1+\mu_j)\big(T_{jt}(r)+T_{jb}(r)\big) + \mu_j\left(\frac{\partial}{\partial r}u_{0j}(r,\theta) + \frac{1}{2}\left(\frac{\partial}{\partial r}w_j(r,\theta)\right)^2\right)\right),$$

$$N_{r\theta_j}(r,\theta) = \frac{1}{2}\mathbb{A}_j(1-\mu_j)\left(\frac{1}{r}\frac{\partial}{\partial\theta}u_{0j}(r,\theta) - \frac{1}{r}v_{0j}(r,\theta) + \frac{\partial}{\partial r}v_{0j}(r,\theta) + \frac{1}{r}\frac{\partial}{\partial r}w_j(r,\theta)\frac{\partial}{\partial\theta}w_j(r,\theta)\right),$$

$$M_{rr_j}(r,\theta) = \mathbb{D}_j\left(-\frac{\partial^2}{\partial r^2}w_j(r,\theta) - \frac{\alpha_j}{d_j}\big(T_{jt}(r)-T_{jb}(r)\big)(1+\mu_j) - \frac{\mu_j}{r}\frac{\partial}{\partial r}w_j(r,\theta) - \frac{\mu_j}{r^2}\frac{\partial^2}{\partial\theta^2}w_j(r,\theta)\right),$$

$$M_{\theta\theta_j}(r,\theta) = \mathbb{D}_j\left(-\frac{1}{r}\frac{\partial}{\partial r}w_j(r,\theta) - \frac{1}{r^2}\frac{\partial^2}{\partial\theta^2}w_j(r,\theta) - \frac{\alpha_j}{d_j}\big(T_{jt}(r)-T_{jb}(r)\big)(1+\mu_j) - \mu_j\frac{\partial^2}{\partial r^2}w_j(r,\theta)\right),$$

$$M_{r\theta_j}(r,\theta) = \mathbb{D}_j(1-\mu_j)\left(-\frac{2}{r}\left(\frac{\partial^2}{\partial\theta\,\partial r}w_j(r,\theta)\right) + \frac{2}{r^2}\left(\frac{\partial}{\partial\theta}w_j(r,\theta)\right)\right). \tag{16}$$

Here μ_j ($j = t, b$) is the Poisson's ratio for the face sheets and $\mathbb{A}_j, \mathbb{D}_j$ ($j = t, b$) are the in-plane and flexural rigidities, respectively, which are given by

$$\mathbb{A}_j = \frac{E_j d_j}{1-\mu_j^2},$$

$$\mathbb{D}_j = \frac{E_j d_j^3}{12(1-\mu_j^2)}.$$

The governing equations are derived through substitution of the stress resultant-displacements relations (16) of the face sheets into the field equations (9), and the compatibility conditions — given in the first and second equations in (8) — between the core and the lower face sheet in the radial and circumferential directions, which combined with the core displacement field (15) yield two compatibility equations.

Hence, the governing equations for the face sheets after some algebraic manipulations read ($j = t, b$):

$$
\mathbb{A}_j \Bigg(\frac{1}{2} r(1+\mu_j)\alpha_j \frac{d}{dr}\big(T_{jt}(r) + T_{jb}(r)\big)
$$

$$
+ \frac{1}{2}(\mu_j - 1)\bigg(\Big(\frac{\partial}{\partial r} w_j(r,\theta)\Big)^2 + \frac{1}{r}\frac{\partial^2}{\partial\theta^2} u_{0j}(r,\theta) + \frac{1}{r}\frac{\partial^2}{\partial\theta^2} w_j(r,\theta)\frac{\partial}{\partial r} w_j(r,\theta)\bigg)
$$

$$
- \frac{1}{2}(1+\mu_j)\bigg(-\frac{1}{r^2}\Big(\frac{\partial}{\partial\theta} w_j(r,\theta)\Big)^2 + \frac{\partial^2}{\partial\theta\,\partial r} v_{0j}(r,\theta) + \frac{1}{r}\frac{\partial^2}{\partial\theta\,\partial r} w_j(r,\theta)\frac{\partial}{\partial\theta} w_j(r,\theta)\bigg)
$$

$$
- r\frac{\partial^2}{\partial r^2} u_{0j}(r,\theta) - r\frac{\partial}{\partial r} w_j(r,\theta)\frac{\partial^2}{\partial r^2} w_j(r,\theta) - \frac{1}{2r}(-3+\mu_j)\frac{\partial}{\partial\theta} v_{0j}(r,\theta) + \frac{1}{r} u_{0j}(r,\theta) - \frac{\partial}{\partial r} u_{0j}(r,\theta)\bigg)
$$

$$
+ (-1)^k r\tau_r(r,\theta) - rn_{rr_j}(r,\theta) = 0,
$$

$$
\mathbb{A}_j \Bigg(-\frac{1}{2}(1+\mu_j)\bigg(\frac{\partial^2}{\partial\theta\,\partial r} u_{0j}(r,\theta) + \frac{\partial^2}{\partial\theta\,\partial r} w_j(r,\theta)\frac{\partial}{\partial r} w_j(r,\theta)\bigg)
$$

$$
+ \frac{1}{2}(\mu_j - 1)\bigg(\frac{\partial}{\partial\theta} w_j(r,\theta)\Big(\frac{\partial^2}{\partial r^2} w_j(r,\theta) + \frac{1}{r}\frac{\partial}{\partial r} w_j(r,\theta)\Big) + r\frac{\partial^2}{\partial r^2} v_{0j}(r,\theta) - \frac{1}{r^2} v_{0j}(r,\theta) + \frac{1}{r}\frac{\partial}{\partial r} v_{0j}(r,\theta)\bigg)
$$

$$
- \frac{1}{r}\frac{\partial^2}{\partial\theta^2} v_{0j}(r,\theta) - \frac{1}{r^2}\frac{\partial}{\partial\theta} w_j(r,\theta)\frac{\partial^2}{\partial\theta^2} w_j(r,\theta) + \frac{1}{2r}(-3+\mu_j)\frac{\partial}{\partial\theta} u_{0j}(r,\theta)\Bigg) + (-1)^k r\tau_\theta(r,\theta) - rn_{\theta\theta_j}(r,\theta) = 0,
$$

$$
-\frac{\alpha_j}{d_j}\mathbb{D}_j(\mu_j+1)\bigg(r\frac{d^2}{dr^2}\big(T_{jb}(r) - T_{jt}(r)\big) + \frac{d}{dr}\big(T_{jb}(r) - T_{jb}(r)\big)\bigg) + \mathbb{D}_j r\frac{\partial^4}{\partial r^4} w_j(r,\theta) + \frac{\mathbb{D}_j}{r^3}\frac{\partial^4}{\partial\theta^4} w_j(r,\theta) + 2\mathbb{D}_j \frac{\partial^3}{\partial r^3} w_j(r,\theta)
$$

$$
+ \big(n_{\theta\theta_j}(r,\theta) + \tau_t(r,\theta)\big)\frac{\partial}{\partial\theta} w_j(r,\theta) + (-1)^k r\sigma_{zzj}(r,\theta) - rq_j(r,\theta) + r\frac{\partial}{\partial\theta} m_{\theta\theta_j}(r,\theta) + r\frac{\partial}{\partial r} m_{rr_j}(r,\theta)
$$

$$
+ \frac{1}{2r^3}\bigg(\Big(-2r\Big(\mu_j r\frac{\partial}{\partial r} u_{0j}(r,\theta) + \frac{\partial}{\partial\theta} v_{0j}(r,\theta) + u_{0j}(r,\theta)\Big) + r^2\alpha_j(\mu_j+1)\big(T_{jt}(r) + T_{jb}(r)\big)\Big)\mathbb{A}_j - 4\mathbb{D}_j(\mu_j - 3)\bigg)\frac{\partial^2}{\partial\theta^2} w_j(r,\theta)
$$

$$
- \frac{1}{2}\mathbb{A}_j\bigg(r\Big(\frac{\partial}{\partial r} w_j(r,\theta)\Big)^2\frac{\partial^2}{\partial r^2} w_j(r,\theta) + \frac{1}{r^3}\Big(\frac{\partial}{\partial\theta} w_j(r,\theta)\Big)^2\frac{\partial^2}{\partial\theta^2} w_j(r,\theta)\bigg)
$$

$$
- \frac{1}{2}\mathbb{A}_j\mu_j\bigg(\Big(\frac{\partial}{\partial r} w_j(r,\theta)\Big)^3 + \frac{1}{r}\Big(\frac{\partial}{\partial r} w_j(r,\theta)\Big)^2\frac{\partial^2}{\partial\theta^2} w_j(r,\theta) + \frac{1}{r}\Big(\frac{\partial}{\partial\theta} w_j(r,\theta)\Big)^2\frac{\partial^2}{\partial r^2} w_j(r,\theta)\bigg)
$$

$$
+ \bigg(\mathbb{A}_j\Big(\frac{\mu_j+1}{2}\big(T_{jt}(r) + T_{jb}(r)\big)\alpha_j - \frac{2\mu_j-1}{2r^2}\Big(\frac{\partial}{\partial\theta} w_j(r,\theta)\Big)^2 - \frac{1}{r}\frac{\partial}{\partial\theta} v_{0j}(r,\theta)
$$

$$
- \frac{1}{r} u_{0j}(r,\theta) + \frac{\mu_j-1}{r}\frac{\partial^2}{\partial\theta\,\partial r} w_j(r,\theta)\frac{\partial}{\partial\theta} w_j(r,\theta) - \mu_j\frac{\partial}{\partial r} u_{0j}(r,\theta)\Big) + r\tau_r(r,\theta) + rn_{rr_j}(r,\theta) + \frac{\mathbb{D}_j}{r^2}\bigg)\frac{\partial}{\partial r} w_j(r,\theta)
$$

$$
+ \frac{1}{r^2}\bigg(\mathbb{A}_j(\mu_j-1)\Big(r\frac{\partial}{\partial r} v_{0j}(r,\theta) - v_{0j}(r,\theta) + \frac{\partial}{\partial\theta} u_{0j}(r,\theta)\Big)\Big(r\frac{\partial^2}{\partial\theta\,\partial r} w_j(r,\theta) - \frac{\partial}{\partial\theta} w_j(r,\theta)\Big)\bigg)
$$

$$
+ \frac{2}{r^2}\mathbb{D}_j(\mu_j - 2)\bigg(\frac{\partial^3}{\partial\theta^2\,\partial r} w_j(r,\theta) - r\frac{\partial^4}{\partial\theta^2\,\partial r^2} w_j(r,\theta)\bigg)
$$

$$
- \bigg(\mathbb{A}_j\Big(r\frac{\partial}{\partial r} u_{0j}(r,\theta) + \mu_j\frac{\partial}{\partial\theta} v_{0j}(r,\theta) + \mu_j u_{0j}(r,\theta) - \frac{\mu_j+1}{2} r\alpha_j\big(T_{jt}(r) + T_{jb}(r)\big)\Big) + \frac{\mathbb{D}_j}{r}\bigg)\frac{\partial^2}{\partial r^2} w_j(r,\theta)
$$

$$
+ m_{rr_j}(r,\theta) - \frac{1}{2}d_j\Big(\tau_r(r,\theta) + r\frac{\partial}{\partial r}\tau_r(r,\theta) + r\frac{\partial}{\partial\theta}\tau_\theta(r,\theta)\Big) = 0. \quad (17)
$$

The two corresponding resulting compatibility equations read:

$$-\frac{1}{12}c^2\frac{d}{dr}\big(T_{ct}(r)-T_{cb}(r)\big)\alpha_c-\frac{1}{2}(c+d_b)\frac{\partial}{\partial r}w_b(r,\theta)-\frac{1}{2}(c+d_t)\frac{\partial}{\partial r}w_t(r,\theta)+u_{0t}(r,\theta)-u_{0b}(r,\theta)$$

$$+\bigg(\frac{c}{G_{rzc}}+\frac{1}{12}\frac{c^3}{E_{zc}r^2}\bigg)\tau_r(r,\theta)-\frac{c^3}{12E_{zc}}\bigg(\frac{1}{r}\frac{\partial}{\partial r}\tau_r(r,\theta)+\frac{\partial^2}{\partial r^2}\tau_r(r,\theta)+\frac{\partial^2}{\partial\theta\,\partial r}\tau_\theta(r,\theta)\bigg)=0,$$

$$-\frac{1}{2}(c+d_b)\frac{\partial}{\partial\theta}w_b(r,\theta)-\frac{1}{2}(c+d_t)\frac{\partial}{\partial\theta}w_t(r,\theta)+\frac{\tau_\theta(r,\theta)c}{G_{\theta zc}}+v_{0t}(r,\theta)-v_{0b}(r,\theta)$$

$$-\frac{c^3}{12E_{zc}}\bigg(\frac{1}{r}\frac{\partial}{\partial\theta}\tau_r(r,\theta)+\frac{\partial^2}{\partial\theta^2}\tau_t(r,\theta)+\frac{\partial^2}{\partial\theta\,\partial r}\tau_r(r,\theta)\bigg)=0,\quad(18)$$

where $k=1,2$ correspond to the upper and the lower face-core interfaces, respectively.

The unknowns in the set of the governing equations (or the fundamental variables of the problem) consist of the in-plane radial and circumferential displacements (u_{0j} and v_{0j}) and the vertical displacement (w_j) of the two face sheets ($j=t,b$), and the two core shear stresses in the radial and circumferential directions (τ_r,τ_θ), respectively. Thus the order of the set of partial differential equations (PDEs) includes two for the in-plane displacements of each face sheets and shear stresses in the core, and four for the vertical displacements of each face sheet. Hence, the total order of the complete set of PDEs is 18, which corresponds exactly to the number of boundary conditions to be imposed at the edges of sandwich plate including both the face sheets and the core; see Equations (11) for the face sheets and Equations (12) for the core.

The general solution to the set of nonlinear PDEs and the corresponding boundary conditions may be reduced to a set of nonlinear ordinary differential equations (ODEs) through the use of methods such as Kantorovich, Galerkin or similar approaches with the aid of periodic functions in the circumferential direction; see for example [Rabinovitch and Frostig 2002a]. In order to understand the effects of the main parameters on the nonlinear thermomechanical response including degradation of the mechanical core properties with increasing temperature, the special case of a radially symmetric (or axisymmetric) circular sandwich plate is studied next.

5. Radially symmetric sandwich plates — nonlinear governing equations

The case of radially symmetric sandwich plates requires that the mechanical properties of all constituents are dependent on the radial coordinate only, that the loads (mechanical and thermal) scheme is radially symmetric, and that the imposed boundary conditions do not depend on the circumferential coordinate. Accordingly, all the dependent variables of the problem must be functions of the radial coordinate only. For completeness, the field equations, constitutive relations and the explicit description of the governing equations for the case of radially symmetric panel is presented in the following.

The field equations for the face sheets ($j=t,b$) are:

$$-rn_{rr_j}(r)-r\frac{d}{dr}N_{rr_j}(r)+(-1)^k r\tau_{rzc_j}(r)+N_{\theta\theta_j}(r)-N_{rr_j}(r)=0,\qquad (-1)^k\tau_{\theta zc_j}(r)-n_{\theta\theta_j}(r)=0,$$

$$\bigg((-1)^{k-1}r\frac{d}{dr}w_j(r)-\frac{d_j}{2}\bigg)\tau_{rzc_j}(r)-\frac{d_j}{2}r\frac{d}{dr}\tau_{rzc_j}(r)+\big(rn_{rr_j}(r)-N_{\theta\theta_j}(r)\big)\frac{d}{dr}w_j(r)+\frac{d}{dr}M_{\theta\theta_j}(r)$$

$$+(-1)^k r\sigma_{zzcj}(r)-rN_{rr_j}(r)\frac{d^2}{dr^2}w_j(r)-rq_j(r)-2\frac{d}{dr}M_{rr_j}(r)-r\frac{d^2}{dr^2}M_{rr_j}(r)=0,\quad(19)$$

where $k = 1, 2$ for the upper and the lower face-core interfaces respectively. Please notice that if no radial in-plane external loads is imposed, then the circumferential shear stresses within the core are zero. Hence the number of equations reduces to two for each face sheet.

The number of boundary conditions at the inner and outer plate radii, R_i, and R_o, changes to three for each face sheet as follows ($j = t, b$):

$$\lambda N_{rr_j}(R_k) - N_{re_j}(R_k) = 0 \quad \text{or} \quad u_{0j}(R_k) - u_{0ej}(R_k) = 0$$

$$\lambda M_{rr_j}(R_k) + M_{re_j}(R_k) = 0 \quad \text{or} \quad Dw_j(R_k) - Dw_{ej}(R_k) = 0$$

$$\begin{aligned} \lambda\Big(R_j N_{rr_j}(R_k) D(w_j)(R_k) &- R_k m_{rr_j}(R_k) \\ + R_j DM_{rr_j}(R_k) &+ \tfrac{1}{2} d_j R_j \tau_{rzc_j}(R_k) \\ + M_{rr_j}(R_k) &- M_{\theta\theta_j}(R_k) \Big) - R_j P_{e_j}(R_k) = 0 \quad \text{or} \quad w_j(R_k) - w_{e_j}(R_k) = 0 \end{aligned} \tag{20}$$

where $\lambda = 1$ for $r = R_o$ and $\lambda = -1$ for $r = R_i$; $k = o$ or i. Notice that due to the radially symmetric constraints there are no boundary conditions imposed with respect to loads and displacements in the circumferential direction.

The stress resultant-displacement relations read:

$$\begin{aligned} N_{rr_j}(r) &= \mathbb{A}_j\left(-\frac{1}{2}(1 + \mu_j)\big(T_{jt}(r) + T_{jb}(r)\big)\alpha_j + \frac{d}{dr}u_{0j}(r) + \frac{1}{2}\left(\frac{d}{dr}w_j(r)\right)^2 + \frac{1}{r}\mu_j u_{0j}(r)j\right), \\ M_{rr_j}(r) &= \mathbb{D}_j\left(-\frac{1}{d_j}(1 + \mu_j)\big(T_{jt}(r) - T_{jb}(r)\big)\alpha_j + \frac{d^2}{dr^2}w_j(r) + \frac{1}{r}\mu_j\frac{d}{dr}w_j(r)\right), \\ N_{\theta\theta_j}(r) &= \mathbb{A}_j\left(\frac{1}{2}\alpha_j(\mu_j^2 - 1)\big(T_{jt}(r) + T_{jb}(r)\big) + \frac{1}{r}(1 - \mu_j^2)u_{0j}(r)\right) + \mu_j N_{rr_j}(r), \\ M_{\theta\theta_j}(r) &= \mathbb{D}_j\left(\frac{\alpha_j}{d_j}\big(T_{jt}(r) - T_{jb}(r)\big)(\mu_j^2 - 1) + \frac{1}{r}(\mu_j^2 - 1)\frac{d}{dr}w_j(r)\right) + \mu_j M_{rr_j}(r). \end{aligned} \tag{21}$$

Here it should be noticed that the stress resultants in the circumferential direction are expressed in terms of displacements, temperatures and stress resultants in the radial direction for brevity. In addition, it is seen that the stress resultants do not depend on the circumferential displacement.

Hence, through substitution of (21) into the field equations (19), and using the r dependent variables in the compatibility equations (18), the governing equations for face sheets ($j = t, b$) in the axisymmetric sandwich plate case read:

$$\begin{aligned} \mathbb{A}_j\Big(\frac{1}{2}(\mu_j + 1)r\frac{d}{dr}\big(T_{jt}(r) + T_{jb}(r)\big)\alpha_j &+ \frac{\mu_j - 1}{2}\left(\frac{d}{dr}w_j(r)\right)^2 \\ - r\frac{d^2}{dr^2}u_{0j}(r) - r\frac{d}{dr}w_j(r)\frac{d^2}{dr^2}w_j(r) &+ \frac{1}{r}u_{0j}(r) - \frac{d}{dr}u_{0j}(r)\Big) + (-1)^k r\tau_r(r) - r n_{rr_j}(r) = 0, \end{aligned}$$

$$\frac{1}{2}\mathbb{A}_j(\mu_j - 1)\frac{1}{r^2}\left(r^3\frac{d^2}{dr^2}v_{0j}(r) - v_{0j}(r) + r\frac{d}{dr}v_{0j}(r)\right) + (-1)^k r\tau_\theta(r) - r n_{\theta\theta_j}(r) = 0,$$

$$-\frac{\alpha_j}{d_j}\mathbb{D}_j(1+\mu_j)\Big(r\frac{d^2}{dr^2}\big(T_{jb}(r)-T_{jt}(r)\big)+\frac{d}{dr}\big(T_{jb}(r)-T_{jt}(r)\big)\Big)-\frac{1}{2}\mathbb{A}_j\mu_j\Big(\frac{d}{dr}w_j(r)\Big)^3$$

$$+\mathbb{D}_j\Big(r\frac{d^4}{dr^4}w_j(r)+2\frac{d^3}{dr^3}w_j(r)-\frac{1}{r}\frac{d^2}{dr^2}w_j(r)+\frac{1}{r^2}\frac{d}{dr}w_j(r)\Big)+(-1)^k r\sigma_{zzj}(r)-rq_j(r)$$

$$+\Big(\Big(\frac{\mu_j+1}{2}\big(T_{jt}(r)+T_{jb}(r)\big)\alpha_j-\frac{u_{0j}(r)}{r}-\mu_j\frac{d}{dr}u_{0j}(r)\Big)\mathbb{A}_j+r\tau_r(r)+rn_{rr_j}(r)\Big)\frac{d}{dr}w_j(r)$$

$$-\mathbb{A}_j\Big(\frac{r}{2}\Big(\frac{d}{dr}w_j(r)\Big)^2+r\frac{d}{dr}u_{0j}(r)+u_{0j}(r)\mu_j-\frac{r}{2}\alpha_j(1+\mu_j)\big(T_{jt}(r)+T_{jb}(r)\big)\Big)\frac{d^2}{dr^2}w_j(r)$$

$$+r\frac{d}{dr}m_{rr_j}(r)+m_{rr_j}(r)-\frac{d_j}{2}\Big(\tau_r(r)+r\frac{d}{dr}\tau_r(r)\Big)=0. \quad (22)$$

And the compatibility equations equal:

$$-\frac{1}{12}c^2\frac{d}{dr}\big(T_{ct}(r)-T_{cb}(r)\big)\alpha_c-\frac{1}{2}(c+d_b)\frac{d}{dr}w_b(r)-\frac{1}{2}(c+d_t)\frac{d}{dr}w_t(r)-u_{0b}(r)+u_{0t}(r)$$

$$+\Big(\frac{c}{G_{rzc}}+\frac{1}{12}\frac{c^3}{E_{zc}r^2}\Big)\tau_{rz}(r)-\frac{c^3}{12E_{zc}r}\Big(\frac{d}{dr}\tau_{rz}(r)+r\frac{d^2}{dr^2}\tau_{rz}(r)\Big)=0,$$

$$\frac{\tau_\theta(r)c}{G_{\theta zc}}+v_{0t}(r)-v_{0b}(r)=0. \quad (23)$$

The interfacial vertical normal stresses read ($j=t,b$):

$$\sigma_{zzj}(r)=-\frac{E_{zc}}{2}\big(T_{cb}(r)+T_{ct}(r)\big)\alpha_c+\frac{E_{zc}}{c}\big(w_b(r)-w_t(r)\big)+\frac{1}{2r}(c-2z_{cj})\Big(r\frac{d}{dr}\tau_{rz}(r)+\tau_{rz}(r)\Big), \quad (24)$$

where $z_{cj}=0,c$ at the upper and the lower interfaces, respectively. The stress and displacements fields of the radially symmetric case can be determined by imposing the constraints that all dependent quantities are only dependent of the radial coordinate r; see (14) and (15).

In addition, when no in-plane external circumferential loads are imposed — see the second equation in (19) — and substituting this result into the second compatibility in (23), the following conditions are obtained:

$$\tau_\theta(r)=0, \quad v_{0t}(r)-v_{0b}(r)=0. \quad (25)$$

The physical interpretation of (25) is that the circumferential displacements in the upper and the lower face sheets must be identical and equal to zero, since no external displacements are imposed in this direction.

It should be noticed that for the case when the mechanical core properties are temperature-dependent, the solution procedure to determine the stress and displacements field of the core follows the approach outlined in [Frostig and Thomsen 2007; 2009], to which reference is made for brevity.

The nonlinear governing equations for the radially symmetric circular sandwich plate case can be expressed by a set of fourteen order ordinary differential equations (ODEs). The boundary value problem constituted by the set of ODEs together with the associated boundary condition can be solved using numerical schemes such as the multiple-point shooting method [Stoer and Bulirsch 1980], or the finite-difference (FD) approach using trapezoid or mid-point methods with Richardson extrapolation or deferred corrections [Ascher and Petzold 1998], as implemented in Maple, along with parametric or arc-length continuation methods [Keller 1992]. Here, the FD approach implemented in Maple has been used. In

the next section the results of a numerical study that discusses the thermomechanical nonlinear response of a radially symmetric sandwich plate are presented.

6. Numerical study

The nonlinear thermomechanical response of a radially symmetric circular sandwich plate with a foam core that has temperature-dependent mechanical properties loaded by a partially uniformly distributed load at mid-span is studied. First, the combined response of a uniformly heated plate with the partially distributed load is discussed with results along the plate and equilibrium curves. The equilibrium curves of temperature versus extreme values of displacements are compared with results of nonlinear finite element analyses (FEA) conducted using ABAQUS/Standard. This is followed by a study that includes the equilibrium curves where a temperature gradient is imposed across the sandwich plate thickness such that the temperature of the lower face sheets is higher than the temperature of the upper face sheet.

The specific sandwich plate configuration (see Figure 2a) consists of a circular sandwich plate with a diameter of 300 mm; two face sheets of 0.5 mm thickness with a coefficient of thermal expansion $\alpha_j = 0.00001$ ($j = t, b$) and made as glass/epoxy composite laminates, and a Divinycell HD-60 foam core with $E_{c0} = 52.5$ MPa and $G_{c0} = 20.2$ MPa (at 20°C) with a thickness of 19.05 mm with $\alpha_c = 0.00035$ made by DIAB [2003]. The supporting system imposed at the edge of the sandwich plate consists of a
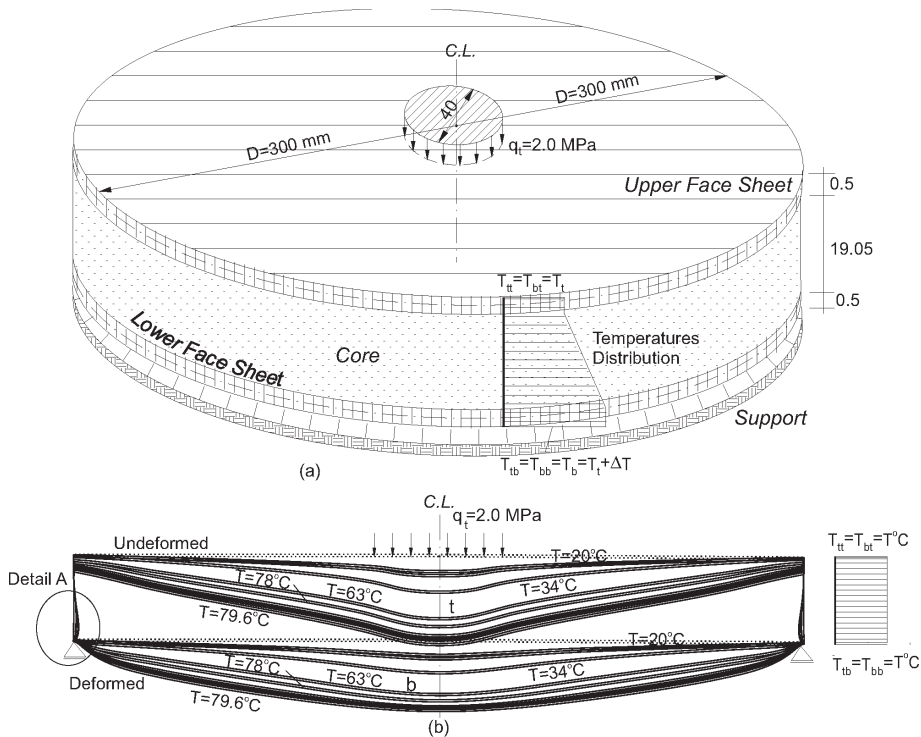
Figure 2. Circular sandwich plate geometry and deformed shapes: (a) plate layout, mechanical and thermal loads and supporting scheme; (b) deformed shape due to mechanical and uniformly distributed load.

horizontally moveable simple supports of the lower face sheet, while the upper face sheet and the core are free of any displacement constrains or stress tractions. In addition, the center of the sandwich plate is assumed to be horizontally immoveable. The loads system includes mechanical loads and an imposed thermal field; see Figure 2a. The mechanical load consists of a patch load of uniform distribution of 2.0 MPa imposed at a circular area around center of plate with a diameter 40 mm at the upper face sheet, and a temperature field with a linear through-thickness distribution in the core and uniform temperatures through the thickness of the face sheets. The thermal gradient, ΔT, raises the temperature imposed on the lower face sheet; see Figure 2a.

The temperature-dependent (TD) core properties are specified according to the Divinycell HD grade PVC foam core data sheet [DIAB 2003], which includes measured material properties in a working range of temperatures between 20 to 80°C. The mechanical properties of Divinycell PVC foam degrades as the temperatures are raised and they are defined here through curve-fitting of the data that appears in [DIAB 2003] (see Figure 3a) as follows:

$$E_{zc}(r, z_c) = E_{c0} f(T),$$
$$G_{rzc}(r, z_c) = G_{c0} f(T),$$
$$f(T) = -2.821963496 \ 10^{-13} \ T^8 + 9.528319971 \ 10^{-11} \ T^7 + 0.03070734934 \ T \quad (26)$$
$$- 1.325134998 \ 10^{-8} \ T^6 - 0.009541812399 \ T^2 + 9.703157671 \ 10^{-7} \ T^5$$
$$+ 0.0008705288588 \ T^3 - 0.00003952259514 \ T^4 + 1.1903,$$

where E_{c0} and G_{c0} refer to the elasticity and shear moduli of the core at $T = 20$°C. Notice that when a thermal gradient is applied to the sandwich plate the mechanical properties of the core are dependent
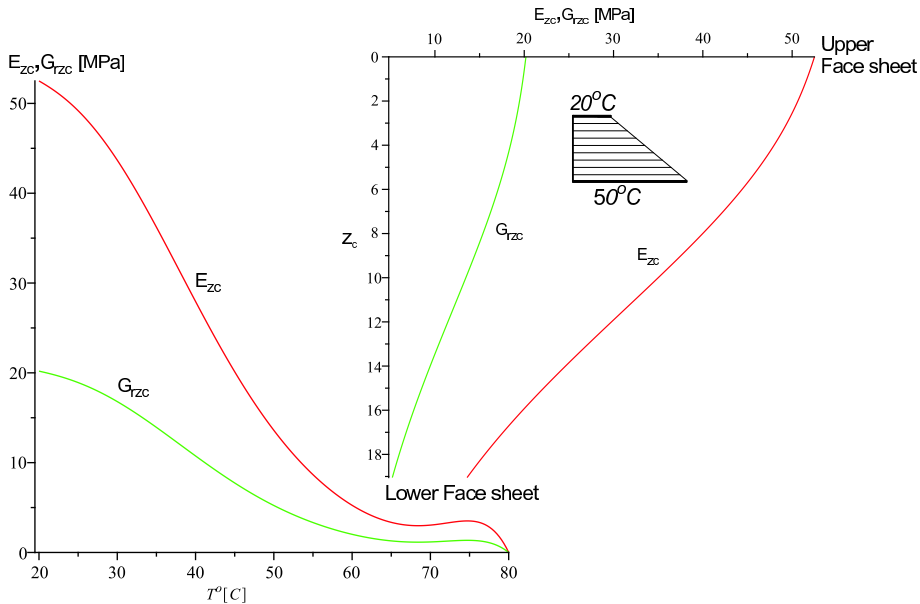

Figure 3. Elastic core moduli: (a) moduli magnitude versus temperatures; (b) moduli distribution through depth of core.

on the vertical coordinate (Figure 3b). In addition, it is assumed here that the temperature dependence is identical for the modulus of elasticity and the shear modulus of the core. For further details see [Frostig and Thomsen 2007; 2009].

The solution procedure uses a parametric continuation method with the temperature T as the parameter. The procedure halts when the solution does not converge or when it violates the assumption of large displacements and moderate rotations (displacements exceeding D/10). The results are also limited to a temperature of 79.7°C, which is closed to the upper limit of the range of operating temperatures for the HD-60 foam considered; see DIAB [2003].

The first case presents the thermomechanical response of a circular sandwich plate with a uniformly distributed temperature through the plate thickness that changes from 20°C to 79.6°C, and a mechanical distributed load of 2.0 MPa partially distributed at center of plate; see Figure 2 for details. The deformed shapes at different temperature levels appear in Figure 2b from which it is observed that the deformation patterns display a significant indentation zone at the upper face sheet and a much smaller at the lower one. Or in other words the indentation deformation decays through the core thickness. It should be noticed that although the mechanical load has not been changed the indentation deepens and narrows as the temperature is raised as a result of the degradation of the temperature-dependent mechanical properties of the core. Moreover, localized in-plane displacements are observed in the core above the lower supports; see Detail A in Figure 2b. In addition, the radial in-plane displacements of the upper and the lower face sheets at the edges of the sandwich plate are very small as a result of the 2D in-plane action of the plate in the radial and circumferential directions although both edges are free to slide horizontally.

The predicted variations of selected structural quantities along the radius of the sandwich plate appear in Figure 4 for different temperatures. The vertical displacements of the face sheets (see Figure 4a) display an indentation at mid-span ($r = 0$) that deepens and narrows as the temperature is raised. It should be noticed that the displacements increase monotonically up to 78°C, after which disproportional increases of the displacements are observed as a result of the development of a limit point; see Figure 5a. In addition, the vertical displacements at the edge of the upper face sheet are not zero, due to the vertical flexibility of the core. The radial variation of the radial and the circumferential bending moment resultants for each face sheet (see Figure 4b) are associated with large values at the edges of the loaded area, around center of plate at the upper face sheet, and even larger in the vicinity of the edge of the lower face sheet due to the presence of the supports at this location. The in-plane face sheet stress resultants in the radial and circumferential directions are associated with tensile values around center, compressive values in the circumferential direction, and zero radial stress resultants at the edge of the sandwich plate; see Figure 4c. Please notice that at low temperatures, both stress resultants are in compression but the radial stress resultants change into tensile values as the temperature is raised, while the circumferential stress resultants change from tensile at center to compression at the plate edge. The radial in-plane mid-height displacements of the face sheets (see Figure 4d) are quite small in comparison with the vertical ones (see Figure 4a) but they reach large values at the face sheet edges at high temperatures. The radial interfacial shear stresses at the face-core interfaces are associated with large values in the vicinity of the edge of the loaded area and much smaller values toward the sandwich plate edge; see Figure 4e. Large interfacial vertical normal stresses are observed within the radial distance of the loaded area, at lower temperatures, as well as at the edge of the plate at high temperatures; see Figure 4f. At lower temperature levels the shear stresses in the core and the interfacial vertical normal stresses at the upper face sheet
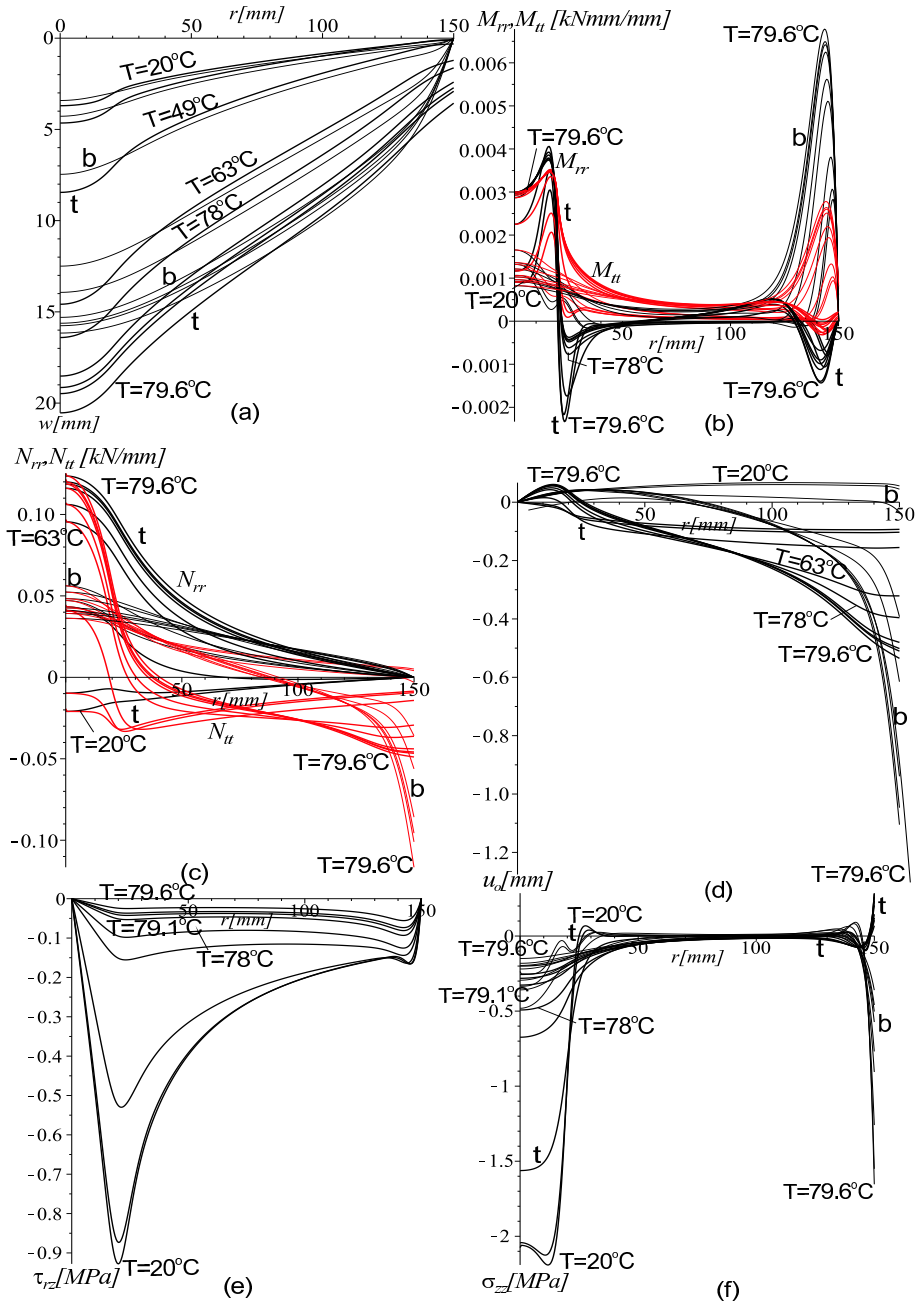
Figure 4. Thermomechanical radial response for a partially distributed load and a uniform temperature distribution. Face sheets: (a) vertical displacements; (b) radial and circumferential bending moments; (c) radial and circumferential in-plane stress resultants; (d) radial in-plane mid-height displacements. Core: (e) shear stresses; (f) face-core interfaces vertical normal stresses. Thicker black lines represent the upper face and thinner ones the lower face; red lines in (b) and (c) represent circumferential magnitudes.
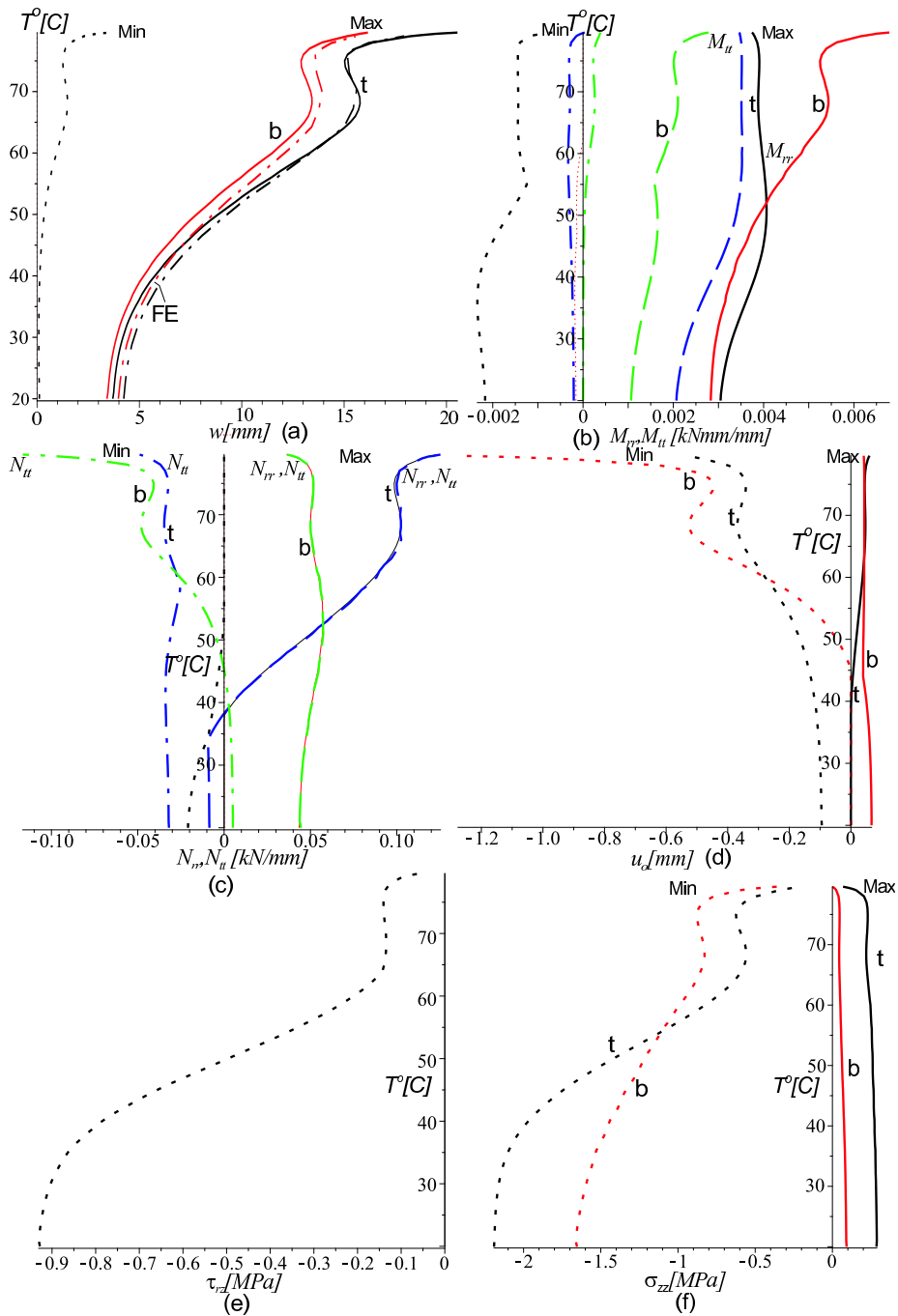
Figure 5. Equilibrium curves of temperature vs. extremum values of selected structural quantities for a partially distributed load and a uniform temperature distribution. Face sheets: (a) vertical displacements; (b) radial and circumferential bending moments; (c) radial and circumferential in-plane stress resultants; (d) radial in-plane mid-height displacements. Core: (e) shear stresses; (f) face-core interface vertical normal stresses.

are almost equal in magnitude to the applied pressure load, and they reduce as the temperature level increases. Actually, what happens is that as the mechanical properties of the degrade it stops carrying any more stresses and each face sheets behave as an independent plate rather than a part of the sandwich panel with a composite action that forms the couple in the face sheets. At the edge of the sandwich plate the interfacial vertical normal stresses change to tension at the upper interface and to compression at the lower interface due to the presence of the edge support system at the lower face sheet and the vertical displacements at the upper face, but without significant effects of the degradation of the mechanical core properties.

The equilibrium curves corresponding to the thermomechanical response are described by temperature versus extremum values of selected structural quantities; see Figure 5. The predicted curves of the extremum vertical displacements of the upper and the lower face sheets predicted by the nonlinear HSAPT model and the nonlinear FEA predictions using ABAQUS/Standard appear in Figure 5a. For details on the FEA modeling such as element types, material properties of the face sheets and material model for the core see [Santiuste et al. 2011]. Figure 5a reveals that loss of stability in the form of a limit point occurs as the temperatures are raised and the mechanical properties degrade. The FEA results compare very well with the HSAPT model, although the FEA results predict a slightly stiffer structure at almost all values of temperatures as expected. Similar trends are observed for the radial and circumferential bending moment resultant curves; see Figure 5b. Here it should be noticed that the largest bending moment resultants occur at the lower face sheet in the vicinity of the support (see also Figure 4b). The in-plane stress resultants in the radial and circumferential directions reveal a loss of stability at high temperatures. In addition, the circumferential stress resultants reach larger values in compression and tension as the temperatures are raised. The radial in-plane mid-height displacements of the face sheets (see Figure 5d) are associated with large values as the temperature is increased and approach the upper temperature range. The shear stresses in the core follow a different trend; see Figure 5e. At low temperatures the interfacial shear stresses are quite large and they decrease as the temperature is raised. The implication of this is that the contribution of the couple that forms in the sandwich plate (known also as the composite action) as a result of the overall bending is significantly reduced as the temperature is raised. The interfacial vertical normal stresses follow a similar trend as the interfacial shear stresses; see Figure 5f. Notice that at low temperatures the extremum compressive stresses at the upper interface are quite large and that they reduce as the temperature increases. The extremum tensile interfacial stresses are almost constant through the entire range of temperatures at the upper and the lower face sheets, and they almost disappear at high levels of temperature.

The effect of a temperature gradient between the upper and the lower face sheets, where the upper face sheet is at a temperature of T, whereas the lower face sheet is at a temperature of $T + \Delta T$. The maximum core temperature is increased to 79°C at the lower face sheet or to a temperature level where solution convergence is not achievable. Notice that under such conditions the moduli of the core are coordinate-dependent (varies in both radial and though-thickness directions) which require a special solution procedure that yields a closed-form solution for the core fields. For details see [Frostig and Thomsen 2007; 2009].

The equilibrium curves of temperature at the upper face-sheet versus extremum values of selected structural quantities for different temperature gradients appear in Figure 6. They consist of the results obtained for the temperature-dependent core (TD) using the moduli of the core that appear in Figure 3
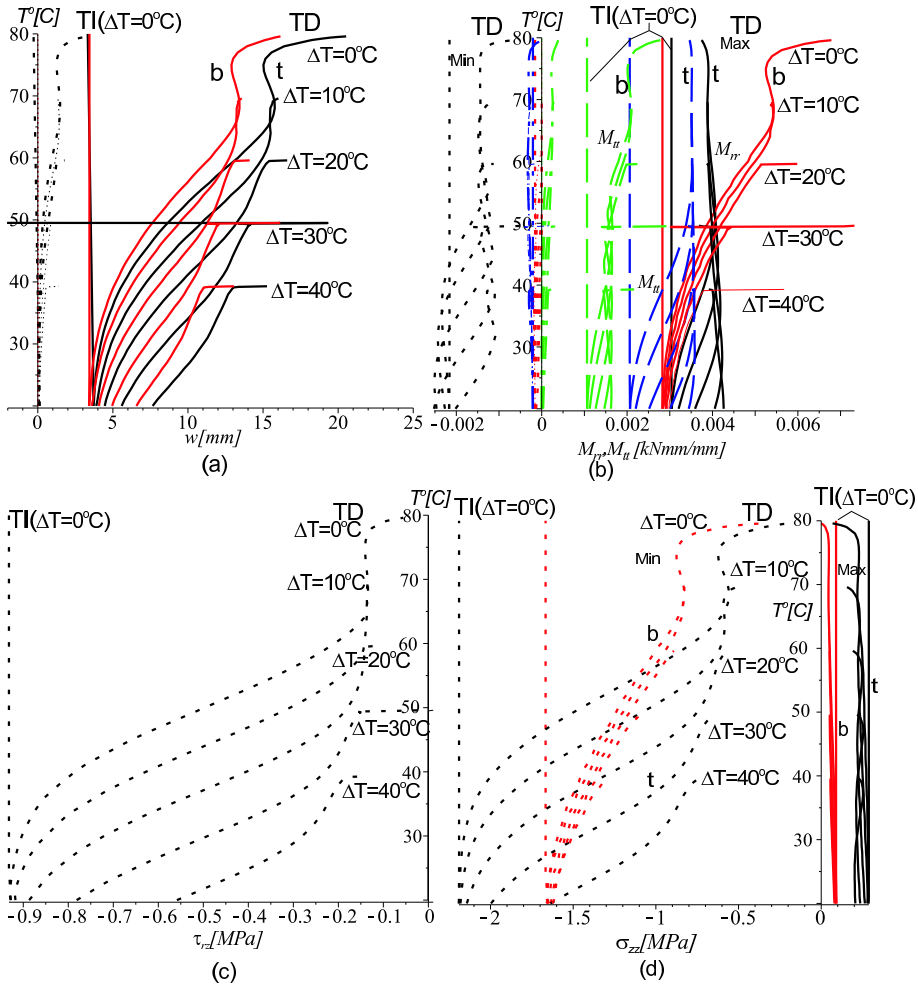
Figure 6. Equilibrium curves of temperature vs. extremum values of selected structural quantities for a partially distributed load and different thermal through-thickness gradients. Face sheets: (a) vertical displacements (HSAPT and FE); (b) radial and circumferential bending moments. Core: (c) shear stresses; (d) face-core interfaces vertical normal stresses.

and the case of a core with temperature-independent (TI) with moduli values that correspond to $T = 20°C$ and a zero thermal gradient. The plots of temperature versus the extreme vertical displacements appear in Figure 6a, and it is seen that at all thermal gradient levels a loss of stability is observed. It occurs when the temperature at the lower face sheet approaches the higher levels of the operating temperature of the core. Please notice that the degradation of core properties at the higher temperature is significant only within a small fraction of the core height near the lower face-core interface. The TI case exhibit linear behavior and is unaffected by the temperature level.

Similar trends are observed for the radial bending moment resultants (see Figure 6b) while the circumferential bending moment resultants are almost independent of the temperature.

The core shear stresses (see Figure 6c) follow an opposite trend; as the temperature is raised the core shear stresses decreases independent of the thermal gradient values. The vertical normal interfacial stresses follow the trends of the shear stresses; see Figure 6d. Notice that as the temperature is raised the vertical normal interfacial stress values decrease. In all cases the TI core exhibit linear results that are independent of the temperature levels and they are completely different than the results obtained when the thermal degradation of the foam core is taken into account.

7. Summary and conclusions

A general and rigorous systematic geometrically nonlinear high-order computational model of circular sandwich plates with general layout and a compliant core material is presented. The mathematical formulations outlines the derivation of the nonlinear field equations; the appropriate boundary conditions; as well as the stress and deformations fields of the core, when the sandwich plate is subjected to mechanical loads in parallel with thermally induced deformations and when the core properties are temperature-independent. The case of a sandwich core with temperature-dependent properties is also treated following the procedure outlined in [Frostig and Thomsen 2007; 2009]. In succession of this the special case of radially symmetric sandwich plates are considered and it yields the nonlinear governing equations for such plates when subjected to combined mechanical and thermal loads.

The results of a numerical study are presented. This includes the nonlinear load response characteristics of radially symmetric circular plates subjected to combined thermal and mechanical loads, as well as the effects of different thermal gradient values through the depth of the core.

The response is also associated with stress concentration regions due to localized effects such as at the edge of the loaded region as well as the support region. The shear and interfacial vertical normal stresses results reveal that as the temperatures are raised the collaboration between the face sheets diminishes and the load transfer mechanism is associated with independent significant bending in each face sheet rather than as part of a composite action that form a couple in an ordinary sandwich panels. Loss of stability is observed as the temperatures approach the upper limit of the range of working temperature. In general, it is associated with very large displacements, bending moments and in-plane stress resultants.

The conducted numerical study reveals that the response becomes unstable as the temperature is increased and the mechanical core properties degrade. Hence, in such cases the design of sandwich structures should be controlled by stability criteria rather than stress constraints.

The effects of imposing different thermal gradients across the core thickness have also been examined. Notice that when the temperature distribution through the core depth is not uniform the core stiffness parameters will vary through the core thickness. This requires a special solution procedure. It has been found that for temperature gradient levels a loss of stability occurs when the temperature at the tensile face sheet approaches the upper limit of the temperature range.

In general, the nonlinear response of a circular sandwich plate is much stiffer than the case of a unidirectional sandwich panel or beam. When comparing with the sandwich panel or beam cases, the presence of circumferential rigidity in addition to the longitudinal rigidity improves the stiffness of the sandwich circular plate. Thus, the presence of a 2D in-plane stress field stabilizes the load response of sandwich plates when compared to the unidirectional panel/beam response characteristics. However, the use of core materials with temperature-dependent mechanical properties that degrade with increasing

temperature yields an unstable response independent of the structural configuration (1D beam/panel or 2D plate). Hence, a reliable design of any type of sandwich structure must take into account the loss of stability that may occur within the working range of temperatures due to thermal degradation when compliant sandwich core materials are used.

Acknowledgments

References

[Allen 1969] H. G. Allen, *Analysis and design of structural sandwich panels*, Pergamon, Oxford, 1969.

[Ascher and Petzold 1998] U. M. Ascher and L. R. Petzold, *Computer methods for ordinary differential equations and differential-algebraic equations*, SIAM, Philadelphia, 1998.

[DIAB 2003] *Data sheet for Divinycell HD grade PVC foams*, DIAB, Laholm, 2003.

[Du 1994] G. Du, "Large amplitude vibration of circular sandwich plates", *Appl. Math. Mech.* **15**:5 (1994), 461–469.

[Du and Li 2000] G. Du and H. Li, "Nonlinear vibration of circular sandwich plate under the uniformed load", *Appl. Math. Mech.* **21**:2 (2000), 217–226.

[Frostig and Thomsen 2007] Y. Frostig and O. T. Thomsen, "Buckling and nonlinear response of sandwich panels with a compliant core and temperature-dependent mechanical properties", *J. Mech. Mater. Struct.* **2**:7 (2007), 1355–1380.

[Frostig and Thomsen 2009] Y. Frostig and O. T. Thomsen, "Nonlinear behavior of thermally loaded curved sandwich panels with a transversely flexible core", *J. Mech. Mater. Struct.* **4**:7–8 (2009), 1287–1326.

[Frostig et al. 1992] Y. Frostig, M. Baruch, O. Vilnay, and I. Sheinman, "High-order theory for sandwich-beam behavior with transversely flexible core", *J. Eng. Mech. (ASCE)* **118**:5 (1992), 1026–1043.

[Gupta and Jain 1982] A. P. Gupta and M. Jain, "Axisymmetric vibrations of annular sandwich plates of linearly varying thickness", *J. Sound Vib.* **80**:3 (1982), 329–337.

[Gupta and Sharma 1982] A. P. Gupta and K. P. Sharma, "Axisymmetric flexure of circular sandwich plate including transverse shear in facings", *Z. Angew. Math. Mech.* **62**:10 (1982), 533–538.

[Hohe and Librescu 2004] J. Hohe and L. Librescu, "Advances in the structural modeling of elastic sandwich panels", *Mech. Adv. Mater. Struct.* **11**:4–5 (2004), 395–424.

[Kao 1970] J.-S. Kao, "Bending of circular sandwich plates due to asymmetric temperature distribution", *AIAA J.* **8**:5 (1970), 951–954.

[Keller 1992] H. B. Keller, *Numerical methods for two-point boundary value problems*, Dover, New York, 1992.

[Librescu and Hause 2000] L. Librescu and T. Hause, "Recent developments in the modeling and behavior of advanced sandwich constructions: a survey", *Compos. Struct.* **48**:1–3 (2000), 1–17.

[Mindlin 1951] R. D. Mindlin, "Influence of transverse shear deformation on the bending of classical plates", *J. Appl. Mech. (ASME)* **8** (1951), 18–31.

[Montrey 1973] H. M. Montrey, "Bending of a circular sandwich plate by load applied through an insert", Research paper FPL 201, Forest Products Laboratory, Forest Service, United States Department of Agriculture, Madison, WI, 1973, Available at http://www.fpl.fs.fed.us/documnts/fplrp/fplrp201.pdf.

[Noor et al. 1996] A. K. Noor, W. S. Burton, and C. W. Bert, "Computational models for sandwich panels and shells", *Appl. Mech. Rev.* (*ASME*) **49**:3 (1996), 155–199.

[Petras and Sutcliffe 2000] A. Petras and M. P. F. Sutcliffe, "Indentation failure analysis of sandwich beams", *Compos. Struct.* **50**:3 (2000), 311–318.

[Plantema 1966] F. J. Plantema, *Sandwich construction*, Wiley, New York, 1966.

[Rabinovitch and Frostig 2002a] O. Rabinovitch and Y. Frostig, "High-order behavior of fully bonded and delaminated circular sandwich plates with laminated face sheets and a "soft" core", *Int. J. Solids Struct.* **39**:11 (2002), 3057–3077.

[Rabinovitch and Frostig 2002b] O. Rabinovitch and Y. Frostig, "Strengthening of RC slabs with circular composite patches: a high-order approach", *Compos. Struct.* **55**:2 (2002), 225–238.

[Rabinovitch and Frostig 2004a] O. Rabinovitch and Y. Frostig, "High-order analysis of reinforced concrete slabs strengthened with circular composite laminated patches of general layup", *J. Eng. Mech.* (*ASCE*) **130**:11 (2004), 1334–1345.

[Rabinovitch and Frostig 2004b] O. Rabinovitch and Y. Frostig, "Delamination effects in reinforced concrete slabs strengthened with circular composite patches", *J. Eng. Mech.* (*ASCE*) **130**:12 (2004), 1436–1446.

[Reddy 1984] J. N. Reddy, *Energy and variational methods in applied mechanics*, Wiley, New York, 1984.

[Rohacell 2004] Evonik Degussa, *Rohacell: WF foam data sheets*, Rohacell, Essen, 2004, Available at http://www.rohacell.com.

[Santiuste et al. 2011] C. Santiuste, O. T. Thomsen, and Y. Frostig, "Thermo-mechanical load interactions in foam cored axi-symmetric sandwich circular plates: high-order and FE models", *Compos. Struct.* **93**:2 (2011), 369–376.

[Selke 1971] L. A. Selke, "Theoretical elastic deformations of solid and cored horizontal circular mirrors having a central hole on a ring support", *Appl. Opt.* **10**:4 (1971), 939–944.

[Sherif 1992] H. A. Sherif, "Free flexural vibrations of clamped circular sandwich plates", *J. Sound Vib.* **157**:3 (1992), 531–537.

[Stoer and Bulirsch 1980] J. Stoer and R. Bulirsch, *Introduction to numerical analysis*, Springer, New York, 1980.

[Thomsen 1995] O. T. Thomsen, "Theoretical and experimental investigation of local bending effects in sandwich plates", *Compos. Struct.* **30**:1 (1995), 85–101.

[Thomsen 1997] O. T. Thomsen, "Sandwich plates with 'through-the-thickness' and 'fully potted' inserts: evaluation of differences in structural performance", *Compos. Struct.* **40**:2 (1997), 159–174.

[Thomsen and Rits 1998] O. T. Thomsen and W. Rits, "Analysis and design of sandwich plates with inserts: a high-order sandwich plate theory approach", *Compos. B Eng.* **29**:6 (1998), 795–807.

[Vinson 1999] J. R. Vinson, *The behavior of sandwich structures of isotropic and composite materials*, Technomic, Lancaster, 1999.

[Wang 1995a] C. M. Wang, "Buckling of polygonal and circular sandwich plates", *AIAA J.* **33**:5 (1995), 962–964.

[Wang 1995b] C. M. Wang, "Deflection of sandwich plates in terms of corresponding Kirchhoff plate solutions", *Arch. Appl. Mech.* **65**:6 (1995), 408–414.

[Zenkert 1995] D. Zenkert, *An introduction to sandwich construction*, Chameleon, London, 1995.

[Zhou and Stronge 2006] D. Zhou and W. J. Stronge, "Modal frequencies of circular sandwich panels", *J. Sandw. Struct. Mater.* **8**:4 (2006), 343–357.

YEOSHUA FROSTIG: cvrfros@techunix.technion.ac.il
Professor, Ashtrom Engineering Company Chair in Civil Engineering
Technion - Israel Institute of Technology, Faculty of Civil and Environmental Engineering, Haifa, 32000, Israel

OLE THOMSEN: ott@me.aau.dk
Professor, Head of Department
Aalborg University, Department of Mechanical Engineering, Pontoppidanstræde 105, 9220 Aalborg Ø, Denmark

SUBMISSION GUIDELINES

ORIGINALITY

Authors may submit manuscripts in PDF format online at the Submissions page. Submission of a manuscript acknowledges that the manuscript is original and has neither previously, nor simultaneously, in whole or in part, been submitted elsewhere. Information regarding the preparation of manuscripts is provided below. Correspondence by email is requested for convenience and speed. For further information, write to one of the Chief Editors:

Davide Bigoni   bigoni@ing.unitn.it
Iwona Jasiuk   ijasiuk@me.concordia.ca
Yasuhide Shindo   shindo@material.tohoku.ac.jp

LANGUAGE

Manuscripts must be in English. A brief abstract of about 150 words or less must be included. The abstract should be self-contained and not make any reference to the bibliography. Also required are keywords and subject classification for the article, and, for each author, postal address, affiliation (if appropriate), and email address if available. A home-page URL is optional.

FORMAT

Authors can use their preferred manuscript-preparation software, including for example Microsoft Word or any variant of TeX. The journal itself is produced in LaTeX, so accepted articles prepared using other software will be converted to LaTeX at production time. Authors wishing to prepare their document in LaTeX can follow the example file at www.jomms.org (but the use of other class files is acceptable). At submission time only a PDF file is required. After acceptance, authors must submit all source material (see especially Figures below).

REFERENCES

Bibliographical references should be complete, including article titles and page ranges. All references in the bibliography should be cited in the text. The use of BibTeX is preferred but not required. Tags will be converted to the house format (see a current issue for examples); however, for submission you may use the format of your choice. Links will be provided to all literature with known web locations; authors can supply their own links in addition to those provided by the editorial process.

FIGURES

Figures must be of publication quality. After acceptance, you will need to submit the original source files in vector format for all diagrams and graphs in your manuscript: vector EPS or vector PDF files are the most useful. (EPS stands for Encapsulated PostScript.)

Most drawing and graphing packages—Mathematica, Adobe Illustrator, Corel Draw, MATLAB, etc.—allow the user to save files in one of these formats. Make sure that what you're saving is vector graphics and not a bitmap. If you need help, please write to graphics@mathscipub.org with as many details as you can about how your graphics were generated.

Please also include the original data for any plots. This is particularly important if you are unable to save Excel-generated plots in vector format. Saving them as bitmaps is not useful; please send the Excel (.xls) spreadsheets instead. Bundle your figure files into a single archive (using zip, tar, rar or other format of your choice) and upload on the link you been given at acceptance time.

Each figure should be captioned and numbered so that it can float. Small figures occupying no more than three lines of vertical space can be kept in the text ("the curve looks like this:"). It is acceptable to submit a manuscript with all figures at the end, if their placement is specified in the text by means of comments such as "Place Figure 1 here". The same considerations apply to tables.

WHITE SPACE

Forced line breaks or page breaks should not be inserted in the document. There is no point in your trying to optimize line and page breaks in the original manuscript. The manuscript will be reformatted to use the journal's preferred fonts and layout.

PROOFS

Page proofs will be made available to authors (or to the designated corresponding author) at a Web site in PDF format. Failure to acknowledge the receipt of proofs or to return corrections within the requested deadline may cause publication to be postponed.

Journal of Mechanics of Materials and Structures